In-situ Laue diffraction to follow dislocation patterning during fatigue

THÈSE N° 7073 (2016)

ÉCOLE POLYTECHNIQUE FÉDÉRALE DE LAUSANNE

POUR L'OBTENTION DU GRADE DE DOCTEUR ÈS SCIENCES

PAR

Ainara IRASTORZA LANDA

EPFL

ÉCOLE POLYTECHNIQUE
FÉDÉRALE DE LAUSANNE

Suisse
2016

Acknowledgements

It is a pleasure to thank the many people who made this thesis a reality.

I would like to start expressing my sincere gratitude to my supervisor Prof. Helena Van Swygenhoven for her continuous support during these four years, for her patience, motivation, enthusiasm and immense knowledge. Her understanding and personal guidance have been of great value for me and I am very grateful to her for giving me the opportunity to be part of the MSS-NXMM-PEM group and for having made possible all the countless good memories I have collected during this research adventure.

I would like to give special thanks to my co-supervisor, Dr. Steven Van Petegem, for his guiding and constructive comments, and for his valuable help throughout this work. Thank you for answering all the questions and queries and for keeping on coming to our office even at the risk of being trapped for hours.

I would also like to thank the members of my dissertation committee, Prof. Andreas Mortensen, Prof. Ludovic Thilly, Prof. Javier Gil Sevillano and Prof. Paul Muralt, for their dedication, time and insightful comments of this thesis.

I am indebted to Alex Bollhalder for his extraordinary help and expertise in the development phase. Thank you for the entertaining conversations during our frequent visits to the workshop. I also want to acknowledge the mXAS beamline people, Dr. Daniel Grolimund, Beat Meyer and Mario Birri, for their constant support and dedication to make the beamline ready for the show. Special thanks to Dr. Stefan Brandstetter for being brave enough to allow us borrowing the detector without which this thesis would not have been possible. Thanks also to Dr. Elisabeth Müller, Dr. Vitaliy Guzenko and Dr. Rolf Brönnimann for sharing their knowledge and helping me to find solutions to different challenges faced during sample preparation. I would also like to thank the collaborators of the project, Dr. Koen Freytag from PSI and Dr. Jens Nellessen and Dr. Steffie Sandlöbes from MPIE – Düsseldorf, for their helpful discussions and interesting inputs. My warmest thanks also go Renate Bercher and Martina Füglister for making somehow -still unclear how though- all the administrative procedures work.

It has been a pleasure working with all colleagues and friends who have contributed to create an enjoyable atmosphere from all the unforgettable stories in the coffee breaks, over lunch, around ice creams, during beamtimes, German course, dinners, hikes and several other events. Many thanks go to former and current colleagues of the MSS-NXMM-PEM group: Mario Velasco, Dr. Deniz Keçik, Dr. Christophe Le Bourlot, Dr. Julia Repper, Dr. Vadim Davydov, Dr. Patrick Schloth, Dr. Manas Upadhyay, Karl Sofinowski, Wei Hsu, Dr. Maxime Dupraz, Marina García, Dr. Efthymios Polatidis and Dr. Miroslav Smid. Special thanks to Nicolò Grilli for all the time dedicated to the simulations of this project, to Dr. Antoine Guitton for his immeasurable commitment to open a new route to prepare the samples, to Dr. Tobias Panzer for his wonderful German-English translations and for getting me into the real Thai world, and to Dr. Michael Wedel for all the pleasant and 'fruity' chats and emails. I am especially grateful to Dr. Cécile Marichal for all her advices, her joy and her enthusiasm shown from the first day. Merci beaucoup Moniata! And of course to my two girls, Saba Zabihzadeh and Zhen Sun: my deepest gratitude for sharing your life stories, for all the laughs and nice moments and particularly for our friendship. I could not have imagined better officemates for these four years. مم نون, 谢谢.

Mi más sincero agradecimiento va dedicado también a las siguientes personas que he tenido el placer de conocer en Suiza y que intencionadamente o sin querer han dejado huella en mí: a Nano por ser el rey de los desmadres, a

Abstract

The macroscopic strength of metals is determined by the dislocation arrangements that are formed when dislocations slip in the crystal lattice in response to the applied stress. Despite the extensive research carried out, the transition from uniform to non-uniform dislocation structures is not yet fully understood. This information is however essential to support the development of computational models that aim to predict dislocation patterning. Lattice rotation caused by the presence of dislocations is, for instance, a parameter that is often not taken into account in computational models although it plays a role in the development of dislocation ensembles. Experimentally following in-situ dislocation patterning including involved lattice rotations at lengthscales comparable to those in simulations is not straightforward. In fact, the current available techniques that have the necessary spatial and angular resolution are either destructive (3D-EBSD) or very time consuming (3D X-ray Laue diffraction).

In this dissertation we present a new experimental approach that allows following lattice rotation and dislocation ensembles time-resolved during deformation. The technique is based on X-ray Laue diffraction scanning in transmission mode, which provides a sub-micron spatial resolution in 2D and statistical information on orientation spread in the third dimension. The in-situ mechanical tests are performed at the microXAS beamline of the Swiss Light Source Synchrotron. The method has been applied to understand dislocation patterning of copper single crystals occurring in the earlier phases of low cycle fatigue. Samples with different crystal orientations (single crystal, coplanar and collinear) have been cyclically deformed up to a maximum of 120 cycles. A dedicated miniaturized shear-fatigue device compatible with Laue diffraction has been constructed for that purpose and a sample preparation based on picosecond laser ablation has been developed.

The developed procedure analyzes the evolving dislocation microstructures in terms of lattice rotation, lattice curvature and geometrically necessary dislocation densities at lengthscales similar to those addressable in computational models. It sacrifices on the fully 3D aspect but it brings the time resolution required to validate ongoing simulations. It has been shown that the error made by integration depends on the dislocation network expected. For instance, the technique can be used to validate 3DDD models or density based dislocation dynamics models when applied in deformation geometries where the formation of 2D dislocation patterns are expected (e.g. vein-channel structure in single slip oriented fatigued samples).

The greatest advantage of this technique is that the evolving regions are easy to follow due to the high rotational sensitivity and time resolution of the method. What is more, the influence of the initial microstructure can be evaluated and quantitative values can be provided. On the other hand, the principal drawbacks are related to the gauge thickness of the samples. Even if the technique can estimate the orientation spread along the third direction, the approach cannot physically resolve the integrated signal along the thickness. This is source of uncertainty when providing actual values of lattice curvatures and geometrically necessary dislocation densities. Another shortcoming is the sensitivity of the method to the energy distribution of the X-ray beam provided in the beamline, which determines the collected signal – the principal basis of the subsequent analysis and interpretation.

Keywords

Zusammenfassung

Die makroskopische Stärke der Metalle wird durch die Versetzungsanordnungen bestimmt, die gebildet werden, wenn Versetzungen in dem Kristallgitter in Reaktion auf die aufgebrachte Spannung gleiten. Trotz der umfangreichen durchgeführten Forschung ist der Übergang von der gleichförmigen zu ungleichförmigen Versetzungsstrukturen noch nicht vollständig verstanden. Diese Information ist jedoch wichtig, um die Entwicklung von Computermodellen zu unterstützen, die die Vorhersage der Versetzungsstruktur zum Ziel haben. Gitterrotation, die durch das Vorhandensein von Versetzungen verursacht wird, ist zum Beispiel ein Parameter, der häufig nicht in Rechenmodellen berücksichtigt wird, obwohl er eine Rolle bei der Entwicklung der Versetzungsstrukturen spielt. In-situ Experiment, die Versetzungsstrukturen einschließlich der beteiligten Gitter Rotationen in Längenbereichen vergleichbar mit denen in den Simulationen verwendeten messen, sind nicht einfach. In der Tat sind die derzeit verfügbaren Techniken, die die notwendige Raum- und Winkelauflösung liefern, entweder destruktiv (3D-EBSD) oder sehr zeitaufwendig (3D-Röntgen Laue-Beugung).

In dieser Arbeit präsentieren wir eine neue experimentelle Methode, welche eine zeitaufgelöste Messung der Gitter Rotation und der Versetzungsstruktur während der Deformation ermöglicht. Die Methode basiert auf der Röntgenbeugungsabtastung im Laue-Transmissionsmodus, die eine sub-mikrometer Auflösung in 2D und statistische Informationen über die Orientierungsverbreiterung in der dritten Dimension bereitstellt. Die In-situ-mechanische Prüfungen wurden an der microXAS-Strahllinie des Swiss Light Source Synchrotron durchgeführt. Das Verfahren wurde angewendet, um Versetzungsstrukturen von Kupfer-Einkristallen zu verstehen, welche in den frühen Phasen eines zyklischen Ermüdungstests auftreten. Die Proben mit unterschiedlichen Kristallorientierungen wurden zyklisch mit maximal 120 Zyklen verformt. Zu diesem Zweck wurde eine optimierte, miniaturisierte Scherung-Ermüdungs-Vorrichtung konstruiert, die kompatibel mit einem Laue-Beugung Aufbau ist. Für die Probenvorbereitung wurde eine Technik auf Basis von Pikosekunden-Laser-Ablation entwickelt.

Die entwickelte Methode analysiert die Evolution von Versetzungen in den Mikrostrukturen in Bezug auf die Gitter Rotation, Gitterkrümmung und geometrisch notwendige Versetzungsdichten in Längenbereichen ähnlich denen, die in den Rechenmodellen zugänglich sind. Es opfert den vollen 3D-Aspekt, bringt aber die notwendige Zeitauflösung, die zur Validierung der laufenden Simulationen erforderlich ist. Es hat sich gezeigt, dass der durch die Integration verursachte Fehler stark von der erwarteten Versetzungsstruktur abhängt. Zum Beispiel kann die Technik verwendet werden, um 3DDD Modelle oder Dichte basierend Versetzungsdynamikmodelle zu validieren, wenn Verformungsgeometrien angewendet werden, bei denen die Bildung von 2D Versetzungsstrukturen zu erwarten sind (z.B. Venen-Kanal Struktur in Ein-Gleitebenen orientierten Ermüdungsproben).

Der größte Vorteil dieser Methode ist, dass sich die entwickelnden Regionen aufgrund der hohen Rotationsempfindlichkeit und Zeitauflösung des Verfahrens einfach zu verfolgen sind. Außerdem können der Einfluss der anfänglichen Mikrostruktur untersucht und quantitative Werte bereitgestellt werden. Auf der anderen Seite hängen die prinzipiellen Nachteile der Methode mit der Probendicke zusammen. Selbst wenn die Technik die Orientierungsverbreiterung entlang der dritten Richtung abschätzen kann, kann die Methode das integrierte Signal entlang der Dicke physikalisch nicht auflösen. Dies ist die Fehlerquelle, wenn Istwerte für die Gitterkrümmungen und die geometrisch erforderlichen Versetzungsdichten bereitgestellt werden. Ein weiterer Nachteil ist die Empfindlichkeit der Methode auf die Energieverteilung des Röntgenstrahls in der Strahllinie, die das gemessene Signal bestimmt - die wesentliche Grundlage für die nachfolgende Analyse und Interpretation.

Stichwörter

Kristallrotation, Versetzungen, Ermüdung, in-situ mechanische Prüfung, Musterbildung, Röntgen mikro-Laue-Beugung

Contents

List of Figures

List of Tables

List of symbols and abbreviations

AlMgSi	Aluminium-Magnesium-Silicon alloy
CLSM	Confocal laser scanning microscopy
CPFE	Crystal plasticity finite element
CSS	Cyclic stress-strain curve
Cu	Copper
DAMASK	Düsseldorf Advanced Material Simulation Kit
DAXM	Differential-aperture X-ray microscopy
DDD	Discrete dislocation dynamics
e-beam	Electon beam
EBSD	Electron backscatter diffraction
ECCI	Electron channeling contrast imaging
EDM	Electric discharge machining
fcc	Face centered cubic
FIB	Focus ion beam
FWHM	Full width at half maximum
GNB	Geometrically necessary boundary
GND	Geometrically necessary dislocation
HAZ	Geat affected zone
hkl	Miller indices
HR-EBSD	High resolution electron backscatter diffraction
HRRSM	High resolution reciprocal space mapping
LDM	Laboratory for Scientific Developments and Novel Materials
LMN	Laboratory of Micro and Nanotechnology
LNM	Laboratory for Nuclear Materials
MPIE	Max-Planck-Institut für Eisenforschung GmbH
OP-S	Oxide polishing solution
PDF	Probability density function
PMMA	Poly(methyl methacrylate)
PSB	Persistent slip bands
PSI	*Paul* Scherrer Institute
Si	Silicon
SLS	Swiss Light Source
SNF	Swiss National Science Foundation
SSD	Statistically stored dislocations
TEM	Transmission electron microscopy

$\boldsymbol{\alpha}$	Local dislocation density tensor
b	Burgers vector
D	Thermal diffusivity
d_{abl}	Diameter of the laser beam
d_{hkl}	Spacing of the (hkl) planes in the atomic lattice
Δx	Spatial separation
$\Delta\boldsymbol{\theta}$	Disorientation vector
$\mathbf{e}$	Euler axis
ϵ_{kij}	Levi-Civita permutation
F	Force
Fl	Fluence
F_o	Fluence threshold for ablation
F_{th}	Force threshold
$\boldsymbol{G}$	Bunge orientation matrix
γ	Shear strain
γ_{pl}	Resolved plastic strain
γ_{xy}^{p}	Resolved plastic shear strain
γ_{xy}^{res}	Total resolved shear strain
Γ	Cumulative resolved plastic shear strain
θ	Angle between *(hkl)* planes and the incident beam
θ_{mis}	Misorientation angle
$\boldsymbol{\theta}$	Lattice rotation vector
$\theta_x, \theta_y, \theta_z$	Rocking rotations around the X, Y and Z- axes
$\boldsymbol{I}$	Identitiy matrix
$\boldsymbol{\kappa}$	Lattice curvature tensor
l	Shear length
l_p	Penetration depth
λ	Wavelength of X-ray beam
m	Schmid factor
$\boldsymbol{R}$	Rotation matrix
ρ	Dislocation density
t	Thickness of the sample
τ_e	Electron cooling time
τ_l	lattice heating time
τ_p	Pulse duration
τ_s	Shear stress
τ_s^*	Saturation shear stress
u	Applied displacement
u'	Retracted displacement
U	Imposed displacement
w	Distance between mobile and fixed areas
$\omega_x, \omega_y, \omega_z$	Decomposed rotations around X-, Y- and Z-axes
Ψ	Azimuthal direction
2θ	Radial direction: angle between incoming and diffracted beam
$\emptyset$	Inner diameter of thin area

Chapter 1   Introduction

Dislocations, line defects in the crystal, move across the crystal lattice in response to the applied stress and self-organize into defined patterns that determine the macroscopic behavior of the materials (Argon, 2007; Kubin, 2013; Kubin et al., 2002). The developed dislocation arrangements depend on the applied loading conditions, orientation of the crystal and the structure and properties of the sample. For instance, Figure 1.1 shows the relationship between the mechanical response and dislocation patterns of tension-compression fatigued copper single crystal oriented for single slip. Three regions can be distinguished in the cyclic stress-strain (CSS) curve depending on the applied resolved shear strain (γ_{pl}) (Mughrabi, 1978) and the obtained saturation dislocation structures are specific to each region:

- In *region A* (γ_{pl} < 0.006%) work hardening occurs and primary slip dominates forming the so-called vein-channel structures.
- In the strain-independent *region B* (0.006% < γ_{pl} < 0.75%), known as 'plateau', the saturation shear stress τ_s^* is constant and is in the range of 28-30 MPa at room temperature (Cheng and Laird, 1981). The regime is characterized by the appearance of persistent slip bands (PSBs) that are considered precursors of cracks.
- In *region C* (γ_{pl} > 0.75%) work hardening occurs but secondary slip becomes more pronounced and as a consequence the labyrinth and cell dislocation structures are formed.
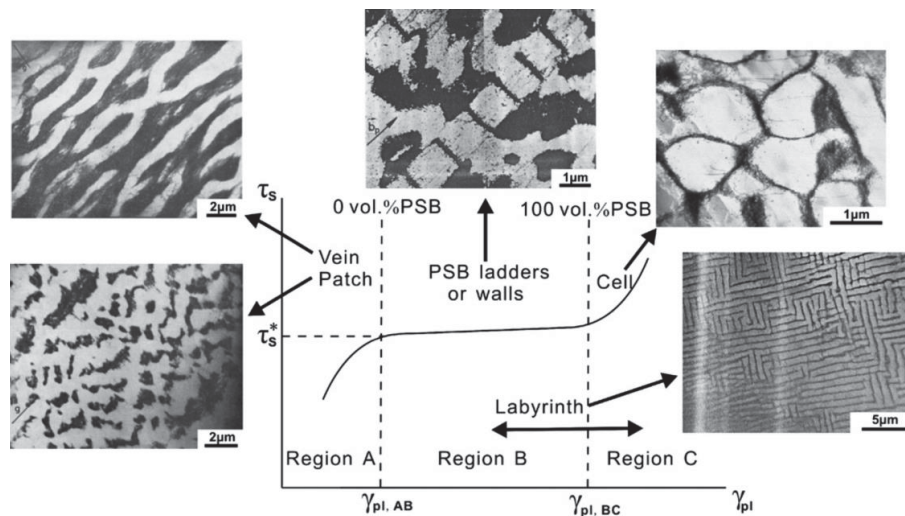
Figure 1.1 CSS curve and dislocation patterns of fatigued Cu single crystal oriented for single slip after (Li et al., 2011)

A lot is known on the fundamental interaction mechanisms of dislocations. However full understanding of how dislocations interact to evolve from a homogeneous distribution to heterogeneous structures and form patterns is still missing (LeSar, 2014). Computational models at all lengthscales (from dislocation dynamics (10^{-7} m) to continuum dynamics (10^{-1} m)) have been used to understand the transition. Even if the typical lengthscale of dislocation patterns is at the micron scale, their formation involves multiple dislocation interactions and slip mechanisms at smaller scales, as well as lattice rotation. That is why the evolution is difficult to describe as each computational model has a characteristic lengthscale and therefore can generally address only particular aspects of dislocation patterning. Recently, the length and time scales of different computational methods have begun to

overlap and hierarchical or concurrent multiscale frameworks are available (Roters et al., 2010; Vattré et al., 2014). They have the potential to provide a real breakthrough in the understanding of dislocation patterning.

Most of the computational models aiming to describe patterning do not take into account lattice rotations caused by the presence of dislocations. How critical the latter are for accurate dislocation pattern prediction is still unclear. Perreault and co-workers (Perreault et al., 2016) have developed a phenomenological model for dislocation motions in 2D lattices and report that lattice rotations create local distortion of the slip planes that can prevent dislocation annihilation of two opposite edge dislocations and assist in the formation of dipoles. Shehadeh (Shehadeh, 2012) has analyzed the influence of lattice rotation in shock-induced deformed copper single crystal and has evidenced that lattice rotation enhances microband formation by activating a kink mechanism that locally reorients the slip planes. Li and co-workers (Li and Zhang, 2014), on the other hand, suggested that the gradual lattice rotation caused during cyclic loading can be the main driving force for the formation of deformation bands in fatigued copper single crystals oriented for double or multiple slip (Li et al., 2002). These works suggest that the influence of lattice rotation in dislocation dynamics is essential during the development of dislocation ensembles during the transition from uniform to non-uniform structures. Thus, to validate ongoing simulations detailed experimental data are required. Albeit, following in-situ dislocation patterning including involved lattice rotations experimentally at lengthscales comparable to those in simulations is not straightforward (Pollock and LeSar, 2013; Dingreville et al., 2015).

This chapter is divided in three sections. The first section is a review of different experimental techniques that can track dislocation dynamics, provide measurements of dislocation density and can evidence lattice rotation. The second section summarizes briefly the latest advances done on computational field regarding patterning, underlining the need for experimental validation. In the last section the motivation and objectives of this investigation are presented.

1.1   Overview of experimental techniques to follow dislocation dynamics

Transmission electron microscopy (TEM) has been traditionally used to observe dislocation microstructures. TEM images taken at specific strains after continuous deformation (Mader et al., 1963; Mughrabi, 1971a, 1971b, 1971c; Prinz and Argon, 1980) or at different stages during fatigue cycling (Ackermann et al., 1984; Buchinger et al., 1985; Mughbrabi et al., 1979; Winter et al., 1981) allows making a reconstruction of the dislocation pattern evolution. This destructive procedure is nowadays still the principal technique used to investigate for example the microstructure progression from planar to cellular structures of engineering materials such as polycrystalline steel subjected to fatigue (Pham and Holdsworth, 2013; Pham et al., 2011).

The advances of the last decade have allowed to couple TEM characterization with in-situ mechanical testing where slip of dislocations can be followed during deformation (Legros, 2014). The range of in-situ applications is very wide. Stress-induced phase transformations (Liu et al., 2016), mechanical annealing (Cui et al., 2016), determination of slip systems (Jing et al., 2016), observations of dislocation nucleation (Oh et al., 2009), strain measurements (Hÿtch and Minor, 2014) or understanding aspects of dislocation patterning during tensile test (Landau et al., 2010) are some of the examples of the versatility. Tomography based 3D-TEM makes it now possible to reconstruct 3D dislocation structures (Hata et al., 2011; Liu et al., 2014) and there are several TEM-based techniques for orientation mapping (Zaefferer, 2011). For instance, with a TEM coupled with precession assisted crystal orientation mapping technique (PACOM), commercially known as ASTAR, misorientation maps can be collected in the nanometer-scale with a sensitivity of 0.10° (Viladot et al., 2013).

The information obtained with TEM misses statistics due to the limited field of view (~ 10 μm^2). It is an ideal to study specific dislocation mechanisms such as dislocation locking versus easy glide and compare to predictions of first-principle calculations (Clouet et al., 2015) or to study dislocation motions (Mompiou et al., 2012) in order to validate molecular dynamics or discrete dislocation dynamics simulations. The limited field of view is a serious constraint to understand dislocation patterning. Additional drawbacks of TEM are sample preparation, during which the microstructure can be altered when getting extremely thin samples, and surface.

Electron channeling contrast imaging (ECCI) can spatially resolve dislocation patterns evolved in the first 50 to 100 nm of the material below the surface at a larger field of view than TEM (Zaefferer and Elhami, 2014). The observed dislocations can be counted and the full dislocation density can be determined. The technique has allowed to determine the distribution of dislocations along depth in a nanoindent (Zhang et al., 2015) and to follow the evolution of dislocation ensembles during in-situ heat treatment (Barnoush, 2012). ECCI has also been used to study dislocation structures of fatigued samples, most investigations however focused on the saturation stage (Ahmed et al., 1997, 1999; Li et al., 1998; Melisova et al., 1997). Ahmed and co-workers (Ahmed et al., 2006) have followed the dislocation structure evolution during cyclic deformation of copper. A short reconstruction of their work is given in Figure 1.2, where it can be observed that a vein-channel structure is formed before its transition to PSBs.
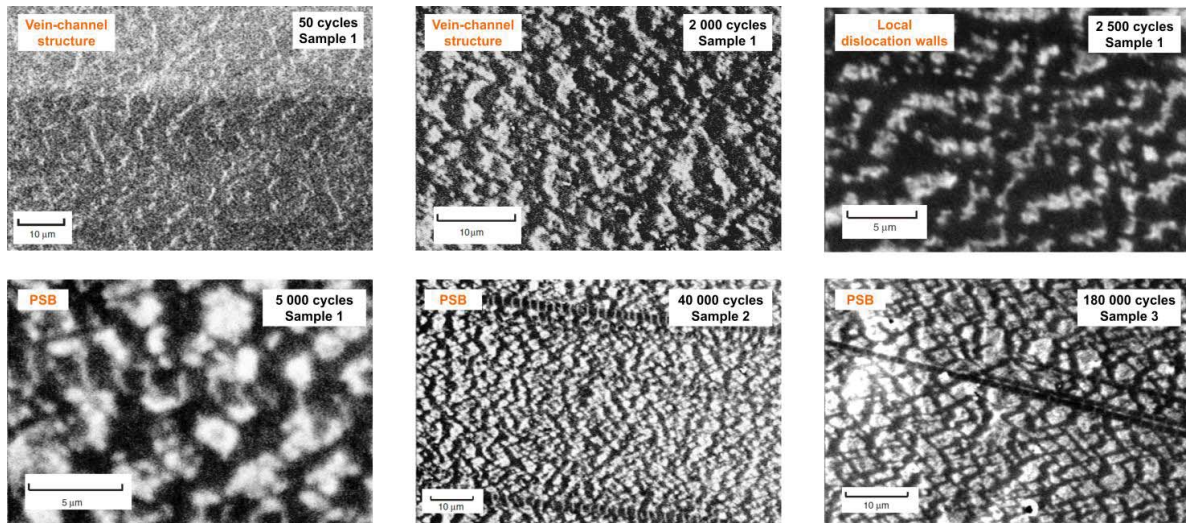
Figure 1.2 Reconstructed dislocation evolution of fatigued Cu single slip (γ_{pl} = 0.20%) after (Ahmed et al., 2006)

ECCI has the advantage of examining larger areas than TEM and can provide quantitative statistical values of width, separation and volume fraction of the dislocation structures formed. Such studies can be performed either examining one sample at different levels of deformation or several different samples. In this sense, ECCI is an excellent technique to validate the patterns predicted by discrete dislocation dynamics and continuum dislocation dynamics simulations. Misoriented regions can also be detected as bright or dark contrast zones but the misorientation values are seldom provided. As it provides only a surface image of the dislocation arrangements, a 3D visualization using destructive serial sectioning is necessary to obtain bulk information, as has been done in (Yamasaki et al., 2015).

Electron backscatter diffraction (EBSD) provides the crystallographic orientation field with angular resolutions of 10^{-2} rad and 10^{-4} rad in the case of high resolution (HR-EBSD) (Wilkinson, 2011). The angular resolution determines the sensitivity to misorientation and strain, which are reported to be 0.5-1° and 5×10^{-3} respectively for conventional EBSD and 0.01° and 10^{-4} in the case of HR-EBSD (Wilkinson and Britton, 2012; Wilkinson et al., 2006a, 2006b). Combined with in-situ heating recrystallization and grain growth processes can be analyzed, and combined with in-situ deformation the lattice rotation of individual grains as well as grain fragmentation or subgrain formation can be followed (Wright and Nowell, 2009). As opposed to ECCI, EBSD can provide information about geometrically necessary dislocation (GND) densities from orientation differences (Pantleon, 2008) and their evolution can be followed.

Figure 1.3 shows the HR-EBSD reconstructed distribution of GND densities of four copper polycrystalline specimens deformed in tension to 0%, 6%, 22.5% and 40% strains (Jiang et al., 2013). The 500 μm^2 maps obtained with 0.5 μm step size cover ~1500 grains, their boundaries marked by dark lines. Before deformation the grain boundaries have higher GND densities, at early stages of deformation the grain averaged GND density is

higher in smaller grains and after 10% strain there is no such inverse relationship. The technique allows following not only large areas but also specific oriented grains and permits analyzing the dislocation structure inside grains. For instance, dislocation cells tend to form in <110> oriented grains, and in <111> and <001> oriented grains more dislocation bands are reported. With HR-EBSD technique orientation and strain dependent tendencies of texture, GND densities and grain size can be analyzed. The EBSD signal however degrades for highly deformed samples (white areas after more than 20% deformation in Figure 1.3).
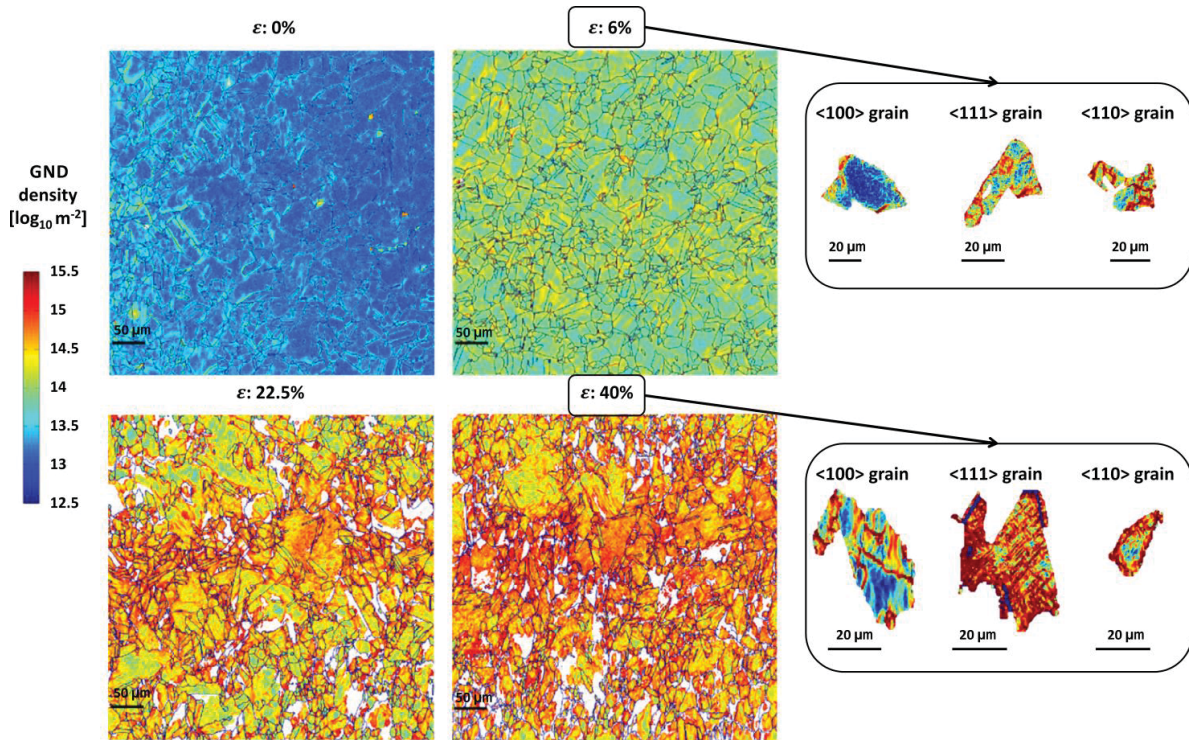
Figure 1.3 Reconstructed evolution of GND densities of copper polycrystal during tensile testing after (Jiang et al., 2013, 2015)

Several studies have been done on single crystals too. Crystal rotation and GND distribution during in-situ micro-compression of pillars (Maeder et al., 2011; Niederberger et al., 2010) or during in-situ 3-point bending (Jiang et al., 2016) have been reported. EBSD can also be coupled with ECCI (Gutierrez-Urrutia et al., 2013). For instance, it has recently been used to investigate the orientation dependence of the formation of dislocation substructures during fatigue for different strain and cycles in polycrystalline steel (Nellessen et al., 2015).

EBSD results can validate the outcome from continuum dynamics simulations. The EBSD technique is, however, a surface technique and in order to extend to bulk information serial sectioning is required (Calcagnotto et al., 2010; Demir et al., 2009; Konijnenberg et al., 2015).

Synchrotron based X-ray diffraction techniques can resolve 3D and non-destructively dislocation structures up to several microns. There are two main techniques: 3D X-ray diffraction (Poulsen et al., 2014) and 3D X-ray Laue diffraction (Larson et al., 2002). The former technique provides structural characterization of polycrystalline materials. High energy (20 – 100 keV) monochromatic beam is used and the sample is rocked to obtain the scattering intensity distribution. Near field (Li et al., 2012) or far field (Margulies et al., 2001; Oddershede et al., 2011, 2015) with sample-to-detector distances of 3-10 mm and 20-100 cm respectively, can be used to investigate rotation, orientation spread and subdivision of grains embedded in bulk polycrystals during deformation. When analyzing a single reflection in a farer field using a sample-to-detector distance of 3.6 m, a very high angular resolution can be obtained at the expense of spatial and time resolution (Pantleon et al., 2014). The technique called high resolution reciprocal space mapping (HRRSM) has been used to study the formation of

dislocation substructures in individual grains during continuous tensile test (Blondé et al., 2014; Jakobsen et al., 2006, 2007; Pantleon et al., 2009), under stress relaxation (Jakobsen et al., 2009; Pantleon et al., 2009) and during strain path changes (Pantleon et al., 2009; Wejdemann et al., 2013). The outcome of the Wejdemann and co-workers' work has been reconstructed in Figure 1.4. By following the reciprocal space map and by analyzing the radial X-ray peak profile and asymmetry the authors were are able to evidence a different behavior when deforming a sample continuously or with a strain path change. In the latter a microplastic regime has been identified where internal stresses are redistributed in order to establish proper load transfer. This regime is not observed during a continuous test.
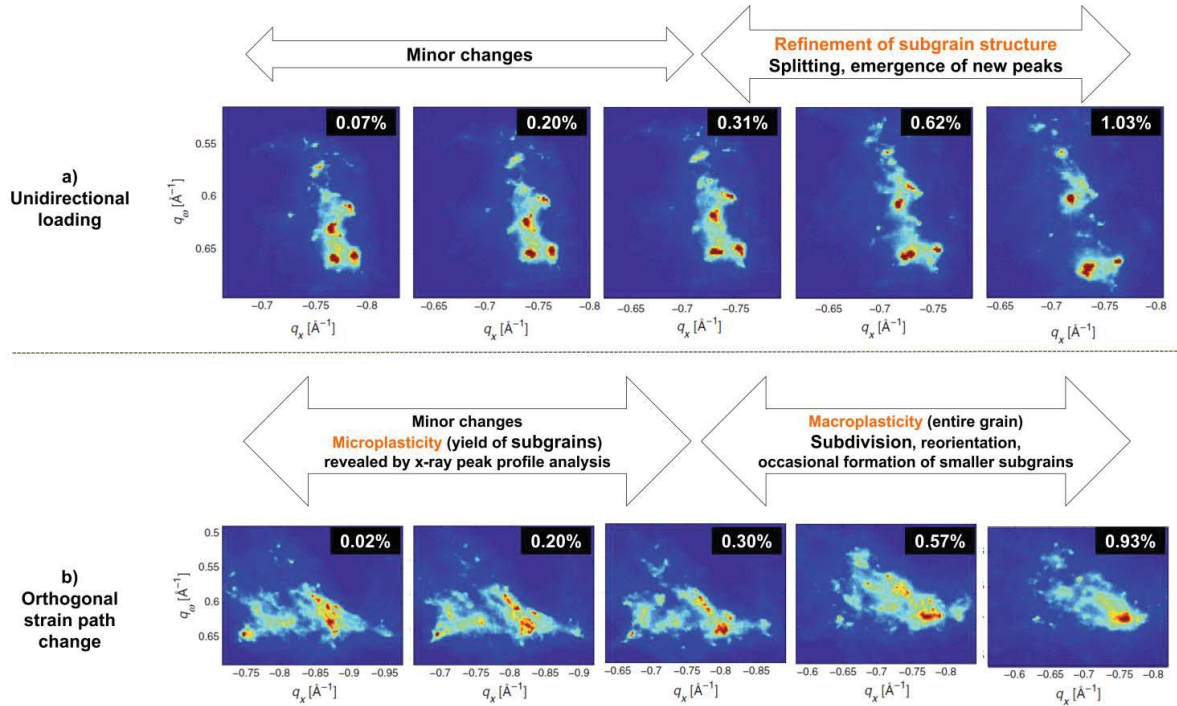
Figure 1.4 Reconstructed evolution of sub-grain structure during in-situ tensile loading of copper 5% pre-deformed without (a) and with (b) strain path change after (Wejdemann et al., 2013)

3D X-ray diffraction is a suitable technique to provide valuable quantitative input for hierarchical models that couple the nano to the meso scale. It is however inappropriate for following dislocation patterning and the involved lattice rotations because none of the techniques have both the necessary spatial resolution and angular resolution.

X-ray Laue diffraction using a polychromatic beam is a well-established technique to investigate lattice orientation and lattice strain of micron-sized single crystalline structures or individual grains in polycrystals. The spatial resolution is at the submicron level depending on the beam diameter (Ice et al., 2011). It can be used in transmission (Swygenhoven and Petegem, 2010) or reflection mode (Liu and Ice, 2014). Typically the energy range used is between 5 to 30 keV but high-energy transmission Laue is available which provides higher penetration depth (Hofmann and Korsunsky, 2013). It has been applied to characterize lattice rotations and distortions of individual dislocations (Hofmann et al., 2013) and to investigate deformation mechanism of single crystals during in-situ testing in compression (Marichal et al., 2013, 2014, Zimmermann et al., 2012a, 2012b; Maaß et al., 2006; Maaß et al., 2007), in tension (Kirchlechner et al., 2012a), in cyclic bending (Kirchlechner et al., 2012b, 2015) and in three-point bending (Leclere et al., 2015). Deformation of polycrystalline materials during in-situ testing (Joo et al., 2004; Korsunsky et al., 2012; Lynch et al., 2014) or post-mortem (Butler et al., 2002; Huang et al., 2009; Magid et al., 2009) has also been explored.

When working in reflection mode, lattice rotation and strain information as a function of depth can be extracted by using white beam differential-aperture X-ray microscopy (DAXM). It consists in passing an absorbing wire near the sample's surface, calculating the differential intensity distribution between two wire positions and then determining the source of the intensity (Larson et al., 2002; Yang et al., 2004). Absolute values of the dislocation density tensor can be obtained with a micron resolution in 3D (Larson et al., 2007). When combining DAXM with additional monochromatic energy scans the full elastic strain tensor is accessible (Levine et al., 2006, 2015) and long-internal stresses in individual dislocation cell walls and in adjacent cell interiors can be calculated similarly to HRRSM. Highly deformed copper single crystals in tension, compression and cyclically have been investigated (Kassner et al., 2009; Levine et al., 2011).

Figure 1.5 shows an example of the local orientations, the elastic strain tensor components and the dislocation density tensor components of an elastically bent silicon foil (Larson et al., 2008). The technique for obtaining 3D information is rather slow (Chung et al., 2007; Pang et al., 2014) and that is why it is generally calculated for 2D slices and not 3D volumes. Mohamed and co-workers (Mohamed et al., 2015) have measured rotation magnitudes, elastic distortion and dislocation density fields of compressed Cu single crystals to compare with results obtained by discrete dislocation dynamics simulations. Because the method is very time consuming, the analysis has only be done after 1.0% and 2.3% compression strains in 2D slices.
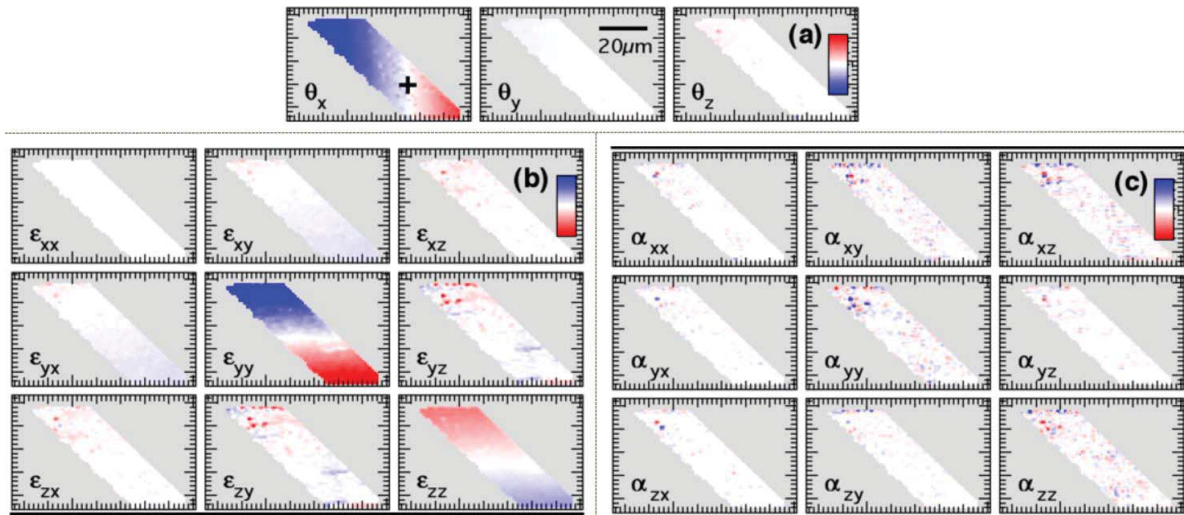
Figure 1.5 2D distribution of local orientations (a), elastic strain tensor (b) and dislocation density tensor (c) of elastically bent Si arch after (Larson et al., 2008)

The results obtained by Laue micro-diffraction can be used as experimental validation of discrete dislocation dynamics and continuum dislocation models. The main drawback is the time resolution required for 3D measurements which restricts the obtained microstructural information to very limited number of stages during the deformation process. In addition, the complexity of performing in-situ experiments during Laue micro-diffraction due to space constrains between the sample and the detector requires specific development of miniaturized mechanical systems.

An overview of the above described experimental techniques is given in Table 1.1. TEM and ECCI provide images of dislocation structures. EBSD and synchrotron based X-ray Laue diffraction are sensitive to orientation and strain and provide average measures of the dislocation content. While EBSD has finer spatial resolution, X-ray Laue diffraction has a finer angular resolution. For 3D characterization, EBSD is destructive. X-ray Laue diffraction can be applied non-destructively but has the disadvantage of being slow. The table clearly demonstrates the need for a time resolved characterization technique with adequate spatial and angular resolution that allows following dislocation patterning and that provides quantitative experimental information for validating ongoing simulation models.

Table 1.1 Brief summary of experimental techniques to characterize dislocation structures and densities

Technique		Resolution		Sensitivity		Obtained data
		Spatial	Angular	Misorientation	Strain	
TEM		0.02 μm	10^{-4}	0.1°	10^{-3}	Individual dislocations and patterns 2D In-situ 3D-information with tomography Restricted to thin films Limited field of view Sensitive to diffraction condition Orientation maps with ASTAR
ECCI		0.02 μm	10^{-4}	Combined with EBSD		Individual dislocations and patterns Superficial (100 nm) 2D In-situ 3D-information after sectioning Full dislocation tensor Requirement of good surface quality Sensitive to diffraction condition
EBSD	Standard	0.02 μm	10^{-2}	0.5°- 1°	5×10^{-3}	Orientation and strain maps GND density information Superficial (<100 nm) 2D In-situ 3D-information after sectioning Degradation of signal for highly deformed materials
EBSD	HR-EBSD	0.02 μm	10^{-4}	0.01°	10^{-4}	
3D X-ray diffraction	Near field	1-2 μm	*1	0.05°-0.1°	10^{-4}	Synchrotron based technique Orientation and strain maps GND density information Sample rotation required Suitable for polycrystals & thick samples 3D In-situ
3D X-ray diffraction	Far field	2-10 μm	*1	0.1°	10^{-4}	
3D X-ray diffraction	HRRSM	10 μm	*1	*2	10^{-4}	
X-ray Laue diffraction		≤1 μm	10^{-4}	0.01°	$10^{-5} - 10^{-4}$	Synchrotron based technique Orientation and strain maps Penetration depth <50-100 μm GND density information Suitable for single crystals or large grain polycrystals DAXM: 3D information (2D slices) Energy scan: full strain tensor (2D slices) Usually 2D In-situ

*1 The angular resolution of the 3D X-ray diffraction techniques depends on many factors (e.g. beam size, sample-to-detector distance, wavelength of the beam, pixel size of the detector). Therefore it can vary from experiment to experiment. Briefly, the larger the sample-to-detector distance the higher the angular resolution. The drawback is the loss of spatial and time resolution.

*2 The HRRSM technique has a very high angular resolution and can analyze substructures in individual grains but it cannot provide misorientation values.

1.2   Overview of computational techniques to predict dislocation patterning

Computational modeling has been carried out to understand dislocation based plasticity at the mesoscale (Kubin, 2013). As previously explained, dislocation patterns have a typical lengthscale at the micron scale and their formation involves multiple dislocation interactions and slip mechanisms at the nanometer scale. That is why the transition from homogeneous to heterogeneous dislocation microstructures with dislocation depleted and dislocation rich zones is difficult to describe (Ananthakrishna, 2007). Even if many theories have been proposed to describe the collective behavior of dislocations to form cell structures under continuous deformation involving multislip condition or the vein-channel structures and the PSBs observed in single slip cyclic

deformations (Amodeo and Ghoniem, 1990; Fournet and Salazar, 1996; Franěk et al., 1991; Hähner, 1996; Hesselbarth and Steck, 1992; Holt, 1970; Kratochvíl, 1988; Kratochvíl, 2001; Kubin, 1993; Saxlová et al., 1997; Walgraef and Aifantis, 1985a, 1985b, 1986), the effort to understand the physics of dislocation patterning is still an ongoing challenge.

Figure 1.6 shows TEM images and schematic diagram of dislocation arrangements of the mentioned structures. Briefly (Argon, 2007; Suresh, 1998):

- *Cell structure:* it consist of regions of high density of dislocations (cell walls) separated by cell interiors of low dislocation density. Cell walls form only about 10% of the total volume and most dislocations are trapped in these walls.
- *Vein-channel structure:* it consists of accumulated primary dislocations in the form of dipoles separated by dislocations free channels. Depending on the γ_{pl} the vein volume fraction varies, reaching the maximum value of 50% in the initial part of plateau region. Very few primary screw dislocations are observed, situated mainly in the channels, and it is believed that they mutually annihilated by cross-slip.
- *PSB structure:* PSB are formed by thin lamellae parallel to the primary glide plane and perpendicular to the primary Burgers vector. They are arranged in a ladder like structure and consist of a dense set of dipolar edge dislocations separated by channels. The channels have at least two orders of magnitude lower dislocation density and they are mainly populated with screw dislocations. Dislocation multiplication happens due to the bowing-out of edge dislocations from the walls and by their transport along channels.

The basic distinction in the patterns arises from the differences in the underlying dislocation mechanisms: vein-channel and PSB structures are structures formed by dipoles, the cell structure on the other hand is not a dipolar configuration.
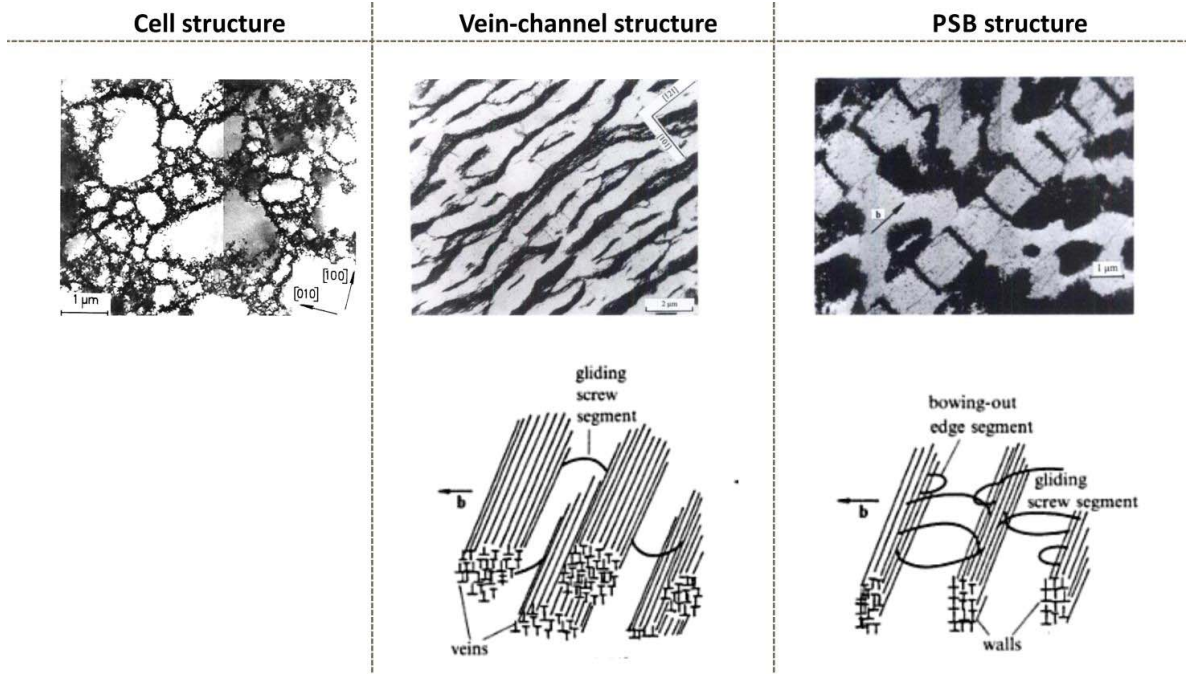
Figure 1.6 TEM and schematics of cell, vein-channel and PSB structures. Pictures taken from (Mughrabi et al., 1986; Suresh, 1998)

In spite of their limitation in length scales and in total strain that can be simulated, discrete dislocation dynamics (DDD) models have given access to detailed information on dislocation clustering. By activating and deactivating different elemental interaction mechanisms they allow to determine which ones play a major role in pattern

formation. Simulations have been done in 2D (Bakó and Hoffelner, 2007; Groma and Bakó, 2000; Groma and Balogh, 1999), in 2.5D (Gómez-García et al., 2006) and in 3D (Hussein et al., 2015; Madec et al., 2002) and have revealed important information. For instance they showed that during continuous deformation elastic dislocation-dislocation interactions alone do not produce cell structures, while short-range interaction and cross-slip or climb appear as the main mechanisms governing dislocation cell formation.

Several aspects about cyclic deformation have been investigated by DDD. Most effort has been put on understanding the plastic deformation inside PSBs (El-Awady et al., 2007; Erel, 2015; Kolář et al., 2015; Kristan and Kratochvíl, 2007, 2010; Po et al., 2014; Schwarz and Mughrabi, 2006). Starting from realistic PSB structures, the fundamentals of dipolar wall formations and dislocation interactions in the PSB channels have been analyzed by (Brinckmann and Van der Giessen, 2004; Erel, 2015) to determine the mechanisms of crack formation in PSBs.

Regarding fatigue patterning, Déprés and co-workers (Déprés et al., 2004, 2006, 2014) have done extensive work by investigating the evolution of dislocation microstructure and mechanical behavior in early stages of the formation of PSBs, by looking at surface marking and crack propagation of low-cycle fatigued polycrystalline steel. Figure 1.7-a shows a section of the dislocation microstructure obtained in cyclically deformed steel by DDD simulations, Figure 1.7-b shows the corresponding schematic description (Déprés et al., 2004). While the dislocation tangles represent the vein structures, the PSBs are made up of rows of parallel prismatic loops aligned in the primary slip system. It is reported that cross-slip is necessary for the formation of PSBs.
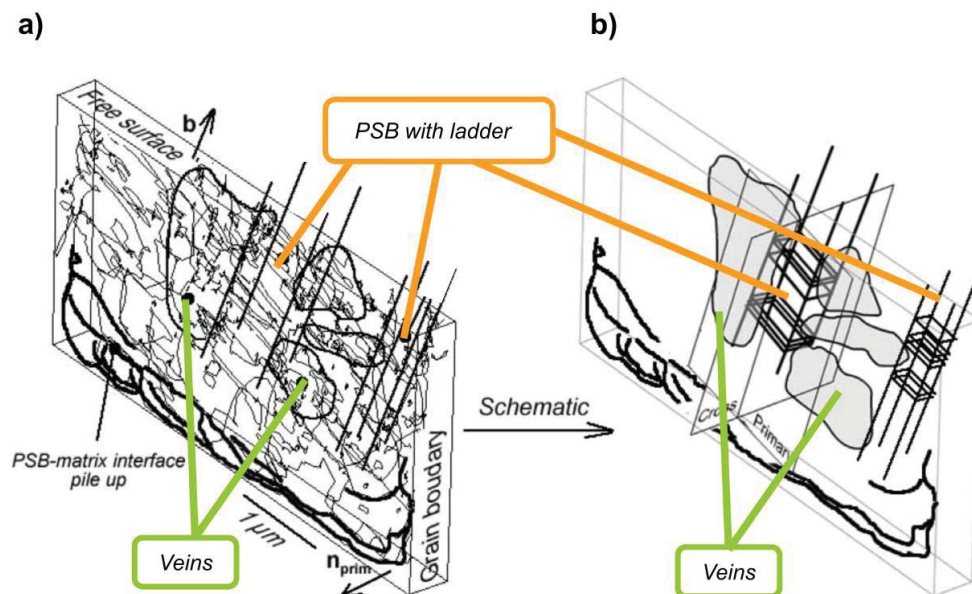
Figure 1.7 Simulated PSB structure in a surface grain of a polycrystalline steel after (Déprés et al., 2004)

More recently, Hussein and El-Awady have analyzed the microstructure evolution and cyclic hardening during the early stages of fatigue loading of single crystal nickel oriented for multiple slip (Hussein and El-Awady, 2016a). They report that not only cross-slip plays an important role in the subsequent evolution of the cell structure, but also the crystal size and the initial dislocation density: for a given initial dislocation density (1 μm^2) the formation of cell structures is not observed in small specimens (<2 μm) but it is in larger crystals (>2 μm). The influence of the crystal size and initial dislocation density in the evolution of the surface roughness was also studied (Hussein and El-Awady, 2016b). It is reported that double cross-slip is the main mechanism for development of surface roughness. Figure 1.8 shows a brief summary of the obtained results: the predicted microstructure is given as 2D TEM-like slices where the cell walls and interiors can be distinguished; the roughness is reported to be proportional to the number of loading cycles and the square of the crystal size.
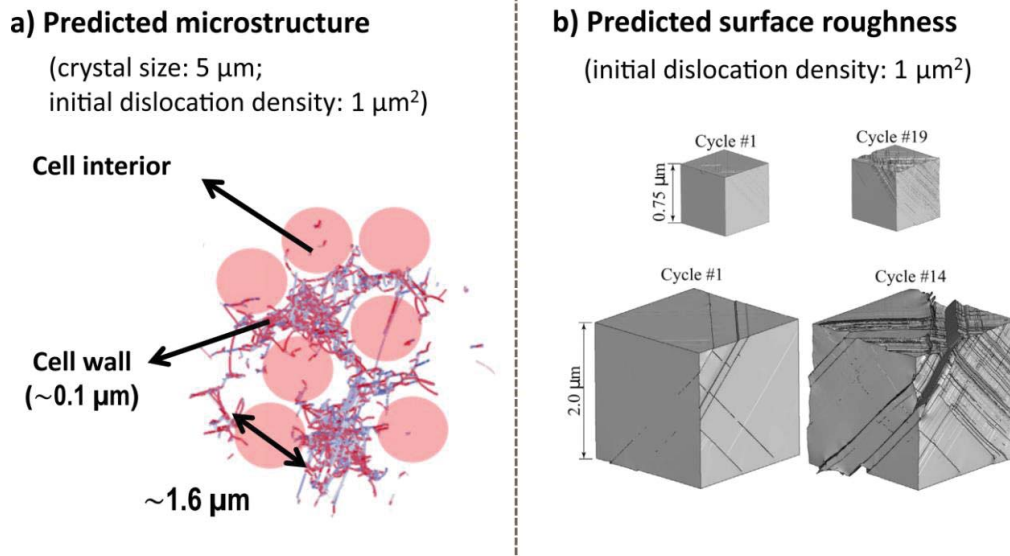
Figure 1.8 Simulated cell microstructure and surface roughness in fatigued single crystal nickel after (Hussein and El-Awady, 2016a, 2016b)

Continuum dislocation dynamics theories have been developed in order to deal with larger scales than those accessible with DDD simulations. In those computational models, dislocations are often separated into two different categories: statistically-stored dislocations (SSD), which evolve from random trapping processes during plastic deformation, and GNDs (Ashby, 1970). The concept of GND was already introduced by Nye (Nye, 1953) to rationalize the compatibility of elastic-plastic deformation in materials experiencing strain gradients. GNDs introduce a characteristic length scale in the continuum formation of plastic deformation and give rise to deformation-induced long-range internal stresses (Mughrabi, 2006a; Needleman and Gil Sevillano, 2003).

Different approaches have been followed to simulate the cell structure formed during continuous deformation:

- Chen and co-workers (Chen et al., 2010, 2013) have qualitatively reproduced the cell structure using the phenomenological approach developed by (Acharya and Roy, 2006). In this framework, dislocations are represented in terms of an overall dislocation density tensor (including only GNDs). In this simple model, slip systems, crystalline anisotropy, dislocation nucleation, lock formation or dislocation line tension are not considered. The model does in some way exhibit a realistic evolution of cell structure (see Figure 1.9-a). Nevertheless, as the model does not take into account SSDs it cannot be applied to predict the initial stages of fatigue dislocation patterning because the dipolar clustering associated to SSDs would not be captured.
- Xia and El-Azab (Xia and El-Azab, 2015a, 2015b) on the other hand use a statistical approach (El-Azab, 2006) that takes into account those inherent properties of dislocations not accounted for by Chen and co-workers. They investigate the cell structure formation and report that the GND distribution is tied to lattice misorientation (see Figure 1.9-b). Besides, their simulations underline the importance of cross slip, short range reaction and density multiplication due to the motion of curved dislocation lines creating the cells. Cell formation is observed to be a dynamic process between refinement, destruction and recreation. The surface distortion created by cells is also predicted.
- Sandfeld and Zaiser (Sandfeld and Zaiser, 2015) have recently presented a model for cell pattern formation based on the framework developed by Hochrainer and co-workers (Hochrainer et al., 2014; Sandfeld et al., 2010). They present the first steps towards a generic model to capture patterning based on GNDs, SSDs and specific kinematics of curved dislocation lines, all of them necessary components to represent 3D processes. Similarly to Xia and El-Azab, they point out that cross-slip and short-range reactions are the "minimum ingredients" for cell formation. Their results are summarized in Figure 1.9-c.

a) Cheng et al. (2013)

GND density   Lattice rotation

b) Xia and El-Azab (2015a,2015b)

Average dislocation density   Lattice rotation   Surface distortion

c) Sandfeld and Zaiser (2015)

Total dislocation density   Edge component of GNDs   GND density
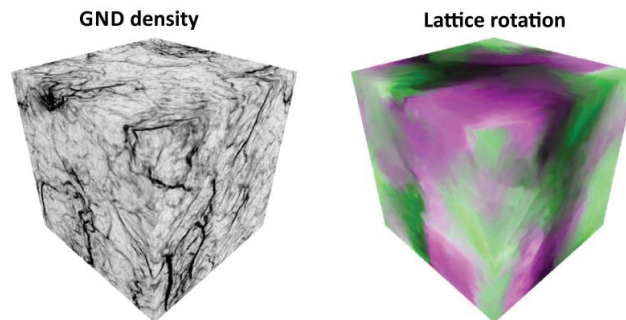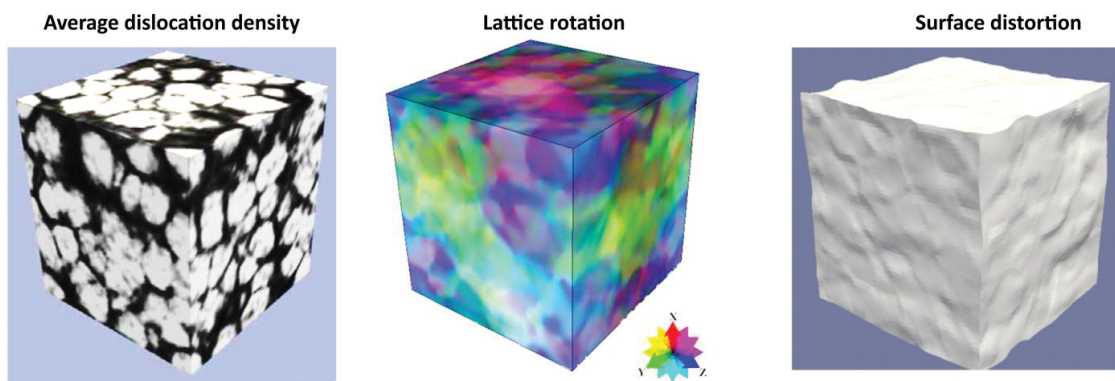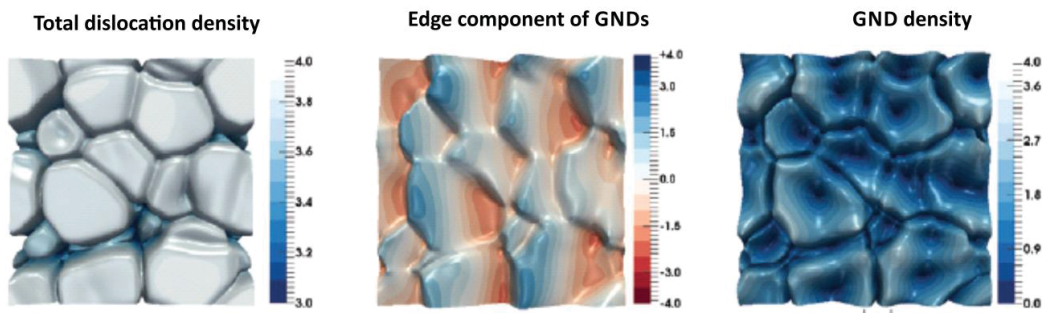
Figure 1.9 Simulated cell patterns: a) after (Chen et al., 2013), b) after (Xia and El-Azab, 2015a, 2015b) and c) after (Sandfeld and Zaiser, 2015)

Continuum dislocation dynamics have also been employed to look at dislocation patterns during cyclic deformation, where the dislocation-rich areas are characterized by edge dislocations in dipole form. These dipoles, which are considered SSDs, play an important role in patterning. According to TEM and X-ray Berg-Barret topography investigations, negligible lattice rotation is observed across veins and PSBs (Neumann, 1987; Wilkens et al., 1980). The details are however dependent on the diffraction conditions and it is nowadays unclear how the lattice rotation evolves (Mughrabi, 2006a). The latest advances in the field can be summarized as follows:

- Kratochvíl and co-workers have developed specific mechanisms for sweeping of narrow dislocation dipoles (Kratochvíl and Sedláček, 2003) and also models to describe the interaction dynamics between dislocations and dipolar loops (Kratochvíl and Sedláček, 2008; Minárik et al., 2010).

- Chapman and co-workers investigated the transition from channel-vein to PSBs (Chapman et al., 2016; Zhu and Chapman, 2014), and reported the importance of incorporating SSDs into macroscopic models to understand the emergence of PSBs. They suggested incorporating two field variables, one to account for GNDs and another for SSDs, whose evolution equations are different.
- Grilli and co-workers (Grilli et al., 2015) have elaborated a new fatigue model incorporating (1) double cross-slip mechanisms to avoid the complete annihilation of opposite signed curved dislocations and (2) new equations for the dipole distance distribution and dislocation multiplication law. It has been implemented in the DAMASK crystal plasticity finite element (CPFE) framework developed by Roters and co-workers (Roters et al., 2010). As shown in Figure 1.10 the emergence of vein and channel structures starting from a randomly perturbed dislocation distribution is predicted after 100 cycles at γ_{pl} =0.1%. It has been observed that these veins cause lattice rotation, as it is discussed in Chapter 5 of this thesis.
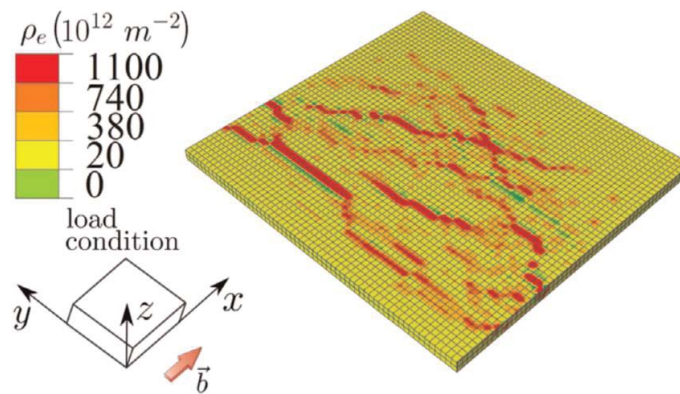
Figure 1.10 Simulated vein-channel structure after (Grilli et al., 2015)

In addition to the simulation results explained above, other aspects of pattern formation and dynamics are currently being investigated in order to expand the current understanding. For instance, Zhou and co-workers (Zhou et al., 2015) examine the dynamics of driven dislocation assemblies and show their similarity to phases observed in superconductors vortices, magnetic domain walls, and charge density wave materials. On the other hand, El-Naaman and co-workers (El-Naaman et al., 2016) consider the influence of high-order strain gradient to account for high slip gradients in small region as continuum models tend to show a much smoother GND field than reality. Further advances are expected that will help to elucidate the mechanisms for dislocation pattern formation, a field that despite its years is not yet mastered.

1.3   Motivation and objectives

The main objective of this thesis is to develop an X-ray Laue diffraction based technique that allows following dislocation ensembles time-resolved during deformation while providing quantitative information on the transition from uniform to non-uniform dislocation structures useful for ongoing simulations. In other words we aim to develop a non-destructive technique that has the spatial and angular resolution required to investigate dislocation patterning with improved time resolution.

Dislocation pattering of copper single crystals occurring in the earlier phases of low cycle fatigue is investigated by analyzing the crystal rotation caused by evolving microstructures with Laue diffraction in transmission mode at the microXAS beamline of the Swiss Light Source (SLS-Switzerland). Information on rotational gradients and GND densities are measured at lengthscales similar to those addressable in computational models. To achieve this a new miniaturized shear-fatigue device compatible with Laue diffraction has been developed. A suitable sample geometry has been designed and different sample preparation methods have been tested. The potential

of in-situ Laue diffraction to follow dislocation patterning is explored and evaluated by underlining its benefits and limitations.

This thesis is carried out in the framework of a collaborative project titled "Constitutive modelling and microstructural validation for crystal plasticity finite element computation of cyclic plasticity in fatigue", where two other PhDs are involved besides the here represented experimental approach (Swiss National Science Foundation SNF – 138240). Nicolò Grilli (LNM, PSI) develops the CPFE code of low cycle fatigue for fcc metals by implementing constitutive laws that can reproduce the typical patterns of cyclic deformation in the DAMASK code. Jens Nellessen (MPIE, Düsseldorf) characterizes the obtained microstructures in fatigued metals using different electron microscopy techniques (EBSD, ECCI, TEM). The work presented in this thesis is part of this synergic approach and in particular aims to develop a new validating experimental method allowing to provide input and verify the computational developments performed by Grilli as well as other computational approaches.

1.4   Thesis structure

The thesis is divided in six chapters.

Chapter 2 explains the development of experimental and technical aspects. It collects details of the developed reversed shear device and sample preparation, the description of how mechanical tests are conducted during in-situ Laue micro-diffraction and the analysis methodology developed to interpret the data. The summary of the tested samples is also given together with the expected dislocation structure.

Chapter 3 shows the result of single slip oriented single crystal and Chapter 4 the results of double slip (coplanar and collinear) orientations.

Discussion of the results is presented in Chapter 5, where the suitability of the employed sample preparation and the mechanical response of the system are reviewed. The observations derived from the results are interpreted in terms of dislocation patterning and benefits and limitations of the technique are assessed.

Chapter 6 recapitulates the conclusions of the thesis, including both the achieved results and the outlook.

Chapter 2   Development of Experimental and Technical Aspects

This chapter is divided in four different sections. The first describes the development of the reversed shear system, the second and third collect the methodology used to perform the in-situ Laue micro-diffraction experiments and the data analysis procedure. The last section gives an overview of the tested samples and the expected dislocation pattern for each orientation.

2.1   Reversed shear system

In this section, the description of the geometry of the specimen, the exploration of different sample preparation routes, the design of the miniaturized reverse fatigue machine and the methodology to conduct the mechanical tests are explained.

2.1.1   Geometry of the sample

There are several constrains to be taken into account when designing the geometry of the sample.

- First of all, the specimen must be compatible with Laue micro-diffraction in transmission mode. Therefore, the gauge thickness of the specimen should be on the order of a few tens of microns, due to X-ray absorption issues and question of integrating the X-ray signal over the thickness.
- Secondly, the specimen has to be able to be deformed in reversed fatigue. Judelewicz et al. (Judelewicz et al., 1994) performed tension-tension fatigue experiment on 20-100 μm thick polycrystalline free-standing copper foils with a dog-bone shape. However, this geometry at small scale is not compatible with fully reversed cycling due to the buckling risk of the sheet under compression.
- Thirdly, the strain distribution must be homogeneous to facilitate the correct development of the novel cyclic-DAMASK-CPFE model. This excludes the geometries used in reversed cyclic bending (Kiener et al., 2010; Kirchlechner et al., 2015) or torsion (Liu et al., 2012) experiments that would satisfy the first two conditions.

For all these reasons it was chosen to perform cyclic fatigue in shear mode. Several publications can be found in the literature describing different shear geometries. The most common ones are summarized in Figure 2.1: a) was used by (Matsuda, 1977), b) by (Rouault-Rogez, 1990), c) by (Funk and Blank, 1984), d) by (Fourmeau et al., 2011), e) by (Rittel et al., 2002), and f) by (Mayr et al., 1995). As can be observed some geometries are deformed in tension-shear [(a), (c) and (d)], whereas others in compression-shear [(b), (e) and (f)]. Recently, an effort to adapt these geometries for small scale testing compatible with SEM or TEM has been carried out (Heyer et al., 2014; Mayer et al., 2015)
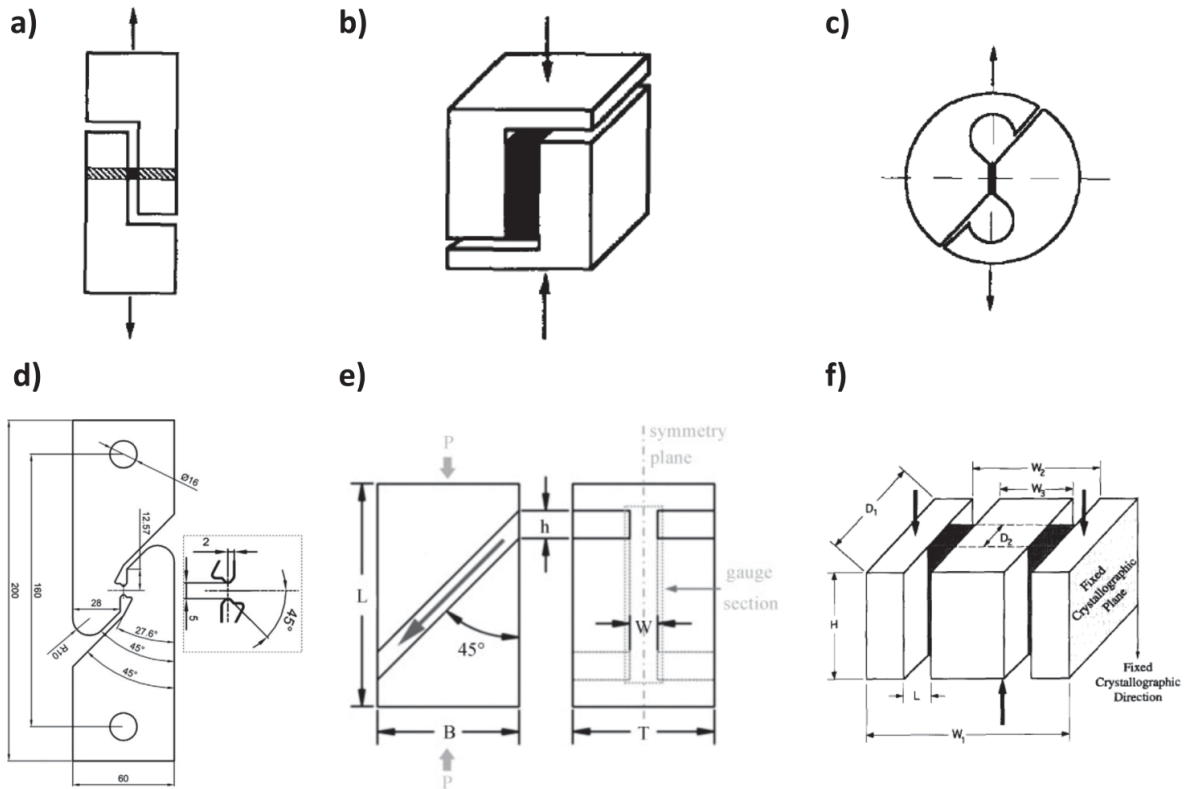
Figure 2.1 Geometries of several shear specimens found in literature: (a-c,f) after (Mayr et al., 1995), (d) after (Fourmeau et al., 2011) and (e) after (Ames et al., 2010)

Similar to the case of the dog-bone geometry, the above-mentioned geometries have the drawback of buckling when performing reversed-cycling or cannot be reversed. The geometry proposed by Miyauchi (Miyauchi, 1984) for planar shear on metal foils overcomes this issue (see Figure 2.2). It consists of two external fixed areas and a central moving area that is displaced. In between, there are two areas where the shear deformation is localized. A proper design of the grips and the machine allows applying reversed shear and therefore perform fully reversed cyclic experiments. For this work a new sample geometry based on this principle has been developed in collaboration with Alex Bollhalder from the Mechanical and Electrical Engineering Group (LDM, PSI).
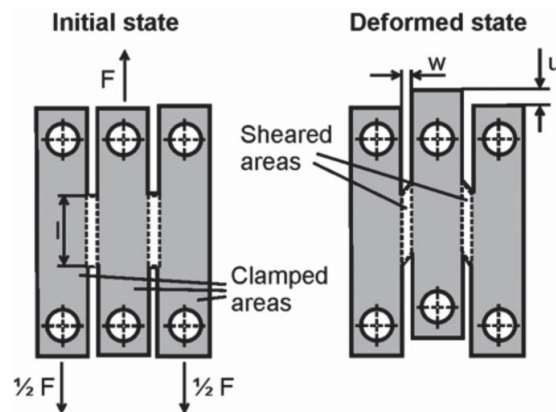
Figure 2.2 Miyauchi's geometry for simple shear test after (Hußnätter and Merklein, 2008)

For the case of thin and uniform thickness foils, the geometrical relationships between applied force (F) and shear stress (τ_s), and between the applied displacement (u) and shear strain (γ) are:

$$\tau_s = \frac{F}{2 \cdot l \cdot t}$$ eq. 1

$$\gamma = \frac{u}{w}$$ eq. 2

As shown in Figure 2.2 l is the length of the sheared area, w is the distance between mobile and fixed areas and t is the thickness of the sample.

FEM simulations were done for a 100 μm thick copper foil with a local Ø 300 nm circular 10 μm thin area in the middle of the shear area. Figure 2.3 shows that high stress is concentrated in the thin area after displacing the mobile area by 200 nm with an applied force of 0.5 N. This suggests the need for a robust, thicker sample geometry still maintaining a local thin area. The disadvantage of this alternative, where the thickness is not uniform in the whole sample, is the loss of control on the real displacement transmitted to the sheared area and therefore loss of control of the strain in the gauge section. However, this can be extracted from the DAMASK-CPFE simulations, since the model has the capacity to simulate the whole specimen (not only the gauge volume) and the applied force-displacement conditions.
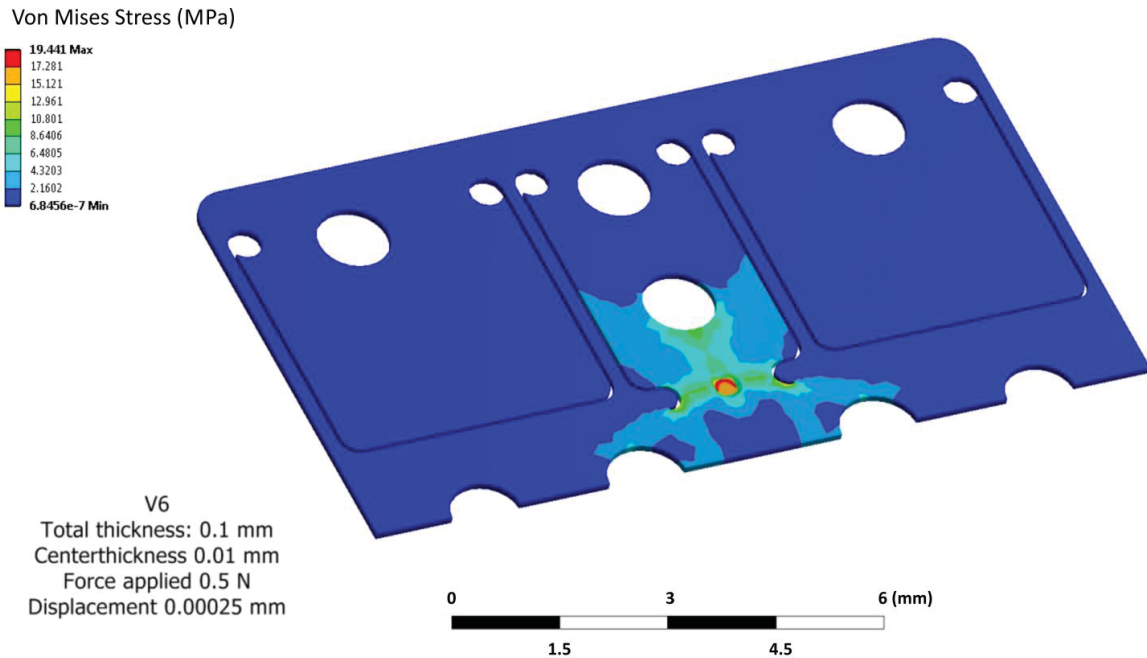
Figure 2.3 FEM simulation of 100 μm thick foil with a local 10 μm thin area in Miyauchi's geometry (courtesy of A. Bollhalder)

Figure 2.4 shows the developed geometry for reversed shear fatigue compatible with Laue micro-diffraction: a) is an illustration of the specimen, b) is the zoom in the shear zone and c) are the drawings of the sample with the dimensions in mm. Further drawings can be found in Appendix A. The two external fixed parts and the central moving area are 2 mm thick. They are separated by channels with a width of 150 μm. In between there are two symmetric 1 mm wide and 150 μm thick grooves, corresponding to shear areas. As illustrated in Figure 2.4-b) the shear areas are further locally thinned in order to work in Laue transmission.

These dimensions are needed to keep robustness during sample manipulation but simultaneously must be able to deform plastically the sample in the locally thin areas during the fatigue experiments. The FEM simulations show that 3.5 N are needed to displace the mobile area by 266 nm when the local thin area is 10 μm in thickness: seven times more than in the case shown in Figure 2.3.
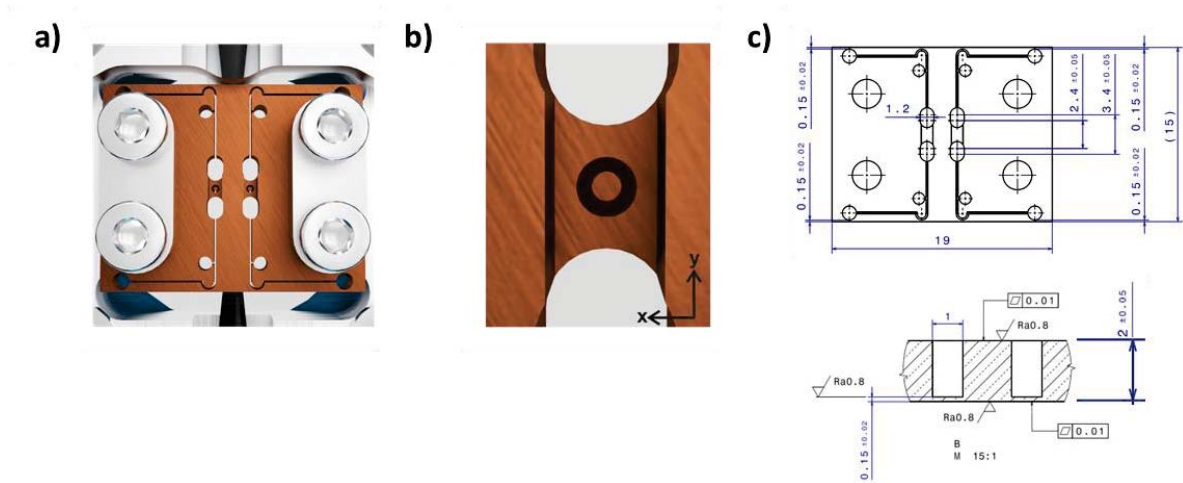
Figure 2.4 Developed sample geometry for reversed shear fatigue compatible with Laue micro-diffraction: a) sketch of the sample, b) zoom of the shear area, c) drawings and dimensions of the specimen

Even if the values of stress and strain in the center of the shear area are only accessible via simulations, the range of stresses can be estimated using *eq. 1*. Figure 2.5 shows the estimated τ_s for forces between 1 and 7 N and several thickness values shown in the legend in µm. The shear length (l) is assumed to be 1.2 mm which corresponds to the shear length in Figure 2.4. For extremely thin samples ($t \sim 10$ µm) τ_s increases drastically when increasing F. For samples with $t > 30$ µm τ_s is maintained below 100 MPa. In reality, due to the gradual reduction in thickness, the actual values are going to be somewhere between the thick and the thin dimensions.
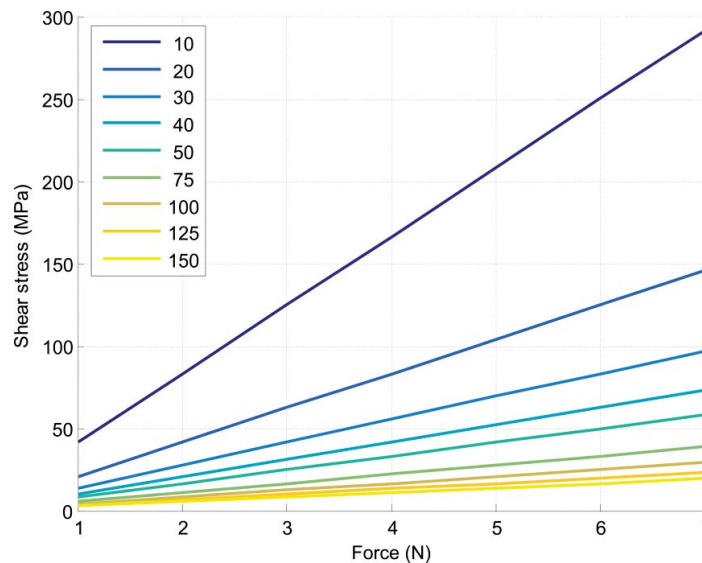
Figure 2.5 Estimated stress in the shear area as a function of applied force and thickness (µm)

One major consideration for this complex sample geometry is the homogeneity of the applied shear in the central thin areas. To probe that, CPFE simulations were performed using the same geometry and crystal orientation as in the experiments in collaboration with Nicolò Grilli. Constitutive laws based on the phenomenological description of (Hutchinson, 1976) and pure copper single crystal parameters (Déprés et al., 2008; Dmitrieva et al., 2009; Overton and Gaffney, 1955) were used. Zero displacement boundary conditions are set on the surface between the copper single crystal and the fixing screws. On the central moving area symmetric boundary conditions are imposed. More details about the model and material parameters used for simulations can be found in Appendix B and in (Grilli et al., 2015).

Figure 2.6 shows the distribution of the γ_{xy} strain tensor component of a single slip oriented sample subjected to cyclic deformation (see Chapter 3 for further details). Simulations show that γ_{xy} is the largest strain component and it is uniform in the area of interest (central part of the thin area where Laue diffraction scans are done).
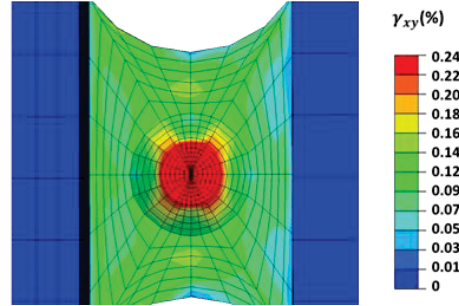
Figure 2.6 Distribution of the γ_{xy} strain tensor component of a single slip oriented sample at maximum force of 5N

Simulations also provided a simple geometrical relationship between the applied displacement in the mobile area (u) and the new geometry. They show that eq. 2 can be updated to

$$\gamma_{xy} \cong \frac{u}{\emptyset}$$

eq. 3

where $\emptyset$ is the inner diameter of the thin area.

The total resolved shear strain is calculated by dividing γ_{xy} by the Schmid factor of the primary slip system/s (m).

$$\gamma_{xy}^{res} = \frac{\gamma_{xy}}{m}$$

eq. 4

The plastic part of the shear strain, γ_{xy}^{p}, is calculated as the half width of the hysteresis loop (Suresh, 1998) as drawn in Figure 2.7.
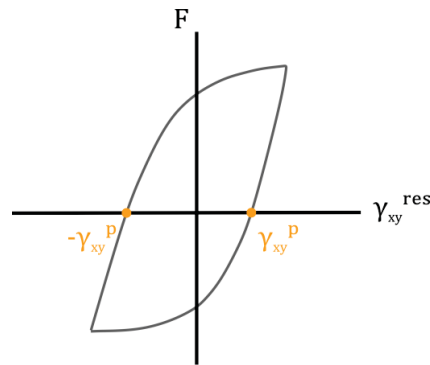
Figure 2.7 Schematic illustration of the F-γ_{xy}^{res} hysteresis loop and determination of γ_{xy}^{p}

2.1.2   Sample preparation

The sample preparation process consists of two steps. In the first step the general shape of the geometry is reached; in the second step the local thin area is obtained.

Figure 2.8 displays the sample preparation sequence. The samples are machined starting from 19×19×2 mm³ copper single crystals with 99.999% purity, purchased from Mateck GmbH, Germany. First bores and grooves

are machined. The back surface is mechanically polished until a roughness <1 μm is obtained using a standard colloidal silica suspension oxide polishing solution (OP-S Suspension, 0.04 μm, Struers). Then the samples are annealed at 800°C for 2 hours with 12 hours cooling time in vacuum (~1 mbar). Later, the samples are mounted on the sample holder with a torque of 0.6 mN in the case of steel holder and with 0.3 mN for copper holders. Finally, the samples are machined by electric discharge machining (EDM) to a Miyauchi's geometry shown in Figure 2.4. Some samples have been subjected to a second annealing between the mounting and the EDM machining steps at 450-500 °C for 2 hours to remove the remaining and the additional damage introduced during mounting. This is possible when the samples are mounted on copper holders and not on steel due to differences in thermal expansion coefficients. The sequence can be followed in Figure 2.8.
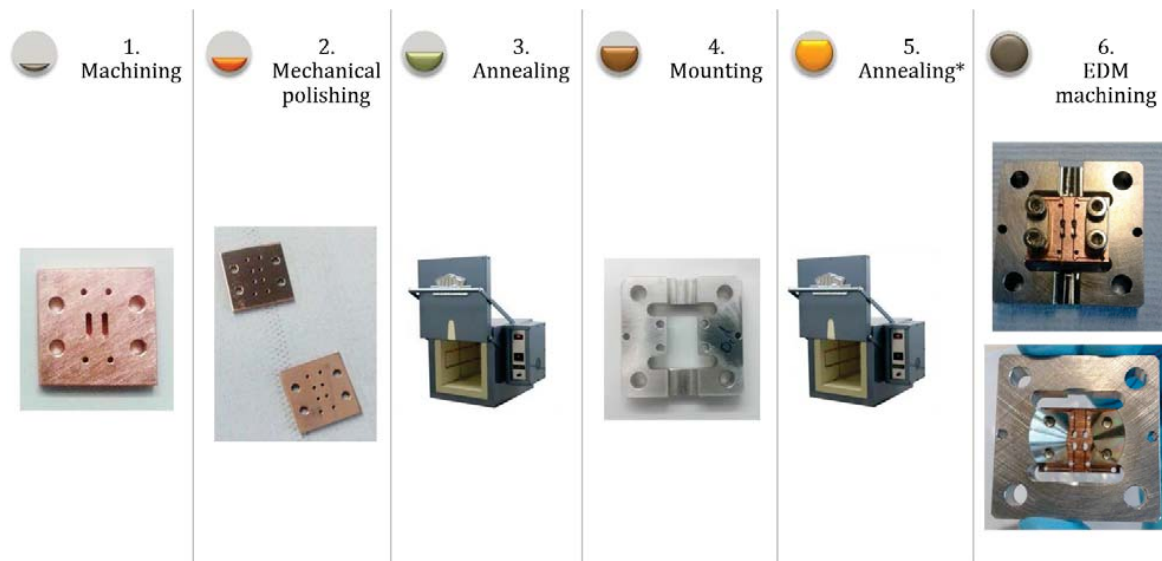
*Only those samples mounted on copper sample holders have been subjected to step 5

Figure 2.8 Sequence of sample preparation prior local thinning.

In a second step the local thin area must be created. This is rather challenging as one needs to find a method to locally thin the sample to tens of microns thickness with a roughness less than 1 μm on a circular area ~400 μm in diameter introducing the minimum damage possible on the sample. The roughness and damage requirement and the sample dimensioning exclude the use of focus ion beam (FIB), the traditional sample technique to prepare miniaturized specimens. That is why other routes have been followed: electron beam lithography and picosecond laser ablation. In what follows these two techniques are explained in more detail.

Electron beam lithography

The viability assessment of the electron beam (e-beam) lithography route was done in collaboration with Dr. Vitaliy Guzenko (LMN, PSI). The method consists of covering the sample with a poly(methyl methacrylate) (PMMA) polymer and exposing the desired area to e-beam in order to disintegrate the polymer. The design of the sample was made compatible with the limitations imposed by the e-beam lithography tool in terms of total height of sample and maximum depth of the shear area. The process is described in Figure 2.9: firstly, the bores and grooves are machined, then the specimen is covered by the PMMA polymer and an Ø400 μm area is exposed to e-beam on both sides. Afterwards, the specimen is mounted on the sample holder and cut to final external dimensions with EDM. Finally the sample is electropolished to remove the metal that has no polymeric protection.
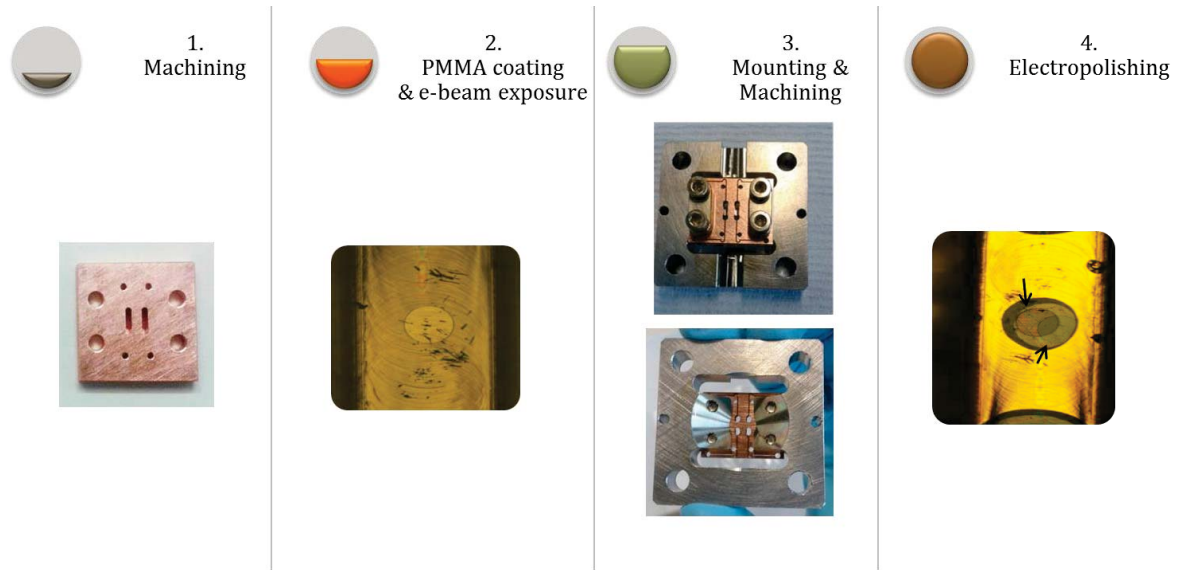
Figure 2.9 Sequence of thinning down via e-beam lithography route

Various electropolishing conditions were tested (e.g. solution, voltage, time, etc.). The results showed that the PMMA was resistant to electropolishing solutions not containing methanol. For instance, electropolishing in 70% H_3PO_4 -30% water (vol/vol) solution at 2V with a copper electrode does not damage the PMMA and the electropolishing process is concentrated on the area where the e-beam exposure is performed. As can be seen in Step 4 of Figure 2.9, when too long electropolishing has been performed a hole in the shear area is created. In fact, one can observe the PMMA circular boundaries on the front and back surfaces, slightly misaligned (see arrows). Essentially the coating remains intact. In samples where the electropolishing did not result in a hole, confocal laser scanning microscope (CLSM) measurement was done to check the quality of the surface. CLSM is an optical imaging technique that enables the reconstruction of 3D structures from the obtained images by collecting sets of images at different depth within a thick object with high optical resolution and contrast. The result (Figure 2.10) shows that the electropolishing process is faster at the boundaries of the PMMA. As a consequence a non-uniform profile is obtained. Thus this sample preparation route to locally thin the shear areas was not further explored.
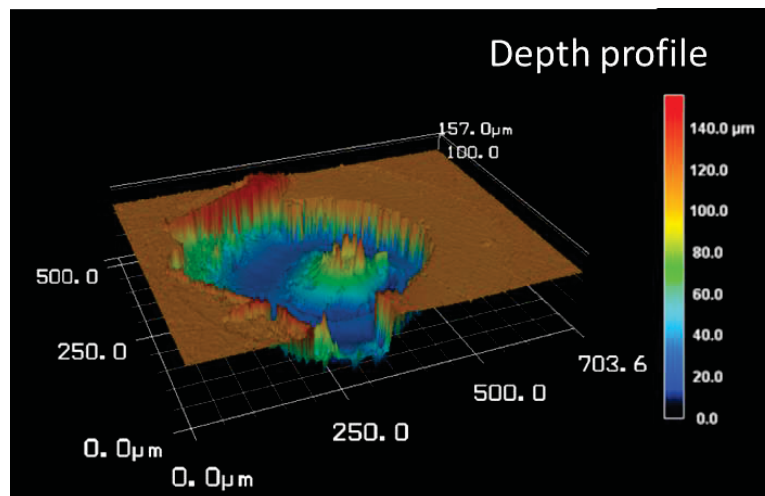
Figure 2.10 Confocal measurement on the e-beam exposed area after electropolishing

Picosecond laser ablation

As an alternative to e-beam lithography, a new sample preparation method has been developed based on picosecond laser ablation (Stafe et al., 2014) in collaboration with Dr. Antoine Guitton (PEM, PSI) and Dr. Rolf Brönnimann (EMPA, Dübendorf). Laser ablation consists in ejecting matter from the sample by irradiation with short, energetic bursts of light. Due to strong absorption of the laser radiation in the surface layer, a high and sudden increase of temperature occurs, which in turn causes material evaporation, as illustrated in Figure 2.11-a. Figure 2.11-b shows schematically the process that occurs inside the material. As the energy of photons is small compared with the energy of the atomic nuclei, the photons only have impact on electrons, which will gain kinetic energy. Eventually, the electrons lose their energy by nudging the internucleei bonding of lattice and ablation occurs (Leitz et al., 2011).
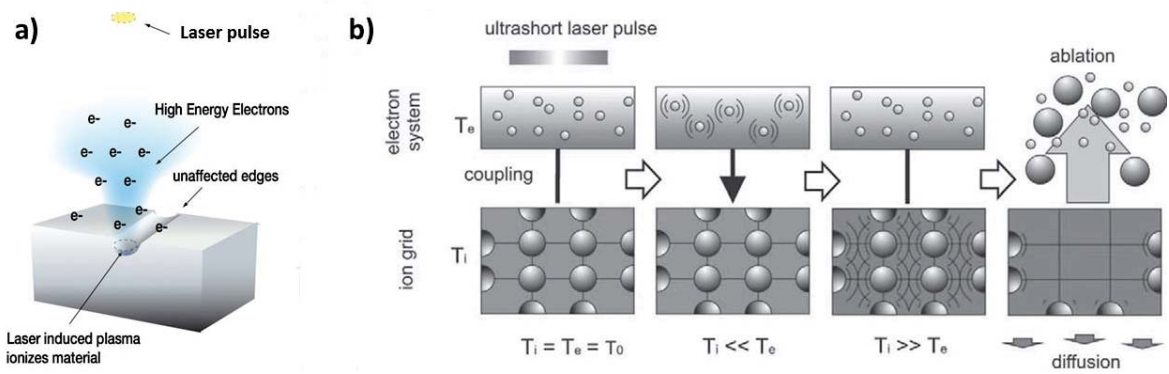
Figure 2.11 Illustration of picosecond laser ablation technique: a) adapted from (Attodyne website, 2013) and b) after (Leitz et al., 2011)

In laser ablation, there are three important time periods:

- The electron cooling time (τ_e): time for an electron to lose its energy to the lattice (e.g. Cu - 10^{-17} seconds)
- The lattice heating time (τ_l): time for the lattice to heat up (start vibrating) (order of picoseconds)
- The pulse duration (τ_p)

The first two time periods are material dependent. The third, the duration of the pulse, can be chosen depending on the tool and has an important effect on the introduction of damage into the material. In general, shorter pulse durations reduce heat diffusion leading to low damage, better surface quality, improved resolution and higher precision (Chichkov et al., 1996; Xiao et al., 2012). Thus, the shorter the pulse the smaller the heat affected zone (HAZ) is (Jandeleit et al., 1996; Meijer, 2004; Schäfer et al., 2002). In the cases of metals, the penetration depth (l_p) is governed by thermal diffusivity (D) and for $\tau_p \geq 10$ ps:

$$l_p = 2\sqrt{D\tau_p}$$
eq. 5

In addition to the duration of the pulse, which is given by the laser type and also determines the repetition frequency and wavelength range, there are additional parameters that influence the laser ablation process.

- The laser fluence is the measure used to describe the energy delivered per unit area

$$Fl = Fluence\left[\frac{J}{cm^2}\right] = \frac{Laser\ pulse\ energy\ [J]}{Effective\ focal\ spot\ area\ [cm^2]}$$
eq. 6

- Sometimes, intensity is more used than fluence

$$Intensity \left[\frac{W}{cm^2}\right] = \frac{Laser\ peak\ power\ [W]}{Effective\ focal\ spot\ area\ [cm^2]} \qquad \text{eq. 7}$$

where
$$Peak\ power\ [W] = \frac{Laser\ pulse\ energy\ [J]}{Pulse\ duration\ [s]} \qquad \text{eq. 8}$$

- Spot diameter in case of Gaussian beam

$$d_{abl} = d_f \sqrt{\frac{1}{2}\ln\left(\frac{Fl}{F_o}\right)} \qquad where \qquad \begin{aligned} &d_f\text{: diameter of the laser beam} \\ &Fl\text{: laser fluence} \\ &F_o\text{: fluence threshold for ablation} \end{aligned} \qquad \text{eq. 9}$$

- Ablation threshold: the minimum energy needed to evaporate the material without melting. The regime just above the threshold is the most interesting for precise material processing as the HAZ is minimized.

In order to get the optimum conditions to locally thin the shear area, several tests have been carried out with a commercial picosecond laser (Lumera Laser GmbH, Germany) operated at 355 nm with 50 KHz and 10 ps pulse duration. The optical images of

Figure 2.12 (a-b) shows the influence of the laser power when ablating polycrystalline copper after one single loop: a) has been ablated with 10 mW and b) with 50 mW. In the former image a rose window imprint is observable but disappears for power values larger than 50 mW, which is determined as the power threshold.

- For that power (50 mW), a linear behavior is found between the ablated depth and the amount of removing steps.
- The first trials have also revealed that a trench is formed in the perimeter of the ablated area. The depth of this trench increases with the amount of material ablated. To overcome this issue, the thinning process is done in a staircase concept as shown in Figure 2.12-c: larger diameters have bigger steps (more loops), smaller diameters have lower steps.
- To reduce the roughness observed in the optical image of Figure 2.12-b, laser pulses are directed by a galvano scanner in a cross hatch pattern towards the surface. The distance between hatch lines is set exactly to 3 digitizing units (~4 μm) of the Digital-to-Analog Converter (DAC) for the galvano scanner to reduce aliasing effects. Additionally, the hatch direction is constantly rotated by 60°. This results in a root-mean-square (RMS) roughness of about 500 nm obtained for a length of ~280 μm as determined with a white light interferometric microscope. The 3D topography view of the flat ablated surface obtained is shown in Figure 2.12-d.
- With the final parameters listed in Table 2.1 ~300 nm per hatch is ablated
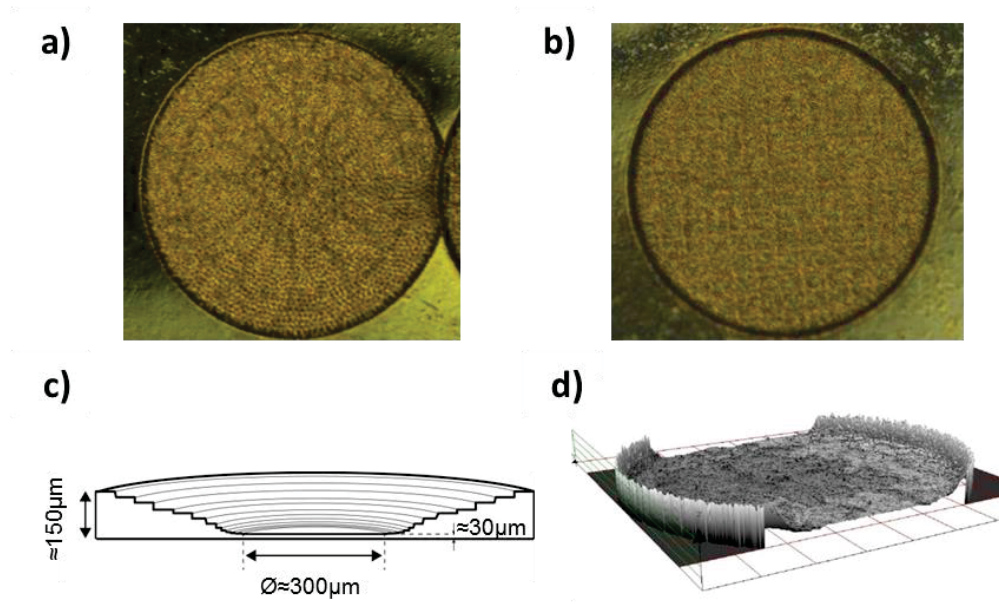
Figure 2.12 Optical images of ablated area in polycrystalline copper using a laser power of a) 10mW and b) 50mW; c) Schematic view of the stair case concept; d) 3D topographic view of the ablated area revealing an RMS roughness of 500nm over a length of 280 μm

Table 2.1 Laser details and ablation parameters

Manufacturer	Lumera (now Coherent), Kaiserslautern, Germany
Model	Super rapid with SHG, THG and first pulse killer
	SHG: Second Harmonic Generation
	THG: Third Harmonic Generation
Maximal power at 355 nm	~4 W
Maximum repetition rate	640 kHz
Material removal method	Layered ablation
Process gas	Ambient air
Wavelength	355 nm
Pulse duration	10 ps
Power	50±2 mW
Frequency	50 kHz
Focal spot size	~5 μm

A study of introduced damage has been done on single crystalline 100 μm thick copper foils purchased from Goodfellow Cambridge Ltd., England. The foils were ablated into a stair shape with the parameters listed in Table 2.1 until a thickness of ~10 μm was reached. The thickness of the thin area was measured by focal depth difference using an optical microscope (Olympus BX51). This contactless method for measuring the thickness avoids introducing further damage in the critical area. Laue scans (see section 2.2 and 2.3 for explanations) were done in an area of 500×500 μm^2 that covers both the ablated and non-ablated zones. Figure 2.13 shows the 2D logarithmic scale diffraction map of a Laue reflection where the ablated thin area is recognizable by the bright blue color. By analyzing the broadening of the Laue reflections the introduced damage can be evaluated. The diffraction patterns outside the red line are used to calculate the average values corresponding to the non-ablated area, the ones inside the black line for the ablated area. The full width at half maximum (FWHM) of the reflections

along the radial (2θ) and azimuthal (Ψ) directions are obtained by fitting a 2D Gaussian function to the diffraction peaks. The mean of all the reflections is summarized in Table 2.2. The values corresponding to an etched 10 µm thick silicon (Si) membrane are given as a reference. The mean values of the table show that the copper samples are more damaged than the silicon reference due to the preparation procedure of the foils. When comparing the ablated and non-ablated cases, the mean values are lower in the ablated area because of reduction in thickness. The fact that the values are not higher suggests that the induced damage by the laser ablation is minimal compared to the initial microstructure. More details of the analysis can be found in (Guitton, A., Irastorza-Landa et al., 2015).
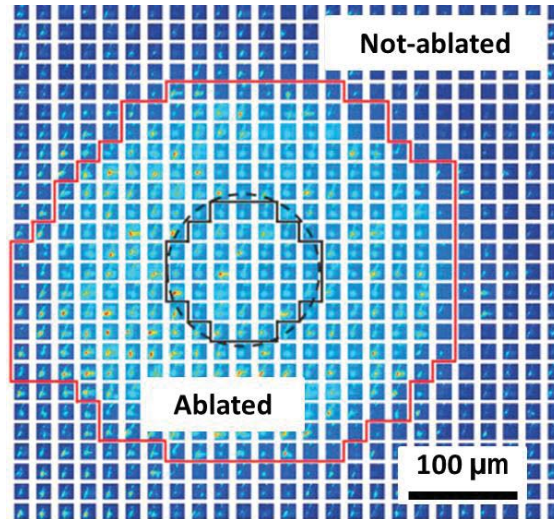
Figure 2.13 2D logarithmic scale diffraction map of a Laue reflection around the ablated zone.

Table 2.2 Mean of FWHM of all Laue reflections along the radial (2θ) and azimuthal (Ψ) directions

Total cycles	$\overline{\Delta 2\theta}$ (°)	$\overline{\Delta\Psi}$ (°)
Cu - ablated	0.14	0.15
Cu – not ablated	0.18	0.22
Si	0.09	0.07

The thinning procedure applied when preparing the shear samples consists of two steps: 1) on the front side a circular area with internal diameter of Ø~300 µm is created by gradual stair-shape reduction as previously described; 2) on the back side a larger rectangular area is removed covering both shear areas. This procedure ensures that any damage that may exist at the surface of the original single crystal is removed in the sensitive area where the Laue diffraction measurements are performed. Figure 2.14 shows the front (a) and back view (b) of the ablated areas. It can be observed in the Figure 2.14-b that the shear areas are also visible on the back side. This is only the case for those samples subjected to a second annealing, and can therefore related to thermally induced internal stress release.

The final thicknesses that are usually obtained are in the order of ~30-50 µm within the circular area. Many attempts have been done to go thinner but in most of the cases the thin area was blown out (Figure 2.14-c).
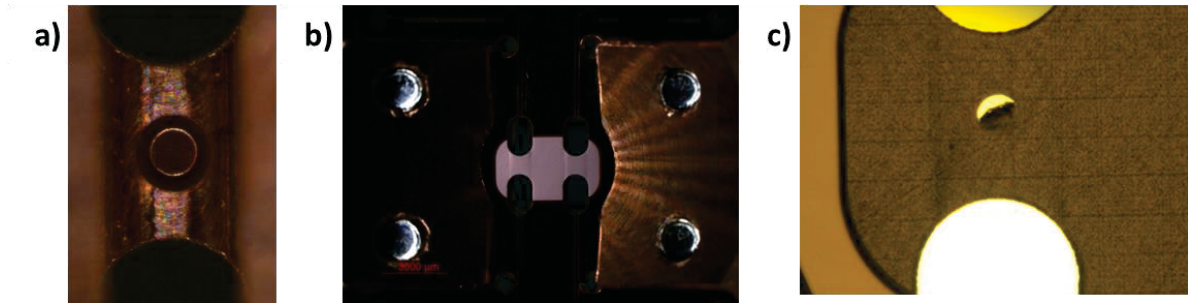
Figure 2.14 Results of picosecond ablation on single crystal copper with final shape: a) stair-shape ablation inside the shear zone; b) ablation in the back-side of the specimen; c) unsuccessful ablation result where the thin area was blown out

2.1.3 Machine

A dedicated miniaturized deformation rig has been built to apply reversible shear and to be compatible with in-situ Laue micro-diffraction. Schematic views of the machine are presented in Figure 2.15: a) front view and b) back view. A real picture of the machine is shown in Figure 2.15-c. The rig has dimensions of 200×90×150 mm³. The frame is made of an AlMgSi alloy. Reversible shear is induced by two pins that sequentially push on either side of the sample. The pins can be displaced by two Smaract linear actuators (SLC-1760) with a 7N blocking force, sub-nanometer scan resolution and 41 mm travel range. Two 5 N load cells (Transducer Techniques, USA) measure the force applied on the pins. In order to compensate gravity a counterweight is installed for the lower linear actuator. By adding additional weight higher forces can be reached (∼7 N). On the top side of the specimen a cantilever is installed in between pin and sample. This system measures the displacement on the top part of the sample with a Renishaw Tonic optical encoder with 20 nm resolution. The center of the sample is located in the middle of the cantilever. As a consequence, for small displacements the measured displacement at the encoder position is considered to be the double of the actual displacement of the sample, which is later converted to strain using *eq. 3*. On the back side an opening of 100° is created for a large angular acceptance necessary to avoid blocking the transmitted beam. The drawings of the machine are attached in Appendix C.
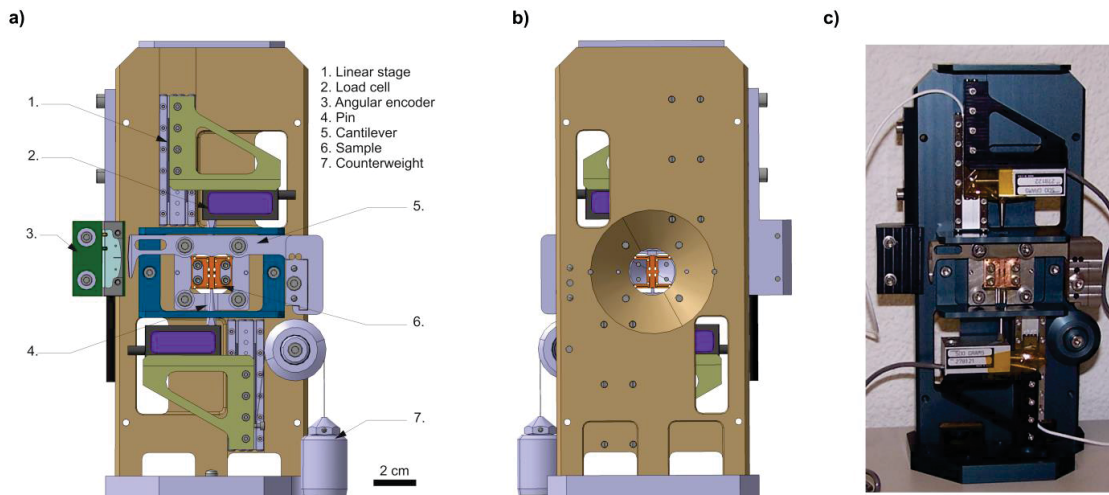
Figure 2.15 Schematic views and real image of the deformation rig that allows applying reversible shear

2.1.4 Mechanical test

The fully reversible cyclic shear experiments are performed under displacement control as explained in Figure 2.16. The first step consists of bringing both pins in contact with the sample. A force threshold ($F_{th} = 20\ mN$) is set to define a touch down condition. During the complete test both pins remain in contact with the sample. During the first quarter of the cycle, a displacement U is imposed to the linear stage that controls pin 1. The

displacement rate is fixed to 4 μm/s. The actual displacement of the pin, measured by the Renishaw system, is lower than U (u). When one pin pushes on the sample the second pin retracts (u'). A PID-control loop ensures that the force on this second pin remains zero and that both pins come back to touch down condition once the maximum displacement is reached. After unloading, the same procedure is repeated for the second half of the cycle.
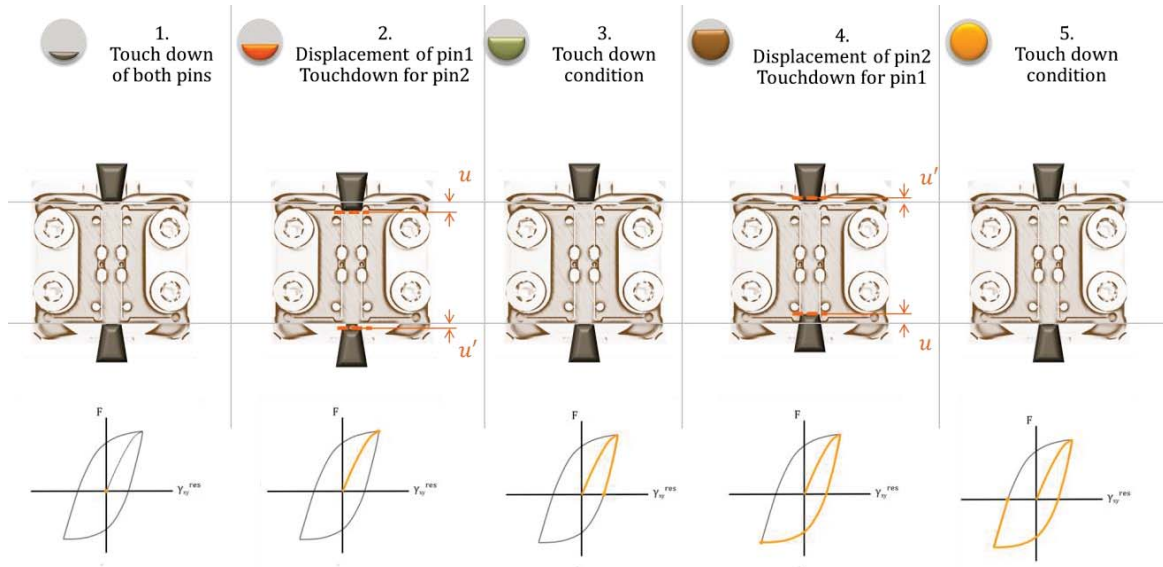
Figure 2.16 Steps during fully reversible shear cycles

A multiple step test methodology is followed to complete the set of cycles (see Figure 2.17): the displacement amplitude is kept constant during a certain number of cycles and afterwards the displacement amplitude is increased to a higher level and more cycles are applied.
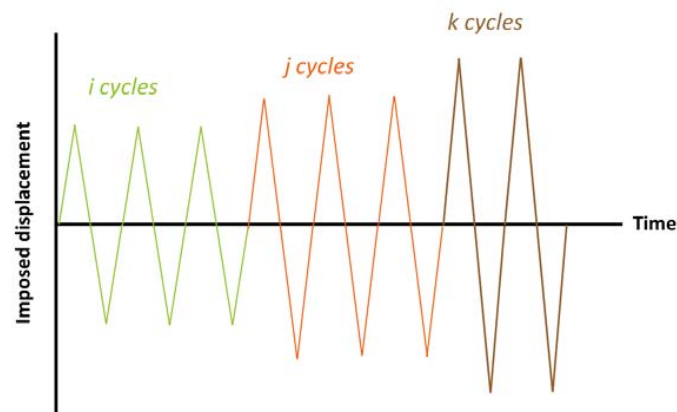
Figure 2.17 Multiple step test methodology

The shear device is controlled with in-house LabVIEW routines written by Dr. Steven Van Petegem. Figure 2.18 shows the snapshot of the interface to control the machine and conduct cyclic mechanical test. Eight main blocks can be distinguished:

- Block 1 shows the evolution in time of the displacement and force of pin 1 (blue), of pin 2 (red) and of the Renishaw signal (green).
- Blocks 2 and 3 control de force, position and speed of pin 1 and pin 2 respectively.

- Block 4 is the control for the touchdown procedure. Both axes can be automatically brought into touchdown condition by setting the force threshold, speed and maximum travel distance. When the pin touches the sample the machine stops and the light blinks.
- Block 5 is used to set the parameters for cycling: number of cycles, imposed amplitude on the linear stage (U) in nm and speed in nm/s.
- Block 6 is used to set parameters for setting the contact conditions during cycling and unloading.
- Block 7 shows the evolution force vs displacement of both pins.
- Block 8 is used to set the path and filename to save the mechanical data.
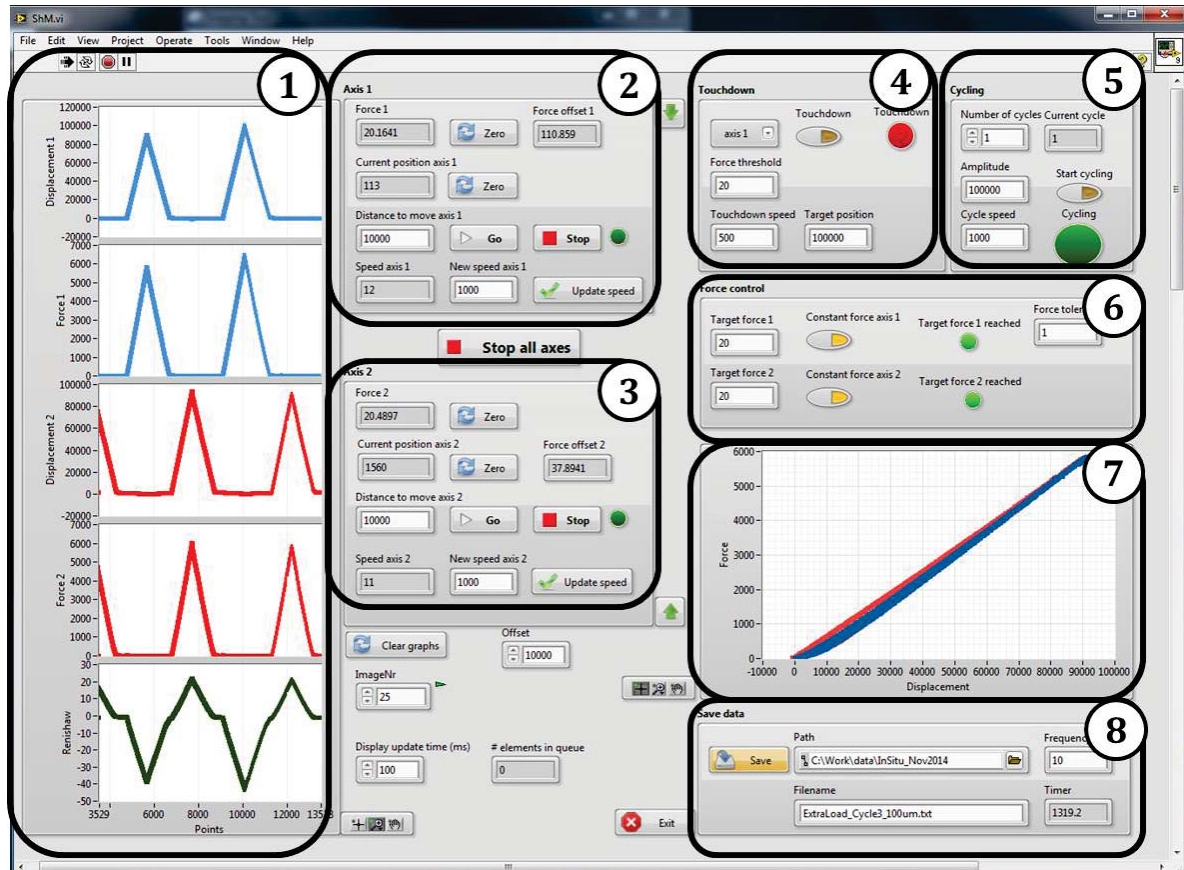
Figure 2.18 Snapshot of the LabVIEW program to control the machine and conduct cyclic mechanical test

2.2   In-situ fatigue during Laue micro-diffraction at MicroXAS beamline

The principle of Laue diffraction is as follows. In Laue diffraction the incoming beam is a polychromatic X-ray beam (range of λ) that interacts with an immobile crystalline sample. d_{hkl} is the spacing of the (hkl) planes in the atomic lattice and θ is the angle between those planes and the incident beam. n is the order of diffraction. When Bragg's law is satisfied for different $\lambda - d_{hkl}$ combination, the constructive interferences result in several Laue spots/peaks/reflections that can be collected on a detector. The indexation of the pattern gives the local crystal orientation.

$$n\lambda = 2d_{hkl}\sin(\theta) \qquad \text{eq. 10}$$

The Laue diffraction experiments have been performed at the MicroXAS beamline of the Swiss Light Source (SLS), located at the Paul Scherrer Institute. At this beamline a pink X-ray beam with energies ranging between 10 and 23 keV are focused with a pair of Kirkpatrick-Baez (KB) mirrors to a spot size smaller than 1 μm^2 as

determined by knife-edge scans. The sample is placed in the focal point, which is located 150 mm downstream from the KB mirrors. The diffraction pattern is detected by a detector placed after the machine. Thus, the working mode is in transmission. Several microscopes are used to locate the sample in the focal point. A beamstop blocks the direct beam to avoid damaging the detector. Figure 2.19 shows real images of the setup installed at the MicroXAS beamline where few elements are labelled by numbers: (1) – Detector, (2) – Diode microscope, (3) – Machine with the sample, (4) – Beamstop, (5) – Sample microscope, (6) – KB mirror.
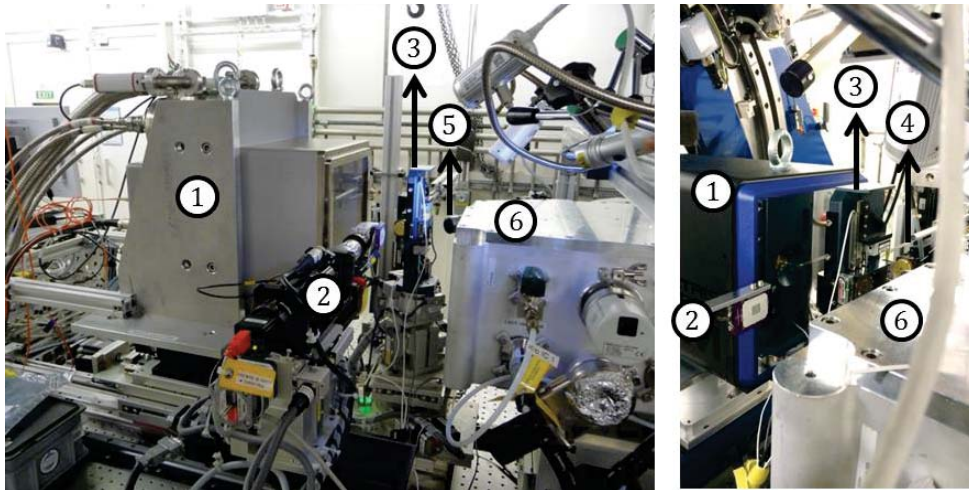
Figure 2.19 Experimental setup at the MicroXAS beamline

Once the center of one of the ablated areas is located in the beam, the sample is scanned through the beam along the X and Y direction and at each point a Laue diffraction pattern is recorded. Scans of 10×25 µm^2 are performed with a step size of 300 nm as illustrated in the schematic shown in Figure 2.20. The same area is scanned after certain amount of cycles to follow the microstructural evolution.

Two angles are drawn in Figure 2.20 to define the position of each Laue reflection: 2θ denotes the angle between the incoming beam and the diffracted beam, and Ψ is the azimuthal angle on the detector plane. Indexation of each pattern gives the average crystal orientation within the illuminated volume. Analysis of the Laue scans provides a spatial resolved misorientation maps as is explained section 2.3.
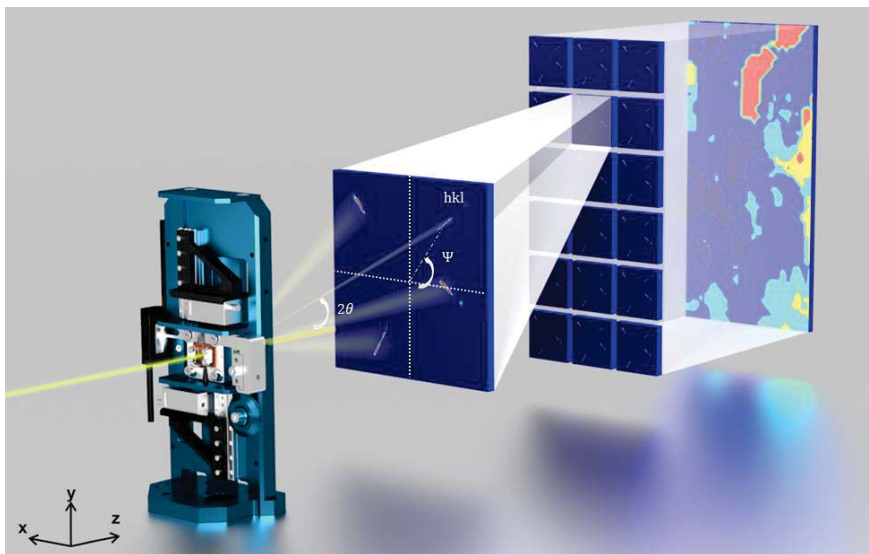
Figure 2.20 Schematic layout of the in-situ X-ray Laue micro-diffraction setup for reversible cyclic shear

Two technical aspects have to be mentioned: the intensity spectrum of the X-ray beam at the MicroXAS and the influence of the properties of the detector.

Influence of intensity spectrum

At the MicroXAS beamline the X-rays are produced by an undulator. It provides a harmonic intensity distribution as it can be seen in Figure 2.21. The flux and the frequency of the harmonics can be tuned by optimizing the gap size (space between the undulator's magnets parts): the smaller the gap, the higher the flux. Due to the presence of these harmonics the intensity can change by one order of magnitude for a minor change in energy. This can be reflected in the shape of Laue reflections. Indeed, from Bragg's law it can be seen that for a given lattice spacing the energy of a diffraction spot is directly related to the diffraction angle. In other words, diffraction spots elongated along the radial direction (variation in diffraction angle) cover a certain energy range. Intensity variations in the Laue peaks can therefore be either related to sample microstructure or to the intensity distribution of the energy.
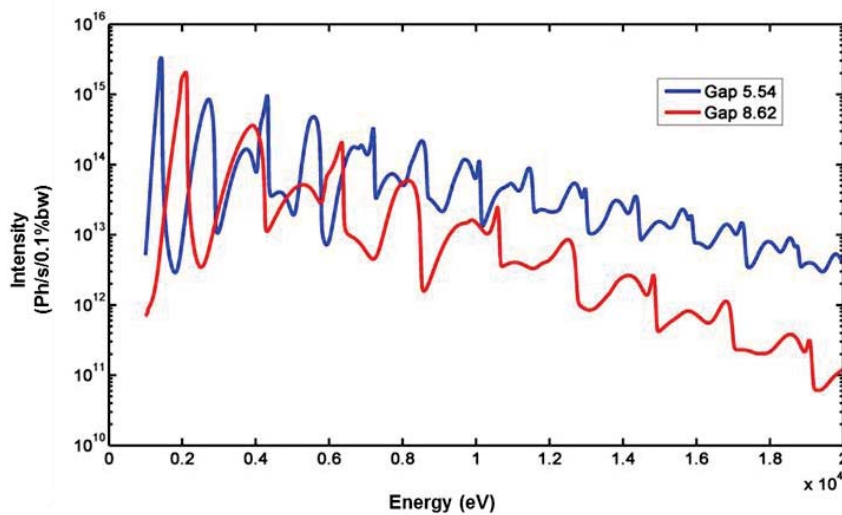
Figure 2.21 Simulated intensity versus the energy for two different undulator gaps at MicroXAS

Figure 2.22 shows an example of the influence of the discontinuous intensity spectrum. It plots a 3D view of a ($\bar{1}31$) peak at 13.7 keV recorded with a gap opening of 5 mm. A sharp drop is observed in the right side of the small sub-peak. The arrow points to the theoretical position where the maximum intensity should lie in order to minimize the indexation error. The position of maximum intensity of other peaks matches the theoretical position which suggests that the drop can be related to the energy drop around the 9th harmonic. As a consequence, this particular peak was not taken into account when analyzing the Laue patterns.
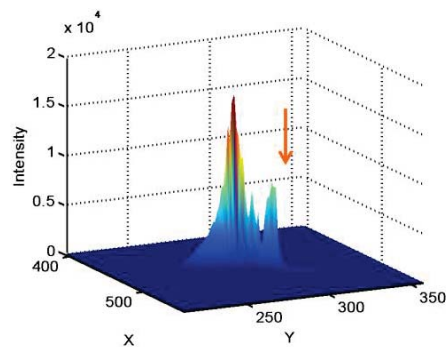
Figure 2.22 3D view of ($\bar{1}31$) peak at 13.7 keV recorded with a gap opening of 5 mm

Influence of detector

The properties of the detector may have a large influence of the quality and duration of the experiment. Following important aspects need to be taken into account:

- *Dynamic range:* the higher the range, the higher the maximum number of counts per pixels. All the pixels with counts higher than the maximum value are considered saturated and thus the full shape of the Laue reflection cannot be analyzed.
- *Readout time:* together with the acquisition time determines the speed at which Laue patterns can be collected: the shorter the time, the faster the scans.
- *Angular acceptance:* the maximum energy at MicroXAS is relatively low. As a consequence diffraction in forward direction is limited. In order to optimize the number of reflections the detector should be placed as close as possible to the sample. On the other hand, for optimal resolution, the sample-to-detector distance should be maximized. Depending on the dimensions of the detector and pixel size an optimum has to be found.

The results shown in this thesis have been collected using a DECTRIS EIGER 4M detector with an active area of 2070×2167 pixels and 75 μm pixel size. It has a dynamic range of 32 bit (maximum counts/pixel: $4.3×10^9$). This state-of-the-art X-ray detector operates in single photon counting mode, provides zero dark signal and zero readout noise and has a continuous readout with 3 μs dead time. The detector was placed 6.5 cm away from the sample, which is equivalent to a total angular acceptance of 135°. The exposure time was 0.3 ms. The setup was calibrated with the aid of a 10 μm thin Si wafer.

More details about the beamline, in-situ mechanical setups installed in the beamline and calibration procedures can be found in the following earlier theses (Maass, 2009; Marichal, 2013; Zimmermann, 2011).

2.3 X-ray data analysis

Each scan consists of 2856 diffraction patterns that are analyzed using an in-house software written in Matlab. A big part of the software was developed by Dr. Steven Van Petegem and various PhD students (Maass, 2009; Marichal, 2013; Zimmermann, 2011). For this thesis, I had written additional Matlab routines in order to deal with the large amount of collected data.

The first step consists in identifying the positions of each Laue peak on the pattern. This is done by an automatic indexation routine. Here the peak positions are defined by a maximum intensity position criterion. This criterion, rather than using the center of mass of the peak, allows detecting new emerging regions. Figure 2.23 illustrates the case of a Laue peak that changes its distribution during fatigue cycles. If the center of mass criterion is used to define the position of the peak, one can observe that the position is rather invariant (purple arrow). However, by choosing the maximum intensity criterion the peak position is constantly changing, reflecting the dislocation dynamics behind. The results obtained by both methods are discussed in section 5.5.
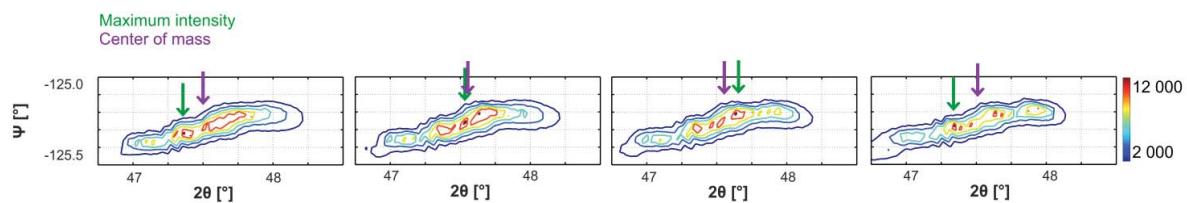
Figure 2.23 Maximum intensity vs. center of mass (the peak corresponds to the evolution of point **B3** in S1-L –Figure 3.16)

Next, the average crystal orientation within the illuminated volume is determined by a refinement procedure yielding a Bunge orientation matrix (G) at each point. This matrix describes the rotation from crystal frame to laboratory frame. As will be shown further, the diffraction peaks may have irregular shapes. As a consequence

the refinement procedure is not perfect. This will be expressed as an indexation error, which is the mean deviation between the theoretical and experimental positions of all Laue peaks, in units of pixels.

Once each pattern is indexed, different spatially resolved maps can be calculated. On one hand, the orientation of each point can be compared to a fixed reference. This procedure is used to calculate misorientation and rotation maps. On the other hand, the orientation of each point can be compared to the orientation of the neighboring point. This is done to calculate the lattice curvature, Nye tensor components and GND density maps. Finally the shape of Laue reflections and the scattering in the orientation are analyzed. They provide information about the heterogeneity across the integrated volume. Figure 2.24 shows a schematic of the analyzed aspects. In the following sub-sections each of them are explained.
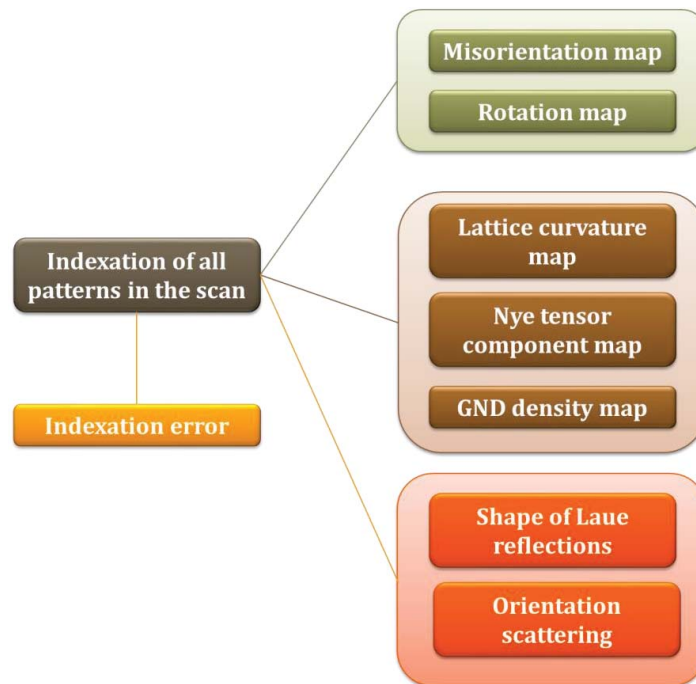
Figure 2.24 Schematic of the analyzed aspects

2.3.1   Misorientation

Misorientation is defined as a difference in the crystalline orientation between two points. It can be described as a single rotation by a positive angle (θ_{mis}) around an axis (**e**) according to the axis-angle representation (Morawiec, 2004). The rotation axis is sometimes called the Euler axis. The misorientation and the Euler axis depend on the chosen reference, but the relative misorientation between both orientations is independent of the reference. The schematic of the axis-angle representation is plotted in Figure 2.25.
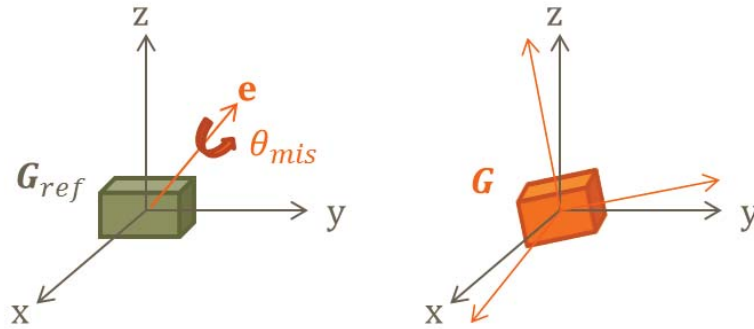
Figure 2.25 Misorientation described by the axis-angle representation

Generally, a reference orientation matrix has been chosen as a point on the Laue map for which the crystal orientation varied the least during cycling.

2.3.2 Rotations

The overall rotation between the reference and the orientation of the point of interest can be decomposed into ω_x, ω_y and ω_z rotations around X-, Y- and Z-axes in the laboratory frame, respectively:

$$\boldsymbol{R} = \boldsymbol{R}_x(\omega_x)\boldsymbol{R}_y(\omega_y)\boldsymbol{R}_z(\omega_z) \qquad \text{eq. 11}$$

This is illustrated in
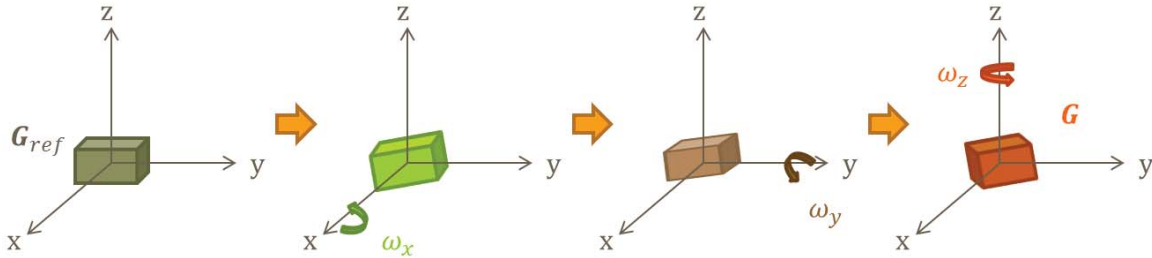
Figure 2.26 Decomposition of rotation in three rotations around X-, Y- and Z-axes

The rotations in 3D are in general not commutative and the overall total rotation matrix ($\boldsymbol{R}$) is sensitive to the multiplication order. For small misorientation values (<1°), however, they are commutative (Morawiec, 2004). Therefore, after decomposing the total rotation into rotations around X-, Y- and Z-axes, ω_x, ω_y and ω_z values are obtained.

The ω_x, ω_y and ω_z values are calculated related to the same reference chosen to compute the misorientation.

2.3.3 Curvature tensor

Calculating the relative misorientation between two neighboring points does not depend on the chosen reference orientation as is the case of θ_{mis}, ω_x, ω_y and ω_z. The curvature tensor κ_{ij} describes the relative misorientation and is defined as the gradient of the rotation about the 'i' axis along the 'j' direction:

$$\kappa_{ij} = \frac{\partial \theta_i}{\partial x_j} \quad \text{with} \ \ \{i,j\} = \{x,y,k\} \qquad \text{eq. 12}$$

where $\boldsymbol{\theta}$ is the lattice rotation vector. The disorientation vector ($\Delta\boldsymbol{\theta}$), analogue to the axis-angle representation, defines the orientation difference between two neighboring points (A and B). In sample coordinates, it can be derived as follows:

$$\Delta\mathbf{G} = \mathbf{G}_A^{-1}\mathbf{G}_B \qquad\qquad\qquad \text{eq. 13}$$

$$\Delta\theta = \arccos\left(\frac{\Delta G_{ii}-1}{2}\right) \qquad\qquad\qquad \text{eq. 14}$$

with ΔG_{ii} the trace of $\Delta\mathbf{G}$.

$$\Delta\theta_k = -\epsilon_{kij}\Delta G_{ij}\frac{\Delta\theta}{2\sin\Delta\theta} \qquad\qquad\qquad \text{eq. 15}$$

with $\{i,j,k\} = \{x,y,z\}$ and ϵ_{kij} the Levi-Civita permutation symbol.

From the disorientation of two points separated spatially by distance $\Delta\mathbf{x}$ the lattice curvatures can be approximated as:

$$\kappa_{ij} \approx \frac{\Delta\theta_i}{\Delta x_j} \quad \text{with} \quad \{i,j\} = \{x,y,z\} \qquad\qquad\qquad \text{eq. 16}$$

When working in Laue transmission mode, the differentiation along the third direction is lost, similar to EBSD. Therefore, only six components of the curvature tensor are available: κ_{ix} and κ_{iy} with $\{i\} = \{x,y,z\}$. This procedure has been applied in EBSD by Pantleon (Pantleon, 2008). It has also been applied in 3D X-ray diffraction by Larson et al. (Larson et al., 2007) who have access to the full curvature tensor.

The geometrical interpretation of the curvature components is given schematically in Figure 2.27. Only κ_{ix} have been plotted but the geometrical explanation is analogue for the other components: κ_{xx} represents torsion around X-axis, κ_{xy} flexion of a plane perpendicular to the Y-axis around the X-axis and κ_{xz} a flexion of a plane perpendicular to the Z-axis around the X-axis.
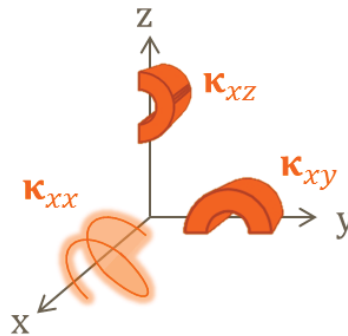
Figure 2.27 Geometrical interpretation of the curvature components

2.3.4 Dislocation density tensor

The local dislocation density tensor ($\boldsymbol{\alpha}$), introduced by Nye (Nye, 1953), measures the density of GNDs and therefore is related to the lattice curvature. In the absence of elastic strain (or small elastic strains, small rotations and small gradient of elastic strain), which is the case for deformed metals, the relationship is given by Nye's formula:

$$\boldsymbol{\alpha} \approx \boldsymbol{\kappa}^{T} - \kappa_{ii}\boldsymbol{I}$$

<div align="right">eq. 17</div>

with κ_{ii} the trace of $\boldsymbol{\kappa}$ and $\boldsymbol{I}$ the identity matrix, which yields:

$$\begin{pmatrix} \alpha_{xx} & \alpha_{xy} & \alpha_{xz} \\ \alpha_{yx} & \alpha_{yy} & \alpha_{yz} \\ \alpha_{zx} & \alpha_{zy} & \alpha_{zz} \end{pmatrix} =$$

$$\begin{pmatrix} \kappa_{xx} & \kappa_{yx} & \kappa_{zx} \\ \kappa_{xy} & \kappa_{yy} & \kappa_{zy} \\ \kappa_{xz} & \kappa_{yz} & \kappa_{zz} \end{pmatrix} - \begin{pmatrix} \kappa_{xx} + \kappa_{yy} + \kappa_{zz} & 0 & 0 \\ 0 & \kappa_{xx} + \kappa_{yy} + \kappa_{zz} & 0 \\ 0 & 0 & \kappa_{xx} + \kappa_{yy} + \kappa_{zz} \end{pmatrix} =$$

<div align="right">eq. 18</div>

$$\begin{pmatrix} -\kappa_{yy} - \kappa_{zz} & \kappa_{yx} & \kappa_{zx} \\ \kappa_{xy} & -\kappa_{xx} - \kappa_{zz} & \kappa_{zy} \\ \kappa_{xz} & \kappa_{yz} & -\kappa_{xx} - \kappa_{yy} \end{pmatrix}$$

As only six components of the curvature tensor are available (κ_{ix} and κ_{iy} with $\{i\} = \{x, y, z\}$) only the components in blue are available.

When combining α_{xx} and α_{yy} the following component can be calculated as well:

$$\alpha_{xx} - \alpha_{yy} = \kappa_{xx} - \kappa_{yy}$$

<div align="right">eq. 19</div>

Note that the dislocation density tensor does not account for SSDs, dislocations of opposite Burgers vectors (b) within the same volume (e.g. dipoles), as their individual lattice distortions are cancelled out (Arsenlis and Parks, 1999).

Each component of the dislocation density tensor, α_{ij}, is a sum of individual dislocation densities (ρ) from different dislocation types (t), each characterized by Burgers vector i and line vector j:

$$\alpha_{ij} = \sum_{t=1}^{N} b_i^t l_j^t \rho^t$$

<div align="right">eq. 20</div>

where N is the number of possible dislocation types.

As only five components are available when working in Laue transmission, the dislocation density of each type of dislocation cannot be determined because the system is indeterminate. It is possible, however, to determine an apparent density of GNDs as (Gupta and Agnew, 2010):

$$\rho_{\text{apparent}} = \frac{1}{b}(|\alpha_{xy}| + |\alpha_{xz}| + |\alpha_{yx}| + |\alpha_{yz}| + |\alpha_{zz}|)$$

<div align="right">eq. 21</div>

The influence of the step size, beam size and the effect of working in Laue transmission are discussed in section 5.5.

2.3.5 Shape of Laue reflections

The shapes of the Laue reflections reflect microstructural gradients inside the gauge volume. Barabash, Ice and co-workers (Barabash and Ice, 2005, 2014, Barabash et al., 2001, 2002, 2003, 2005; Ice and Barabash, 2007; Ice et al., 2005) have developed an advanced approach based on Krivoglaz' work (Krivoglaz, 1969) for calculating the peak profile for basic dislocation structures. This approach takes into account the influence of particular organizations of dislocations on the Laue peaks (i.e. SSDs, GNDs and geometrically necessary boundary dislocations (GNBs)). However, when multiple slip systems are involved, either from the beginning or during load, the Laue peaks start often to broaden, split and/or streak in a non-interpretable manner.

The influence of different basic dislocation organizations on the Laue peaks is illustrated in Figure 2.28 and can be summarized as follow:

- SSDs (Figure 2.28-a) do not cause any macroscopic lattice rotation or bending as there are equal numbers of dislocations with positive and negative Burgers vector (b). They contribute to a homogeneous symmetric broadening of the Laue peak.
- GNDs (Figure 2.28-b) are excess of dislocations of one particular sign in presence of a plastic strain gradient. They cause streaking along a certain direction, which is directly related the nature of the GNDs. Two directions are shown in Figure 2.28: ξ and v. The former is perpendicular to the line direction of the dislocation and the scattering vector and determines the dislocation type of the GNDs; the latter is orthogonal to ξ and the scattering vector. Note that each Laue reflection has different sensitivity depending on the angle between the scattering vector of the planes and the Burgers vector of the dislocation: the lower the angle, the higher the sensitivity.
- GNDs may group into walls and form GNBs (Figure 2.28 -c). The boundary creates a local angular misorientation (θ_m) between the two sides of the crystal and the magnitude depends on the distance between dislocations (h):

$$\frac{b}{h} = 2\sin\frac{\theta_m}{2}$$

<div align="right">eq. 22</div>

GNBs cause further streaking but the intensity distribution is discontinuous. If the misorientation is sufficiently large, the Laue reflection splits.
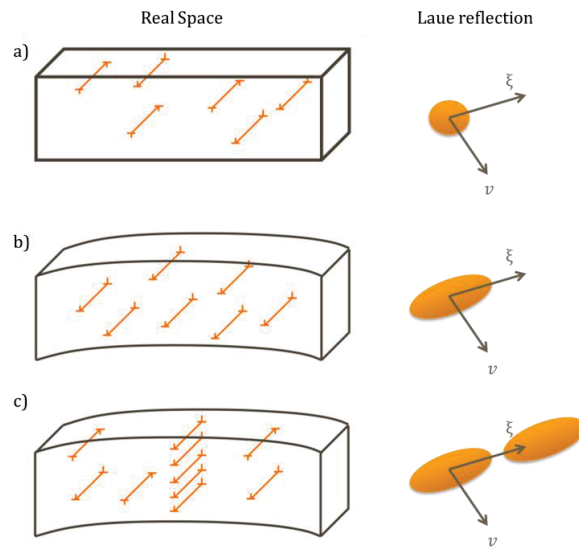
Figure 2.28 Influence of different simple dislocation organizations on the Laue peaks. Adapted from (Ice and Barabash, 2007)

2.3.6 Orientation scattering

As Laue diffraction experiments are performed in transmission geometry, each Laue diffraction spot represents the averaged signal across the sample thickness. Orientation gradients within the gauge volume result in a spreading of the Laue spots. Statistical information of this spreading can be obtained by a template-matching technique as suggested by Gupta and Agnew (Gupta and Agnew, 2009) and later used by Hofmann et al. (Hofmann et al., 2012).

The basic idea is schematically shown in Figure 2.29. Firstly the experimental peak profiles are binaried by setting the pixel intensity to 0 when the peak intensity is less than a threshold and to 1 for all other points with higher intensity (black areas). The threshold is defined individually for each Laue reflection as the 15-20% of the

volume integral of the intensity. Then virtual Laue diffraction patterns for various crystal orientations that deviate slightly from the average orientation (yellow points) are generated: the orientation of the crystal is virtually rocked around the mean position by rotating about the X, Y and Z- axes with a step size of 0.03° such that orientation an grid $|\theta_x|= |\theta_y|=|\theta_z|=1.5°$ is covered (patterned areas). When all virtual positions of each reflection lie inside the black areas, a match is found (green points). When at least one of the virtual positions is out of the black areas, the orientation is not considered as a match. With all the matched crystal orientations, a picture of the orientation spread within the gauge volume in terms of three rocking rotation angles (θ_x, θ_y, θ_z) can be plotted.
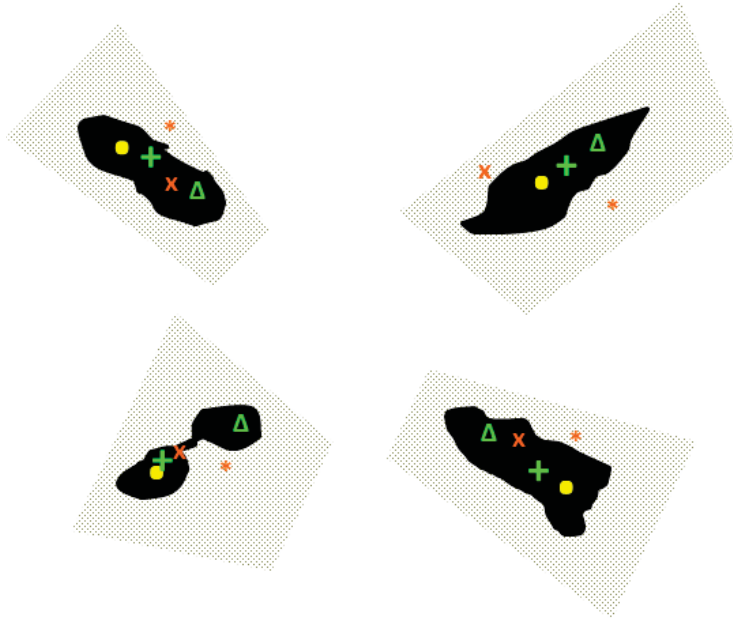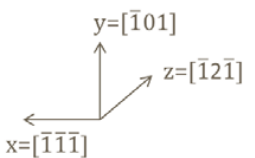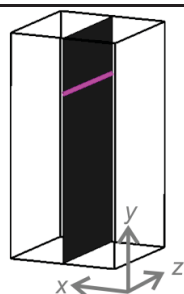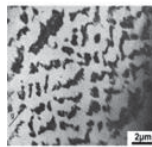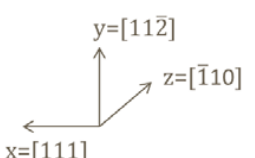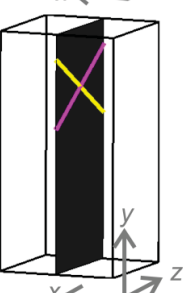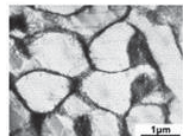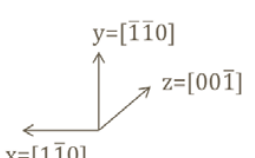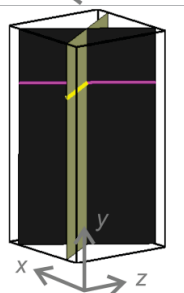
Figure 2.29 Principle of the template matching

2.4 Sample overview

In this thesis, copper single crystals in three different orientations have been tested: single slip, coplanar double slip and collinear double slip. The crystallographic axes, active slip planes and corresponding Schmid factor for shear deformation are given in Table 2.3. The active slip systems are represented in a cuboid too, where the lines represent the dislocation lines of primary slip systems. The expected dislocation structure for single slip oriented fatigued sample are the so called channel-vein structure (Ackermann et al., 1984; Ahmed et al., 2006). For coplanar a cell structure is expected in the (111) plane (Li et al., 2011). Collinear orientation is not accessible in tension-compression experiments. Therefore no literature information is found about the saturated stage after fatigue.

The successfully tested and analyzed samples are summarized in Table 2.4. The sample preparation condition relates to the number of annealing steps (see section 2.1.2). The optically measured thickness and diameter are given. Each sample has been subjected to different total amount of cycles, which is shown in the last column of the table.

Table 2.3 Summary of the orientation of the tested samples

Orientation	Crystallographic axes*	Active slip plane/s	Schmid factor	Representation of active slip systems	Expected dislocation structure
Single slip	y=[$\bar{1}$01] z=[$\bar{1}$2$\bar{1}$] x=[$\bar{1}\bar{1}\bar{1}$]	(111)[$\bar{1}$01]	1		
Coplanar	y=[11$\bar{2}$] z=[$\bar{1}$10] x=[111]	(111)[$\bar{1}$01] (111)[0$\bar{1}$1]	0.866 0.866		
Collinear	y=[$\bar{1}\bar{1}$0] z=[00$\bar{1}$] x=[1$\bar{1}$0]	(1$\bar{1}$1)[110] ($\bar{1}$11)[110]	0.816 0.816		

* Y-axis corresponds to shear-load axis and Z-axis to beam axis.

Table 2.4 Summary of the characteristics of the analyzed samples

Orientation	Sample	Condition	Thickness	Diameter	Total cycles
Single slip	S1-L	Single annealing	31 μm	297 μm	120
Single slip	S1-R	Single annealing	31 μm	300 μm	120
Coplanar	S2-Cp	Double annealing	31.5 μm	304 μm	95
Collinear	S2-Cl	Double annealing	31.4 μm	301 μm	80

Chapter 3   Single slip results

In this chapter the results of the in-situ fully reversed cyclic shear experiments for copper single crystals oriented for single slip are introduced. The mechanical data, microstructural evolution in terms of misorientation angle, rotations about *X-Y-Z*-axes, lattice curvatures and GNDs, and analysis of the Laue reflections are presented for two samples: sample S1-L (left shear zone) and sample S1-R (right shear zone).

3.1   Single slip orientation

Samples oriented for single slip have easy glide on the $(111)[\bar{1}01]$ system when loaded in shear (Schmid factor of 1). The list of Schmid factors for all slip systems is shown in Table 3.1. The $(111)[01\bar{1}]$ and $(111)[1\bar{1}0]$ have a 50% lower Schmid factor. Both share the same plane as the primary slip system but with different Burgers vector. The $(1\bar{1}1)[\bar{1}01]$ system, which has the same Burgers vector as the primary system but a different slip plane, has a Schmid factor that is a third of the value of the primary slip system. All other slip systems have a much lower Schmid factor. Figure 3.1 shows the primary slip system in a cuboid and the crystal orientation in the laboratory frame.

Table 3.1 Schmid factors for single slip orientation

Slip system	Plane			Direction			Schmid Factor
1	1	1	1	$\bar{1}$	0	1	1
2	1	1	1	0	1	$\bar{1}$	0.5
3	1	1	1	1	$\bar{1}$	0	0.5
4	1	$\bar{1}$	1	$\bar{1}$	0	1	0.333
5	$\bar{1}$	$\bar{1}$	1	0	$\bar{1}$	$\bar{1}$	0.167
6	$\bar{1}$	$\bar{1}$	1	$\bar{1}$	1	0	0.167
7	$\bar{1}$	1	1	0	1	$\bar{1}$	0.167
8	$\bar{1}$	1	1	$\bar{1}$	$\bar{1}$	0	0.167
9	1	$\bar{1}$	1	0	$\bar{1}$	$\bar{1}$	0.167
10	1	$\bar{1}$	1	1	1	0	0.167
11	$\bar{1}$	$\bar{1}$	1	1	0	1	0
12	$\bar{1}$	1	1	1	0	1	0
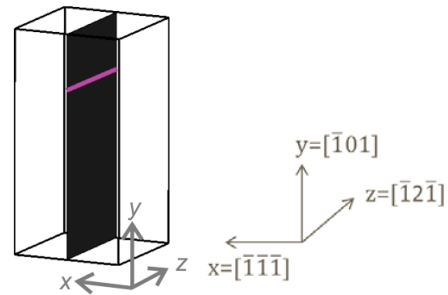
Figure 3.1 Crystal orientation and primary slip system (plane and dislocation line) for single slip orientation. Y-axis corresponds to shear-load axis and Z-axis to beam axis.

3.2   Mechanical data

The sample oriented for single slip has been subjected to a total of 120 cycles, subdivided into five series, where the plastic strain amplitude was gradually increased from 0.027% to 0.295%. The force response as a function of resolved shear strain for the last cycle of each series is shown in Figure 3.2. The number of cycles, force at maximum positive displacement and the resolved total and plastic shear strain amplitudes are also listed in Table 3.2. The crystal shows small hysteresis for plastic shear strain amplitudes < 0.095%, and larger for higher amplitudes.
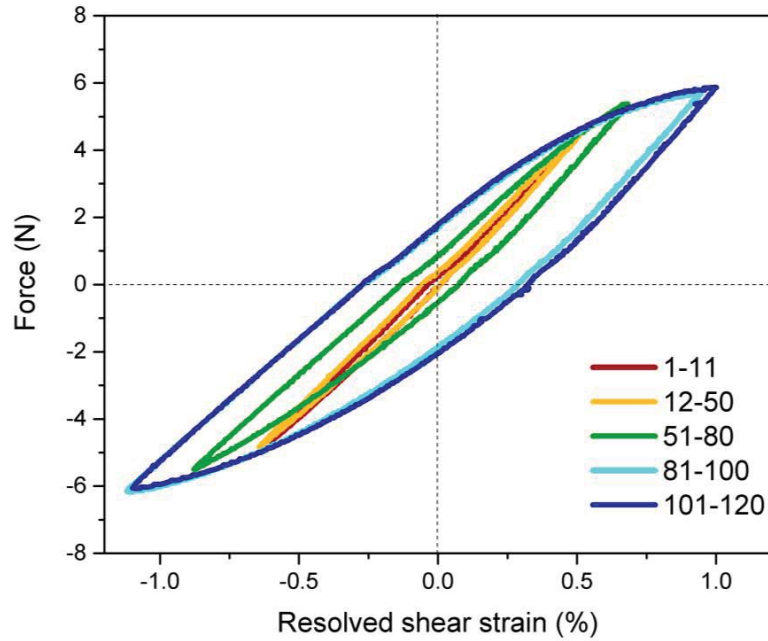
Figure 3.2 Mechanical response of single slip oriented sample

Table 3.2 Number of cycles, maximum force and resolved total and plastic shear strain amplitudes for single slip orientation

Total cycles	Maximum force (N)	Resolved total shear strain (%)	Resolved plastic shear strain (%)
1-11	4.50	0.51	0.027
12-50	4.77	0.54	0.040
51-80	5.38	0.68	0.095
81-100	5.69	0.95	0.285
101-120	5.86	1.00	0.295

3.3   Sample S1-L

3.3.1   Evolution of misorientation angle

The evolution of the misorientation angle of sample S1-L during fatigue is shown as a function of cycles in Figure 3.3-a. The initial microstructure consists of a few misoriented regions with dimensions of the order of μm^2. Region **A** is rotated by 0.15°, region **B** by 0.22°, and regions **C**, **D** and **E** by values less than 0.14°. In region **C** there are some hot spots with misorientation values of 0.21°. The probability density function (PDF) has an arbitrary shape with the mode value of 0.1° (Figure 3.3-b). The description of the PDF distribution is given in Appendix D.

During the first 50 cycles, the misorientation distribution changes continuously. Region **A** and **E** shrink and lower the misorientation magnitude. Regions **B** and **D** get fragmented and the overall misorientation value reduces. In the right edge of region **D**, however, a small cluster of 0.21° misorientation appears. Region **C** shows the opposite trend: its overall rotation increases, probably to accommodate the initial hot spots. Analysis of the PDF reveals that the mode has been shifted to a value of 0.07°.

After additional 30 cycles (total of 80), the scanned region mostly homogenizes to a "background" containing only rotation gradients below 0.05°. Region **A** has almost disappeared and region **C** lowers its misorientation value. Region **D** reassembles and reaches the same initial rotation value. Overall, some pre-existing features remain, such as the fragmented region **B** with maximum misorientation of 0.24°, and the footprints of regions **C, D** and **E**, with a rotation of ~0.13°. There is another area, located in the left side of region **E**, labelled **E'**, which has the same misorientation value and that has emerged from the pre-existing heterogeneity. All these traces are contributing to a sub-peak with the sub-mode around 0.13° in the PDF.

During the last 40 cycles at large plastic strain amplitude, new highly rotated areas appear. The onset of these regions is observable after a total of 100 cycles, but they further grow in rotation values and in dimensions during the last 20 cycles (e.g. regions **D'** or **F**). At the end, two 0.22° misoriented regions are formed, one which evolved from the previous fragmented region **B**, and another (marked **F**) from a region that was part of the "background". These red rotated areas are slightly elongated in the $Y=[\bar{1}01]$ slip direction and are contributing to the sub-peak around 0.22° in the PDF plot. Region **D'** expands and contains some hot red spots inside; region **D** reduces its size.
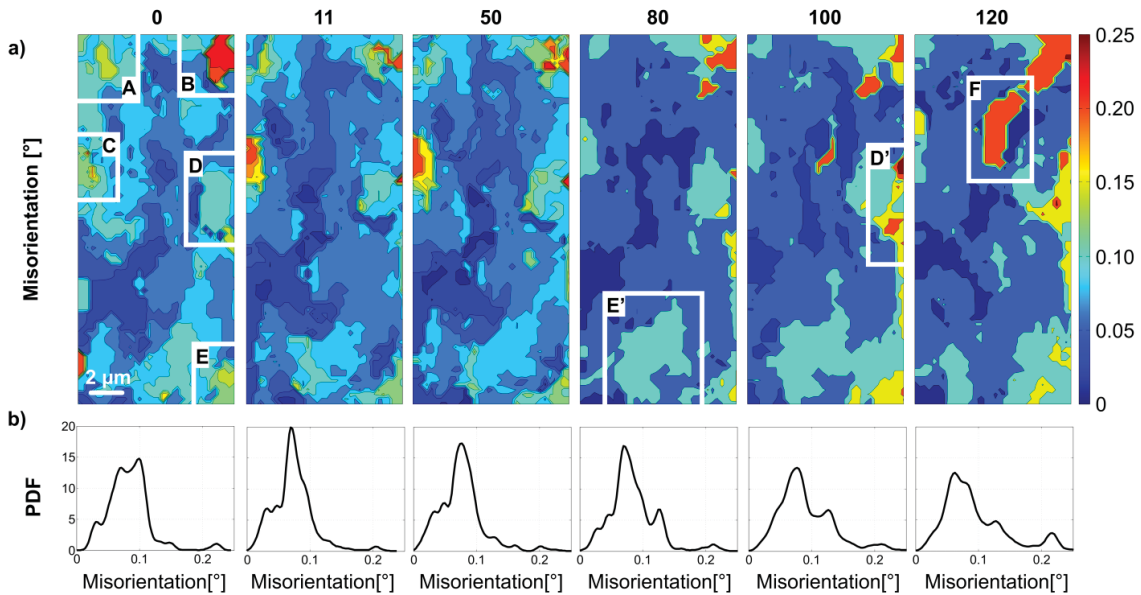
Figure 3.3 Evolution of misorientation angle of sample S1-L. a) Spatial resolved maps; b) PDF functions

3.3.2 Evolution of rotations about X-Y-Z- axes

Figure 3.4-a-c presents the evolution of the amount of rotation around the *X-, Y-*, and *Z-* axes (ω_x, ω_y and ω_z). The scale bars for these rotations are |0.2°|, |0.1°| and |0.25°| respectively. For each cycle, the PDFs of ω_x, ω_y and ω_z are plotted in Figure 3.4-d. On these plots a grey band with a width of |0.03°| is shown. As the rotation angles within this band are very low, the exact values should be taken with care since the rotation axes are not well defined. The description of the PDF distribution is given in Appendix D.

As in the case of the misorientation map (Figure 3.3), the initial distributions of ω_x, ω_y and ω_z before cycling are not homogeneous. Some domains in the upper part of the ω_x map are rotated positively (e.g. region **A** with $\omega_x \sim$ 0.04° - yellow) and other domains negatively, e.g. region **E** ($\omega_x < $ -0.05° - dark blue). More locally, one can also find small regions with higher values of $\omega_x \sim$ 0.20°, as is for instance the case in region **C**. The ω_y values are generally smaller in magnitude, with largest values of $\omega_y \sim$ -0.07° (e.g. region **D**). The rotation around the *Z*-axis is the most pronounced: positive rotated areas with $\omega_z \sim$ 0.08° (region **E** and surrounds of region **B**) or $\omega_z \sim$ 0.22° (region **B**) can be found. These areas are embedded in a matrix with negative values for $\omega_z \sim$ -0.06° (light blue). These domains contribute to sub-peaks in the PDF curve.
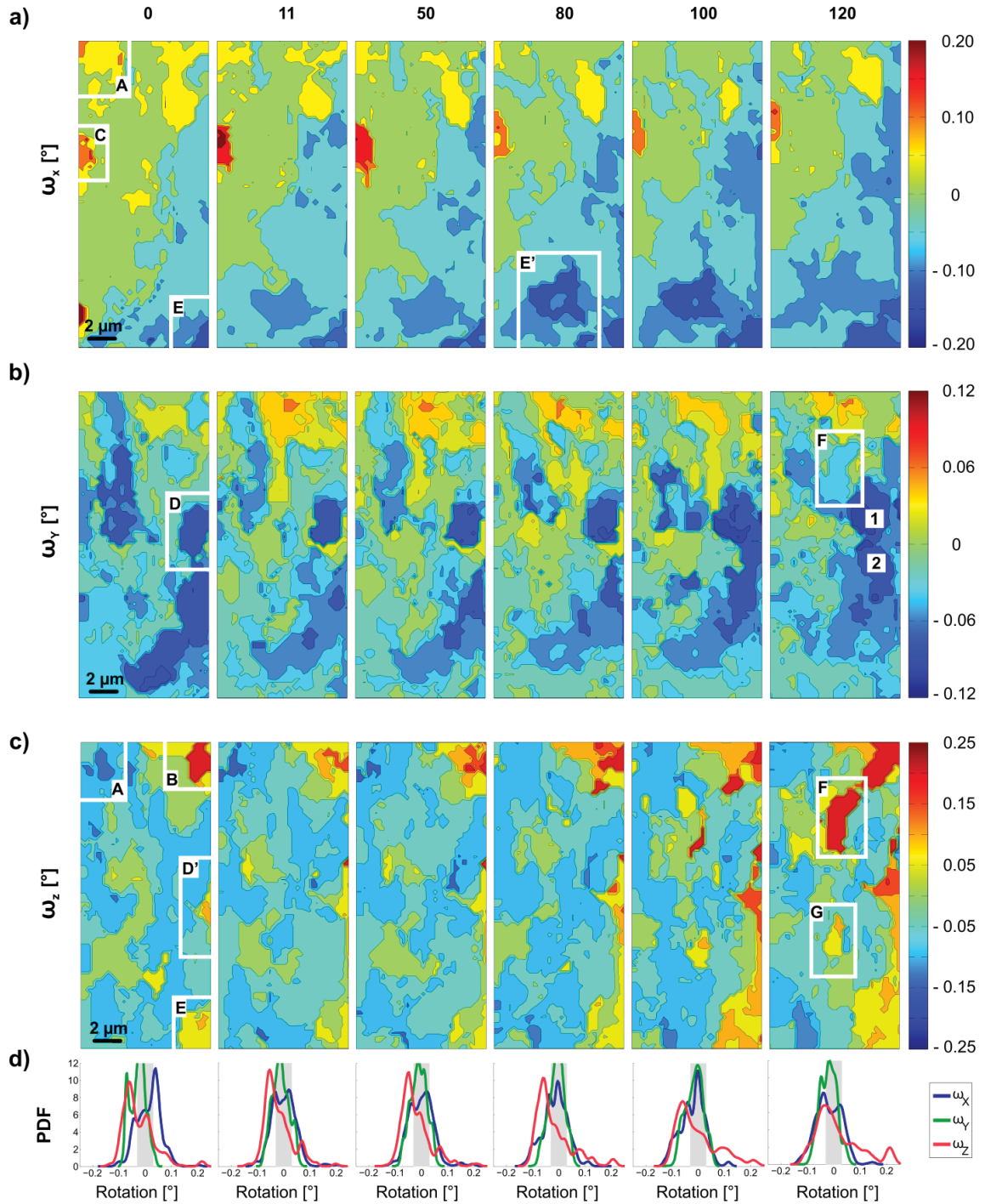
Figure 3.4 Evolution of rotations on the X-, Y-, and Z- axes (ω_x, ω_y and ω_z) of sample S1-L

The misorientation map and ω_z map have the strongest correlation. There are, however, some differences: region **D'**, which is invisible in the misorientation map until step 100, is recognizable at step 0 in the ω_z map.

During the first 80 cycles at low and intermediate amplitude, the initial rotational heterogeneity is accommodated. As it was observed in the evolution of misorientation maps, the domains start fragmenting, and in general the PDFs tend to narrow. The yellow domains in the ω_x maps for example get smaller. Only region **C** increases its ω_x value. On the other hand, new blue areas appear (region **E'**) and the initial ones expand. The dark

blue-domains of the ω_y map also shrink their size and magnitude. The upper part of the map tends to rotate to positive ω_y, but the value is never larger than 0.05°. The evolution of ω_z during cycling is very similar to what was observed for the misorientation map: the pronounced fragmentation of regions **B** and **E,** and vanishing of region **A.** Region **D'** tends to slowly expand and increase its rotation about the *Z*-axis.

During the last 40 cycles, the ω_z maps are the ones experiencing most of the changes. The regions with high misorientation value also have the higher positive rotation about the *Z*-axis (regions **B**, **F** and **D'**). The three regions grow in size and in magnitude upon cycling. There is another region (named **G**) that is not visible in the misorientation map but has relatively high rotation about *Z*-axis. The PDF also confirms the development of domains with large positive ω_z with modes around 0.07° (yellow), 0.12° (orange) and 0.21° (red). In the ω_y maps after cycle 120, two defined globes with $\omega_y \sim$ -0.07° are apparent (marked as 1 and 2). One corresponds to the initial region **D** and lies between two highly + ω_z rotated regions (region **F** and **D'**); the other one is located below region **D'**. Region **F** has also negative rotation about *Y*-axis ($\omega_y \sim$ -0.04°). No special changes are visible in the ω_x maps.

3.3.3   Lattice curvatures and dislocation density tensor components

Figure 3.5 shows the evolution of the lattice curvature components upon cycling in mrad/µm. The same scale bar (|8 mrad/µm|) has been given to all the components for better comparison. Most of the lattice curvature components mark the perimeter of the abovementioned misoriented regions (see Figure 3.3-a) and exhibit changes during fatigue.

- The maps of κ_{xx} and κ_{xy} components are given in the first two rows. Before cycling (step 0) they already mark the perimeter of regions **C**, **D'** and **E**. Upon cycling, these traces of κ_{xx} and κ_{xy} still mark the boundaries of the three misoriented regions and none of the curvature components vanish (e.g. one can follow the expansion of regions **B** and **E**).
  There is another region, named **H,** which is not distinguishable in the misorientation map (Figure 3.3-a) and ω_x, ω_y and ω_z maps (Figure 3.4-a-c) but shows κ_{xx} and κ_{xy} curvatures. This heterogeneous region is relatively invariant during fatigue as its physical location and features do not exhibit major changes.
  At map 80 few boundaries are marked with arrows in the κ_{xx} and κ_{xy} maps. These boundaries are initially discontinuous, whereas after 80 cycles and until the last cycle they become connected.
  The onset of region **F** is visible at map 100 and is clearly defined at step 120. There is another region (**G**) with identical features below it. Nevertheless, this region is not created during fatigue as its traces already exist from the beginning (**G'**).
- The κ_{yx} and κ_{yy} maps are shown in the third and fourth rows. Initially there are areas without κ_{yx} and κ_{yy}. Mainly the perimeter of regions **B**, **G'** and **E** are recognizable before cycling.
  At the beginning there is a faint mark of region **A** that vanishes upon cycling. Region **B**, on the other hand, is always present and the fragmentation observed in the misorientation map (Figure 3.3-a) can be tracked.
  Regions **G'** and **E** follow the same evolution as described above. Both maps are relatively clean of traces during the homogenization process, until step 80, after which region **D'** is noticeable.
  In the last maps the formation of region **F** and expansion of **D'** can be followed. Region **G** is recognizable at step 120 too.
- The footprints of κ_{zx} and κ_{zy} are the less pronounced among all the lattice curvature components and are shown in the last two rows. In the initial maps mainly region **B** and **C** can be detected. There are also a few lines marked with arrows that are present during the 120 cycles.
  After 100 cycles, the onset of region **F** is visible and after 120 cycles, the boundaries of the region are clearly marked.
  The lower parts of these maps do not show any strong κ_{zx} and κ_{zy} curvature changes.
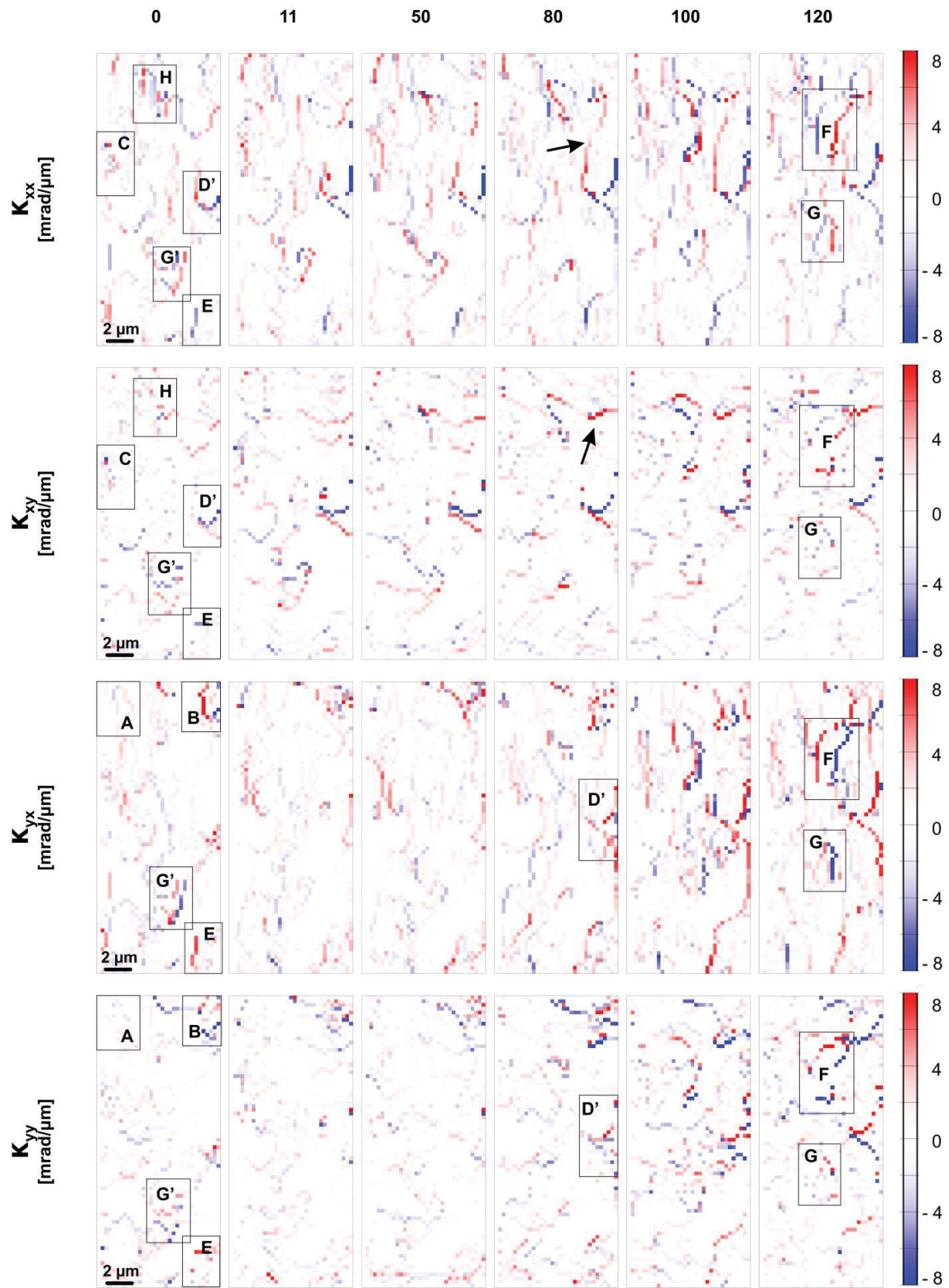
Figure continues on the next page
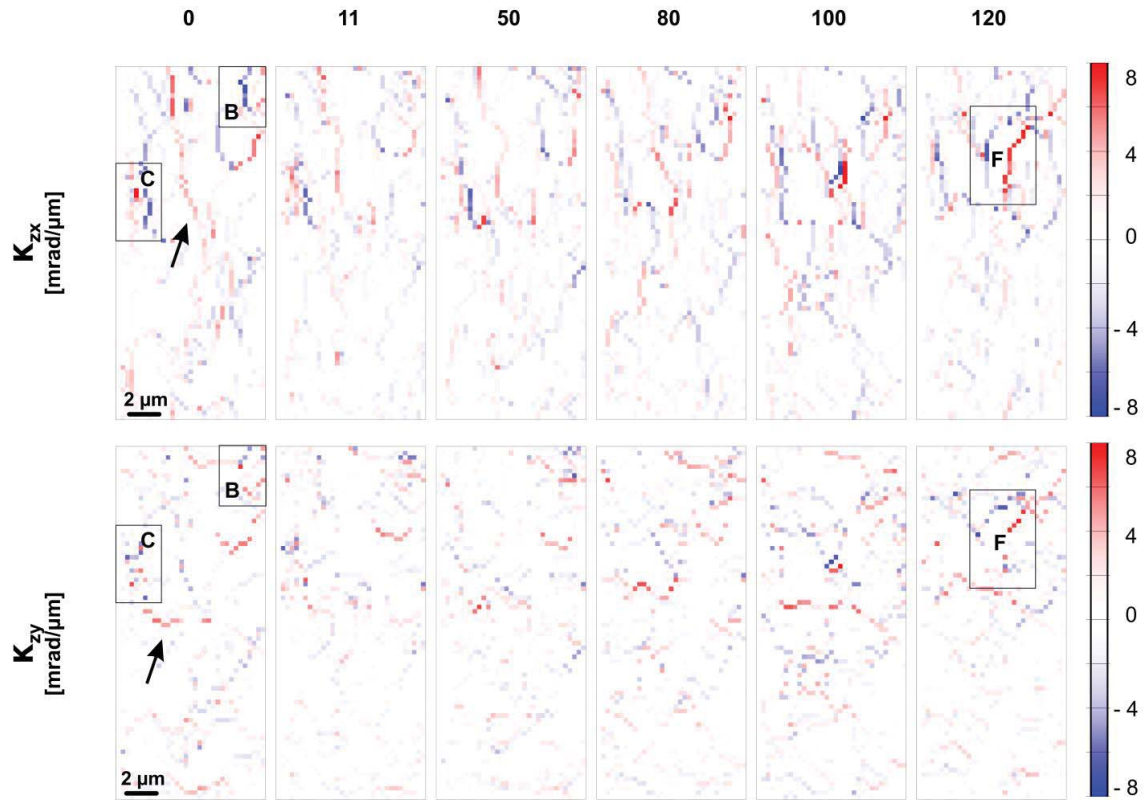
Figure 3.5 Evolution of lattice curvatures and dislocation density components of sample S1-L

The dislocations corresponding to the primary slip system for single slip orientation have their Burgers vector parallel to $Y=[\bar{1}01]$ and line direction in the Z-axis. These straight dislocations cause κ_{zx} and κ_{zy} lattice curvatures. As already mentioned mainly regions **B**, **C** and **F** show κ_{zx} and κ_{zy} footprints. The former two have these traces from the beginning; the latter has evolved from the low misoriented background. This suggests that region **F** is result of fatigue deformation.

All the lattice curvatures that define the evolved region **F** observed in Figure 3.5 can be interpreted following Figure 2.27. Their geometrical meaning is given in Figure 3.6. On the left wall, region **F** has negative torsion around X-axis, and the plane perpendicular to X-axis has positive flexion around the Y-axis and negative around Z-axis. Reverse signs are found in the right wall. On the upper side, the region has positive torsion around Y-axis and the plane perpendicular to the Y-axis has negative flexion around both X-axis and Z-axis. The lower part has opposite values.
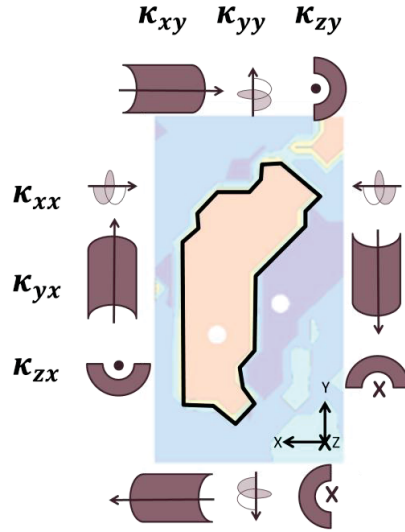
Figure 3.6 Representation of the observed lattice curvatures around region **F**

The α_{zz} and $\alpha_{xx} - \alpha_{yy}$ maps are plotted in Figure 3.7 where most of the regions already mentioned are observable. Regions **B**, **D'** and **F** are the most noticeable, but **E** and **G** can be easily distinguished too. Regions **C** is less sharply defined and region **A** is mainly invisible. In the α_{zz} map the boundaries of some regions have alternating signs particularly on the curved areas (e.g. **E** and **F** at step 120). In both maps the traces are rather strong and evident during the 120 cycles. As in the curvature maps the density of the traces is higher in the upper part of the maps than in the lower part.
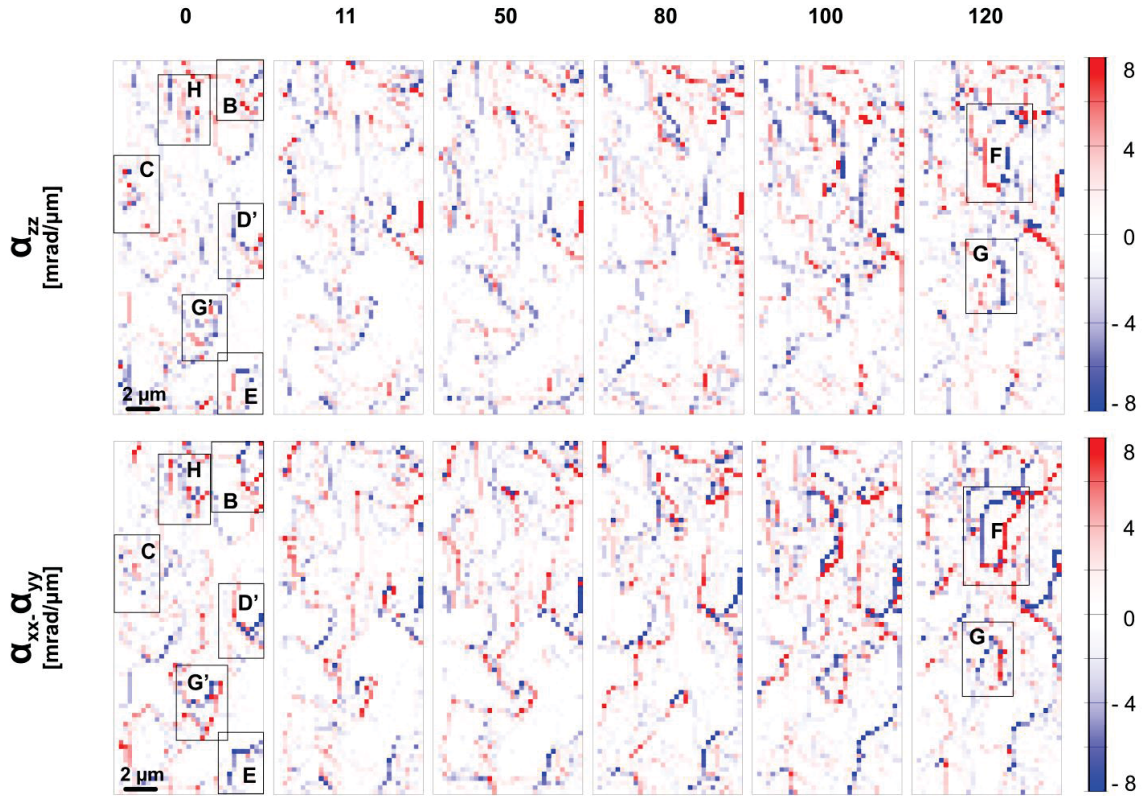
Figure 3.7 Evolution of α_{zz} and $\alpha_{xx} - \alpha_{yy}$ components of sample S1-L

The statistical distribution of each lattice curvature and dislocation density tensor components at cycle 0 and cycle 120 are graphically depicted as boxplots in Figure 3.8. Briefly, each box represents the middle fifty (interquartile = IQR) of the population and the whiskers and arms extend till $|1.5 \times IQR|$. The points plotted as '+' symbol are outliers that are values outside the $|1.5 \times IQR|$ range. The median of all distributions, the central mark of the box that is almost invisible, is ~ 0 mrad/µm and it does not change after 120 cycles. Visual description of boxplots is given in Appendix D.

Before deformation, all the lattice curvature components are roughly below $|10$ mrad/µm$|$. κ_{yx}, α_{zz} and $\alpha_{xx} - \alpha_{yy}$ have some outliers higher than $|10$ mrad/µm$|$. In the later some values are as high as $|15$ mrad/µm$|$. At cycle 120 the boxplots show that outliers of κ_{xx}, κ_{xy}, κ_{yx}, κ_{yy} and α_{zz} exceed $|10$ mrad/µm$|$, whereas the limits of κ_{zx} and κ_{zy} stay below $|10$ mrad/µm$|$. The distribution of $\alpha_x - \alpha_{yy}$ broads considerably and values almost as high as $|30$ mrad/µm$|$ are reached.
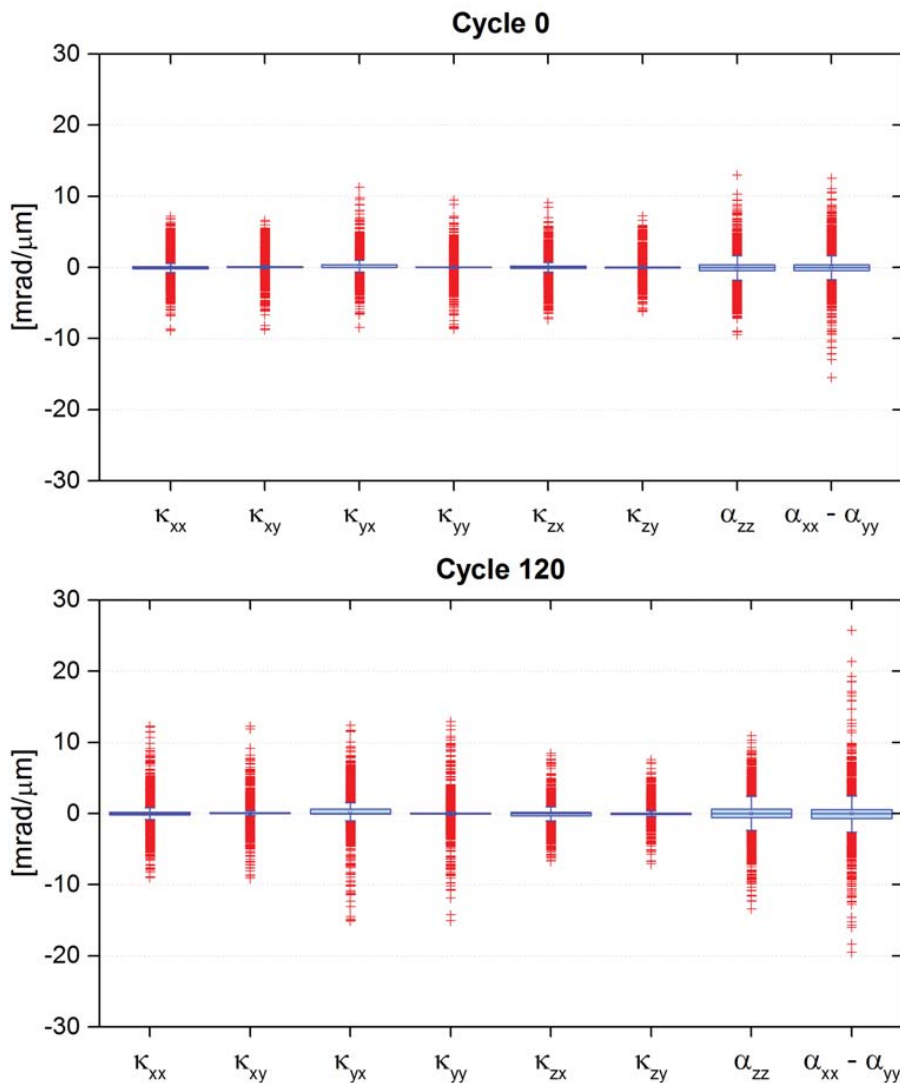
Figure 3.8 Statistical distribution of the lattice curvature and Nye tensor components of sample S1-L

3.3.4 Evolution of apparent GND density

The apparent GND density evolution of sample S1-L is displayed in Figure 3.9. Already in the as-prepared state several tracks with non-zero GND density can be observed due to the sample preparation technique. They are

heterogeneously distributed and the highest density traces mark partially the perimeter of rotated regions (eg. **B**, **C** and **D'**). Others, however, cross regions that have similar misorientation angle (regions **H** and **G'**). The latter means that among regions with similar rotation angle, there are sub-regions with different Euler axis.

During the first 80 cycles, the GND density distribution exhibits a dynamical behavior; in some areas the GND density decreases whereas in others it increases. The initial faint traces ($\sim$10-20 μm^{-2}) redistribute as consequence of the reorganization observed in the misorientation map and ω_x, ω_y, ω_z rotation maps (see Figure 3.3-and Figure 3.4). After a total of 80 cycles, they are still present even if the misorientation map shows a homogeneous low misoriented background. The fragmented region **B** and also region **D'** have the higher density GND traces ($\sim$20-80 μm^{-2}). There is strong correlation with the ω_z map. For instance, right to region **C** there are several closed circuits of GND traces (pointed with white arrows) that do not have direct connection with the misorientation map but are associated to low misoriented regions observable in ω_z (Figure 3.4- c).

At cycle 100, a new cluster with a GND density of 100 μm^{-2} is observed corresponding with the onset of region **F**. At cycle 120, region **F** has grown into a homogeneous rotated region surrounded by high density GND boundaries, ranging from 70-130 μm^{-2}. Also Region **B** and **D'** are defined by GND walls. Region **G** is also visible but the density of GNDs is lower than in the previous mentioned areas: maximum of 60 μm^{-2}.
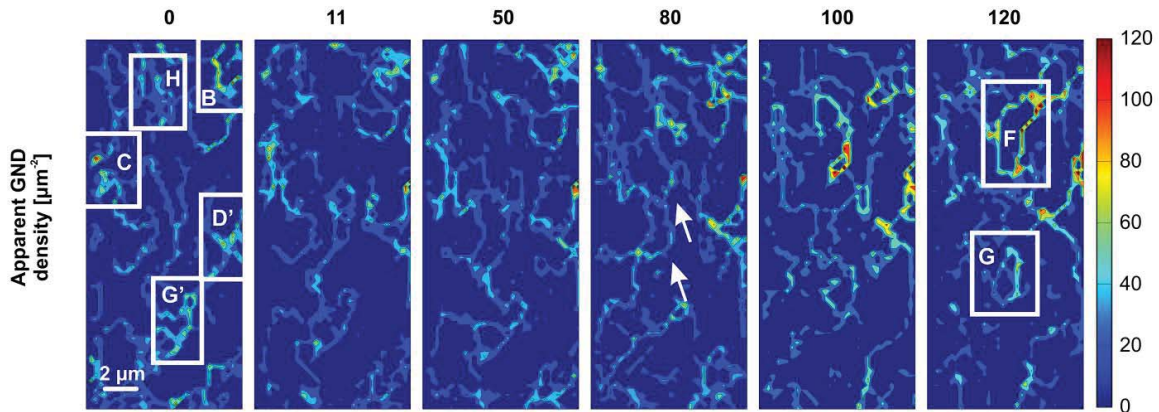
Figure 3.9 Evolution of apparent GND density of sample S1-L

Taking into account the fact that the dislocation lines of the primary dislocations are parallel to the *Z*-axis and assuming that each pixel represents a volume of $\sim$0.5$\times$0.5$\times$30 μm^3 defined by the scanning step size, X-ray beam size and sample thickness, the length of dislocations in μm can calculated from the GND densities. As can be observed in the maps of Figure 3.10 there are always non–zero traces (yellow-green) that corresponds to GNDs with lengths between 100 and 300 μm. Upon cycling there are regions where the GND dislocations increase their length. In some cases this is related to an area that is increasing its misorientation (e.g. region **D'** from cycle 50 to 120). Other times the misorientation value is similar but the length of GND dislocation changes (e.g. region **B** at cycle 0 and at cycle 120). The former situation can be related to a pile-up of dislocations that increase the length; the latter can be related to a restructuring of the microstructure. At cycle 120, Region **F** is defined by a perimeter where the GND dislocations at each measurement point have a length between 300 and 800 μm (green and pink respectively). The implication of the dislocation length is interpreted in section 5.4.
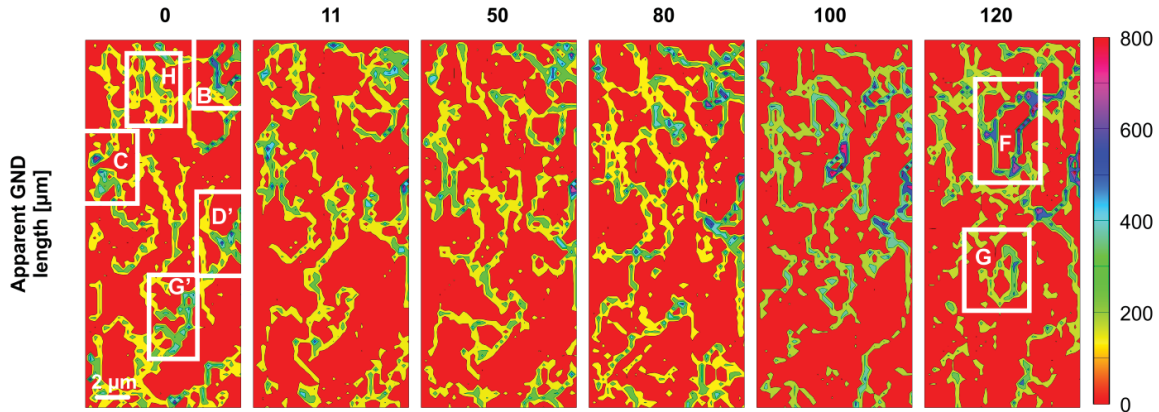
Figure 3.10 Evolution of the distribution of GND length of sample S1-L

3.3.5 Analysis of Laue reflections and orientation spread

In this section, some of the interesting regions already mentioned above are examined more closely. This helps to understand the evolution of the microstructure upon cycling. Table 3.3 presents the angles between the Burger's vector and the normal of the planes related to the diffraction spots. The lower the value the more sensitive the reflection is to a dislocation with that Burger's vector. According to the table (400) and (004) are the most sensitive reflections to the primary dislocations: both form 45° angle with b =[$\bar{1}$01] (shadowed column). In addition, the former reflection is sensitive to dislocations with b = [1$\bar{1}$0], [101] and [110] but insensitive to [0$\bar{1}$1] and [011], and the latter is sensitive to dislocations with b = [0$\bar{1}$1], [011] and [101] but insensitive to [1$\bar{1}$0] and [110]. Therefore each of these reflections may show different insights depending of the activity in different slip systems. For visual representation the most sensitive values are written in green and the insensitive in red.

Table 3.3 Angles between the Burger's vector and the normal of the planes related to the observed Laue reflections

(hkl)\ b	[$\bar{1}$01]	[0$\bar{1}$1]	[1$\bar{1}$0]	[011]	[101]	[110]
1$\bar{3}\bar{3}$	50	90	50	13	71	71
0$\bar{2}\bar{2}$	60	90	60	0	60	60
400	45	90	45	90	45	45
313	90	71	71	50	13	50
$\bar{2}$20	60	60	90	60	60	0
$\bar{3}\bar{3}$1	50	50	90	71	71	13
004	45	45	90	45	45	90

In what follows regions **B** and **F** are examined in more detail.

Region F

During cycling region **F** has developed from a region with initial low misorientation. At step 120 it has a high rotation about the *Z*-axis with boundaries that are well defined by GND walls. Figure 3.11 shows a zoom-in of the misorientation map of this region at cycles 0, 80, 100 and 120. Two positions are indicated for which the evolution of the (400) diffraction peak is shown: position **1F** is located in the area where region **F** is going to be formed and position **2F** is in outside but near to this area. In the latter position the misorientation remains small during cycling. Initially, both peak profiles are relatively narrow as expected for a single crystal. The reflection has some tails to be assigned to the defects introduced during sample preparation. In position **1F**, the volume

over which the signal is integrated progressively splits in sub-regions during the mechanical test, evidencing dislocation accumulation. After 120 cycles the volume has largely rotated over 0.22° and the reflection has a primary peak with residual traces with lower intensities. On the contrary, the peak profile in position **2F** only slightly changes its intensity distribution during homogenization (until cycle 80) and stays mostly unaffected by the last shear cycles.

Analysis of the other high intensity diffraction peaks shows that the initial profiles are similar in both positions **1F** and **2F**. The shape of reflections at step 0 and 120 for position **1F** are shown in Figure 3.12. The (004) reflection exhibits considerable broadening after 120 cycles. The positions of the other two reflections remain similar after cycling, and some sub-splitting and intensity drop are detected. This confirms that during shear cycling, mainly the primary slip system is activated.
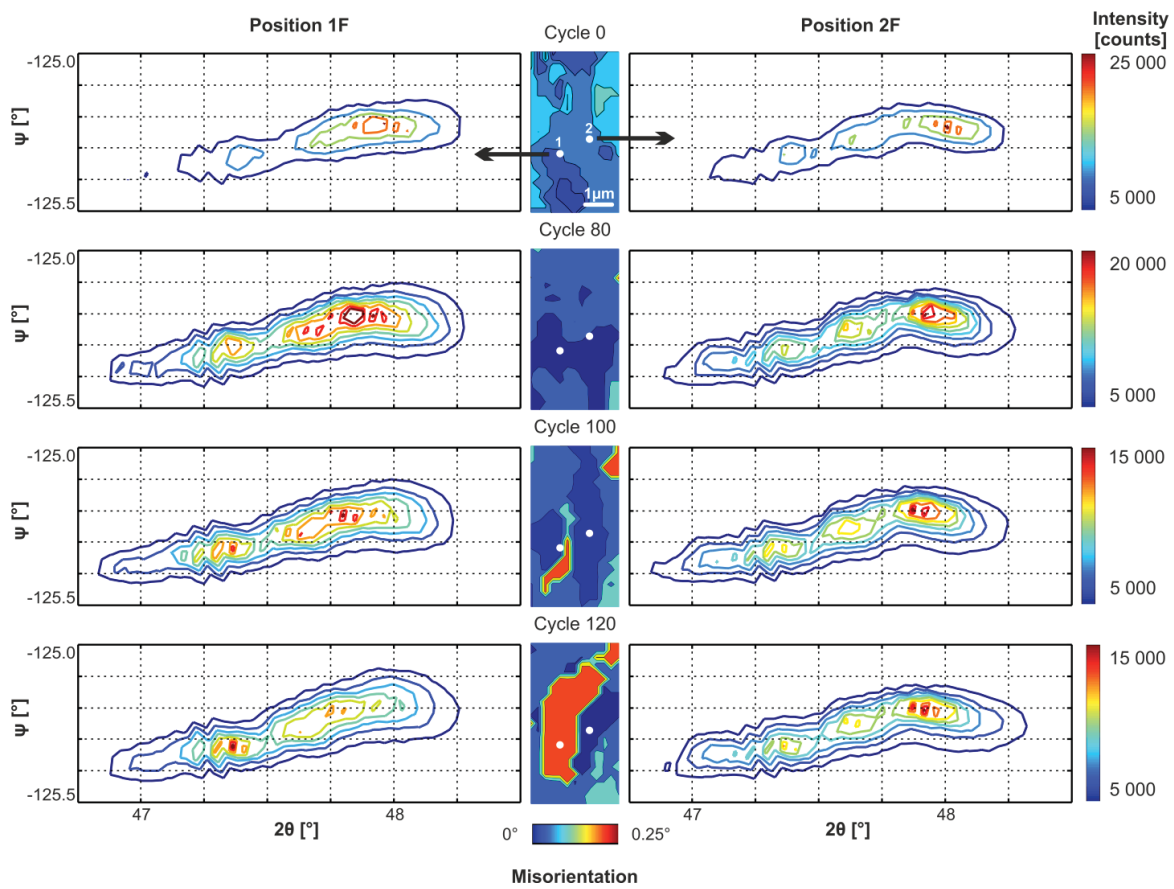
Figure 3.11 Evolution of the (400) diffraction peak in region **F** of sample S1-L
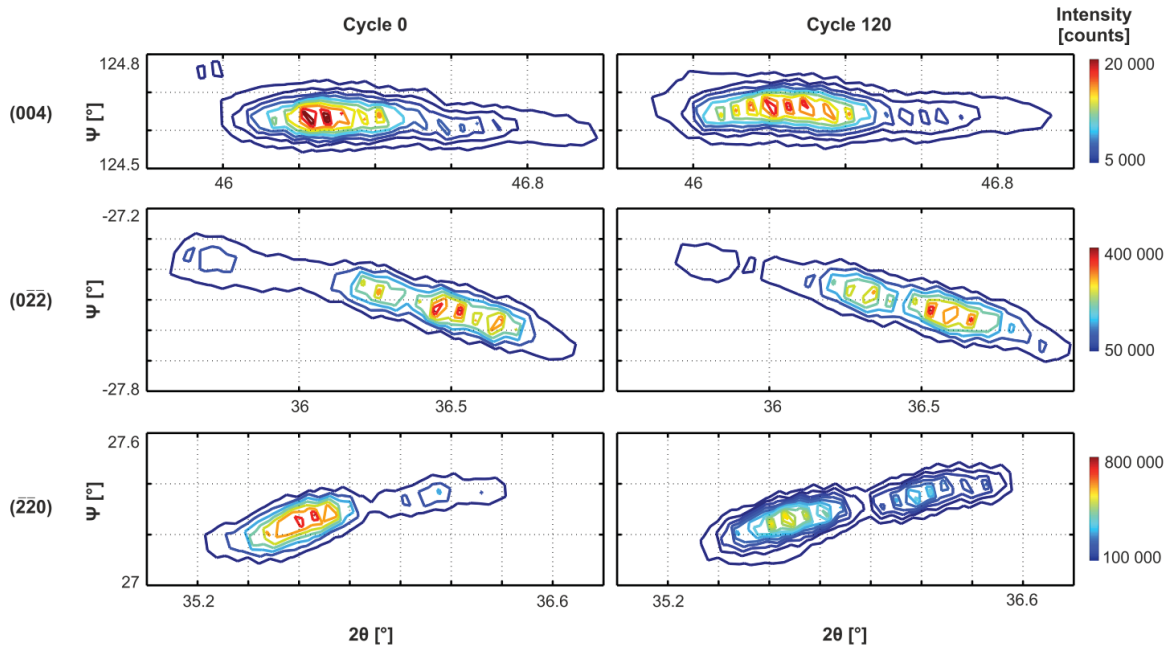
Figure 3.12 Diffraction peaks inside region **F** (position **1F**) at cycle 0 and 120 of sample S1-L

To investigate the axis about which the crystal in position **1F** has rotated from cycle 0 to 120, we have plotted the directions that the (400) peak would follow when the crystal rotates around the *X*-, *Y*-, and *Z*-axes (θ_x, θ_y and θ_z) (Figure 3.13). The arrows represent +0.2° rotation around each axis. The figure shows that the rotation seems to correspond to the *Y*-load axis on this particular peak, but note that the overall rotation is given by the rotation measured in all diffracted peaks.
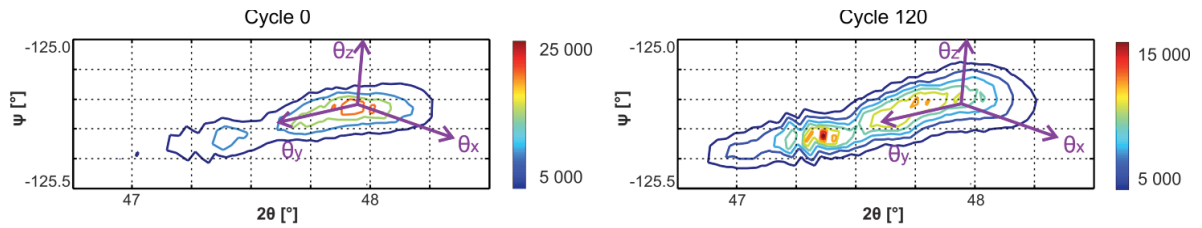
Figure 3.13 (400) diffraction peaks inside region **F** (position **1F**) at cycle 0 and 120 with rotation directions about *X*-,*Y*-,*Z*-axes

To get statistical information on the orientation spread in the illuminated volume the template matching technique is applied in position **1F** and position **2F** at cycle 0 and cycle 120. Figure 3.14 shows the misorientation spread in the illuminated volume, where the small rotation angles around *X*-, *Y*-, and *Z*-axes (θ_x, θ_y and θ_z) are given in degrees. It is important to note that the number of points within a certain orientation region is not proportional to the volume of that region. The color of each point (presented by the scale bar) corresponds to the normalized intensity of the (400) reflection shown in Figure 3.11. The orientation spread prior to cycling is very similar for positions **1F** (Figure 3.14-a) and **2F** (Figure 3.14-b), which can be ascribed to the initial defect content due to the sample preparation. After 120 cycles the positions of the points with maximum intensity for the cloud of position **1F** are shifted (Figure 3.14-c) and a new misoriented region is formed as indicated in Figure 3.14 by the black arrow. This evidences the formation of a volume with different

orientation and whose orientation spread is less than that of the initial microstructure. Traces of the initial microstructure are still observable suggesting that the new region did not yet grow over the entire sample's thickness over which the signal is integrated. The new position is shifted in θ_y ($\sim$0.4°) as analyzed in Figure 3.13. On the other hand, the points with maximum intensity for the cloud corresponding to position **2F** (Figure 3.14-d) remain at similar positions.
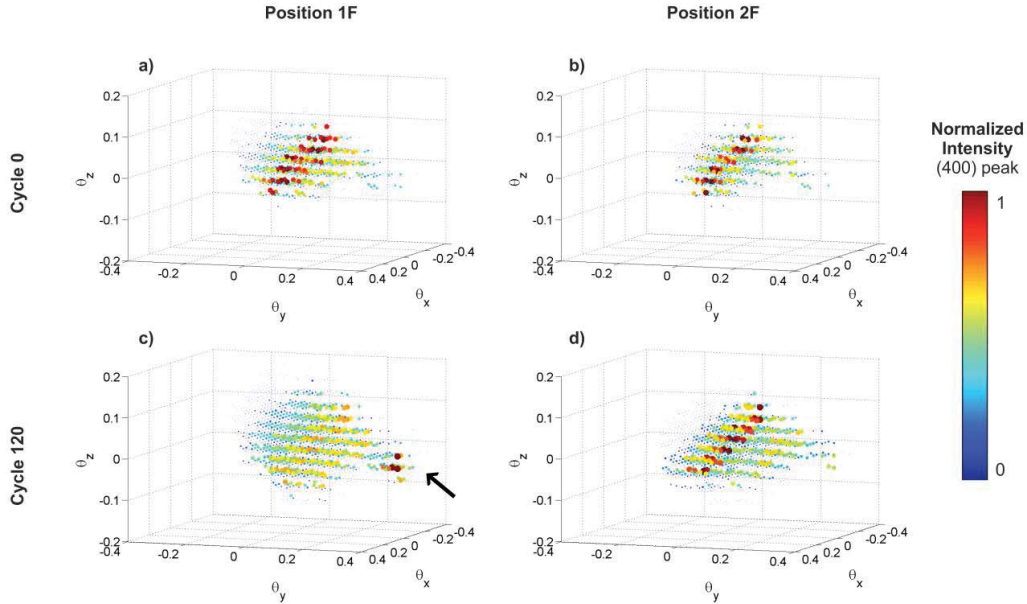
Figure 3.14 Orientation scattering in the integrated volume of positions **1F** and **2F** in region **F**

Other points in region **F** at cycle 120 have been analyzed and the results of six points are shown in Figure 3.15-a. Two of the points are located in the upper part of region **F** (**aF** and **bF**) and the other four at the boundaries (**nF** - north, **eF** - east, **wF** – west and **sF** - south). The shape of the (400) reflection and the orientation spread of these six points are shown in Figure 3.15-b and Figure 3.15-c respectively. In all the points part of the integrated volume has the same rotation features as position **1F** in Figure 3.11: the position of maximum intensity points are indicated by the black arrows. The orientation spread, on the contrary, varies from point to point and the distribution of the cloud is different at each point.

Comparing the orientation spread of position **1F** in Figure 3.14 with those of points **aF** and **bF** evidences small variations in orientation spread across the thickness. For instance the initial microstructure seems to be less distorted in the bottom part of region **F** than in the top, most probably due to the proximity of region **B**.

In all the boundary points of region **F** the (400) reflection shows sub-peaks similar to the peak at cycle 100 in Figure 3.14. This is because in these points the beam is illuminating partially a volume inside region **F** and partially outside that region. Due to differences in microstructure at each point (**nF**, **eF**, **wF** and **sF**) the orientation spread is different.
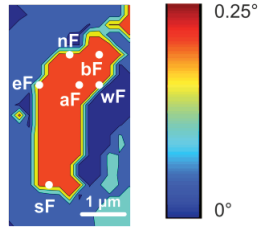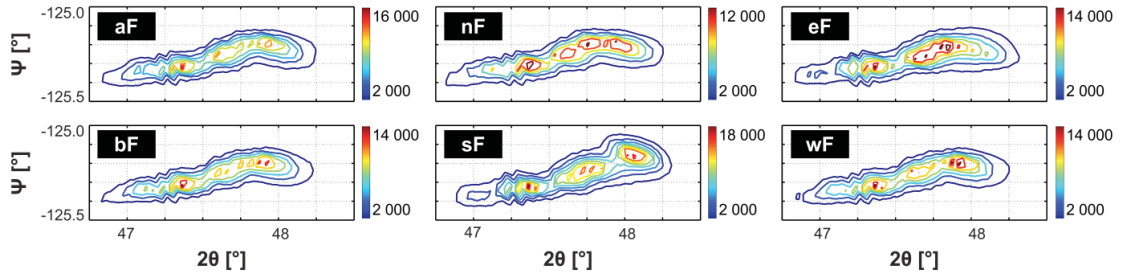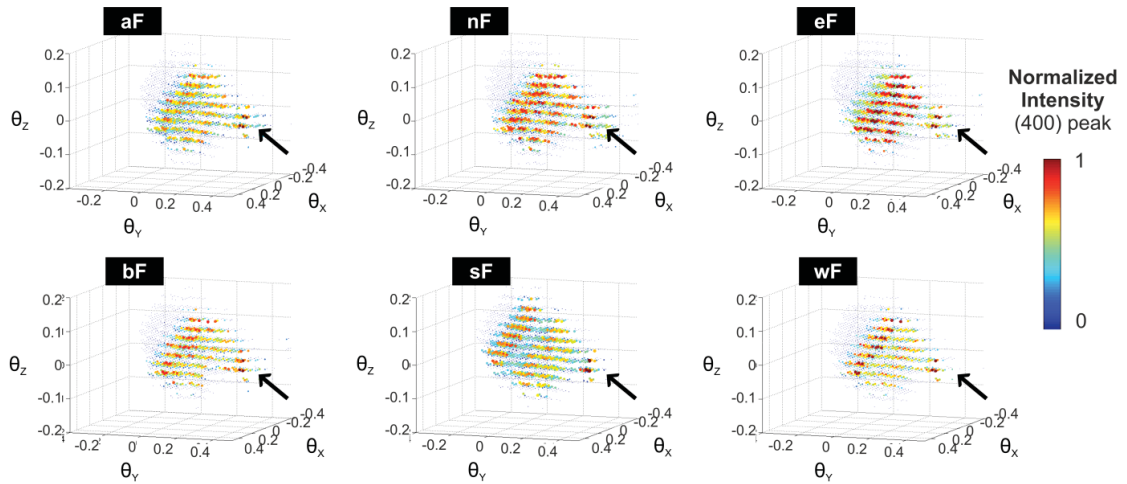
Figure 3.15 (400) diffraction peak and orientation spread in the integrated volume at several positions of region **F** (cycle 120)

Region B

Region **B** has from the beginning a high misorientation and is rotated around the *Z*-axis (see Figure 3.3-a and Figure 3.4-c). Its evolution can be followed in the second column of Figure 3.16. During the first 80 cycles the region becomes fragmented. After cycling with high strain amplitude (from cycle 80 to 120) the region reorganizes until the final features resemble the ones of region **F**. In the figure, three positions are selected: one outside region **B** (position **1B**) and two inside (positions **2B** and **3B**). Position **2B** is located in the center of region **B** where fragmentation occurs; position **3B** is located in the lower part of region **B** where the misorientation lowers at step 50 and 80 before being part of highly misoriented area after 120 cycles.

Columns 1, 3 and 4 of Figure 3.16 show the (400) reflection of each position (**1B**, **2B** and **3B**) after cycle 0, 50, 80 and 120. The initial peak shapes are not the same: in position **1B** the peak looks similar to the peaks in region **F** prior to cycling (Figure 3.11), whereas in positions **2B** and **3B** the (400) reflection is more streaked due to the presence of dislocations. During cycling, the reflection at position **1B** seems almost unaffected as was the case for the low misorientation in point **2F** in region **F** (see Figure 3.11). The reflections at the other positions, on the other hand, continuously split into sub-region due to the movement of dislocations while remaining streaked.

The number of sub-regions after 120 cycles is higher in position **2B** than in position **3B**. During cycling the position of maximum intensity in point **2B** has just barely shifted, however in point **3B** the positions of sub-regions with maximum intensity change continuously (pointed by arrows) while the initial and final positions are very similar. These observations point to the conclusion that there are immobile dislocations agglomerated in region **B** that do not participate to microstructural homogenization during cycling.
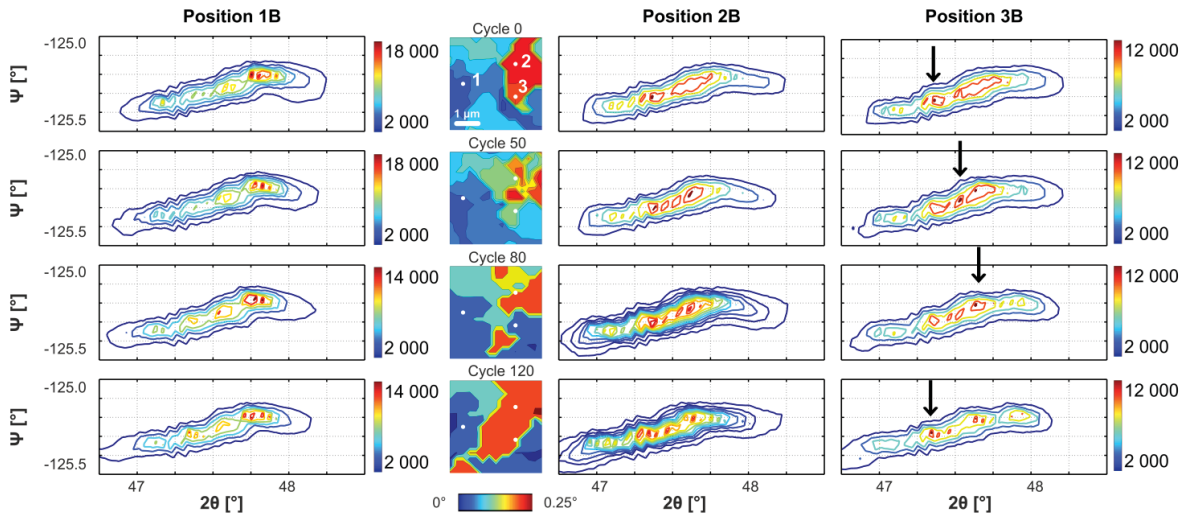
Figure 3.16 Evolution of the (400) diffraction peak in region **B** in sample S1-L

Figure 3.17 shows the orientation spread in the illuminated volume for these three points at different steps (0, 50 and 120). The orientation spread at position **1B** prior to cycling is very similar to those at positions **1F** and **2F** in region **F,** but for positions **2B** and **3B** the initial spread is considerably larger. A sub-region is already present in all three positions, indicated by black circles, but the intensity of the sub-region is higher in positions **2B** and **3B** than in **1B**. During the 120 cycles the points with maximum intensity for the cloud of position **1B** remain at similar positions, meaning that the initial microstructure is almost unchanged. On the contrary, the distributions in positions **2B** and **3B** are continuously changing. In position **2B**, the points with high intensity redistribute; in position **3B** the amount of high intensity points decreases after 50 cycles and after cycle 120 they are distributed in roughly three regions (pointed by arrows). In addition, the intensity in the sub-region of point **2B** remains high after 50 cycles and decreases after cycle 120. In point **3B** the sub-region gradually shrinks and almost disappears after 120 cycles. In summary, the overall evolution at both positions **2B** and **3B** is dominated by the initial microstructure.
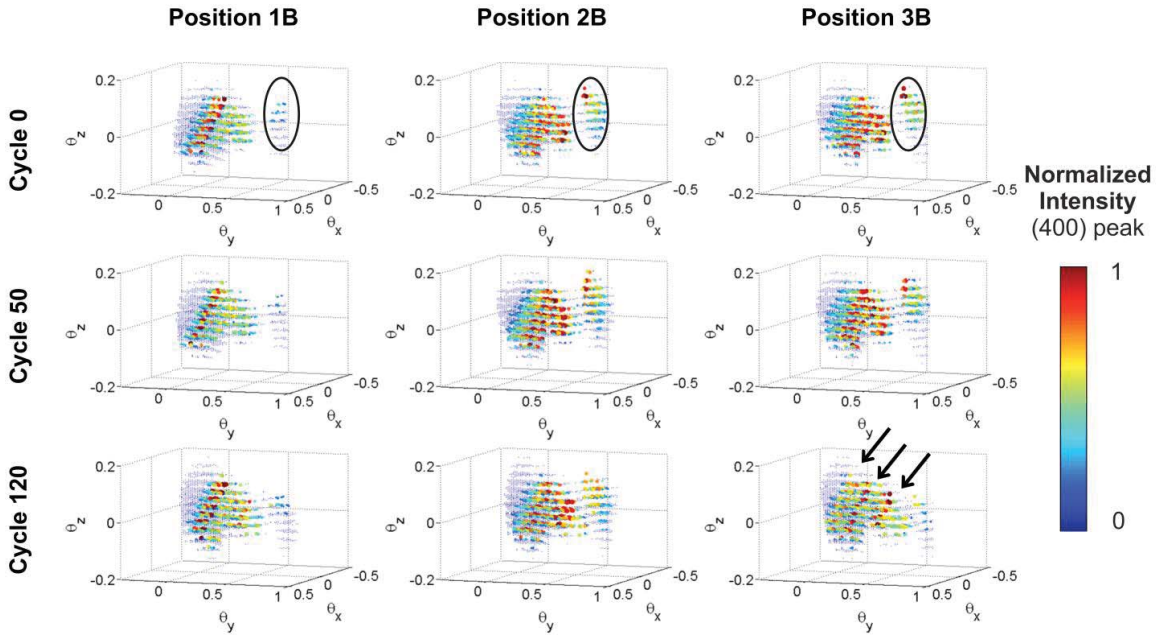
Figure 3.17 Misorientation spread in the integrated volume of three points in region **B** in sample S1-L

3.3.6   Indexation error

The distribution of the indexation error is shown in Figure 3.18 where 7 peaks were taken into account to find the orientation. The averaged indexation error is 7.70±1.21 pixels which is not negligible. Some of the abovementioned regions such as **C** and **D'** are observable in the error maps and therefore they may be artifact, others are not correlated. Particularly there is no evidence of region **F** in these maps.
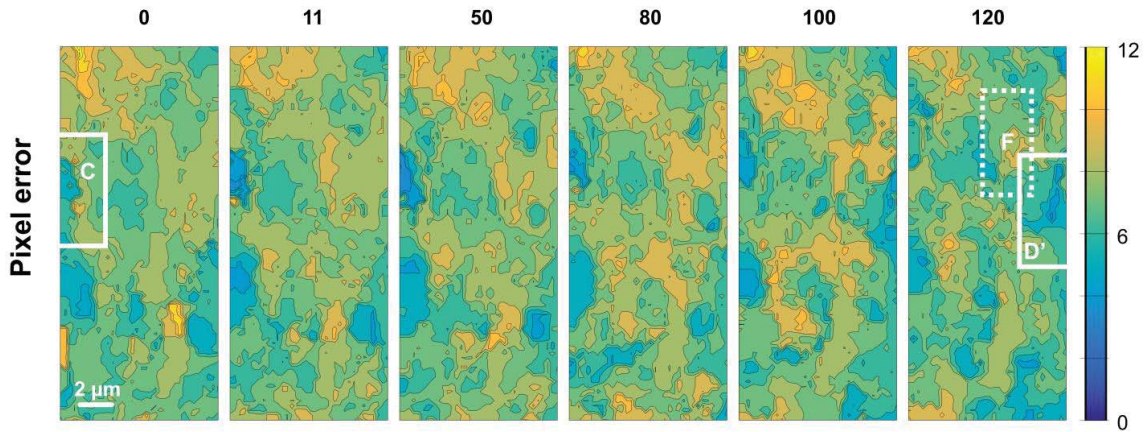
Figure 3.18 Indexation error distribution for each map in sample S1-L

3.4   Sample S1-R

3.4.1   Evolution of misorientation angle

Figure 3.19-a shows the evolution of the misorientation angle of sample S1-R. The initial microstructure shows some heterogeneity, as in sample S1-L (Figure 3.3-a). There are three misoriented regions (**A**, **B** and **C**) with a size larger than 1 μm². These regions have higher misorientation values (>0.25°) compared to what was observed in sample S1-L. Region **A** is composed by a rounded sub-area misoriented by ~0.30° (red) and an extended arm misoriented by ~0.27° (orange). Region **B** is misoriented by the same amount (~0.27°) and shows inside some red hot spots. Region **C** is mostly misoriented by ~0.30°. The lower part of the misorientation map has an overall misorientation of 0.19° and regions **B** and **C** are embedded in that matrix. The rest of the map exhibit a homogenous background with misorientation of 0.11° incorporating some non-rotated areas (dark blue) close to region **A**. The PDF curve (Figure 3.19-b) confirms the described distribution: the principal mode value is 0.10° and a sub-peak at 0.19° and two around 0.28° can be recognized. The description of the PDF distribution is given in Appendix D.

The initial configuration is reorganized during the first 50 cycles. A new yellow zone appears in the lower part of region **A**, probably to accommodate the existent sharp transition from ~0.27° to almost ~0°. The red zone shrinks slightly its size. In the upper part of region **A** new highly misoriented islands appear (~0.28° - orange), which are not connected to region **A**. On the other hand, regions **B** and **C** disappear completely. The matrix also fragments and only few traces remain misoriented ~0.15°. The central part of the map shows a low misoriented background (~0.07°) that extends its area upon further cycling. The upper and lower parts of the map remain misoriented with values between 0.10° and 0.15°. The PDF curve at step 50 shows three main peaks at 0.10°, 0.13° and 0.27°.

When increasing plastic strain amplitude from cycles 50 to 80, new rotated areas emerge. Those areas are located near the previously vanished regions **B** and **C** and therefore are labeled as **B'** and **C'** in the cycle 100 map. Their misorientation magnitude is also comparable to the initial value (~0.27°). The amount of rotation in the surroundings of these new islands also increases. The configuration in the lower part become similar to that of the initial microstructure: misoriented regions are embedded in a moderate misoriented matrix (~0.18°), but no red-hot spots are observable. In the upper part of the map, region **A** extends and gets combined with the above regions that have developed earlier. The PDF shows that the main peak becomes wider and the sub-peak around 0.27° increases.

From cycle 80 to 120, region **A** becomes larger with a mean misorientation value of 0.28° (orange). There is a yellow subarea (misoriented ~0.20°) slowly spreading and absorbing the initial red island (map after cycle 100). Only two red spots are visible, which after 120 cycles grow in size. In region **B'** a big orange island has developed, the position, size and shapes of which are continuously changing. The evolution of region **C'**, on the other hand, is more gradual. It starts as a small island misoriented by 0.20°, then grows in size and is misoriented by 0.27°. After 120 cycles, its shape is elongated and similar to cycle 0. Two small hot spots are noticeable. In addition, new two regions **D** and **E** become visible after cycle 120. The onset of the former region is observable after 50 cycles (pointed by the white arrow), where there is already a small yellow spot that keeps its size until cycle 100. During the last 20 cycles it enlarges and finally region **D** is formed by a yellow subarea neighbored by a moderately rotated area (0.15°) below it. Preliminary traces of region **E** are apparent after 80 cycles (pointed by the white arrow), but the region shows dynamic behavior since at cycle 100 there is no evidence of the misoriented region. All the new rotated regions result in a PDF with a wide continuous plateau (from 0.07° till 0.17°). Furthermore the peak at 0.27° becomes even more pronounced, which implies the growth of the orange areas.
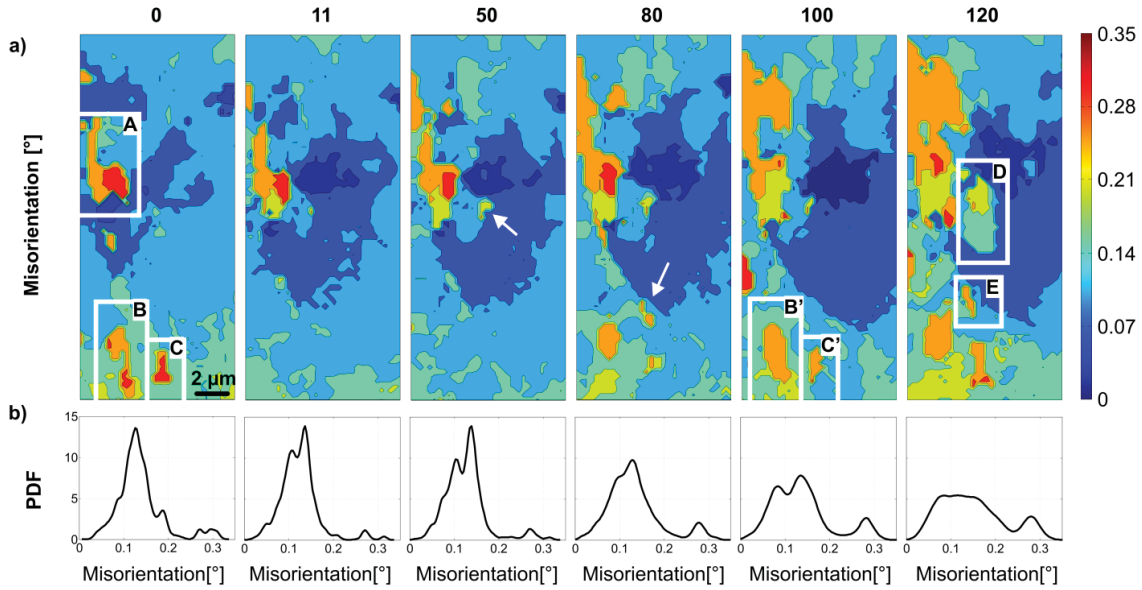
Figure 3.19 Evolution of misorientation angle of S1-R sample. a) Spatial resolved maps; b) PDF functions

3.4.2 Evolution of rotations about X-Y-Z- axes

Figure 3.20-a-c presents the evolution of the amount of rotation around the *X-, Y-,* and *Z-* axes (ω_x, ω_y and ω_z). The scale bars for these rotations are |0.35°|, |0.3°| and |0.25°| respectively. For each cycle, the PDFs of ω_x, ω_y and ω_z are plotted in Figure 3.20-d. On these plots a grey band with a width of |0.03°| is shown. As the rotation angles within this band are very low, the exact values should be taken with care since the rotation axes are not well defined. The description of the PDF distribution is given in Appendix D.

The rotations in sample S1-R are higher than those of S1-L (see Figure 3.4-a-c). Moreover, the highest rotations observed here are around the *X-*axis (ω_x) and not the *Z-*axis (ω_z), as was the case in sample S1-L. In fact ω_z has lowest absolute values.

Analysis of the ω_x map of sample S1-R at step 0 shows that the scanned area is divided in two parts: the right part with negative rotation ($\omega_x \sim$ -0.09° - light blue) and the left part with positive rotation ($\omega_x \sim$ 0.07° - light green). Regions **A**, **B** and **C**, defined in the misorientation maps, have high rotation magnitudes ($\sim$ 0.25°, 0.18° and 0.18° respectively). They contribute to the sub-modes in the PDF. The ω_y map, on the other hand, has the upper part rotated negatively ($\omega_y \sim$ -0.07° - light blue) and the lower part positively ($\omega_y \sim$ 0.06° - yellow). Region **A** is rotated by $\omega_y \sim$ +0.14° and has some hot spots of $\omega_y \sim$ 0.20°. The rotation values of regions **B** and **C** are even higher ($\omega_y \sim$ 0.22°). The ω_z map shows a transition from negative to positive ω_z rotation values when crossing from top-left to bottom-right (from $\omega_z \sim$-0.08 – blue to $\omega_z \sim$0.15 – red). Even if region **A** is not visible, regions **B** and **C** are. Their rotation value is $\sim$0.08° embedded in a 0.13° matrix (orange).

During cycling, the right side of the scanned area remains negatively rotated around the *X-*axis. The magnitude of rotation, however, shifts slightly from $\omega_x \sim$-0.07° to -0.04° as can be seen in the PDFs when comparing step 0 to step 120. By contrast, high activity is observed on the left side of the ω_x map. Region **A** has always high ω_x rotation (0.22° - 0.26°) and grows in size. The sub-mode at high ω_x values gets larger with increasing number of cycles. At cycle 50, positively rotated regions **B** and **C** disappear and the area where they were located turns to negative ω_x rotation ($\omega_x \sim$ -0.07°). This is reversed from cycle 80 on, when the area shows again a positive rotation ($\omega_x \sim$0.10°). Regions **B'**, **C'** and **E** start developing at cycle 80 and after 120 cycles are rotated $\omega_x \sim$ 0.20°. Region **D** is rotated 0.15° (orange) with a subarea rotated $\omega_x \sim$ 0.20° (red). As can be observed, there is a strong correlation between the ω_x map and the misorientation map.
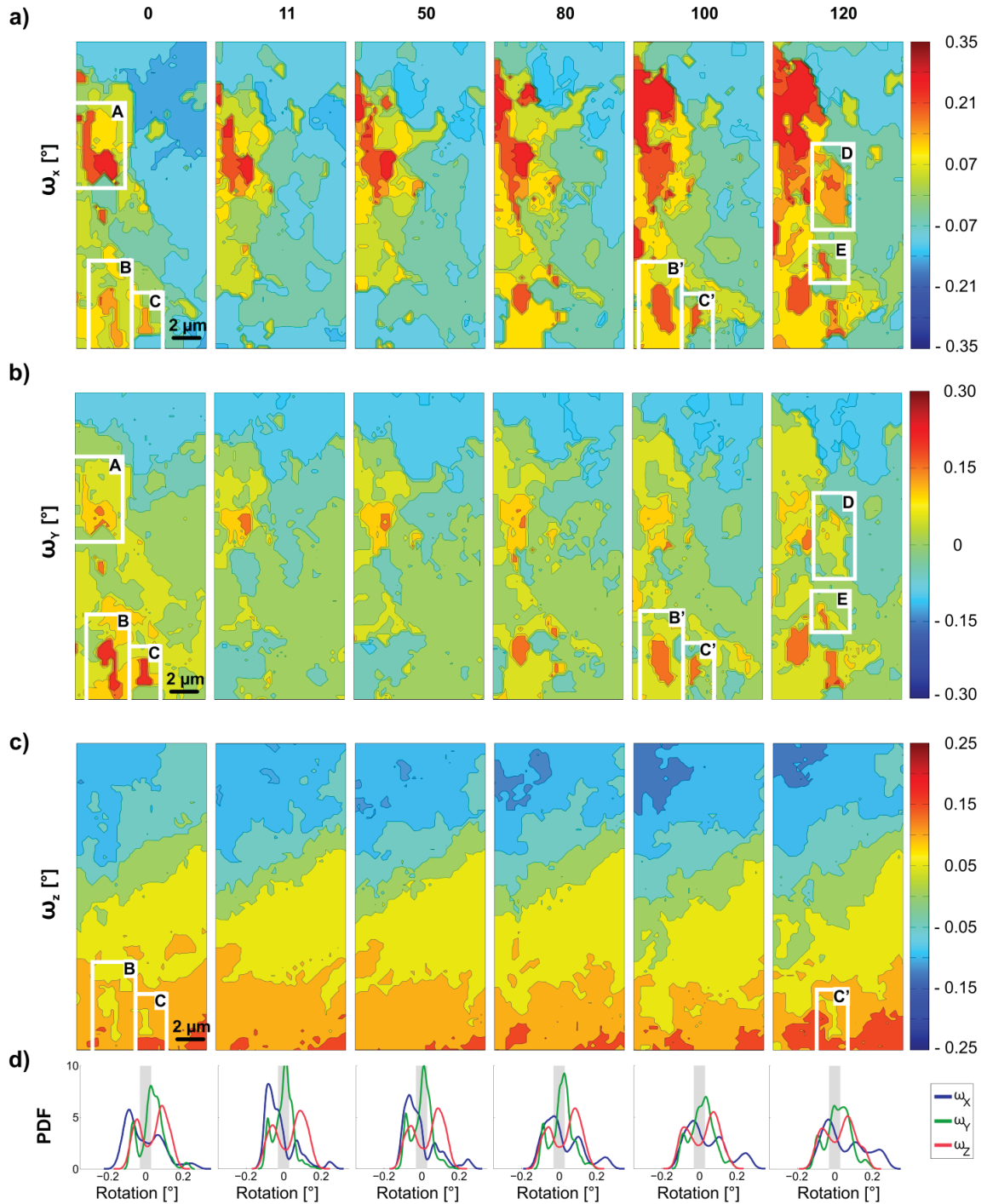
Figure 3.20 Evolution of rotations on the X-, Y-, and Z- axes (ω_x, ω_y and ω_z) of sample S1-R

The evolution of the ω_y maps is rather similar to that described for ω_x but with lower values. Looking in detail there are some differences. Region **A** does not expand and merges with the area located above. In fact, region **A** reduces its size and its ω_y value upon cycling. The evolved regions **B'**, **C'** and **E** are the domains with the largest ω_y rotation at cycle 120 ($\omega_y \sim 0.20°$).

The evolution of the ω_z maps, on the contrary, has no correlation with the evolution observed in the misorientation map. The gradual transition from $-\omega_z$ to $+\omega_z$ when examining the scanned area from top to bottom remains during the 120 cycles. None of the regions are visible except region **B** and **C** at the beginning and region **C'** at the end. Their rotation value are rather low ($\omega_z \sim 0.05°$).

3.4.3 Lattice curvatures and dislocation density tensor components

Lattice curvature components of sample S1-R are plotted in Figure 3.21. Scale bars have been limited to |10 mrad/µm| for κ_{xx}, κ_{xy}, κ_{yx} and κ_{yy} components and to |3 mrad/µm| for κ_{zx} and κ_{zy} for visibility reasons.

One of the most noticeable facts is the strong boundary that exists in the upper part of the spatially resolved maps. Initially vertical and latter inclined, it appears in the four κ_{xx}, κ_{xy}, κ_{yx} and κ_{yy} components (pointed with an arrow at cycle 120). This boundary is also present in the ω_x and ω_y maps (see Figure 3.20-a-b) and defines the misorientation boundary between the left and right side in the spatially resolved maps.

Surprisingly κ_{xx} and κ_{xy} and also κ_{yx} and κ_{yy} are almost identical. Moreover, not only do they have similar values but also the sign of the curvature matches. This was not the case in the S1-L sample where they had opposite sign, and different features could be detected in each map (see Figure 3.5).

Regions **A, B** and **C** can be distinguished in the four κ_{xx}, κ_{xy}, κ_{yx} and κ_{yy} maps. The expansion of region **A** and the evolution of **B** and **C** are easy to follow. In fact, the initial traces of the latter two regions are not swept away during the low amplitude cycles. There are remaining traces of region **B** and **C** at steps 11 and 50.

The origin of region **D** and **E** can also be ascribed to pre-existing structures that cause distortion on the crystal. They are pointed as **D'** and **E** in map 50 but their presence can be tracked back to map 0.

Moreover there are clear loops in the upper part of the maps that are present during the whole process and that hardly change their position or size (inside black circle). Those domains are insensitive to cycling.

The evolution of κ_{zx} and κ_{zy} maps is slightly different. Initially, the traces of lattice distortion are agglomerated above region **A** and in the neighborhoods of regions **B** and **C**. These last two regions can be differentiated but not as clearly as in the κ_{xx}, κ_{xy}, κ_{yx} and κ_{yy} maps. After the first 50 cycles, the initial traces become faint, and it is only after cycling wiht intermediate/high strain amplitude that the rotated regions are clearly visible in the maps (regions **B'** and **C'** at map 120). Regions **D** and **E** do not have κ_{zx} and κ_{zy} lattice curvatures. Contrary to S1-L sample, there is no evidence of formation of new regions having κ_{zx} and κ_{zy} components after 120 cycles, which did not show these traces from the beginning.

The α_{zz} and $\alpha_{xx} - \alpha_{yy}$ maps, shown in Figure 3.22, mark the boundaries of the described regions **A**, **B**, **C**, **D** and **E**. At step 120, the left side of the map is filled by interconnected regions with dislocation density traces mainly in their perimeter, whereas the right side is almost clean. The boundaries of the regions in the α_{zz} map have alternating signs along their perimeter. The $\alpha_{xx} - \alpha_{yy}$ show less traces than the α_{zz} map.
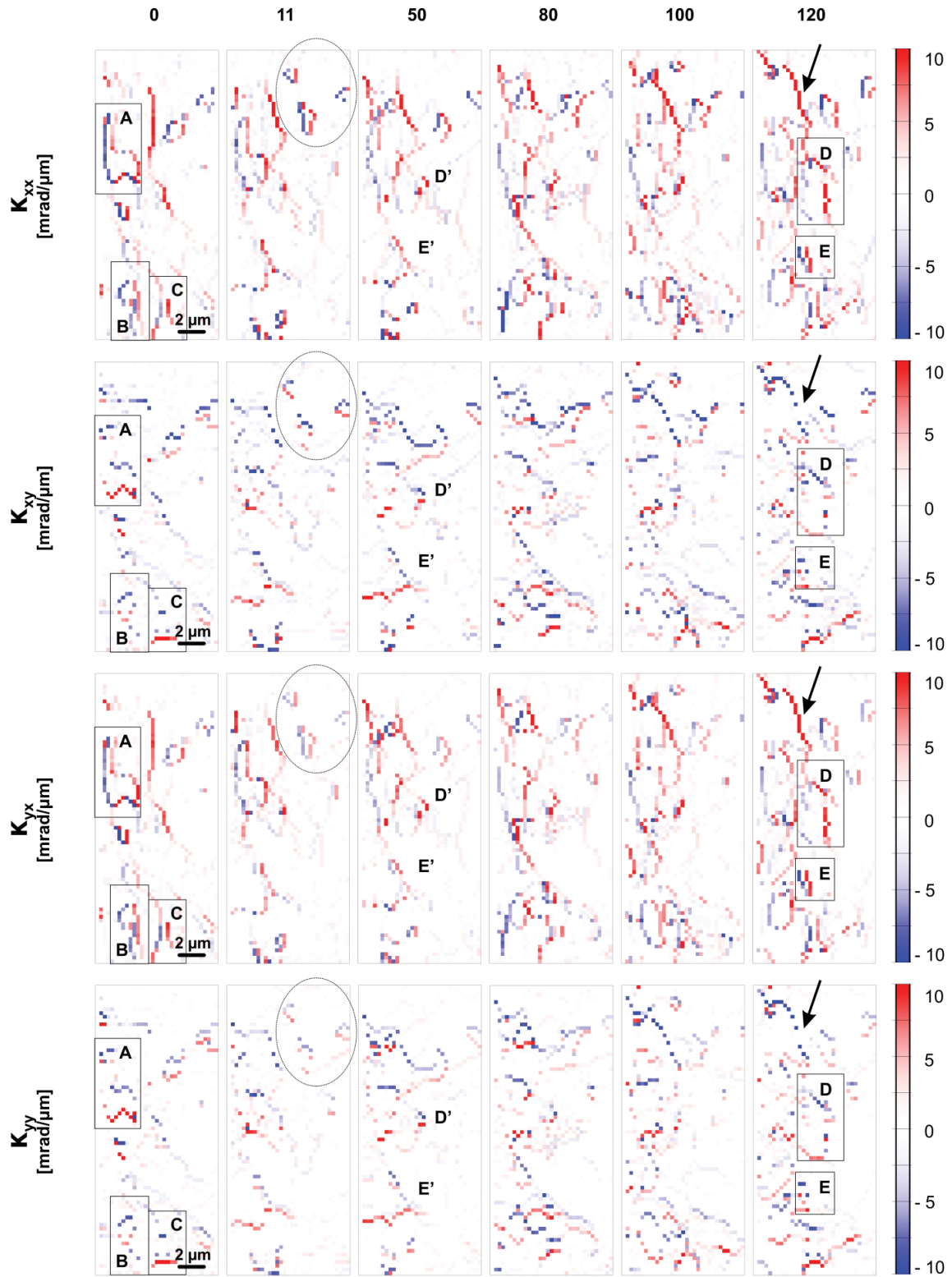
Figure continues on the next page
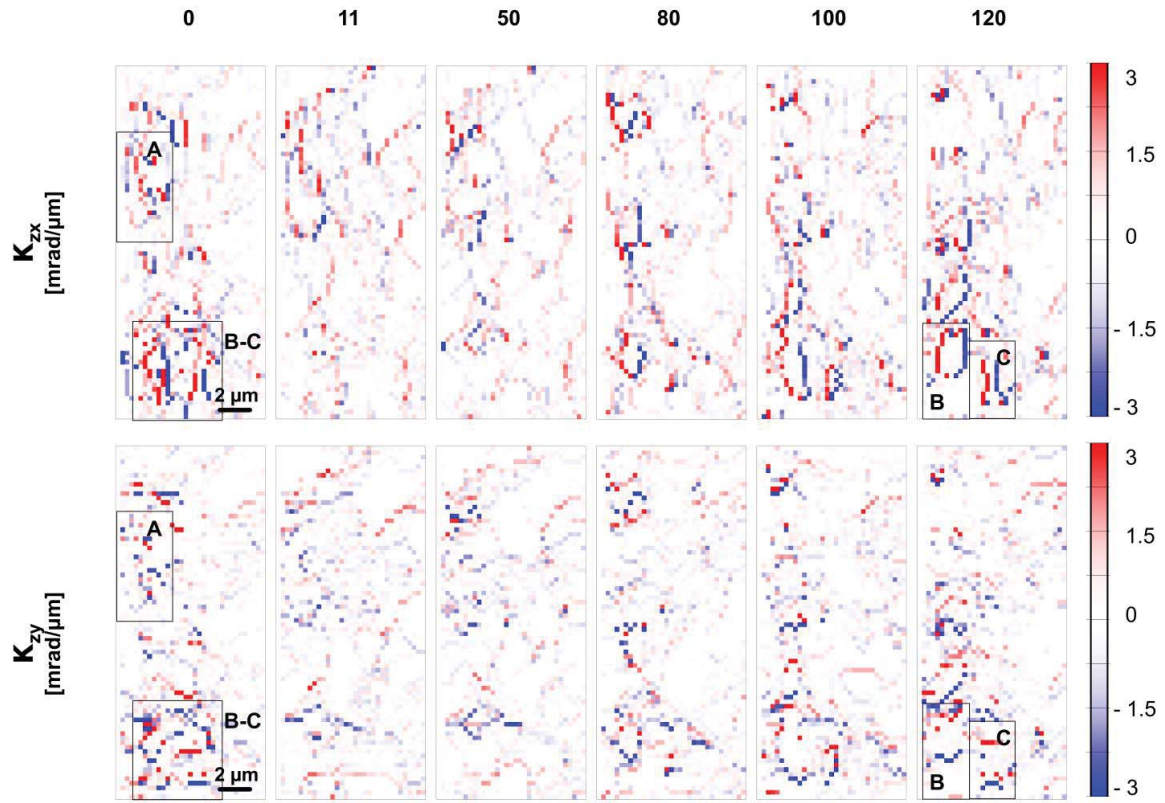
Figure 3.21 Evolution of lattice curvatures and some Nye tensor components of sample S1-L
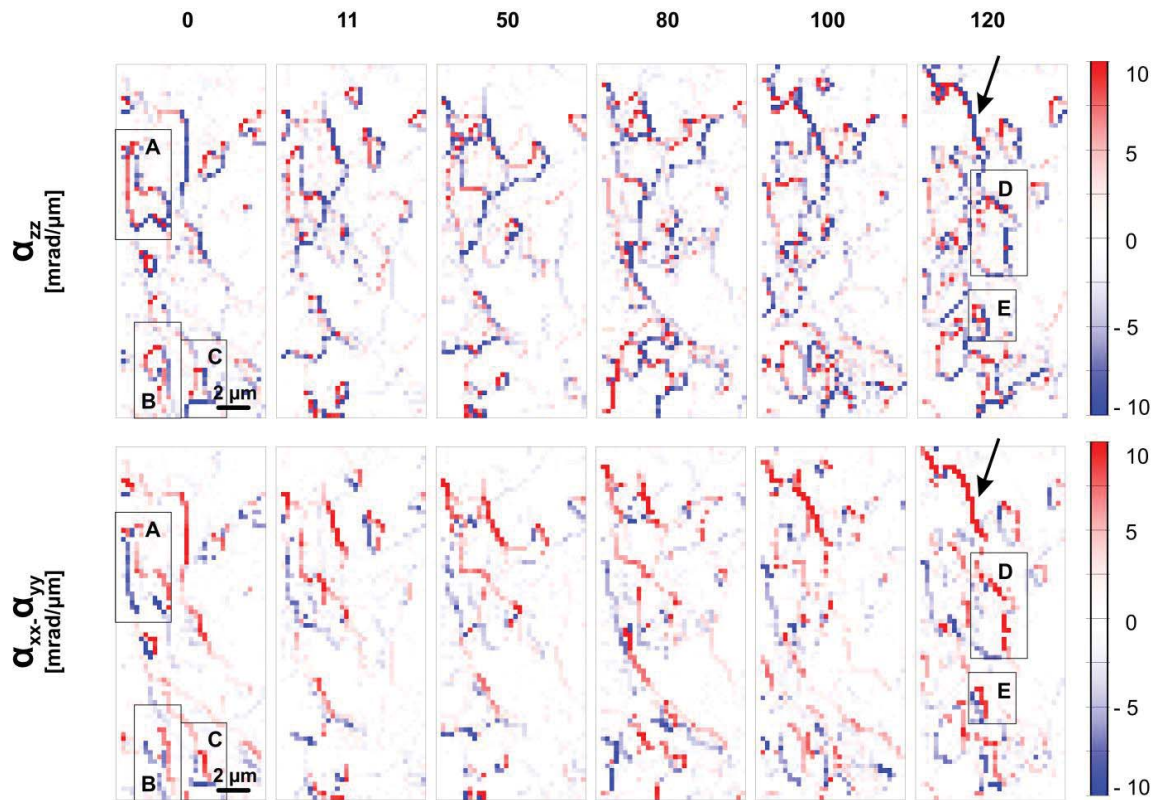
Figure 3.22 Evolution of α_{zz} and $\alpha_{xx} - \alpha_{yy}$ components of sample S1-R

The statistical distribution of each lattice curvature and dislocation density tensor components map at cycle 0 and cycle 120 are graphically depicted as boxplots in Figure 3.23 (see Appendix D for detailed information about statistical representation as boxplots) The median of all distributions is ~0 mrad/µm and it does not change after 120 cycles. Before deformation, κ_{zx} and κ_{zy} lattice curvature components are below |10 mrad/µm|, κ_{xx}, κ_{xy}, κ_{yx}, κ_{yy} and $\alpha_x - \alpha_{yy}$ below |20 mrad/µm| and α_{zz} have some outliers larger than |20 mrad/µm|. These values are larger than those of the S1-L sample (see Figure 3.8).

At cycle 120 the boxplots show that κ_{xx}, κ_{xy}, κ_{yx}, κ_{yy} and $\alpha_x - \alpha_{yy}$ increase their extreme values but never exceed |20 mrad/µm|. On the other hand, the limits of κ_{zx} and κ_{zy} shrink slightly. α_{zz} reaches values almost as high as |30 mrad/µm|.
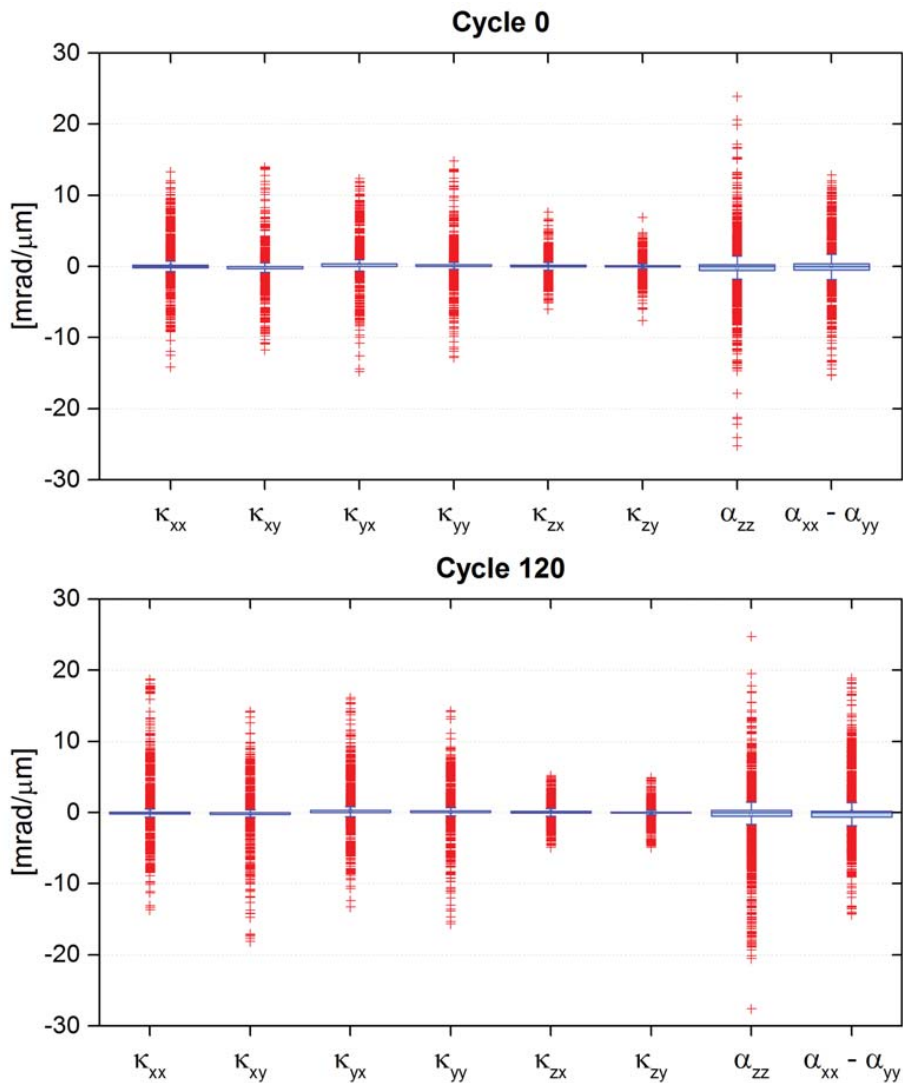
Figure 3.23 Statistical distribution of the lattice curvature and Nye tensor components of sample S1-R

3.4.4   Evolution of apparent GND density

Figure 3.24 shows the evolution of the apparent GND density in sample S1-R. The initial microstructure contains four well-defined high-density closed circuits that define the rotated regions **A**, **B** and **C**, and a small highly rotated island below region **A** (pointed by an arrow).

There are additional features that are invisible in the misorientation map (Figure 3.19), but could be detected in the $\omega_x, \omega_y, \omega_z$ rotation maps (Figure 3.20) or lattice curvature maps (Figure 3.21). For instance, the straight line that separates the map in left and right with different ω_x rotation; or the small domains with closed GND boundaries and low misorientation value that remain permanent during cycling. These features are indicated in map 11 by white arrows.

Additionally, there are a few non-zero initial GND traces in the surrounding of regions **A**, **B** and **C**. Their density is on the order of ~20-30 μm^{-2}, which is higher than for the initial traces observed in sample S1-L (see Figure 3.9.).

During the first 50 cycles, the apparent GND density decreases and the positions of the traces change in order to accommodate the initial heterogeneity. Most of the traces of the lower part of the initial map are swept away but a few clusters remain. In the upper part of region **A**, named **A'**, new density traces appear as a consequence of the reorganization described in the misorientation section. The density is on the order of 50 μm^{-2}.

After 80 cycles, the faint discontinuous traces disappear and the remaining GND footprints mark the perimeters of the rotated regions observable in the misorientation map (**A**, **B'**, **C'** and **E'**), as well as sharp misorientation change boundaries. Region **A'** has evolved into a closed region with dislocation densities higher than 120 μm^{-2}.

During the last 40 cycles, there are few substantial changes. Regions **B'**, **C'** and **E** are formed from the previous arrangements and have a defined closed circuit of GNDs in their perimeter. Region **D** is defined by a non-closed loop. In the area of region of **A'** the close circuit opens and after 120 there is a high density inclined wall (~100 μm^{-2}).
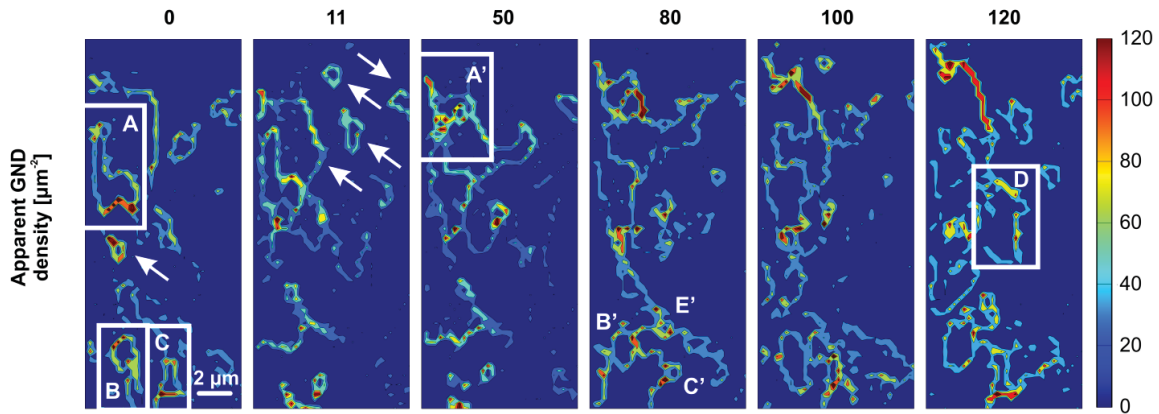
Figure 3.24 Evolution of apparent GND density of sample S1-R

3.4.5 Analysis of Laue reflections and orientation spread

The misorientation maps show that S1-R sample is more heterogeneous than S1-L (compare Figure 3.19 to Figure 3.3). The left side of the spatially resolved maps of S1-R has higher initial misorientation values than the right side. The misoriented areas increase in size and in misorientation magnitude during cyclic deformation. In addition, the ω_z maps show that the orientations change uniformly along the vertical direction. To gain further insight the shape of Laue reflections are analyzed.

The angles between the Burgers vector and the normal of the planes related to the observed Laue reflections are given in section 3.3.5.

Heterogeneous microstructure

Figure 3.25 shows the evolutions of two positions: **A'** which is located on top of region **A** and **R** that is located in the right side of the map. As can be observed in Figure 3.25–a position **A'** has initially a low misorientation but after 120 cycles its value has increased to 0.28°. Position **R** corresponds to a relatively low misoriented region

and its value does not change as much as in position **A'**. The shape of the Laue peaks of positions **R** and **A'** are in Figure 3.25-b and Figure 3.25-c respectively.

The Laue peaks of position **R** show that the initial microstructure is not free of defects. While (400) and ($\overline{2}\overline{2}0$) reflections are rather round, (004) and (0$\overline{2}\overline{2}$) peaks are streaked. Several sub-regions are detectable. During cycling the peaks mostly keep their shape and position. Only at step 120 a slight shift of the position of the maximum intensity of reflection (004) is detected (point by arrows).

The initial microstructure at position **A'** is more heterogeneous according to the Laue shapes:

- The (400) peak has similar shape as the (400) peak in **R** but is shifted in position.
- The ($\overline{2}\overline{2}0$) peak is split into two sub-peaks: one streaked and another rounded but with lower intensity. The maximum intensity is not in the same position as in **R**.
- Several high-intensity sub-peaks are observed in the streaked (004) peak similar to (004) reflection at position **R**. At position **A'** the tails are more elongated and even a sub-region with low intensity is observable.
- The (0$\overline{2}\overline{2}$) reflection is also streaked and two clearly separated sub-peaks are visible, where both exhibit a high intensity. Initially, the maximum intensity lies in the right sub-peak as pointed by the arrow.

This description evidences the initial difference in crystallographic orientation between positions **A'** and **R** as most of the peaks are shifted in position. Moreover the presence of two crystallites along the depth of the sample in position **A** is evidenced from the split (0$\overline{2}\overline{2}$) peak. In order to investigate whether the splitting corresponds to a low angle boundary the streaking directions are plotted on top of the Laue shapes corresponding to position **A'** at step 0 (see Figure 3.26). The labelling corresponds to that given in Table 3.1 and the possible streaking directions on each peak are labeled in red. By analysing the three streaked peaks, it was concluded that the boundary cannot be described by a set of GNDs of one particular type.

The evolution of the peaks at position **A** shows that the position of maximum intensity shifts in peak (0$\overline{2}\overline{2}$) from one sub-peak to the other sub-peak (pointed by the arrows). The transition happens gradually: at step 50 both sub-peaks have similar intensity but the automatic indexation routine still picks the initial sub-peak for determining the orientation in that position. Closer look to peak (400) also show a shift in the azimuthal direction but with much smaller magnitude (pointed by arrows).

Analysis of the (0$\overline{2}\overline{2}$) peak in other regions of the spatially resolved maps, e.g. regions **A**, **B**, **C**, shows also the presence of the described initial splitting. The peaks of the right side of the map, where no regions are evolving, do not show that splitting.

a) Misorientation [°]
and physical location of points
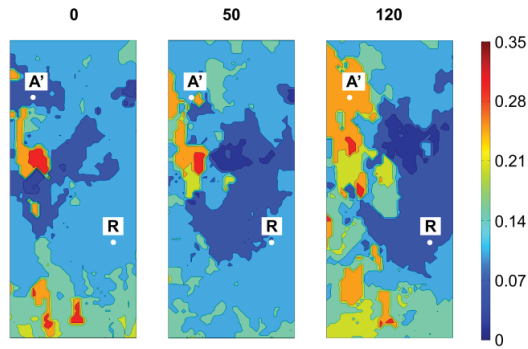
b) Most intense diffraction peaks at point R
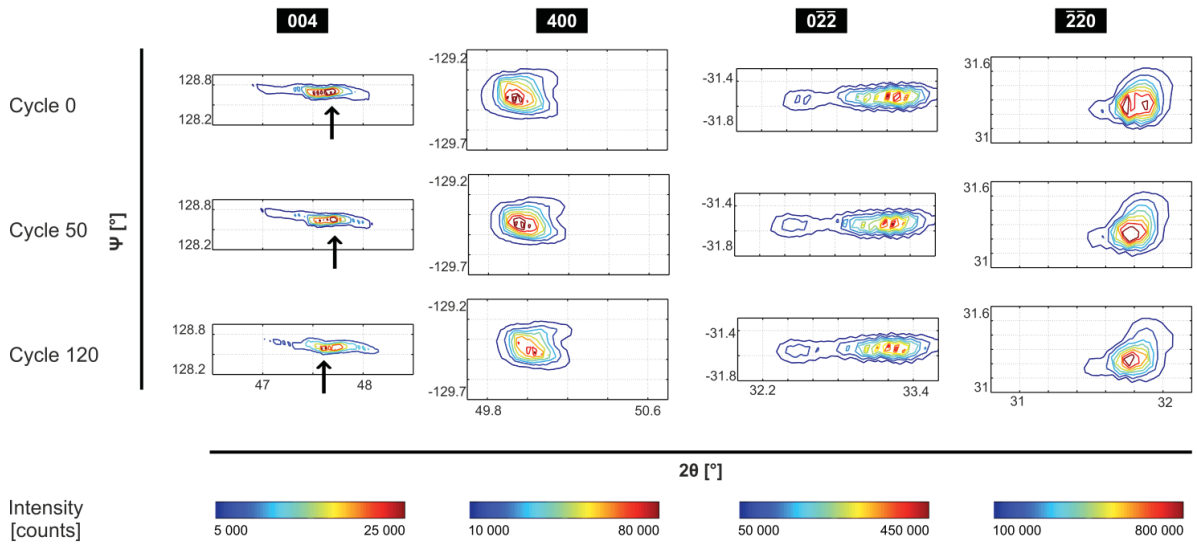
c) Most intense diffraction peaks at point A'
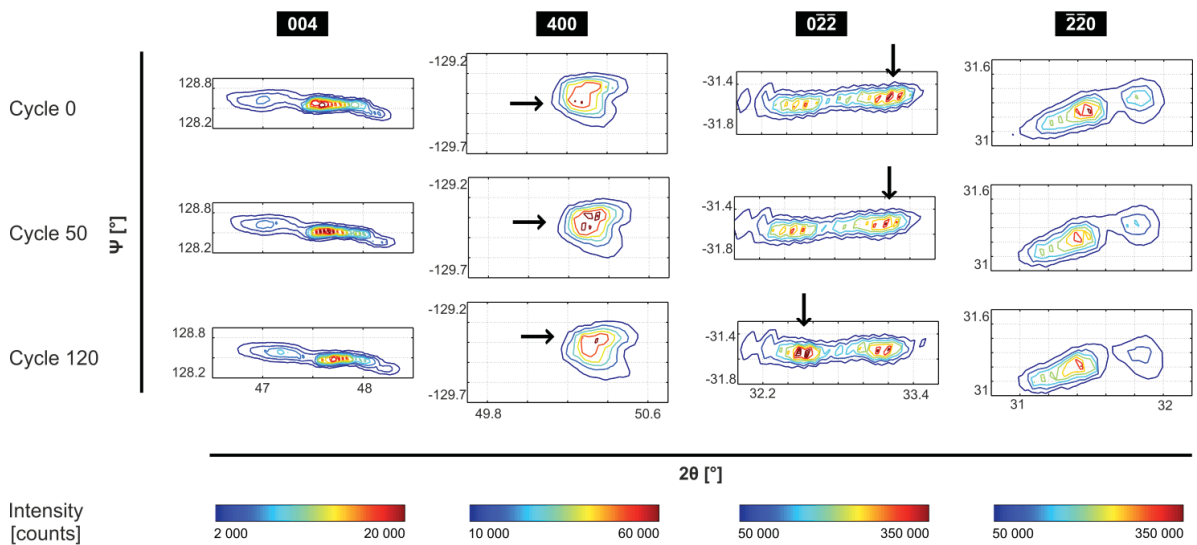
Figure 3.25 Evolution of misorientation and shape of four diffraction peak in position **A'** and position **R** of sample S1-R
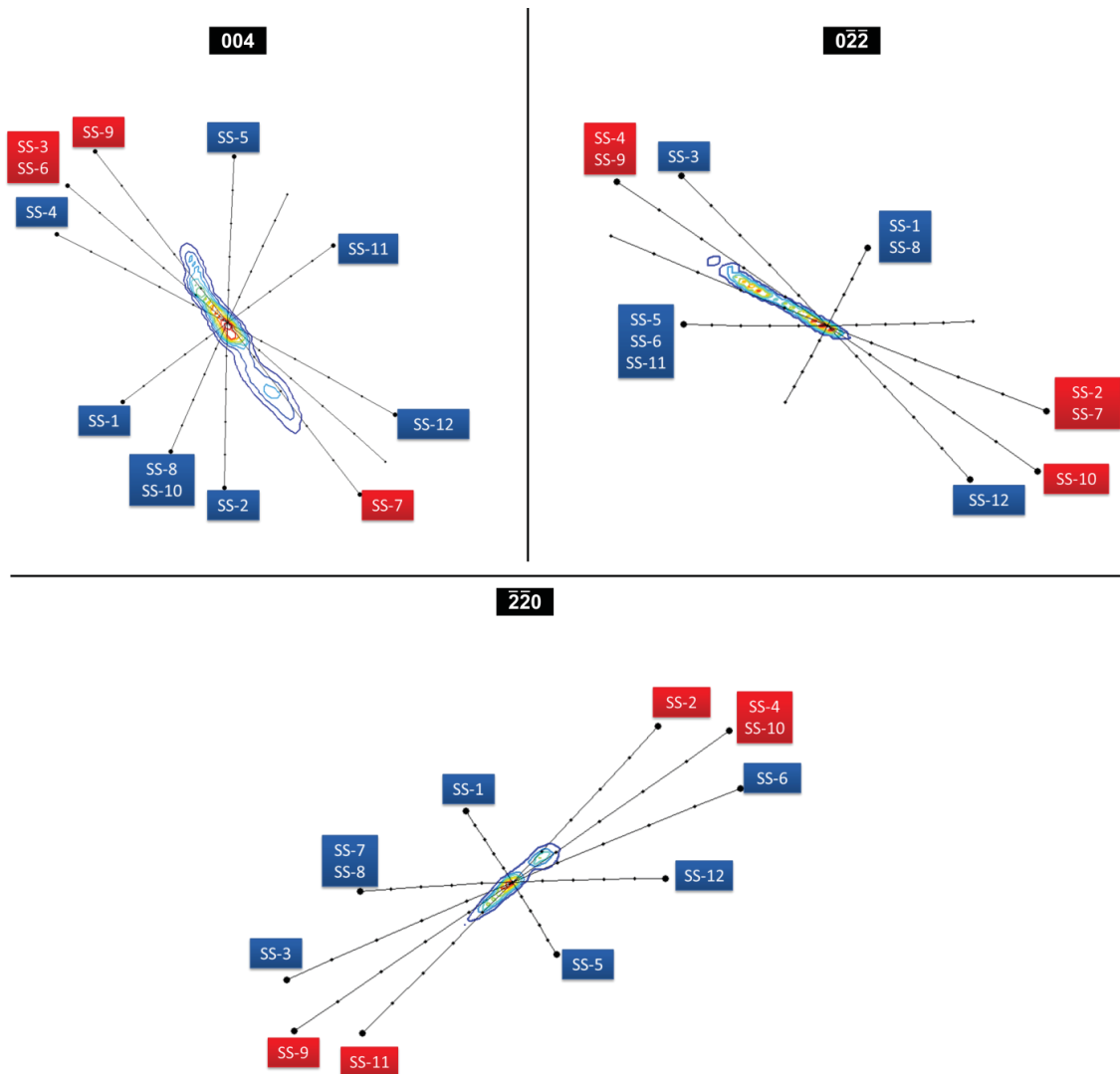
Figure 3.26 Streaking directions on top of the Laue reflections of position **A'** at step 0.

The orientation spread at both positions **R** and **A'** has been calculated at cycles 0, 50 and 120 and is shown in Figure 3.27. The color of each point corresponds to the normalized intensity of the $(0\bar{2}\bar{2})$ reflection shown in Figure 3.25. Before deformation both positions show high intensity points around the average orientation. The broadening is slightly larger in position **A'** than in position **R**. In the former position, there are additionally other points that have a high intensity around θ_y =-0.50°, where the spread is narrower. During 120 cycles, the cloud of position **R** does not exhibit major changes: the position and the amount of high intensity points remain roughly similar and there is no formation of sub-regions. In position **A'**, on the other hand, the position of the points with maximum intensity gradually shifts to the sub-region. After 120 cycles, there are almost no high intensity points in the initial region. The shapes of the clouds of positions **R** and **A'** are also different, which evidences the difference in microstructure at both positions.
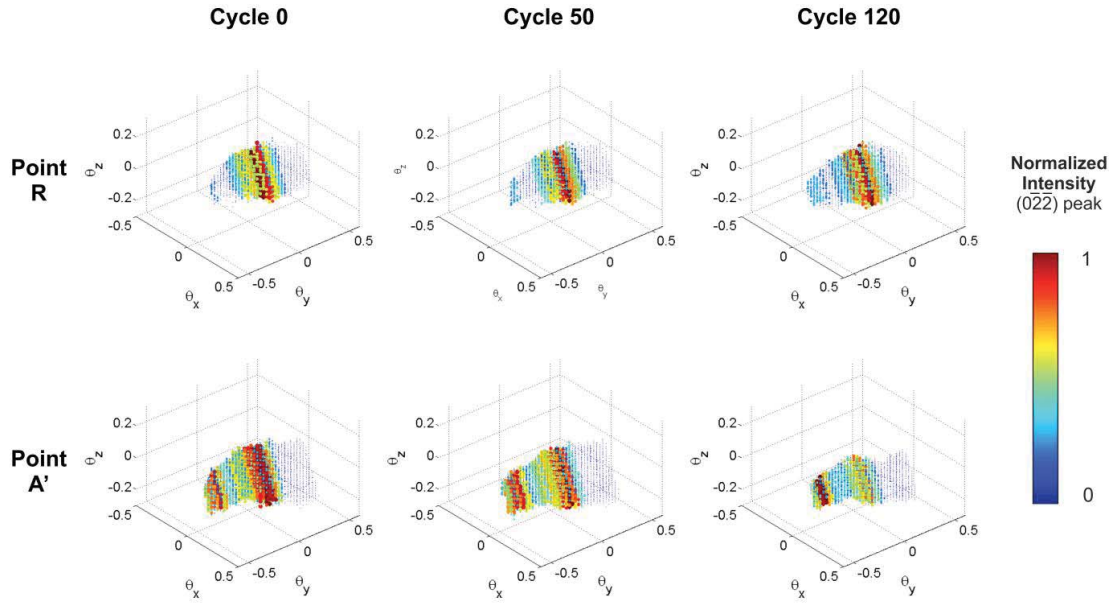
Figure 3.27 Orientation spread in positions **R** and **A'** at step 0, 50 and 120

Gradient in the rotation about Z-axis

The vertical gradient in the rotation about *Z*-axis (ω_z map - Figure 3.20-c) has been inspected by looking the shape of the Laue peaks for different positions along the vertical direction. As an illustration the $(0\bar{2}\bar{2})$ reflection for different points located in the right side of the map, where the microstructure is less distorted, is shown in Figure 3.28. All these peaks show several sub-peaks. The position of the maximum intensity gradually shifts from one sub-peak to another sub-peak when moving from position **P1** to **P4**. The same behavior is also observed for the other peaks. There is however no collective movement of the peaks, which would have suggested that the microstructure is bent along the Z axis. Instead, it suggests that different crystallites along the thickness contribute to the high intensity of the peaks. A similar behavior is also observed when inspecting the Laue reflections for points located at the left side of the map.
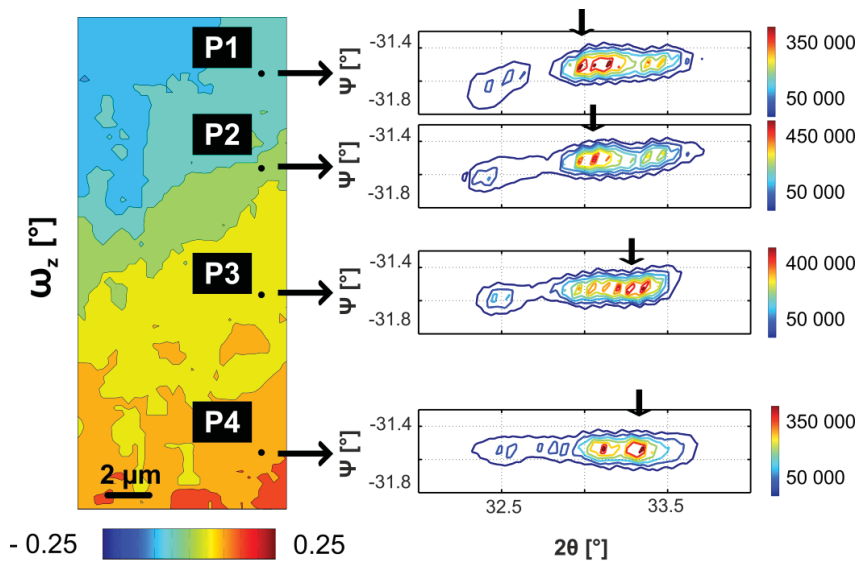
Figure 3.28 $(0\bar{2}\bar{2})$ diffraction peak at different points of the spatial map at cycle 0 in sample S1-R

3.4.6   Indexation error

The distribution of the indexation error is shown in Figure 3.29 where 8 peaks were taken into account to refine the crystal orientation. The averaged error is 5.46±0.99 pixels, which is slightly lower than in sample S1-L but still relatively high (see Figure 3.18). None of the abovementioned regions can be detected in the error maps but it is evident that the error values are higher in the lower part of the maps and during the first 80 cycles in the middle of the map.
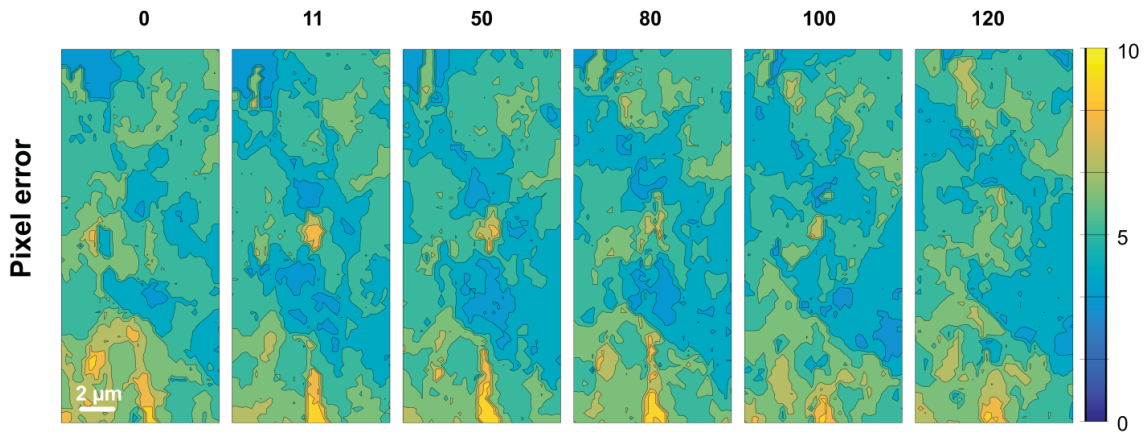
Figure 3.29 Indexation error distribution for each map in sample S1-R

3.5   Summary

The major observations derived from the results of single slip oriented fatigued samples can be summarized as follows:

- When the initial dislocation structure is not too heterogeneous, one can observe that the microstructure homogenizes during the first cycles. From there, new misoriented regions are formed that are surrounded by a GND wall and do not have apparent GNDs inside.
- In regions where few non-mobile dislocations are present, the homogenization process is less effective and the presence of dislocations influences the location of areas where larger misorientations are formed.
- At positions with high initial non-mobile dislocation densities, the applied cycles are not sufficient to move the defects and the misoriented regions expected for single slip fatigue are not observed.
- During sample preparation the crystal was damaged so crystallites with different orientation across the sample thickness could be observed. Both sides of the shear zones do not necessarily have same initial microstructure even if they belong to the same sample and have been prepared at the same time and with same procedure.
- The orientation spread analysis provides additional information in the third direction that is lost when plotting 2D maps.

Chapter 4   Double slip results

In this chapter the results of the in-situ fully reversed cyclic shear experiments for copper single crystals oriented for double slip are introduced. The mechanical data, microstructural evolution in terms of misorientation angle, rotations about *X-Y-Z-* axes, lattice curvatures and GNDs, and analysis of the Laue reflections are presented for two orientations: coplanar and collinear. Only one case for each orientation is presented, named S2-Cp and S2-Cl respectively.

The aim of these experiments is to observe whether the observed microstructural evolution is different comparing to single slip and also to analyze the differences between both double slip orientations.

4.1   Coplanar double slip

Samples oriented for coplanar slip have easy glide on the $(111)[\bar{1}01]$ and $(111)[0\bar{1}1]$ systems when loaded in shear. Both of them share the same glide plane but have different slip direction. A list with the Schmid factors for all slip systems is shown in Table 4.1. The $(1\bar{1}1)[\bar{1}01]$ and $(\bar{1}11)[01\bar{1}]$ systems have a three times smaller Schmid factor compared to the primary slip systems. Both share one of the slip directions of the principal systems but glide on different plane. The $(\bar{1}11)[110]$ system, which has a different slip plane and slip direction compared to the primary systems, has a Schmid factor that is a fifth of the value of the primary slip system. All other slip systems have a much lower Schmid factor. Figure 4.1 shows the schematics of the primary slip systems in a cuboid and the crystal orientation in the laboratory frame. The magenta line corresponds to a dislocation line with $b=[\bar{1}01]$ in (111) plane and the yellow line to a dislocation line with $b=[0\bar{1}1]$ in the same plane.

Table 4.1 Schmid factors for coplanar orientation

Slip system	Plane			Direction			Schmid Factor
1	1	1	1	$\bar{1}$	0	1	0.866
2	1	1	1	0	$\bar{1}$	1	0.866
3	1	$\bar{1}$	1	$\bar{1}$	0	1	0.289
4	$\bar{1}$	1	1	0	$\bar{1}$	1	0.289
5	$\bar{1}$	1	1	1	1	0	0.192
6	$\bar{1}$	$\bar{1}$	1	0	1	1	0.096
7	$\bar{1}$	$\bar{1}$	1	1	0	1	0.096
8	$\bar{1}$	1	1	1	0	1	0.096
9	1	$\bar{1}$	1	0	1	1	0.096
10	1	$\bar{1}$	1	1	1	0	0.096
11	1	1	1	1	$\bar{1}$	0	0
12	$\bar{1}$	$\bar{1}$	1	1	$\bar{1}$	0	0
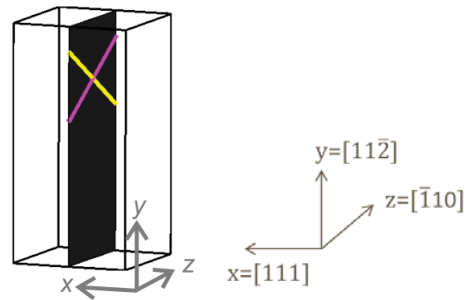
Figure 4.1 Crystal orientation and primary slip systems (plane and dislocation lines) for coplanar orientation. Y-axis corresponds to shear-load axis and Z-axis to beam axis.

4.1.1   Mechanical data

The sample oriented for coplanar double slip has been subjected to a total of 95 cycles, subdivided into five series, where the resolved plastic strain amplitude was gradually increased from 0.062% to 0.229%. The force response as a function of resolved shear strain for the last cycle of each series is shown in Figure 4.2. The

number of cycles, force at maximum positive displacement and the resolved total and plastic shear strain amplitudes are listed in Table 4.2. Between cycle 1 and cycle 65 the hysteresis gradually increases. For the last series (cycles 66-95) a larger increase is observed.

Comparing to the mechanical response of single slip oriented crystal (see Figure 3.2) the force at a given resolved strain amplitude is higher for coplanar slip. This suggests that the coplanar sample is harder. In fact, during the last series the force limit of the setup has been reached. However the maximum resolved plastic strain amplitude is still 22% lower than the one reached in the single slip sample.
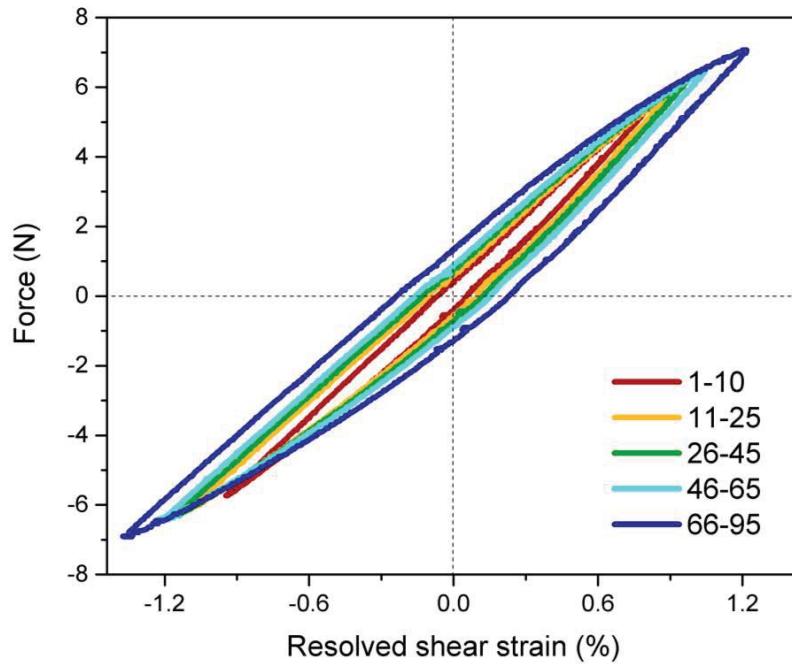
Figure 4.2 Mechanical response of coplanar double slip oriented sample

Table 4.2 Number of cycles, maximum force and resolved total and plastic shear strain amplitudes for coplanar orientation

Total cycles	Maximum force (N)	Resolved total shear strain (%)	Resolved plastic shear strain (%)
1-10	5.47	0.79	0.062
11-25	5.78	0.86	0.094
26-45	6.15	0.93	0.121
46-65	6.48	1.01	0.152
66-95	7.09	1.17	0.229

4.1.2   Evolution of misorientation angle

The evolution of the misorientation angle of S2-Cp sample as a function of cycles is shown in Figure 4.3-a. The initial microstructure consists of several misoriented areas. The dimensions of the misoriented areas are clearly larger compared to the single slip sample. On the other hand the magnitudes of the misorientation are much lower; maximum 0.15° for S2-Cp as compared to 0.25° for S1-L (Figure 3.3) and 0.35° for S1-R (Figure 3.19).

At step 0 the spatially resolved misorientation map can be divided in several regions: regions **A** and **B** exhibit low misorientations (~0.03° - 0.05°), region **C** has the highest misorientation (~ 0.14°-0.15°), and regions **D** and **E** have an intermediate misorientation of ~ 0.10° - 0.11° and occupy the largest areas. The areas between the mentioned regions exhibit misorientations between 0.05° and 0.10°. They gradually accommodate the transition between the misoriented areas, except between regions **A** and **C** which are neighbouring regions. The PDF function is shown in Figure 4.3-b and presents a continuous distribution of misorientations with the mode around 0.10° and two sub-peaks at 0.07° and 0.12°. The description of the PDF distribution is given in Appendix D.
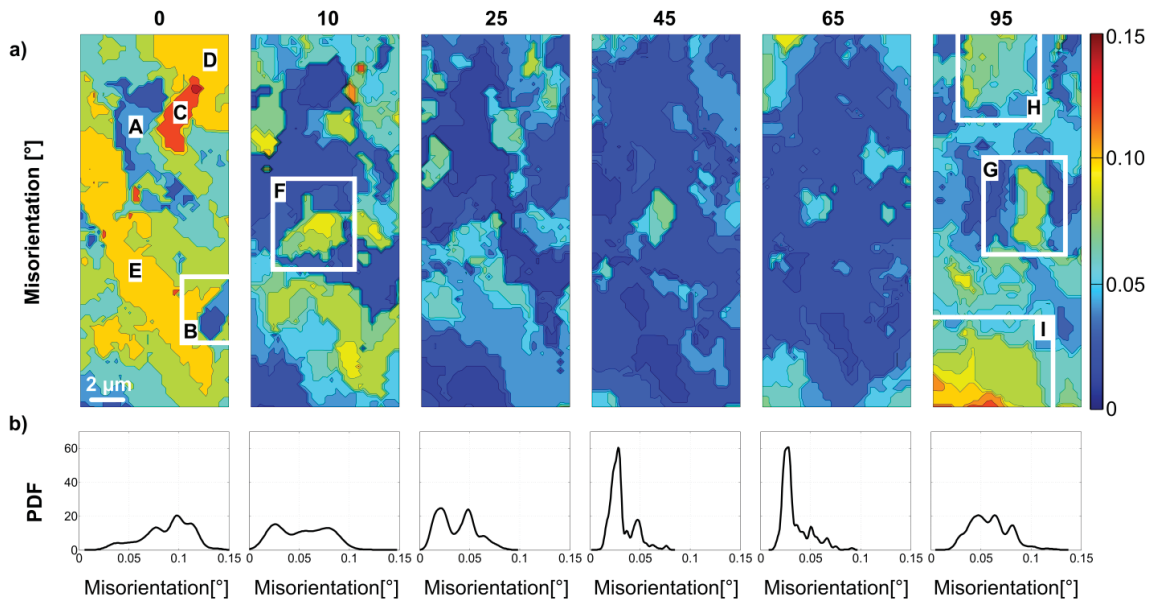
Figure 4.3 Evolution of misorientation angle of sample S2-Cp. a) Spatial resolved maps; b) PDF functions

During the first 10 cycles, the misorientation distribution changes considerably and similar to S1-L sample (Figure 3.3) a homogenization process starts. Regions **C**, **D** and **E** fragment and lower their misorientation. More specifically, region **C** splits in three pieces with misorientation values of 0.09°, 0.11° and 0.13° and region **D** has an average misorientation of 0.07°. The homogenization of region **E** is slower, presumable due to its large size. The upper part of region **E** vanishes and joins the low misoriented region **A**. The lower part of **E**, on the other hand, still is misoriented with a large area rotated by ~0.08°. In the middle of the misorientation map a non-homogenized region still remains, labeled **F**, and it has a maximum misorientation of 0.08°. Large area of the map has a misorientation of about 0.03° as suggested by the PDF. The distribution extends till 0.10°.

During further cycling at higher strain amplitudes the homogenization process continues. The maps after cycles 45 and 65 exhibit mostly very low misorientations (~0.03°), with some residual traces in the four corners and the footprint of region **F** in the middle of the maps. The PDFs show a main peak at 0.03° with few sub-peaks at higher angles. The highest misorientation values are in the range of 0.08° - 0.10°.

In the last 30 cycles at the highest strain amplitude, the misorientation map changes considerably. The PDF also reveals this change. New misoriented regions emerge out of the low misorientation areas, e.g. regions **G** and **H**. However, these regions do not have defined boundaries and their misorientation value is not constant in the

whole region. In the lower left side of the map there is an area (region **I**) that has increased its misorientation value to ~ 0.12° at cycle 95 and expanded its size. The PDF shows that there are three small sub-peaks in the interval from 0.04° to 0.08°.

4.1.3 Evolution of rotations about X-Y-Z- axes

Figure 4.4-a-c presents the evolution of the amount of rotation around the *X-, Y-*, and *Z-* axes (ω_x, ω_y and ω_z). The scale bar for these rotations is |0.10°|. For each cycle, PDFs of ω_x, ω_y and ω_z are plotted in Figure 4.4-d. On these plots a grey band with a width of |0.03°| is shown. As the rotation angles within this band are very low, the exact values should be taken with care since the rotation axes are not well defined. The description of the PDF distribution is given in Appendix D.

The initial distribution of ω_x, ω_y and ω_z shows the abovementioned initial heterogeneities. The ω_x map shows that most of the scanned area has low positive rotation about the *X*-axis (~0.03°). This area includes regions **A**, **B**, **C** and **E**. Region **D**, on the other hand, has the highest ω_x rotation (~0.06°). There is another small loop in the bottom-right corner, pointed with an arrow, which also has similar misorientation values. The bottom-left part of the map has negative small ω_x rotation (~-0.02°).

The initial ω_y map shows that all the areas with intermediate and high misorientation misorientation values exhibit a positive rotation around the *Y*-axis (e.g. regions **C** and **D** are rotated 0.06° and 0.05° respectively, region **E** mostly 0.07° with a hot spot in the lower part of 0.085°) .The intermediate misoriented surroundings of these regions have also positive rotation. The low misoriented regions **A** and **B** have almost no rotation around the *Y*-axis. The ω_y maps are the rotation maps having the strongest correlation with the initial misorientation map (see Figure 4.3).

The ω_z map, on the other hand, shows that nearly the complete scanned area has negative rotation around the *Z*-axis: region **C** has ω_z~ - 0.11°, region **D** ω_z~ - 0.07° and region **E** ω_z~ - 0.09°. Similar to ω_y map, the low misoriented regions **A** and **B** have almost no rotation around the *Z*-axis. The small loop of the bottom-right corner mentioned in the ω_x map has ω_z~ 0.02°.

During cycling, the scanned area homogenizes and the rotation magnitudes decrease. After the first 10 cycles, the scanned area exhibits almost no rotation anymore around the *X*-axis. Only the lower part of the fragmented region **E** has ω_x~ - 0.04°. All the areas that are misoriented have a rotation around the *Y*-axis. The values range from ω_y~ 0.02° to 0.10°. The ω_z map shows that the area still exhibits a negative rotation around *Z*-axis but the magnitudes are lower compared to cycle 0. The small loop at the bottom-right corner has disappeared.

At cycle 45, most of the map does not show any rotation around the *X*-axis. Only region **F** has negative rotation ω_x~ - 0.07°. The ω_y map is fragmented but the rotation magnitudes are low. In fact, most of the area has ω_y <|0.03°|. In the ω_z map most of the area exhibits basically no rotation around the *Z*-axis. Similar to ω_y map, the values are ω_z <|0.03°|. The upper and lower left corners have the highest ω_z rotations, 0.07° and 0.05° respectively. The microstructure after 65 cycles is rather similar compared to cycle 45, except for a few differences. For instance, region **F** has shrunk and the corners with high ω_z have increased their size.

In the last 30 cycles, the changes observed in the misorientation map are also present in the rotation maps. The initial high correlation of ω_y map with the misorientation map disappears since the rotation values of ω_y are below |0.03°|. Interestingly and contrary to the initial configuration, the scanned area exhibits negative rotations around the *X*-axis and positive around *Z*-axis. Region **G** has ω_x~ - 0.07° and ω_z~ 0.05°. Regions **H** and **I** have ω_x~ - 0.05° and ω_z ranges from 0.05° to 0.11° depending on the position in the region.

It is interesting to follow the evolution of ω_x, ω_y and ω_z values in the PDFs. At step 0 ω_x and ω_y are shifted to positive values whereas ω_z to negative. The latter has higher values than the former two. During the first 25 cycles, the distributions shift to the neutral grey band. Still part of the map has negative ω_z and positive ω_y. At

cycles 45 and 65 most of the distribution is concentrated inside the grey band. At step 65 the distribution tail of ω_z extends to positive values. After a total of 95 cycles, the scanned area has negative ω_x and positive ω_z values.
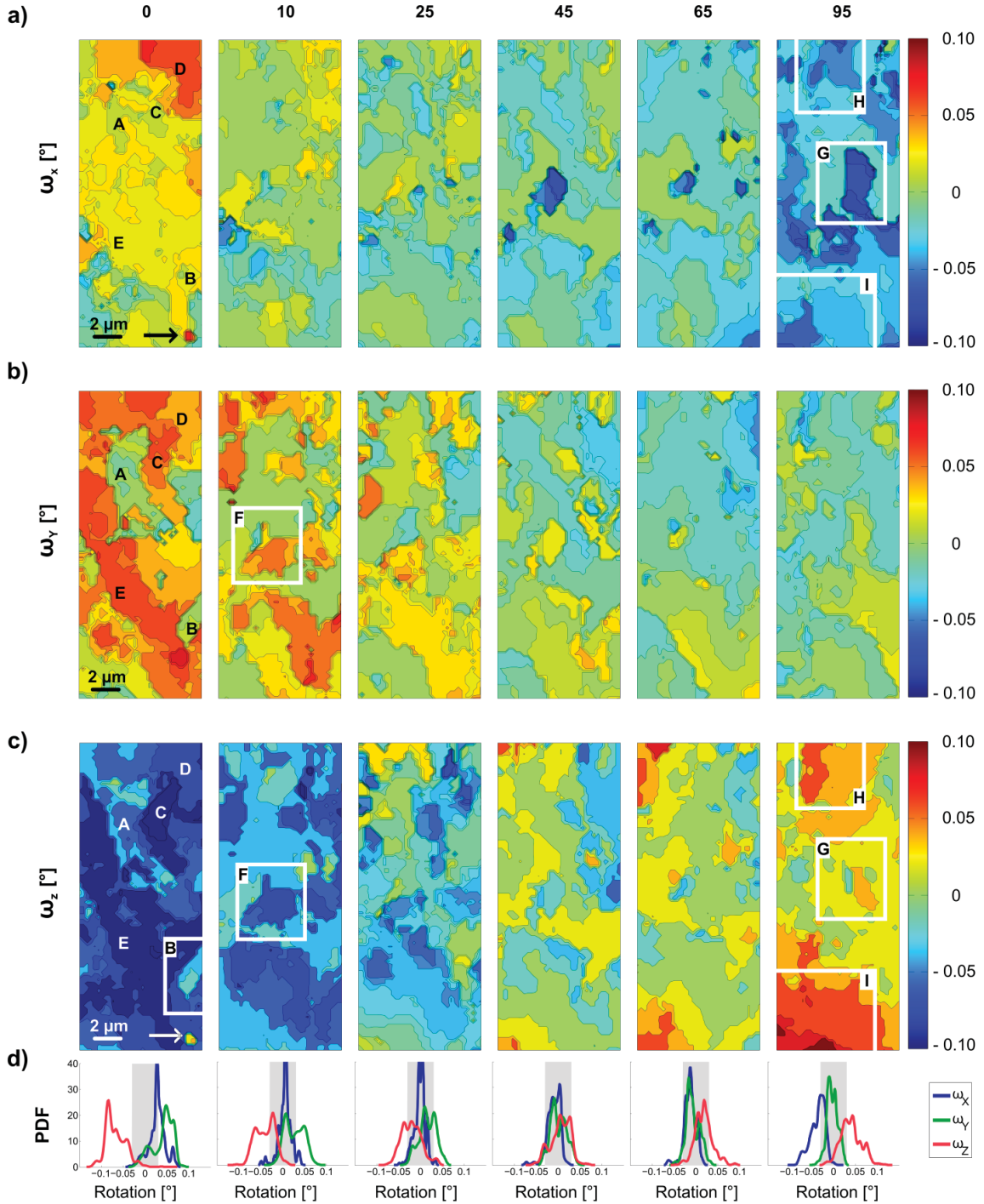
Figure 4.4 Evolution of rotations on the X-, Y-, and Z- axes (ω_x, ω_y and ω_z) of sample S2-Cp

4.1.4 Lattice curvatures and dislocation density tensor components

Lattice curvature components of sample S2-Cp are plotted in Figure 4.5. Scale bars have been limited to |3mrad/μm| for all components for better comparison.
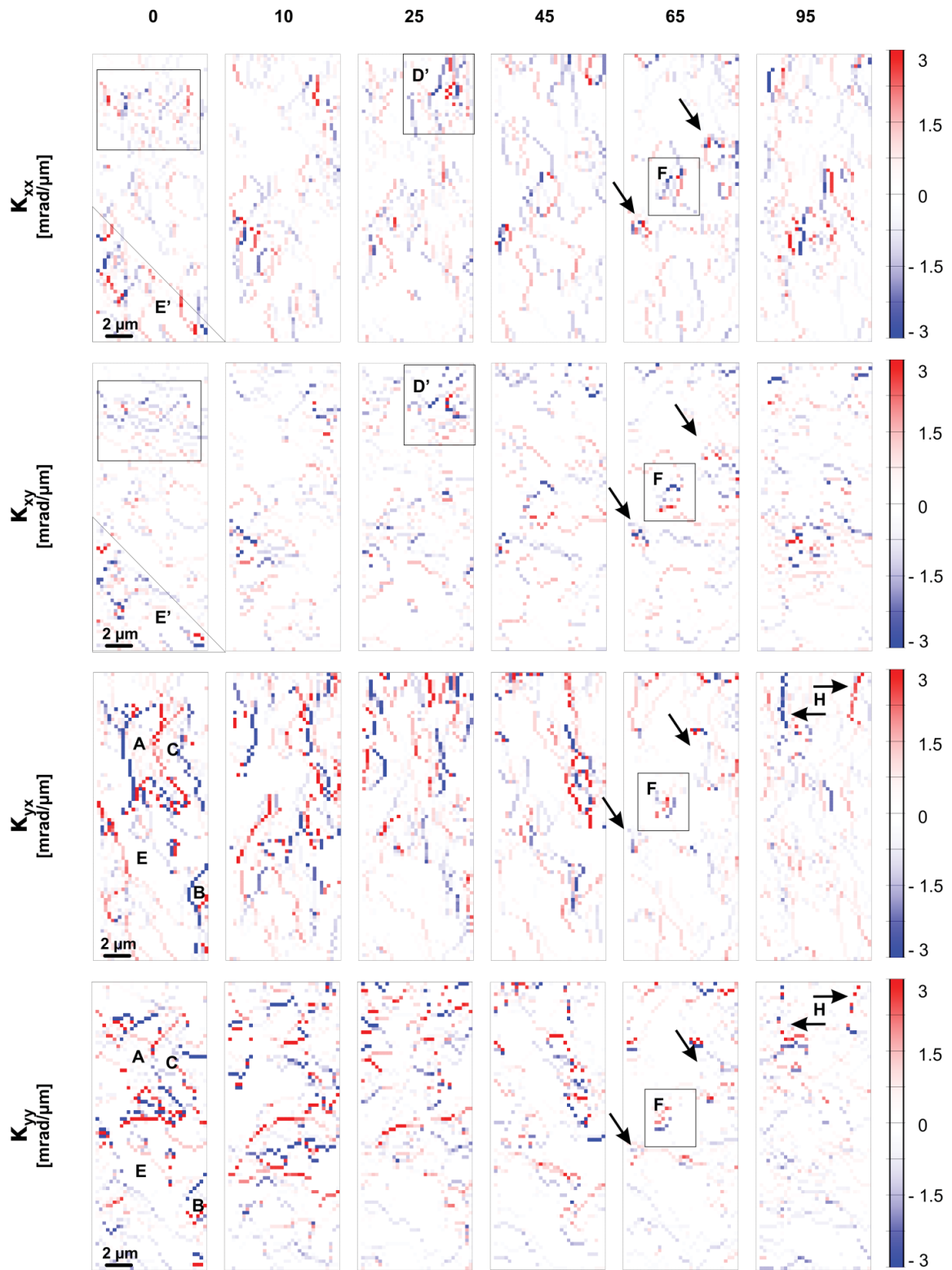
Figure continues on the next page
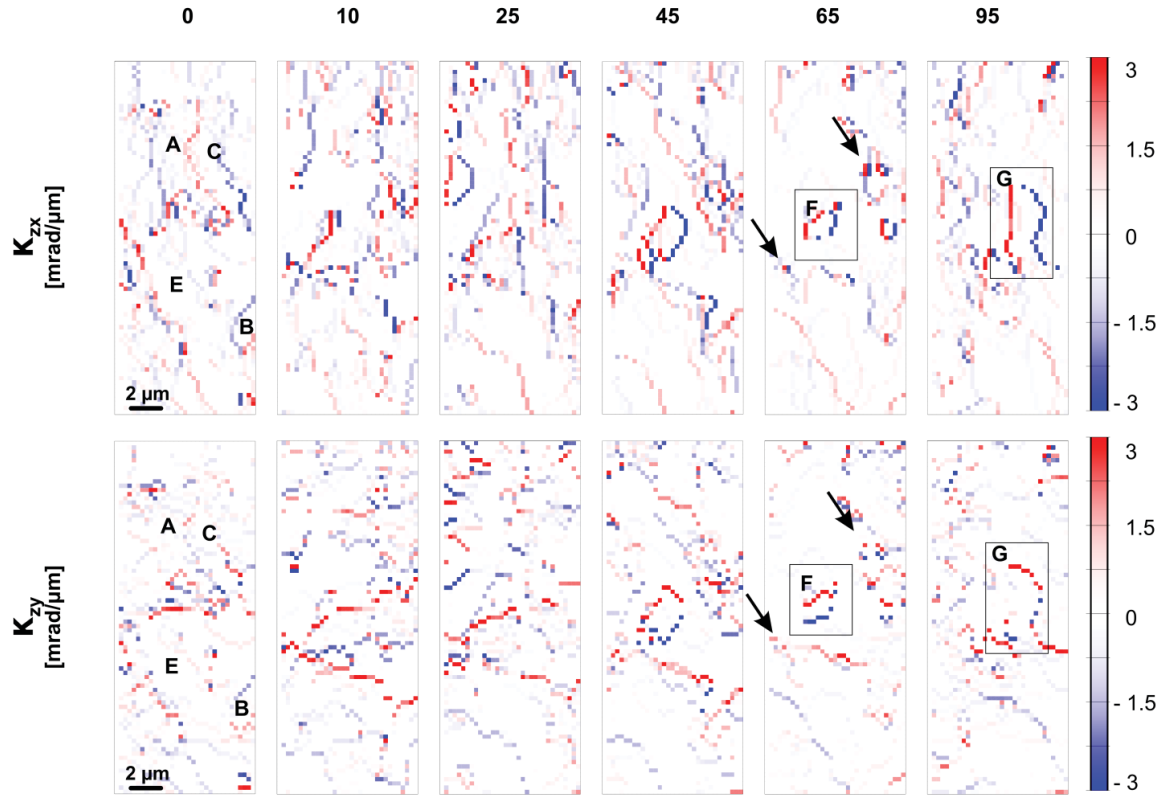
Figure 4.5 Evolution of lattice curvatures and dislocation density components of sample S2-Cp

The correlation of the lattice curvature maps with the misorientation map is not as strong as for the case of the single slip oriented samples (see Figure 3.5 and Figure 3.21). For instance, none of the regions above-mentioned are noticeable in the κ_{xx} and κ_{xy} maps. Initially there are few traces below region **E**, labelled as **E'**, that slowly vanish during cycling. In the upper part of the maps, marked with a black rectangle, there are also traces which after 25 cycles are mainly agglomerated in the right upper corner, labelled **D'**. At cycles 45 and 65, the main κ_{xx} and κ_{xy} traces define three small rounded regions in the middle of the map. These three regions are the one that are still misoriented: one corresponds to traces of region **F** and the other two are marked with arrows. After 95 cycles these traces redistribute and do not vanish. Most of the traces are agglomerated in the neighborhood of region **G**, but the perimeter of this misoriented region does not have strong κ_{xx} and κ_{xy} curvatures.

κ_{yx} and κ_{yy} maps have the strongest correlation with the misorientation map. Regions **A** and **B**, and partially **C** and **E** can be observed. There is a high agglomeration of traces in the lower part of region **A**, next to region **E**. Upon cycling the boundaries divide and the traces get shorter. At cycle 10 and 25 the traces mark the perimeter of the misoriented fragmented areas and after 65 cycles region **F** and the other two small regions can be distinguished. Surprisingly after 95 cycles almost all κ_{yx} and κ_{yy} footprints disappear and only few vertical lines in region **H** are left (marked with arrows).

In the initial maps of κ_{zx} and κ_{zy} components one can also notice regions **A**, **B** and **E**. The values of the boundary traces are lower than in the κ_{yx} and κ_{yy} maps. After the homogenization, at cycles 45 and 65, the same regions as in the other four maps can be observed: the traces of region **F** and the two small areas. After 95 cycles region **G** is the best defined area. Similar to κ_{xx} and κ_{xy} maps there are more traces in its surrounding too.

As the line directions of the edge dislocations belonging to the primary activated slip systems are not parallel to any of the laboratory axes, one cannot correlate each dislocation type to a particular lattice curvature. The

overview of the evolution of the lattice curvature maps show that there is a higher activity in the last four components (κ_{yx}, κ_{yy}, κ_{zx} and κ_{zy}) as compared to the κ_{xx} and κ_{xy} components.

The α_{zz} and $\alpha_{xx} - \alpha_{yy}$ maps are plotted in Figure 4.6. In general, the areas that have κ_{xx} lattice curvature do not have κ_{yy} curvature, and vice versa. These components define α_{zz} and $\alpha_{xx} - \alpha_{yy}$ (see section 2.3.4). That is why, at step 0 both maps look alike, except in region **E'** or on top of region **A** and **C** where the sign is reversed. In these areas is where κ_{xx} traces are located. After 95 cycles there is almost no κ_{yy} trace and thus both maps are identical but reversed in sign.
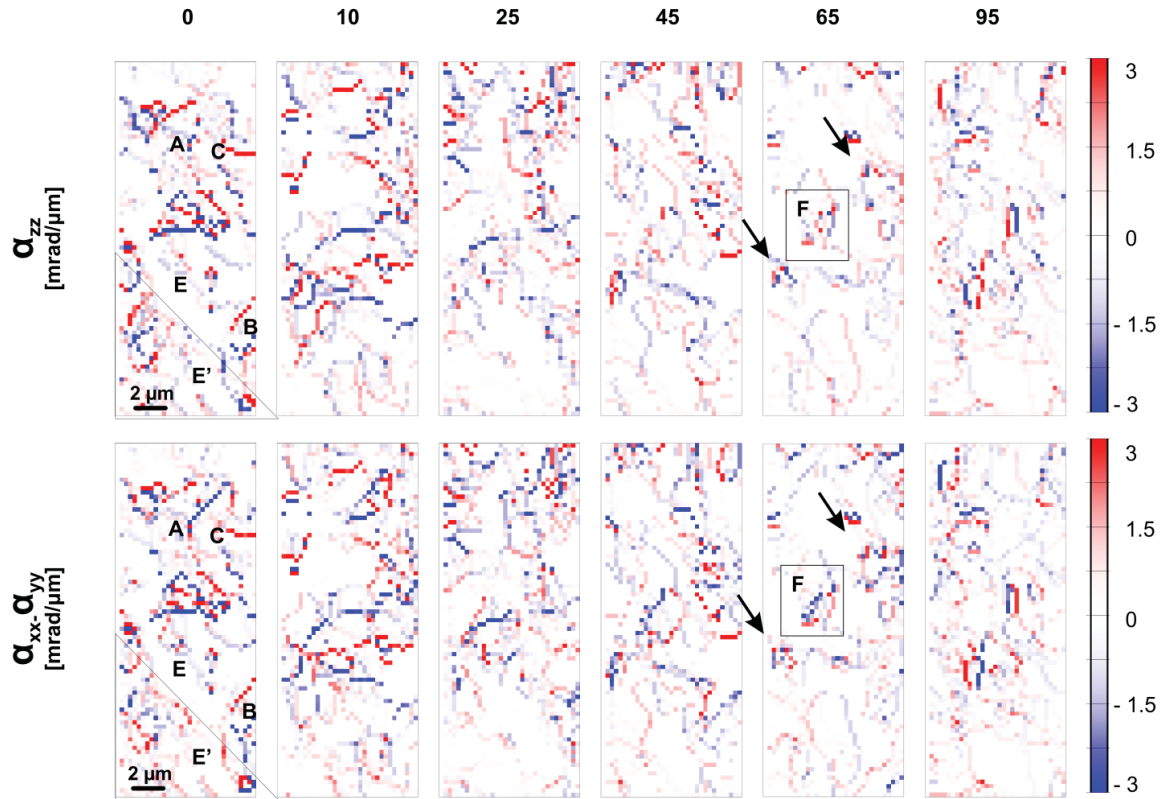
Figure 4.6 Evolution of α_{zz} and $\alpha_{xx} - \alpha_{yy}$ components of sample S2-Cp

The statistical distribution of each lattice curvature and dislocation density tensor components map at cycles 0 and 95 are graphically depicted as boxplots in Figure 4.7 (see Appendix D for detailed information about statistical representation as boxplots). The median of all distributions is ~0 mrad/µm and it does not change after 95 cycles. Before deformation, all components are lower than |10 mrad/µm| and particularly κ_{xx} and κ_{xy} values are even lower than |5 mrad/µm|.

After 95 cycles the boxplots show that, except α_{zz} and $\alpha_{xx} - \alpha_{yy}$, all components have a distribution below |5 mrad/µm|. α_{zz} and $\alpha_{xx} - \alpha_{yy}$ exhibit outliners above |5 mrad/µm| but never exceeding |10 mrad/µm|. Their distribution is identical but reversed in sign.

In the single slip samples, the initial lattice curvature and dislocation density tensor values are higher (see sections 4.1.4 and 4.2.4) and their distributions tend to broaden instead of narrowing.
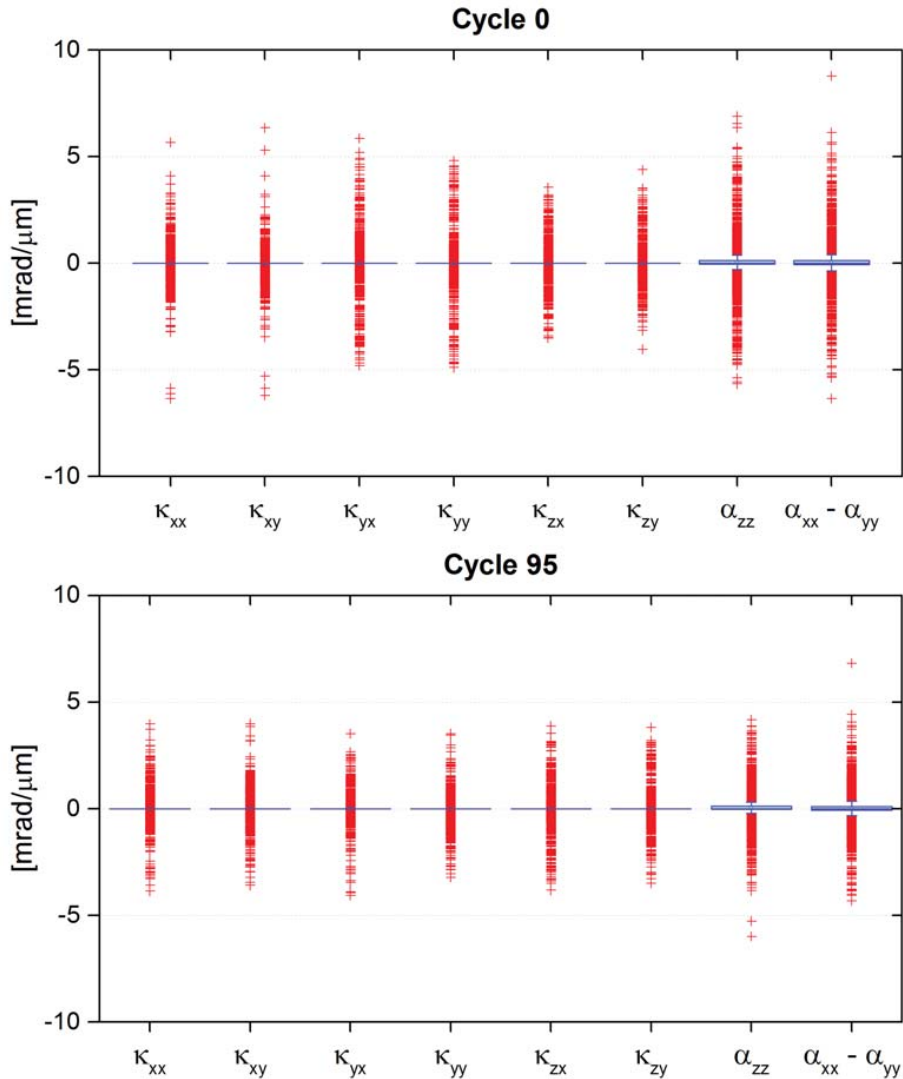
Figure 4.7 Statistical distribution of the lattice curvature and Nye tensor components of sample S2-Cp

4.1.5   Evolution of apparent GND density

The apparent GND density evolution of sample S2-Cp is displayed in Figure 4.8. At cycle 0, the boundaries of region **A** and **B** are clearly defined. Along the perimeter of region **A** several red-yellow hot spots are observable (e.g. in the lower part of the region **A** or in the top-left side). Their density is between 30-50 μm^{-2}, values that are lower than those observed for the single slip oriented sample (see Figure 3.9 and Figure 3.24). Inside region **E** there are almost no GNDs; below this region there are some traces with densities of 10 μm^{-2}. The small loop in the bottom-left corner exhibits a GND density higher than 50 μm^{-2}. The highly misoriented region **C** is also visible in this map but the traces are rather faint ($\sim$10 μm^{-2}).

During the first 45 cycles, the GND density traces redistribute according to the homogenization process described above (see sections 4.1.2, 4.1.3 and 4.1.4). There is less agglomeration of GNDs and the areas with low misorientation remain free of GNDs. The strongest GND footprints correspond to the boundaries of the higher misoriented domains shown in the misorientation map (Figure 4.3). The density of these traces is in the order of $\sim$20-30 μm^{-2}, with some hot spots with values of 50 μm^{-2}.

At cycle 45, the traces of region **F** are clearly defined by a closed circuit of GNDs. There are several areas with entangled GND traces (pointed by arrows) that are localized at the positions of the residual misoriented areas. After 65 cycles, the GND density map is clearer as the mentioned jumbles and region **F** shrink. The GND density at these marks is in the order of ~20-30 μm^{-2}, with some hot spots with values of 50 μm^{-2}.

The last 30 cycles introduce more GND entangles in area that previously exhibit a very low GND density. In the left side of the map at cycle 95 the GND traces are connected to each other and the network almost cross the entire map. The average density is ~10 μm^{-2}. Region **G** is defined by a circuit that is almost closed with density values of 20 μm^{-2}. This region has also evolved from a GND free area. The domains with high GND density after cycle 65 have disappeared.
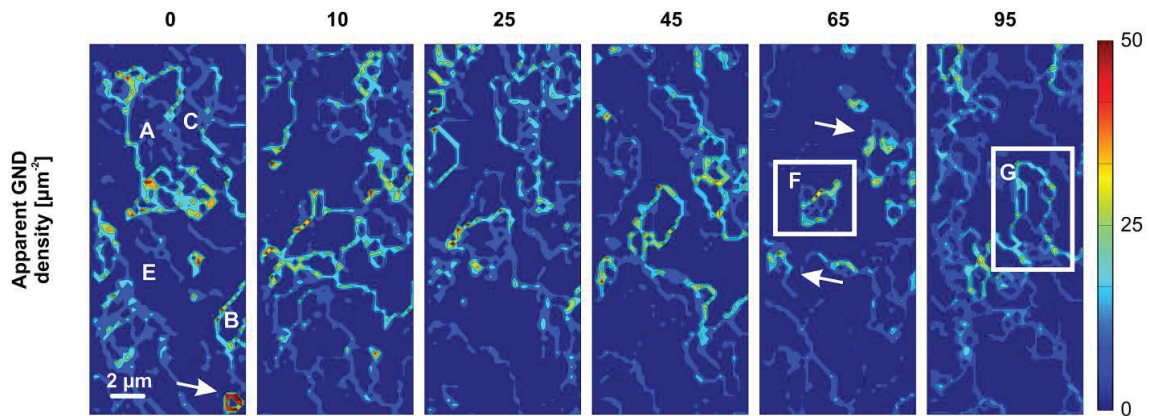
Figure 4.8 Evolution of apparent GND density of sample S2-Cp

4.1.6   Analysis of Laue reflections and orientation spread

In this section, the evolution of the Laue reflections and the orientation spread at different points are analyzed in order to obtain better insight into the dislocation dynamics in sample S2-Cp. Table 4.3 presents the angles between the Burger's vector and the normal of the planes related to the observed Laue reflections. The lower the value the more sensitive the reflection is to a dislocation with that Burger's vector. For visual representation the most sensitive values are written in green and the insensitive in red. According to the table:

- The $(1\bar{1}\bar{3})$ and $(31\bar{1})$ reflections are mainly sensitive to edge dislocations with $b = [\bar{1}01]$. The former reflection is insensitive to $b=[110]$ and the latter to $b = [011]$.
- The $(1\bar{1}3)$ reflection is most sensitive to edge dislocations with $b = [0\bar{1}1]$ and $b = [101]$. It is insensitive to those with $b=[110]$.
- The $(\bar{1}3\bar{1})$ is insensitive to primary edge dislocations with $b=[\bar{1}01]$, and mainly sensitive to those with $b=[110]$ or $b=[011]$.

According to the Schmid factors table (Table 4.1), the principal slip systems have $b = [\bar{1}01]$ and $b = [0\bar{1}1]$ (shadowed columns in Table 4.3). Therefore changes in reflections $(1\bar{1}3)$ and $(31\bar{1})$ should reflect activity of $(111)[\bar{1}01]$ primary slip system, and variations in both $(1\bar{1}3)$ and $(\bar{1}3\bar{1})$ reflections should show activity of $(111)[0\bar{1}1]$ primary slip system.

Table 4.3 Angles between the Burger's vector and the normal of the planes related to the observed Laue reflections

(hkl)\ b	[$\bar{1}$01]	[0$\bar{1}$1]	[110]	[011]	[101]	[1$\bar{1}$0]
1$\bar{1}$3	**31.48**	64.76	**90**	64	64.76	64.76
31$\bar{1}$	**31.48**	64.76	**31.45**	**90**	64.76	64.76
1$\bar{1}$3	64.76	**31.45**	**90**	64	**31.48**	64.76
$\bar{1}$3$\bar{1}$	**90**	64.76	**31.45**	**31.45**	64.76	64.76

Related to their particular evolution observed in the misorientation maps, the orientation scattering of the following points shown in Figure 4.9 are analysed:

- Point **A,** which always has low misorientation.
- Points **C**, **E** and **F** which initially have intermediate-high misorientations and slowly decrease their value. At cycle 65 points **C** and **E** have the same misorientation as the background but point **F** is still misoriented. After 95 cycles its misorientation decreases.
- Point **G,** which initially exhibits an intermediate misorientation, a low misorientation after cycle 65 and a higher misorientation after cycle 95.
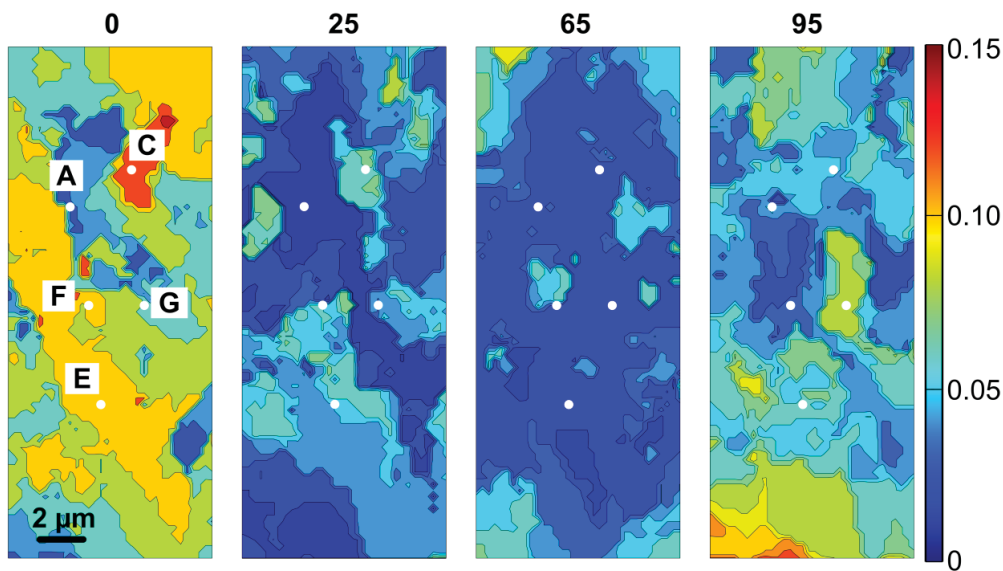
Figure 4.9 Evolution of misorientation in selected points for orientation scattering analysis in S2-Cp

The orientation scattering at cycles 0, 25, 65 and 95 is going to be shown together with reflection (31$\bar{1}$), which is one of the streaked peaks that is sensitive to both active Burgers vectors.

Low misorientation (point A)

Figure 4.10 shows the evolution of orientation scattering and the shape of the (31$\bar{1}$) peak of point **A** during cycling. Initially the peak reveals the presence of several crystallites in the integrated volume. During the first 65 cycles the (31$\bar{1}$) reflection narrows and only two main sub-peaks can be observed. After 95 cycles, the peak broadens and so does the scattering cloud. The position of the points with maximum intensity hardly changes during cycling, in agreement with its nearly constant misorientation value.
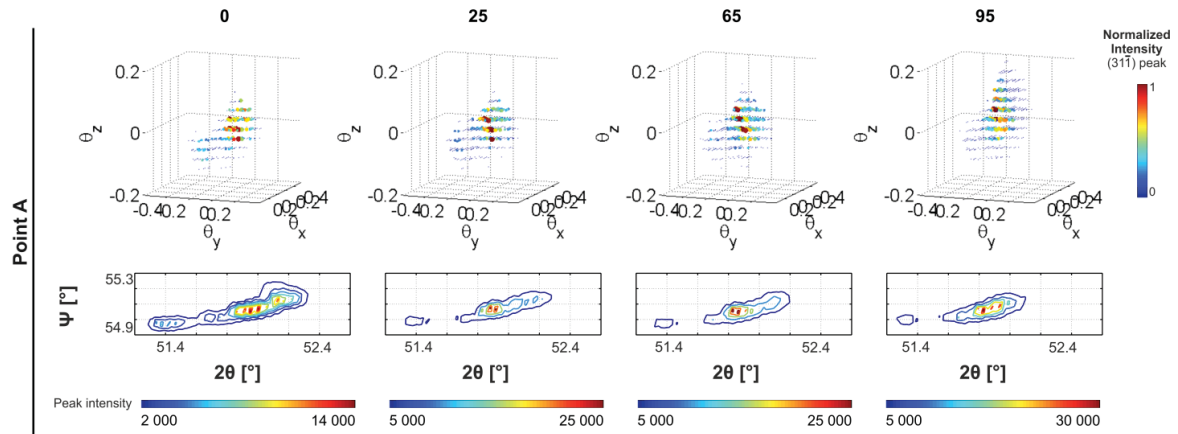
Figure 4.10 Orientation scattering in the integrated volume and $(31\bar{1})$ diffraction peak at point **A** in S2-Cp

One can compare the initial orientation spread at point **A** in S2-C to other initial orientation spreads in slip oriented samples. Table 4.4 collects some volume values of the orientation spread clouds at point **1F** and **2F** in S1-L sample (see Figure 3.14), points **R** and **A'** in S1-R sample (see Figure 3.27) and point **A** in S2-Cp sample (see Figure 4.10). The initial cloud at point **A** in S2-Cp samples has half of the volume than **1F** and **2F** points in S1-L. The points examined in sample S1-R have in turn double the volume than those points in S1-L. This underlines the influence of the sample preparation route since S2-Cp has been subjected to a second annealing (see sections 2.1.2 and 2.4). The source of differences between S1-L and S1-R, and between point **F** and **A'** in S1-R, has already described in section 3.4.5.

Table 4.4 Volume of the orientation spread clouds

Sample	S1-L		S1-R		S2-Cp
Point	1F	2F	F	A'	A
Volume [°³]	0.0258	0.0324	0.0683	0.0964	0.0107

Decreasing misorientation upon cycling (points C, E and F)

Figure 4.11 shows the evolution of orientation scattering and the shape of the $(31\bar{1})$ peak at points **C**, **E** and **F** during cycling. All the points show several crystallites in the integrated volume. The initial orientation scatter is slightly different at each point but all of them are a bit broader than at point **A**. The position of maximum intensity in all points a priori looks the same but when comparing all the reflections there are subtle differences. Hence, the indexation yields slightly different orientation matrices. Note that the misorientation values in S2-Cp (see Figure 4.3) are lower than in single slip oriented samples (Figure 3.3 and Figure 3.19) and as a consequence the shift is not so evident in the graphs.
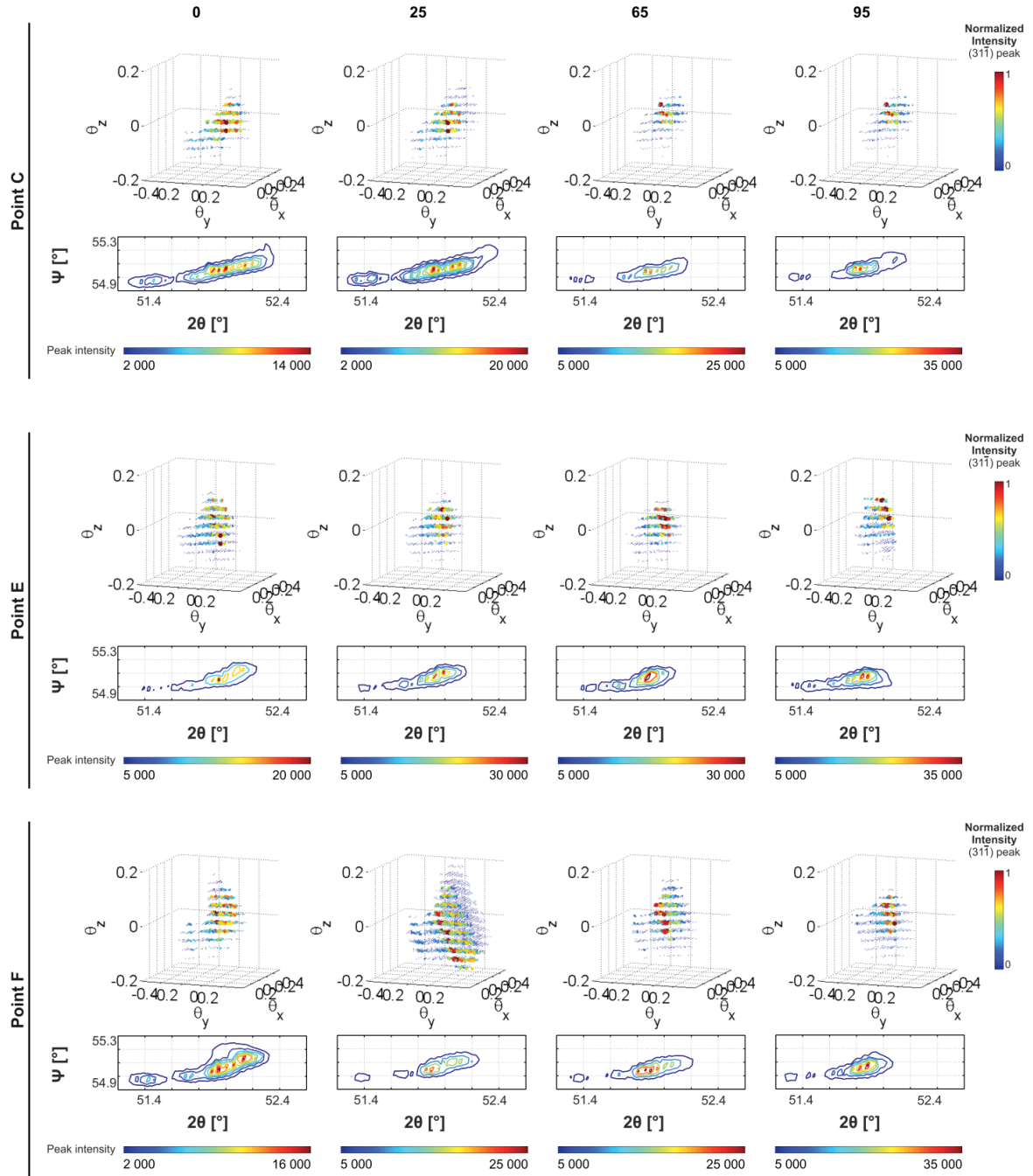
Figure 4.11 Orientation scattering in the integrated volume and $(31\bar{1})$ diffraction peak at points **C**, **E** and **F** in S2-Cp

During cycling, point **C** behaves similar to point **A**. During the first 65 cycles the $(31\bar{1})$ peak and orientation spread gets narrower and only two main sub-peaks remain. From cycle 25 to 65 there is a clear shift in the position of the points with maximum intensity, which corresponds to the decrease of the misorientation. At cycle 95 both the shape and the orientation scattering are similar to step 65.

In point **E** the $(31\bar{1})$ peak initially does not show so many crystallites in the integrated volume but the orientation scattering is not narrower. During cycling the reflection is constantly changing its shape and the

points with maximum intensity in the scattered cloud are changing their position. The total cloud is smaller after 95 cycles than at step 0.

The evolution in point **F** varies the most. After 25 cycles the ($31\bar{1}$) peak narrows but the scattering volume exhibits a broadening in orientation similar to those observed in single slip oriented samples (see Figure 3.14 or Figure 3.17 as examples). After 65 cycles the cloud narrows again and after 95 cycles the points with maximum intensity shift their position.

Increasing misorientation at final cycles (point G)

Figure 4.12 shows the evolution in point **G**. Even if the misorientation is rather low at cycles 25 and 65 (Figure 4.3), the orientation spread and the shape of Laue peaks reveal that the microstructure is rather heterogeneous across the thickness. In fact, the ($31\bar{1}$) diffraction peak is always streaked and several sub-peaks can be observed. Similar to point **E** and **F** the steady state is not reached as both the peak and the scattering cloud are continuously changing.
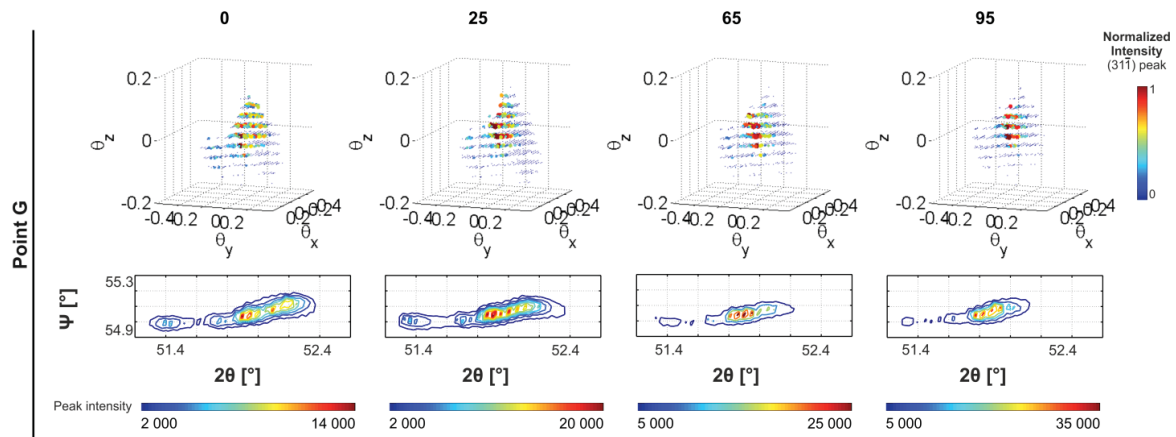
Figure 4.12 Orientation scattering in the integrated volume and ($31\bar{1}$) diffraction peak at point **G** in S2-Cp

Summary

Overall, the initial orientation spreads at different points in S2-Cp sample are lower than those of single slip oriented samples. While the evolution in single slip samples is more sequential, here there is no clear trend. The continuous variations in the Laue shape and changes in orientation spread in a given point after cycles, together with the differences between all the examined points, evidence the high microstructural activity in S2-Cp, which is not reflected in the 2D maps shown in previous sections. From the orientation spread clouds, however, it is not possible to determine the misorientation between the crystallites observed in the peaks.

4.1.7   Indexation error

The distribution of the indexation error is shown in Figure 4.13 where four peaks were taken into account to find the orientation. The averaged error is 1.64 ± 0.44 pixels which is lower than both samples oriented for single slip (see Figure 3.18 and Figure 3.29). The error distribution map has few features similar to the misorientation map at step 0 where some of the sharp boundaries match. In the other maps such correlation is not detected.
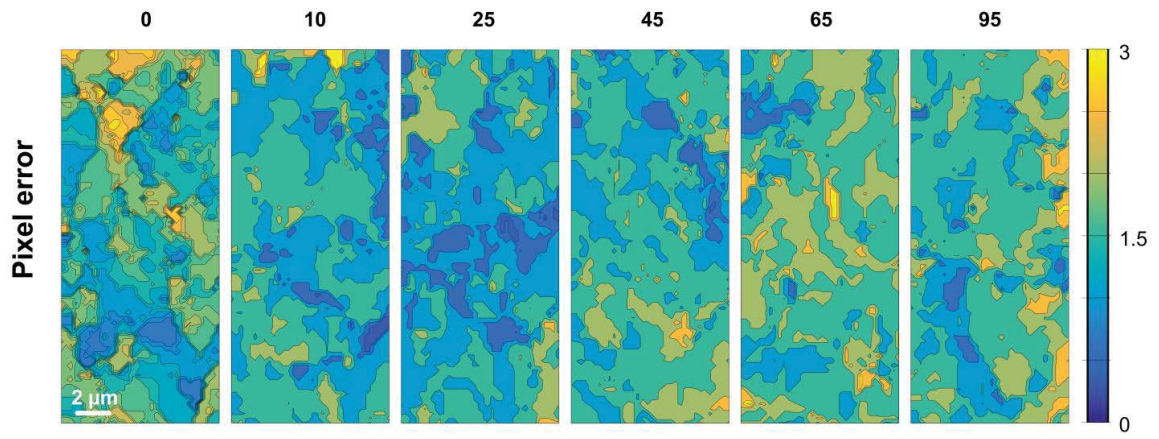
Figure 4.13 Indexation error distribution for each map in sample S2-Cp

4.2   Collinear double slip

Samples oriented for collinear slip have easy glide on the $(1\bar{1}1)[110]$ and $(\bar{1}11)[110]$ systems when loaded in shear. Both of them share the same slip direction but have different slip plane. A list of Schmid factors for all slip systems is given in Table 4.5. The $(1\bar{1}1)[\bar{1}01]$, $(1\bar{1}1)[011]$, $(\bar{1}11)[101]$ and $(\bar{1}11)[0\bar{1}1]$ have a Schmid factor that is half of the value of that of the primary slip system. Each of them share one of the planes of the principal systems but have different slip direction. All other slip systems have zero Schmid factor. Figure 4.14 shows the schematics of the primary slip systems in a cuboid and the crystal orientation in the laboratory frame. The magenta line corresponds to a dislocation line with $b=[110]$ in $(1\bar{1}1)$ plane and the yellow line to a dislocation line with same Burgers vector but in $(\bar{1}11)$ plane.

Table 4.5 Schmid factors for collinear orientation

Slip system	Plane			Direction			Schmid Factor
1	1	$\bar{1}$	1	1	1	0	0.816
2	$\bar{1}$	1	1	1	1	0	0.816
3	1	$\bar{1}$	1	$\bar{1}$	0	1	0.408
4	1	$\bar{1}$	1	0	1	1	0.408
5	$\bar{1}$	1	1	1	0	1	0.408
6	$\bar{1}$	1	1	0	$\bar{1}$	1	0.408
7	$\bar{1}$	$\bar{1}$	1	1	$\bar{1}$	0	0
8	$\bar{1}$	$\bar{1}$	1	1	0	1	0
9	$\bar{1}$	$\bar{1}$	1	0	1	1	0
10	1	1	1	1	$\bar{1}$	0	0
11	1	1	1	$\bar{1}$	0	1	0
12	1	1	1	0	$\bar{1}$	1	0
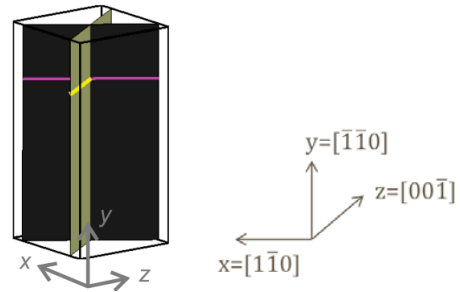
Figure 4.14 Crystal orientation and primary slip systems (planes and dislocation lines) for collinear orientation Y-axis corresponds to shear-load axis and Z-axis to beam axis.

4.2.1   Mechanical data

The sample oriented for collinear double slip has been subjected to a total of 80 cycles, subdivided into five series, where the resolved plastic strain amplitude was gradually increased from 0.057% to 0.107%. The force response as a function of resolved shear strain for the last cycle of each series is shown in Figure 4.15. The number of cycles, force at maximum positive displacement and the resolved total and plastic shear strain amplitudes are listed in Table 4.6. The crystal exhibits a gradual slow increase in the width of the hysteresis loop for all applied plastic shear strain amplitudes.

Comparing to the mechanical response of single slip (Figure 3.2) and coplanar oriented crystal (Figure 4.2), for a given resolved strain amplitude the required force is higher for the collinear sample, which suggests that it is harder. After 80 cycles and almost reaching the force limit of the system, the maximum resolved plastic strain amplitude is only 65% of that reached in coplanar slip.
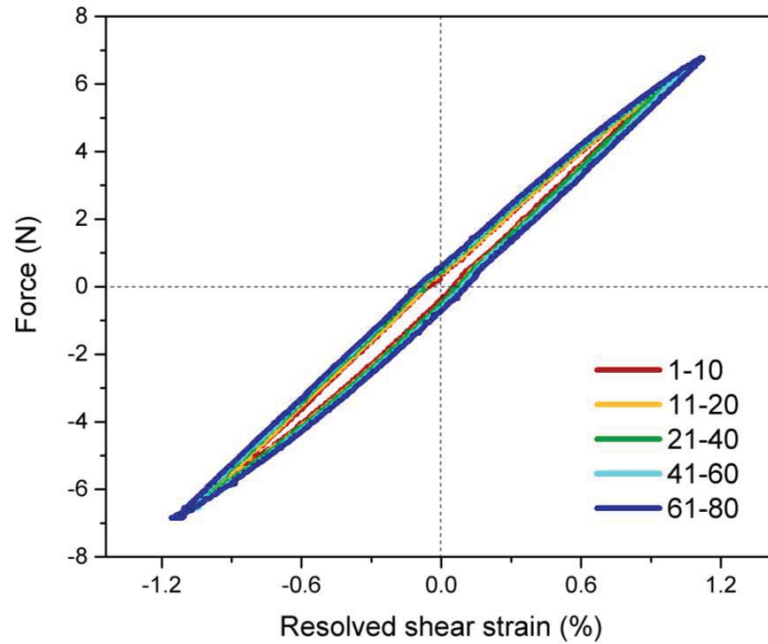
Figure 4.15 Mechanical response of collinear double slip oriented sample

Table 4.6 Number of cycles, maximum force and resolved total and plastic shear strain amplitudes for collinear orientation

Total cycles	Maximum force (N)	Resolved total shear strain (%)	Resolved plastic shear strain (%)
1-10	5.49	0.84	0.057
11-20	5.81	0.91	0.074
21-40	6.13	0.95	0.087
41-60	6.45	1.01	0.099
61-80	6.77	1.08	0.107

4.2.2 Evolution of misorientation angle

The evolution of the misorientation angle of S2-Cl sample as a function of cycles is shown in Figure 4.16-a. The initial microstructure is divided in three areas: the upper-right zone with the highest misorientation (region **A**), the middle-diagonal area which has the lowest misorientation (region **B**), and the lower-left corner with intermediate misorientation (region **C**). The three regions contribute to the three peaks present in the PDF function shown in Figure 4.16-b. The description of the PDF distribution is given in Appendix D. The misorientation angle in region **A** varies from 0.13° to 0.20°, the average misorientation value of region **B** is ~0.04° and of region **C** ~0.09°. These values are lower than in the single slip oriented samples (Figure 3.3 and Figure 3.19) but higher than in the coplanar sample. This initial microstructure is very different from the other samples studied in this work.

During the first 20 cycles the initial heterogeneities are accommodated: the boundaries defining each region move and overall the misorientation values decrease. Region **A** shrinks and exhibits more uniform misorientation values of ~0.11°. Region **B** remains with a misorientation value of ~0.02°. Region **C**, on the other

hand expands. Contrary to region **A**, this region is not uniform and different fragments with misorientation values ranging from 0.06 - 0.08° (bright blue) to 0.10° (green). The PDF curve shows that the maximum misorientation value at step 20 has lowered to 0.16°, and that most of the area has a misorientation value of ~0.10°.

During the last 60 cycles (cycles 21-80) the misorientation maps show the gradual transformation of the microstructure. Region **A** gets fragmented and lowers the misorientation value to 0.08°. As a consequence, the boundary with region **B** is less well-defined. Region **C**, on the other hand, continues increasing its size and misorientation. At cycle 80, there are domains with misorientation of ~0.13° (yellow) and hot orange spots of ~0.16°. The PDF shows that the map is divided in two areas, one with average misorientation around 0.04° (region **B**) and a second with misorientation from 0.08° to 0.16° (regions **A** and **C**).

Opposite to what it was observed in the single slip and coplanar double slip cases, the initial three regions still are visible after 80 cycles and there is no clear evidence of formation of new regions in the misorientation map.
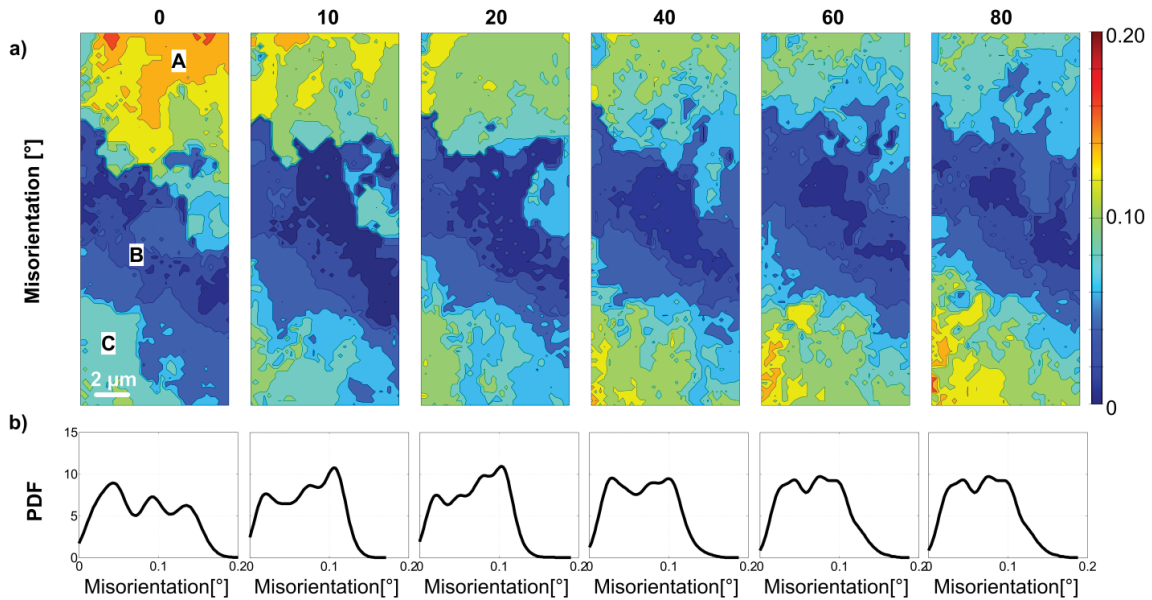
Figure 4.16 Evolution of misorientation angle of sample S2-Cl. a) Spatial resolved maps; b) PDF functions

4.2.3   Evolution of rotations about X-Y-Z- axes

Figure 4.17-a-c presents the evolution of the amount of rotation around the *X-*, *Y-*, and *Z-* axes (ω_x, ω_y and ω_z). The scale bars for these rotations are |0.2°|, |0.15°| and |0.05°| respectively. For each cycle, the PDFs of ω_x, ω_y and ω_z are plotted in Figure 4.17-d. On these plots a grey band with a width of |0.03°| is shown. As the rotation angles within this band are very low, the exact values should be taken with care since the rotation axes are not well defined. The description of the PDF distribution is given in Appendix D.

The initial distribution of ω_x, ω_y and ω_z maps shows the three regions. Region **A** has positive rotation around the *X*-axis with magnitudes ranging from 0.09° to 0.15°. The boundary with region **B** is clearly noticeable due to the sharp transition of ω_x from ~0.09° to 0°. In fact, both region **B** and **C** exhibit nearly no rotation around the *X*-axis; only few domains in region **C** have ω_x~-0.05°. The ω_y map also show similar features but with lower values. Region **A** exhibits an averaged ω_y~0.06° (light orange) with some fragments with ω_y~0.08° (darker orange). The transition to region **B**, which shows no rotation about ω_y is more gradual than in the ω_x map. The change to region **C** is also progressive. This region is negatively rotated around the *Y*-axis with ω_y~-0.07° but also contains areas with ω_y~-0.10°. Most of the ω_z rotations are in the interval of 0 to |0.03°| but there are some domains in

region **A** and **C** that have higher rotations around the *Z*-axis. The former has some domains with positive rotation $\omega_z \sim 0.04°$ (red) and the latter with negative rotation $\omega_z \sim -0.04°$ (dark blue).
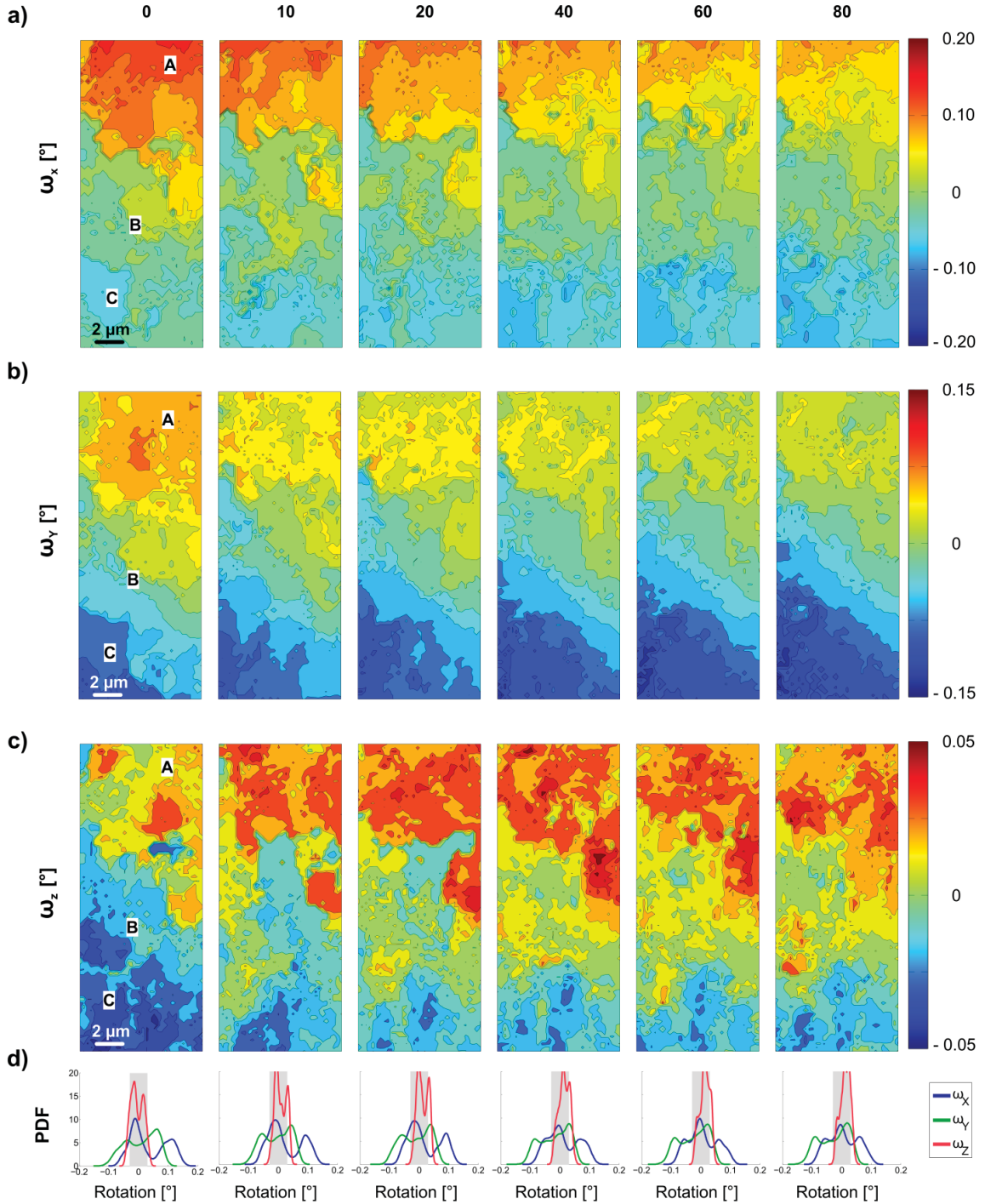
Figure 4.17 Evolution of rotations on the *X-, Y-,* and *Z-* axes (ω_x, ω_y and ω_z) of sample S2-Cl

During cycling the rotation maps evolve so that:

- Region **A** has during all the cycles the maximum rotation around the *X*-axis. ω_x, however, decreases from an average of 0.11° at cycle 0 to 0.05° at cycle 80. Its size is also reduced. The ω_x rotation of region **B** is

negligible during all 80 cycles. The initial negatively rotated region **C** expands and increases its rotation value to $\omega_x \sim$ -0.07°.

- The evolution of ω_y show that region **A** lowers its positive ω_y rotation from 0.06° to 0.03° in the first 20 cycles and remains almost constant with further cycling. Region **C**, on the other hand, increases its negative ω_y rotation value to -0.09° with some spots of the order of -0.14° located in the left corner at cycle 80. The area corresponding to region **B** does not show any particular evolution.
- During the 80 cycles the ω_z values basically do not exceed the |0.03°| band. During the first 40 cycles region **A** slightly increases its rotation about Z-axis to 0.04° but during the last cycles it reduces again. Region **C** lowers its misorientation and after the first 10 cycles the lower 2/3 part of the map has $\omega_z \sim$0.

Similar to coplanar S2-Cp sample (see Figure 4.4), the strongest rotation of collinear S2-Cl is around the *X*-axis and the weakest around the *Z*-axis. In S2-Cl there is no apparent formation of any particular region in the rotation maps.

4.2.4 Lattice curvatures and dislocation density tensor components

Lattice curvature components of sample S2-Cl are plotted in Figure 4.18. Scale bars have been limited to |2 mrad/μm| for all components for better comparison.

In all initial maps the regions **A**, **B** and **C** can be distinguished. Region **A** is rather clean of trace from lattice curvature except in the upper-left corner and in the middle-right side close to region **B**.. The former area corresponds to a domain inside region **A** that has a low misorientation value similar to region **B** (see Figure 4.16). The boundary with region **B** is better defined in the first four κ_{xx}, κ_{xy}, κ_{yx} and κ_{yy} maps than in the last two, κ_{zx} and κ_{zy}, where the traces are faint. Region **B**, contrary to region **A**, has many alternating lattice curvature traces. Region **C** exhibits only few traces inside and its boundary with region **B** is mainly visible in the κ_{yx} and κ_{yy} maps.

During cycling the boundaries between regions break and the differentiation between the regions is less clear. Upon cycling region **A** increases the number of κ_{xx}, κ_{xy}, κ_{yx} and κ_{yy} traces, similar to the trace-ensemble observed at cycle 0 in region **B**. The low misoriented area embedded in region **A** disappears. The initial traces of region **B** are present until cycle 40. Afterwards the region is rather clean of lattice curvature traces. Region **C** follows a similar trend as region **A**. Initially clean of traces, after 80 cycles the whole region is full of entangled footprints. This is particularly evident in the κ_{yx} and κ_{yy} maps.

Similar to the misorientation map (Figure 4.16) and ω_x, ω_y and ω_z maps (Figure 4.17) there is no formation of a particular defined region. Also, as the line directions of the edge dislocations belonging to the primary activated slip systems are not parallel to any of the laboratory axes, one cannot correlate each dislocation type to a particular lattice curvature. The overview of the evolution of the lattice curvature maps show that there is high activity in the κ_{yx} and κ_{yy} components, intermediate in κ_{xx} and κ_{xy} and almost nothing in κ_{zx} and κ_{zy}.

The α_{zz} and $\alpha_{xx} - \alpha_{yy}$ maps are plotted in Figure 4.19. The scale bars have been limited to |3 mrad/μm| for clarity. In both maps the evolution described for the lattice components apply: initially the three regions are separated by sharp boundaries that upon cycling get fragmented and eventually vanish. Region **A** and **C** are at cycle 0 almost free of dislocation density tensor components but after 80 cycles there are many traces. These traces are not as in the previous samples marking the perimeter of particular areas (see Figure 3.5, Figure 3.21 and Figure 4.5) but they are a collection of red/blue points meaning that from point to point the disorientation is changing. Region **B** after 80 cycles cleans the initial traces.
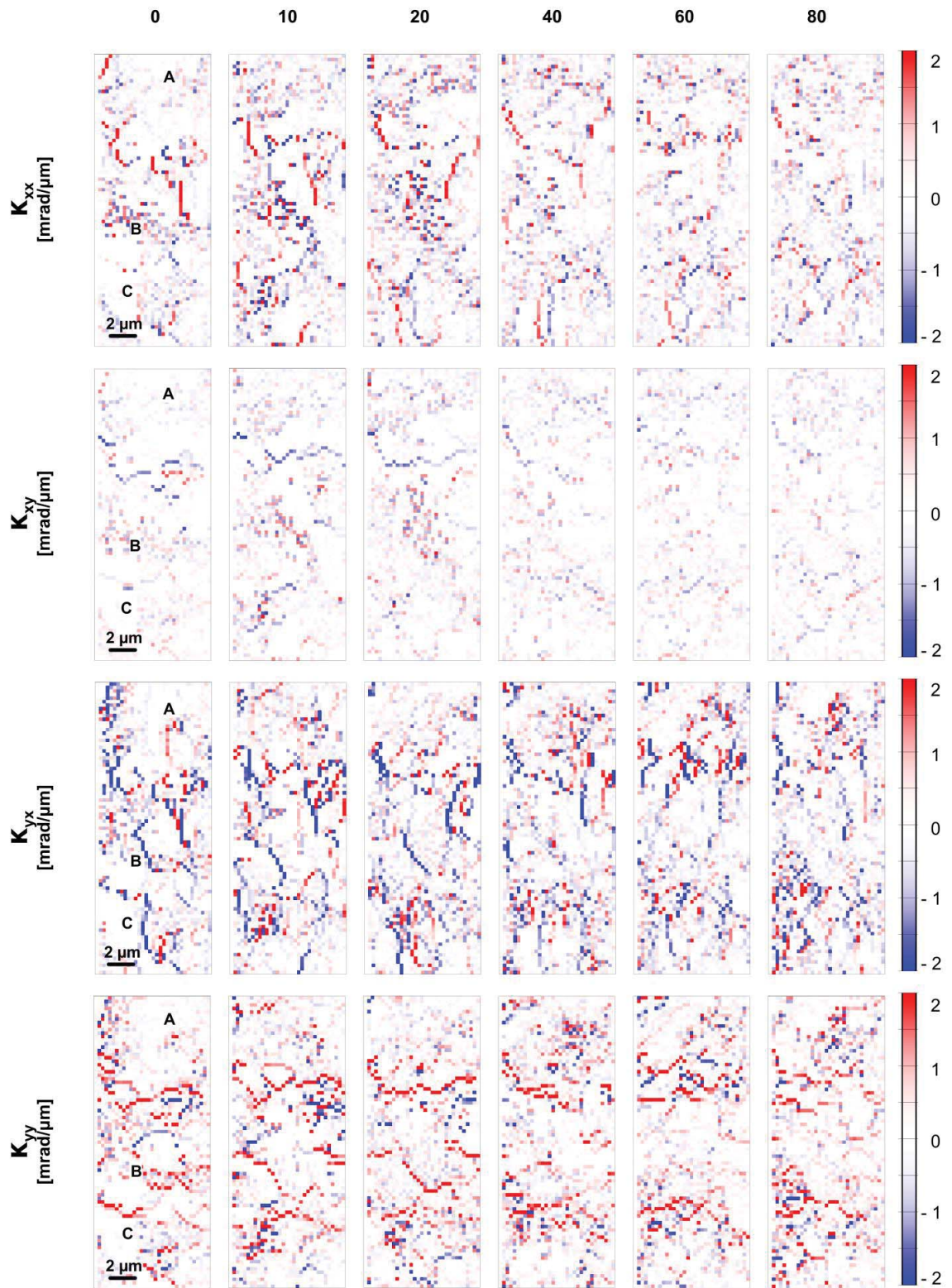
Figure continues on the next page
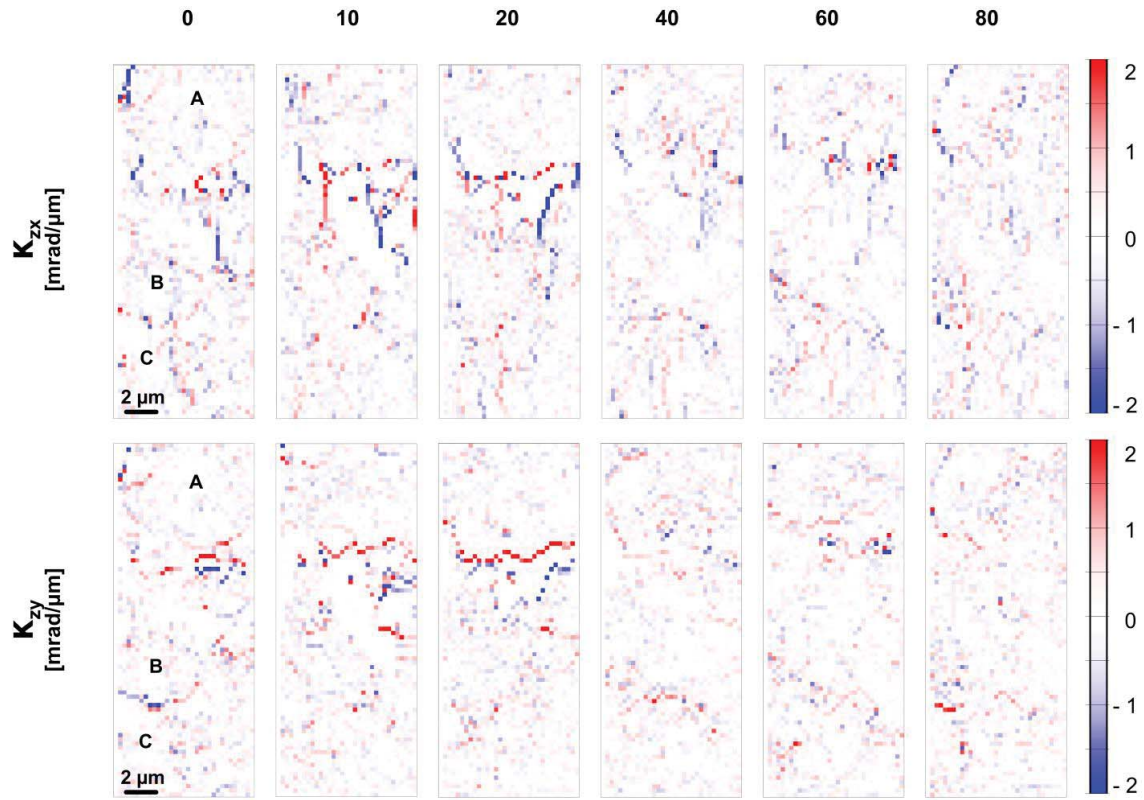
Figure 4.18 Evolution of lattice curvatures and dislocation density components of sample S2-Cl
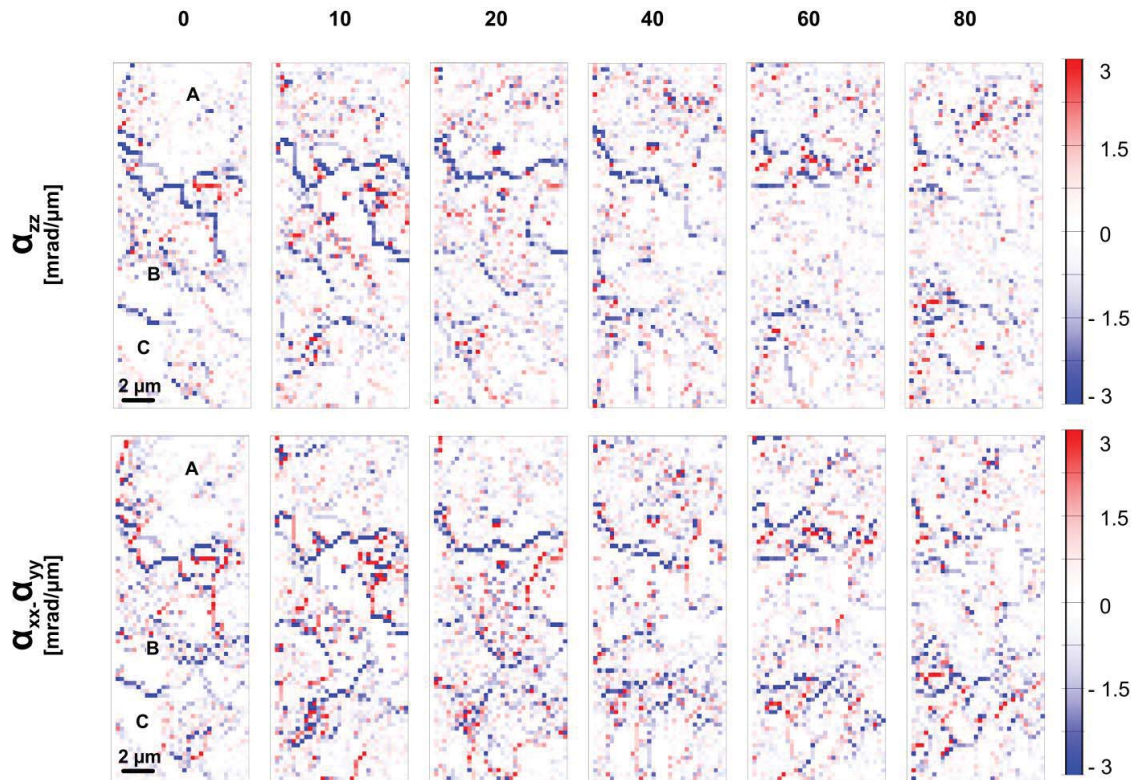
Figure 4.19 Evolution of α_{zz} and $\alpha_{xx} - \alpha_{yy}$ components of sample S2-Cl

The statistical distribution of each lattice curvature and dislocation density tensor components map at cycle 0 and cycle 80 are graphically depicted as boxplots in Figure 4.20 (see Appendix D for detailed information about statistical representation as boxplots). The median of all distributions is ~0 mrad/µm and it does not change after 80 cycles. Before deformation, almost all components are below $|5$ mrad/µm$|$. Only κ_{yx}, κ_{yy}, α_{zz} and $\alpha_{xx} - \alpha_{yy}$ slightly exceed those values.

After 80 cycles the boxplots have hardly changed. In comparison to the single slip (Figure 3.8 and Figure 3.23)and coplanar samples (Figure 4.7), the values found for the collinear sample are the lowest and its distribution is the one which changed the least.
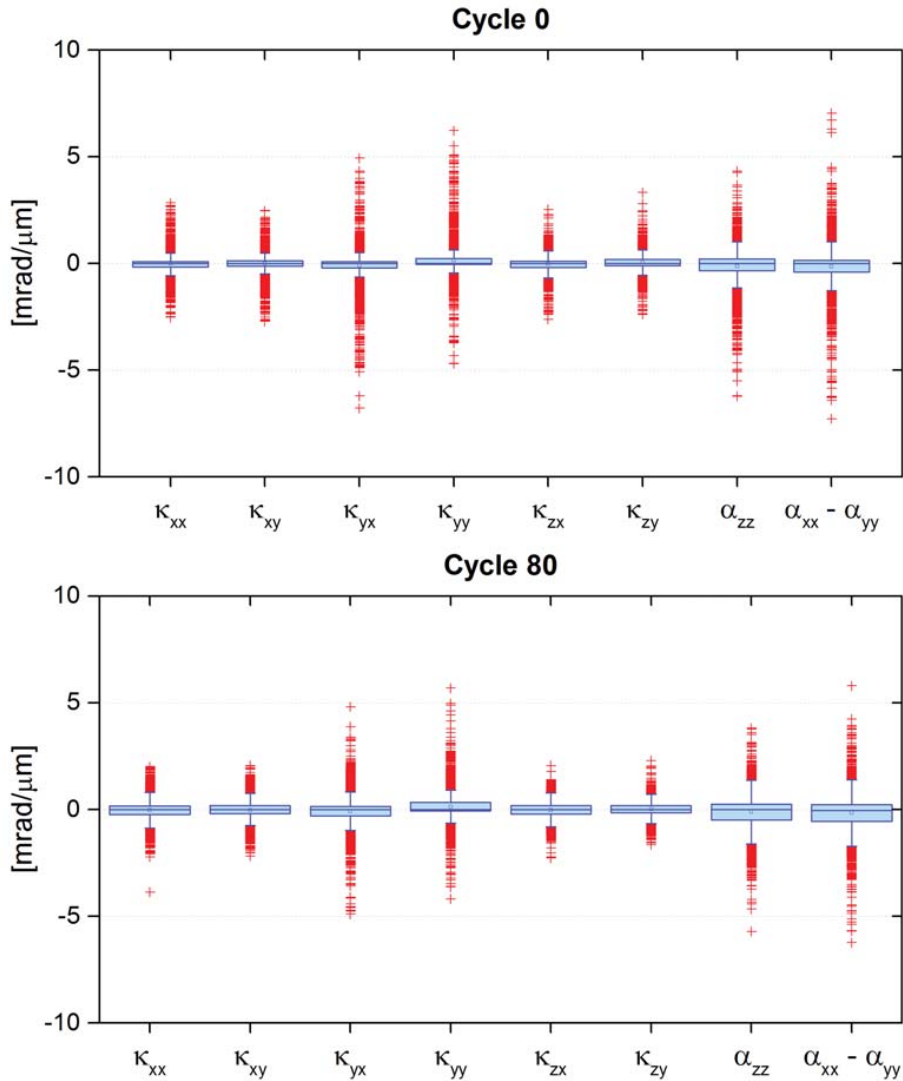
Figure 4.20 Statistical distribution of the lattice curvature and Nye tensor components of sample S2-Cl

4.2.5   Evolution of apparent GND density

The evolution of apparent GND density of sample S2-Cl is displayed in Figure 4.21. At cycle 0 the boundaries between regions are clearly defined by GND traces marking the transition. Their density is in the order of ~25-40 µm^{-2}. The low misoriented area inside region **A** is also marked in its perimeter by GND traces with similar dislocation density. While inside region **A** and **C** there are almost no initial GNDs, region **B** has several GND traces with densities of the order of 5-20 µm^{-2}.

After the first 20 cycles, the boundary between region **A** and **B** is still present and is continuous across the map. Its average density is ~33 μm^{-2} but there are some hot spots as high as ~50 μm^{-2}. At cycle 20 region **B** has still the initial GND traces inside and inside region **C** new ones have appeared with a density of the order of ~10 μm^{-2}.

At cycle 40 the boundary **A-B** gets fragmented and the traces inside region **B** start disappearing. Inside region **A**, on the other hand, new low-density traces appear. With further cycling up to cycle 80, the wall marking the transition from region **A** to **B** vanishes and almost the complete map is full of GND jumbles that are randomly distributed. The averaged density is in the order of ~5-10 μm^{-2} but there are some spots particularly located in region **A** and **C** with densities of ~20 μm^{-2}.
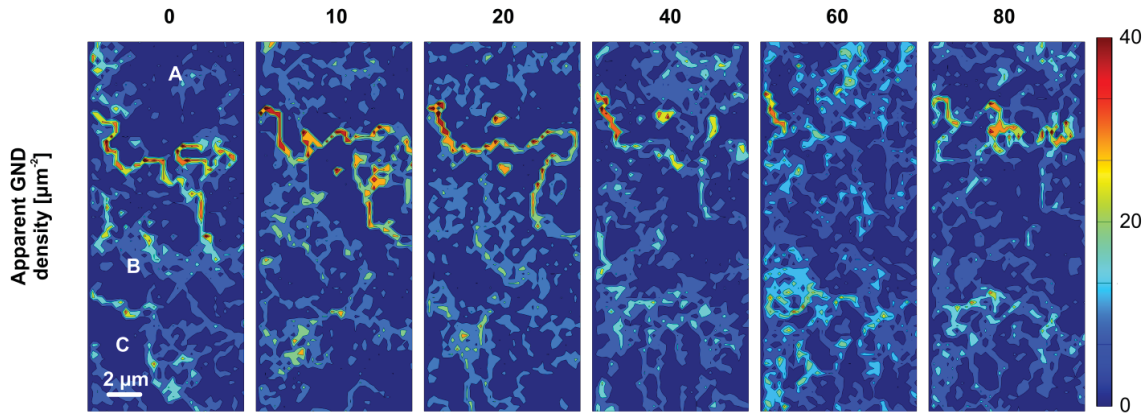
Figure 4.21 Evolution of apparent GND density of sample S2-Cl

4.2.6   Analysis of Laue reflections and orientation spread

The analysis of the Laue reflections and the orientation spread in sample S2-Cl is not as straightforward as in the other samples. First of all, there are 16 indexed reflections which strongly constrains the procedure to determine the average crystal orientation in each point. On the other hand, the S2-Cl is the hardest among all the tested and additionally it is the one subjected to fewer cycles and at lower plastic resolved shear strain. Therefore, one can expect smaller lattice rotations than S1-L, S1-R and S2-Cp samples. In fact, even if the 2D maps plotted in the previous sections show certain degree of gradual evolution in lattice rotation, the movement of each reflection is less noticeable than in single slip and coplanar samples (sections 3.3.5 m 3.4.5 and 4.1.6).

All the reflections are listed in Table 4.7 where the angles between the Burger's vector and the normal of the planes related to the Laue reflections are also given. The lower the value the more sensitive the reflection is to a dislocation with that Burger's vector. For visual representation the most sensitive values are written in green and the insensitive in red. According to the table, the main reflections sensitive to the two principal slip systems sharing b=[110] are (131), ($\bar{3}\bar{1}1$), ($\bar{1}\bar{3}1$), (311), (242) and (422) (shadowed column).

Table 4.7 Angles between the Burger's vector and the normal of the planes related to the observed Laue reflections

(hkl)\\b	[110]	[0$\bar{1}$1]	[$\bar{1}$01]	[011]	[101]	[1$\bar{1}$0]
131	**31.48**	64.76	**90**	**31.48**	64.76	64.76
$\bar{1}$31	64.76	64.76	64.76	**31.48**	**90**	**31.48**
$\bar{3}$11	64.76	**90**	**31.48**	64.76	64.76	**31.48**
$\bar{3}\bar{1}$1	**31.48**	64.76	31.48	**90**	64.76	64.76
$\bar{1}\bar{3}$1	**31.48**	**31.48**	64.76	64.76	**90**	64.76
1$\bar{3}$1	64.76	**31.48**	**90**	64.76	64.76	**31.48**
3$\bar{1}$1	64.76	64.76	64.76	**90**	**31.48**	**31.48**
311	**31.48**	**90**	64.76	64.76	**31.48**	64.76
$\bar{4}$02	50.77	71.57	**18.43**	71.57	71.57	50.77
$\bar{4}$22	73.22	**90**	**30.00**	54.74	73.22	**30**
$\bar{2}$42	73.22	73.22	54.74	**30**	**90**	**30**
042	50.77	71.57	71.57	**18.43**	71.57	50.77
242	**30**	73.22	**90**	**30**	54.74	73.22
422	**30**	**90**	73.22	54.74	**30**	73.22
402	50.77	71.57	71.57	71.57	**18.43**	50.77
0$\bar{4}$2	50.77	**18.43**	71.57	71.57	71.57	50.77

Due to the reasons explained above and as no particular region has evolved during cycling three random points, each one belonging to a different region (**A**, **B** and **C**), are analysed. Figure 4.22 shows the orientation spread at cycles 0 and 80 calculated using the highest intensity reflections. The colour of each point corresponds to the normalized intensity of the ($\bar{3}\bar{1}$1) reflection which is also shown in Figure 4.22. Initially, the distribution of the maximum intensity inside the scattered cloud for each point (**A**, **B** and **C**) is different. The difference is barely noticeable in the Laue shape Ψ-2θ plots but the misorientation map included in the left side of the figure shows that each point is misoriented respect to each other. The initial orientation spread is larger at point **A** than in points **B** and **C** (see the volume of the orientation spread clouds in Table 4.8). Surprisingly the volume of the cloud is larger than in point **A** in S1-R (compare values in Table 4.4). In points **B** and **C**, on the other hand, the cloud is in the same order than in single slip oriented samples.

Table 4.8 Volume of the orientation spread clouds in S2-Cl sample

Point	A	B	C
Volume [°³]	0.1174	0.0244	0.0251

After 80 cycles, the position of the points with maximum intensity in point **B** and the shape of the reflections remain similar. In points **A** and **C** a shift is observed. In the former the shift is in the direction towards point **B** and that is why the misorientation value lowers; in the latter the shift is getting away from point **A** and **B**. That is why, the misorientation in point **C** increases and the rotation maps show different rotations in point **A** at cycle 0 (positive ω_x and ω_y) and in point **C** at cycle 80 (negative ω_x and ω_y).

The scattering volume in point **C** has enlarged after cycling but the spread of the points with high intensity is similar.
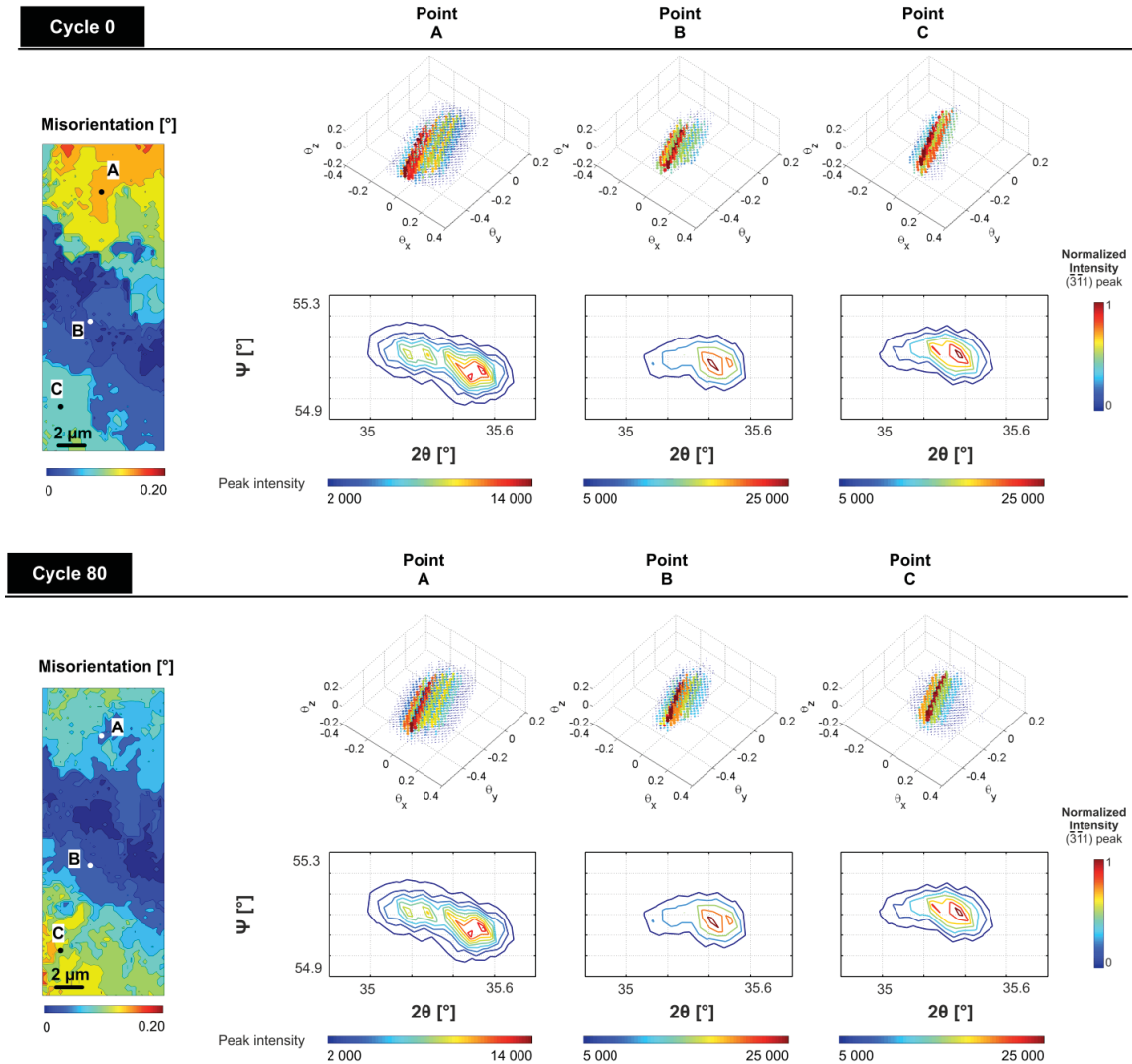
Figure 4.22 Orientation scattering in the integrated volume and $(\overline{3}\overline{1}1)$ diffraction peak at points **A, B** and **C** in S2-Cl

4.2.7 Indexation error

The distribution of the indexation error is shown in Figure 4.23 where 16 peaks were taken into account to find the orientation. The averaged error is 2.79±0.62 pixels which is lower than both samples oriented for single slip (Figure 3.18 and Figure 3.29) and slightly higher than in the coplanar (Figure 4.13). The error distribution maps show higher errors in the patterns near the transition from region **A** to **B** but the distribution homogenizes after 80 cycles.
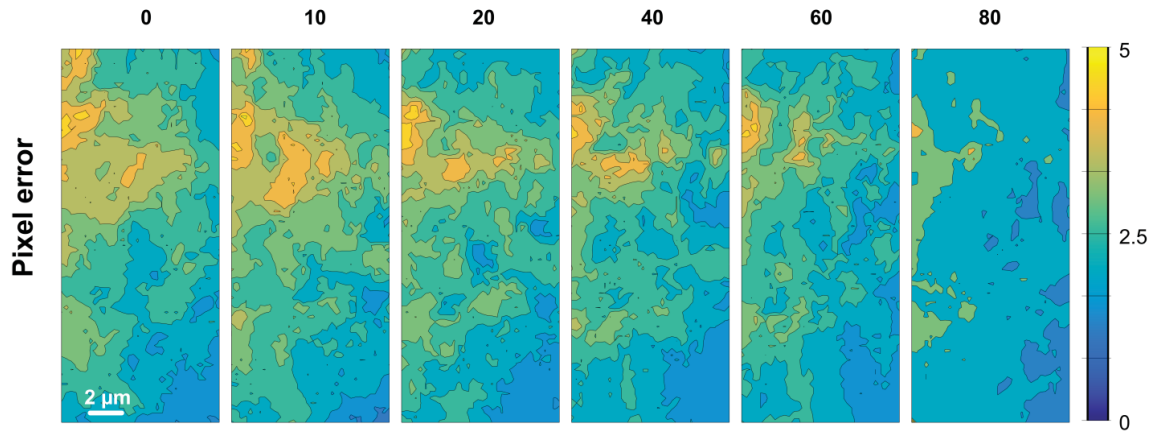
Figure 4.23 Indexation error distribution for each map in sample S2-Cl

4.3   Summary

The major observations derived from the results of double slip oriented fatigued samples can be summarized as follow:

- Introducing a second annealing in sample preparation process, between mounting and picosecond laser ablation, may reduce the initial heterogeneities observed in samples oriented for single slip.
- In all investigated samples there is a homogenization process where the initial microstructure is accommodated. Depending on the applied strain amplitudes and crystal orientation the process can require more cycles.
- Both samples oriented for double slip are harder compared to the single slip sample. Also, the collinear orientation is harder compared to the coplanar one.
- Rotation-wise there is no evidence of dislocation structure formation in any of the double slip oriented samples under the applied conditions.
- From the orientation spread clouds it is not possible to quantify the misorientation between the crystallites observed in the Laue peaks.

Chapter 5   Discussion

The aim of the performed research is to explore to which extend in-situ Laue diffraction can be used to follow the development of dislocation structures during deformation. A lot of details on the dislocation evolution in cyclically fatigued single crystals are known. However there are also aspects that are still missing such as the involved lattice rotations. This information is required in order to validate currently ongoing simulations. Therefore we have developed a new in-situ method and performed experiments on copper single crystals in three different orientations during the early stages of cyclic fatigued. We have measured the lattice rotations, curvatures and corresponding apparent GNDs. For that purpose, a dedicated miniaturized device has been constructed, Matlab scripts have been developed for analyzing the diffraction data and a sample preparation based on picosecond laser ablation has developed as shown in Chapter 2. Below we address important results coming out of the presented research:

- *Suitability of picosecond laser ablation to prepare the samples*
- *Mechanical response of the system and the effect of the crystal orientation*
- *Dynamics of dislocations according to the applied deformation conditions*
- *Early formation of dislocation patterning in single slip oriented sample*
- *Benefits and limitations of the technique*

5.1   Is picosecond laser ablation suitable for preparing small scale samples?

Picosecond laser ablation has been used to locally thin the samples. A pulse duration near 5 to 10 ps is reported to be a good tradeoff between minimum thermal damage and the avoidance of non-linear effect through multiphoton processes characteristic in the femtosecond regime (Dausinger et al., 2003). It is known that the process can introduce some structural changes in the HAZ in terms of dislocations, recrystallization and/or amorphization (Harzic et al., 2002). Molecular dynamics simulations predict that the HAZ in the picosecond pulse regime exhibits a negligible concentration of defects such as vacancies and dislocations distributed over the surface (Bouilly et al., 2007). It is important to note that the extend of the affected region depends on the material, laser and ablation parameters (Le Harzic et al., 2005; Stafe et al., 2014).

The broadening of the Laue reflections is sensitive to dislocation defects in the probed volume (Ice and Barabash, 2007). Our Laue study performed on a copper single crystal foil shows that the induced damage is minimal when comparing the ablated and not ablated areas (Guitton, A., Irastorza-Landa et al., 2015). Analysis of Laue reflections taken from the prepared shear samples reveal that the starting microstructure is not free of defects (sections 3.3.5, 3.4.5, 4.1.6 and 4.2.6). The orientation scattering of Laue reflections is larger in the single slip oriented samples than in the double slip specimens. The latter have however been subjected to a second annealing before the picosecond laser ablation. This points to a fact that most of the introduced damage observed in the shear samples has to be ascribed to the entire sample preparation process and that picosecond laser ablation is only responsible for a minor part of the damage.

Thus, the ultra-short pulsed laser ablation technique, either in the picosecond pulse regime (Guitton, A., Irastorza-Landa et al., 2015) or in the femtosecond regime (Echlin et al., 2015), has the potential to prepare small scale samples. Note that besides the limited damage introduced, another advantage is the rate of material removal which is much faster than the popular FIB process. The technique opens new possibilities for machining new geometries such as flat large membranes.

5.2 Mechanical response of the system and effect of the crystal orientation

In this section three aspects of the developed system are discussed: (1) influence of having built an asymmetric system in the mechanical response, (2) sensitivity of the obtained mechanical, and (3) the mechanical response of the three orientations.

5.2.1 Consequences of an asymmetric mechanical loading system

The developed miniaturized machine allows deforming samples cyclically in shear mode. The mechanical response is measured by two load cells and the cantilever system, which is located on top of the sample. This gives the response of the whole system and not local information in the thin area. As observed in the mechanical data of the tested samples (Figure 3.2, Figure 4.2 and Figure 4.15), the non-symmetricity of the device results in deviations from ideal force-strain curves. Even if the curves have been corrected to compensate the fact that the sample acts as a spring, the cantilever system is not very precise for reversed cycles. As a consequence, the transition from positive to negative load is not perfect and results in non-standard features in the force-strain plots (e.g. straighter lines in the second unloading than in the first one, discontinuities on the slopes when reversing force, small bumps at low forces, etc.) (see Figure 5.1). This excludes analysis of the Bauschinger effect from the force-strain curve and determination of the yield force from the force-strain curves.
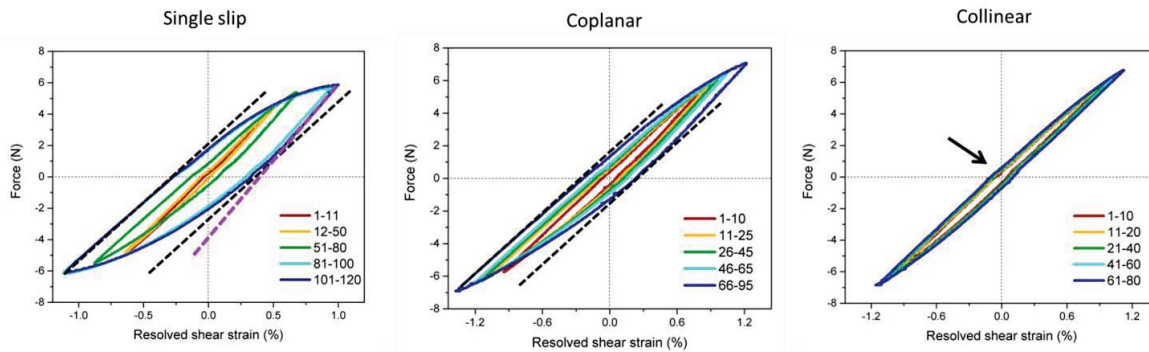
Figure 5.1 Review of the mechanical response for different crystal orientation

All the experiments are performed with a constant displacement rate imposed in the linear stages (U=4 µm/s) (see section 2.1.4 for details). Table 5.1 shows the real measurements done by the angular encoder (u) for each crystal orientation. These values are an order of magnitude smaller. This evidences the non-linear transfer between the displacement of linear stage and the displacement of the pin. The difference is not significant when comparing the crystal orientations. There is however an important difference when values for positive load and reversed load are compared. This is again due to the asymmetry of the system.

Table 5.1 Displacement rate obtained by angular encoder

Crystal orientation	Displacement rate (nm/s)	
	Positive-load	Reversed-load
Single slip	90	66
Coplanar	106	78
Collinear	105	83

Figure 5.2 shows the schematic diagram of the machine where each box represents an element. The ensemble formed by the linear stage, load cell and pin moves along the fixed structure. The cantilever and the sample are

also connected to the structure. The blue and red arrows are the representations of transmission systems to account for the observed reduction of the displacement and displacement rate between the elements.

- For the same displacement amplitudes and displacement rates in the upper and lower driving ensembles, the cantilever measures reduced values. The blue arrows represent that loss.
- The values are also different depending if the signal is coming from the top or the bottom due to gravity and the elements in between. That is why the blue arrows do not have the same color and there is an additional arrow between the sample and cantilever to account for the additional loss.
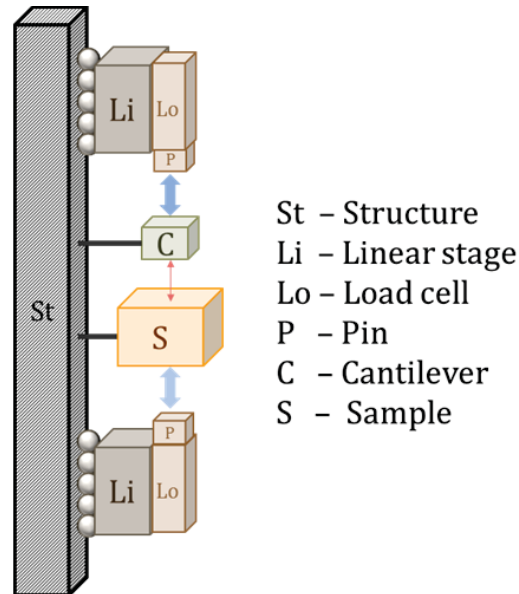
Figure 5.2 Schematic diagram of the machine and representation of transmission systems between elements

5.2.2 Mechanical data

All the mechanical tests are done following a multiple step test methodology: the strain amplitude is kept constant during a certain amount of cycles, afterwards the strain amplitude is increased to a higher level and more cycles are done. As an illustration cycles 50 to 53 and 80 of the single slip case have been plotted in Figure 5.3. A similar behavior is observed in all other situations where the strain amplitude is increased. The figure shows that the first force-strain curve after an increase in strain amplitude is different to the previous one (e.g. 51 to 50). The consecutive cycles with the new strain amplitude (from 52 till 80), on the other hand, do not show notable variations. This should not be interpreted as having already reached the cyclic stability after only one cycle. The experimentally measured mechanical data is a response of the whole system; what happens locally in the thin area is at the moment only accessible by simulations. This is for each of the crystal orientation discussed in section 5.3.

Cycle number	Strain amplitude (%)
50	0.040
51-53 and 80	0.095
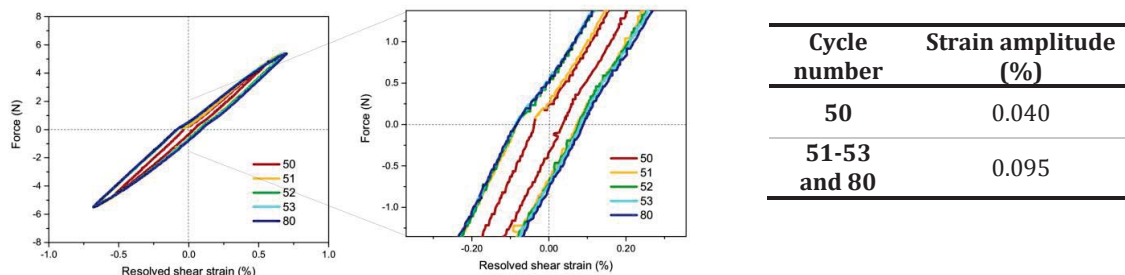
Figure 5.3 Mechanical response when increasing displacement amplitude

5.2.3   Different response depending on crystal orientation

Figure 5.4 shows the force reached as function of the resolved shear strain for the different crystal orientations. The strain hardening behavior shows that the single slip orientation is the softer and that the collinear is the hardest orientation. This is in good agreement with the discrete dislocation calculations that show that the collinear interaction is the strongest interaction in the fcc crystal structure (Madec et al., 2003).

It also has to be pointed out that in the coplanar and collinear cases the system's load limit of 7 N was reached.
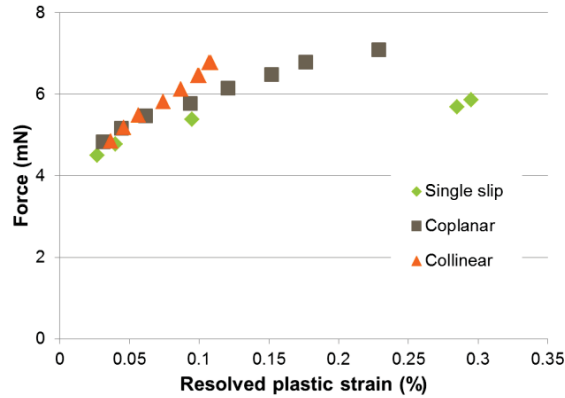
Figure 5.4 Orientation dependence on strain hardening

5.3   Dynamics of dislocations

Combining mechanical testing with Laue micro-diffraction allows following the dynamics of dislocations during fatigue by examining the lattice rotation and the shape of reflections. As the applied experimental conditions are different for each crystal orientation (see sections 3.2 for single slip, 4.1.1 for coplanar and 4.2.1 for collinear case), the final stage reached in each sample is not equivalent. In order to have a nominal measure at the end of the cyclic loads, a cumulative resolved plastic strain has been calculated as:

$$\Gamma = 4 \sum_{i=1}^{N} \gamma_{pl,i}$$

<div align="right">eq. 23</div>

where, $\gamma_{pl,i}$ is the resolved plastic shear strain amplitude in the ith cycle and N is the total number of cycles.

This parameter is used as an approximate measure of permanent damage in fatigue (Suresh, 1998). Even if it is not suitable for low plastic strain amplitudes cases and few cycles, it allows comparing the three tested cases from the experimental measurements. Figure 5.5 shows Γ for each orientation. The sample oriented for single slip is the crystal that has been fatigued the most, followed by coplanar and finally collinear. Therefore, it is expected to see more evolution for the single slip orientation.
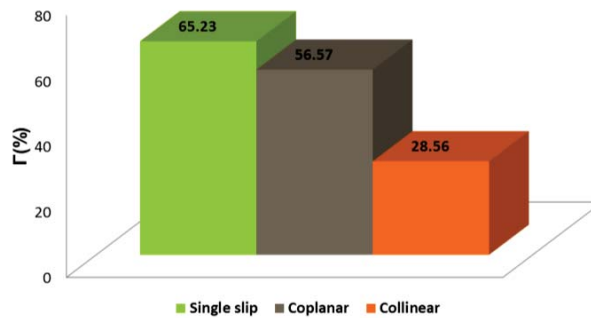
Figure 5.5 Cumulative resolved plastic strain for different crystal orientations

Experimentally, the stress and strain in the thin area are not measurable with our device. In order to get better insight into the deformation process, simulations using the experimental displacement amplitudes are done, where the simulated sample geometry is similar to the experimental one. More details are given in section 2.1.1, in appendix B and in (Grilli et al., 2015). The simulated stress-force relationship and the evolution of total strain and its distribution for the three crystallographic orientations are shown and discussed in relation to the experimental results.

5.3.1   Stress-force relationship

Figure 5.6 shows the computed relationship between the σ_{xy} stress in the center of the thin area and the force at maximum load for samples oriented in single slip, coplanar and collinear. Each point in the plot corresponds to a particular cycle; some numbers are indicated as reference. The stress values lie in the range of stresses estimated in Figure 2.5 and are of the same order of magnitude as the normalized bending moments obtained in cyclically deformed copper single crystal micro-beams (Kiener et al., 2010).

Comparing the stress-force levels of coplanar and collinear to single slip oriented case, one can observe that higher forces are required in double slip oriented samples to reach the same stress level. For instance, 35 MPa are reached in single slip by applying 3.5 N whereas ∼ 6 N are needed in both double slip orientations. The harder behavior of double slip orientations is also captured experimentally (see Figure 5.4).

The three graphs show similar change in the stress-force slope. At low initial displacements the slope between the stress and the force is steep. At some point (red dots) the slope between stress and force lowers dramatically and the stress in the center of the thin area is rather constant for all forces. The transition does not correspond to an increase in displacement. The reason behind this is that the saturation value of the primary slip resistance parameter has been reached in the center of the thin area (see appendix E for the evolution of the slip resistance parameter used in the simulation in the case of single slip). In other words, the center of the thin area cannot computationally harden further and the stress is going to be constant in the following cycles. Beyond that cycle the imposed strain amplitude has to be also accommodated by the surroundings, which continue hardening.
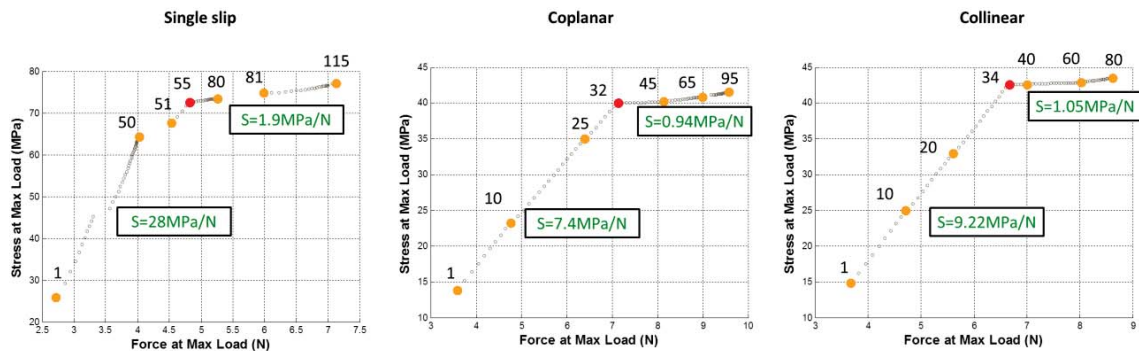
Figure 5.6 Relationship between simulated stress and force for single slip, coplanar and collinear oriented samples (courtesy of N. Grilli)

5.3.2   Evolution of total strain and its distribution

Single slip orientation

Figure 5.7 compares the simulated total strain (grey line) and experimental strain (blue line) versus the number of cycles of single slip oriented samples. The experimentally measured strain is obtained using the relationship given by $eq.3$ (section 2.1.1). The red arrows point to the cycles where an increase in displacement amplitude has been applied and the colored points correspond to particular cycles that were also shown in Figure 5.6. The corresponding total strain distribution is displayed after specific cycles in Figure 5.8.
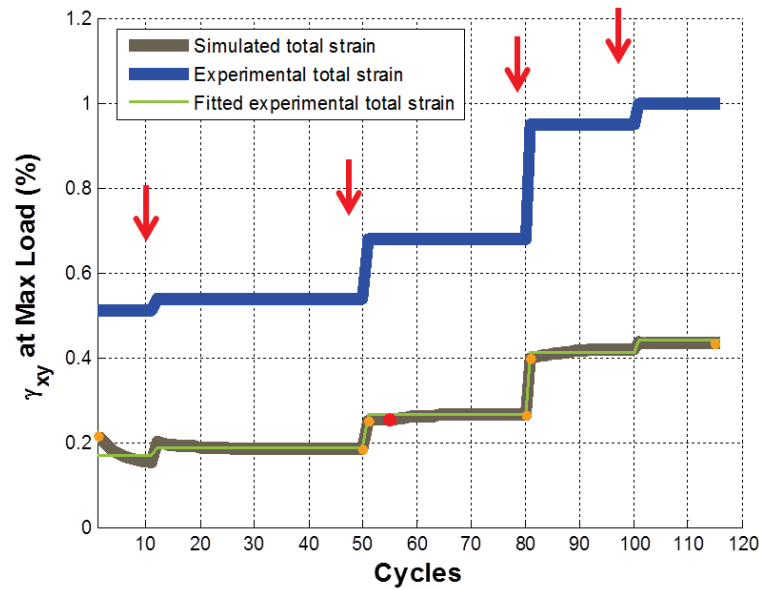
Figure 5.7 Evolution of the computed and experimental γ_{xy} strain with the cycles of single slip orientation (courtesy of N. Grilli)
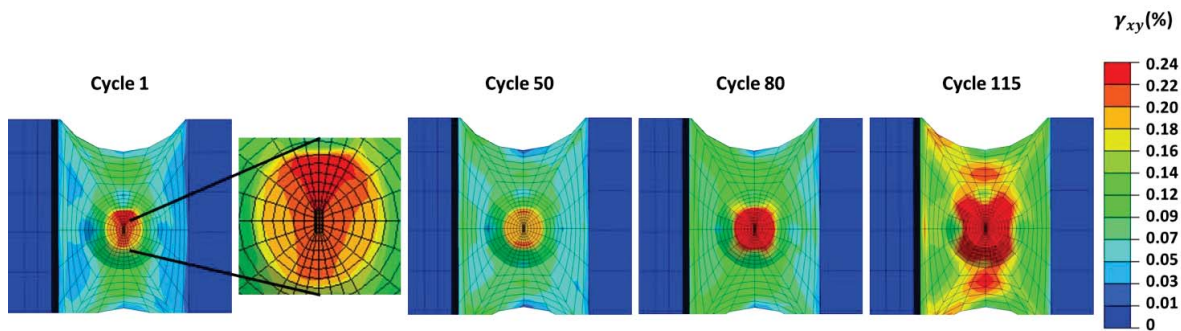
Figure 5.8 Evolution of total strain distribution at different cycling stages in single slip oriented samples (courtesy of N. Grilli)

Overall one can say that upon cycling the total strain values are rather constant. Closer inspection reveals that at low displacement amplitudes the simulated strain tends to decrease (cycle 1 to 30 without considering the jump after increased displacement amplitude) and eventually stabilizes (cycles 30 to 50). During those cycles the central point of the thin area hardens but the slip system resistance has not reached the saturation value (red point). The rate is related to the cumulative resolved plastic strain. Concurrently Figure 5.8 shows that after the first cycle the strain distribution is not uniform across the circular thin area. In the smaller area where Laue scans were performed (shown in a zoom-in) the strain is however homogeneous. During the following cycles the strain is redistributed in the thin area (see cycle 50).

Once the saturation value of the primary slip resistance parameter has been reached in the center (cycle 55), the stress in the center of the thin area remains constant (see Figure 5.6) but the surroundings continue hardening. As in the surroundings the primary slip resistance parameter has not reached the saturation value, its strain decreases (analogue behavior as during the initial cycles in Figure 5.7). Thus in order to maintain equilibrium between the central point and its surroundings, the strain in the thin area has to increase (see cycle 55 on). Note that in the single slip case the increase is not so important. The strain distribution in Figure 5.8 evidences a uniform distribution in the circular thin area (see cycle 80). For the highest displacement amplitudes (cycle 81 to 120) the thin area cannot accommodate the imposed deformation anymore and the strain distribution extends to

the thicker area (see cycle 115). It is in these cycles (from 80 to 120) that experimentally a higher hysteresis in the experimental mechanical data is observed (see Figure 3.2).

As it can be observed in Figure 5.7 after step 50 the computed strain exceeds the initial computed strain. This is in good agreement with the microstructural evolution observed in the experimental results (see Figure 3.3 and Figure 3.19). The initial microstructure is accommodated after the first map at step 11 due to the imposed strain. The changes from map 11 to 50 are however minor. After cycle 50, the evolution in lattice rotation is more pronounced: the strain is higher than that initially imposed and it maintains or increases slowly during the last 70 cycles (from cycle 50 to 120).

Comparing the simulated and experimental curves they are very similar, except that the absolute values differ. Both curves scale linearly as shown by the green fitted line in Figure 5.7 (see appendix F for the linear fit). Note that the difference between the experimental and simulated strain, force and stress curves can find their origin in many factors such as small differences in overall sample geometries, or differences in the parameters used in simulations. Thus, the strain values provided in Figure 3.2 and Table 3.2 have to be taken indicatively and not absolute.

Double slip orientations

Figure 5.9 shows the evolution of the computed and experimental total strain for coplanar and collinear oriented samples. Same representation system as in Figure 5.7 is used. The corresponding total strain distributions are displayed after specific cycles in Figure 5.10.

The initial strain amplitudes in both orientations are similar and almost double to that imposed in single slip. As a consequence the strain distribution after cycle 1 extends even to the thick areas (see Figure 5.10-cycle 1). During the first 30 cycles in both double slip orientations the computed strain decreases. The trends in both orientations are rather similar and after 40-45 cycles both orientations show similar strain distribution and value.
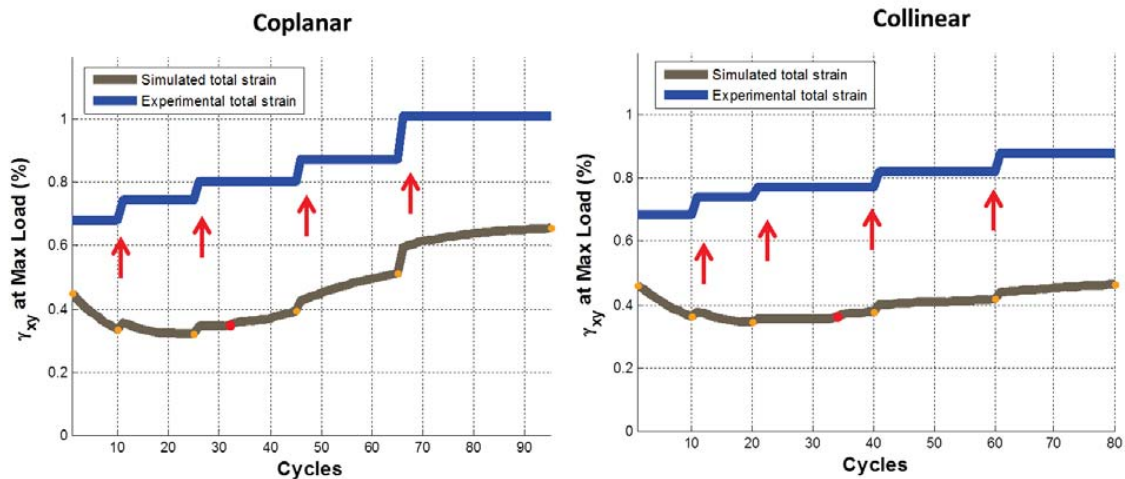
Figure 5.9 Evolution of the computed and experimental γ_{xy} strain with the cycles of double slip orientations (courtesy of N. Grilli)
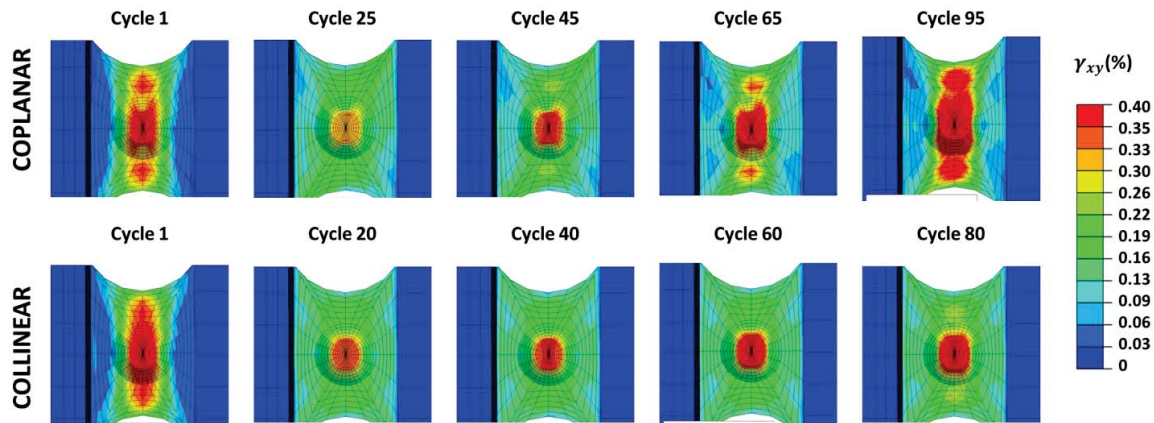
Figure 5.10 Evolution of total strain distribution at different cycling stages in coplanar and collinear oriented samples (courtesy of N. Grilli)

Due to the imposed displacement values (compare the jumps in the experimental total strain blue lines) the computed strain evolution at higher amplitudes differs.

-   The strain amplitudes in the coplanar sample are higher than in the collinear sample, and therefore the strain increases faster. After cycle 65 the strain distribution is extended to the thicker part. Besides, after the last amplitude increase the strain value goes far beyond the initial imposed strain. This is evident in the strain distribution at cycle 95 shown in Figure 5.10. Interestingly, the misorientation map in Figure 4.3 can follow the change. Additionally, the hysteresis in the last series (cycles 66-95) is more pronounced (see Figure 4.2).

-   In the collinear case the strain evolution is steadier: the strain at cycle 80 does not exceed the initial imposed strain value and the strain distribution is concentrated in the thin circle. The misorientation map in Figure 4.16 does not reveal any transformation either. At the same time the hysteresis in mechanical data is rather similar in all series (Figure 4.15).

5.3.3   Summary

The information provided by simulations underline the importance of a good design of the multistep mechanical test. The first cycle determines the strain threshold for observing further microstructural changes. Until the initial imposed strain is not surpassed, the spatially resolved maps do not evidence significant lattice rotation evolution. Additionally, the orientation of the crystal also plays a role as the hardening behavior is different and therefore the multistep mechanical test has to be adapted to each condition to obtain similar degree of evolution. In this sense it would have been a better approach to start with a lower initial strain amplitude in double slip oriented cases and increase the amount of cycles in each series at higher amplitudes before reaching the restrictive force limit of the device.

On the other hand the complex evolution of the computed strain evidences that the simple geometrical relationship between displacement and strain given by $eq.$ 3 does not capture absolute values, however in some cases it captures well the trends. At small imposed displacements (single slip case) and when the strain is rather steady at high amplitudes (collinear case), both experimental and simulated curves can be linearly scaled. Depending on the initial strain threshold, the relationship during initial cycles may fail. When the strain evolution at high amplitudes is not constant (coplanar case), the curves cannot be fitted linearly. See appendix F for the linear fits.

5.4 Early formation of dislocation patterning: single slip orientation

The so-called channel-vein dislocation structure is expected for the single slip orientation under the applied shear strain conditions explained in section 3.3. The veins consist mainly of edge dipole bundles of primary dislocations that are aligned approximately perpendicular to the primary slip direction and extended in the third dimension surrounded by GNDs. The channels are almost dislocation-free regions, where dislocations travel back and forth during cycles, having low SSDs and no GNDs.

In section 3.3, an early transition from homogenous to heterogeneous microstructure is observed. The evolution of the misorientation and GND traces are given in Figure 3.3 and Figure 3.9 respectively, where the formation of region **F** can be followed. After 120 cycles, an area misoriented predominantly around Z-axis by 0.22° and with GND walls in its perimeter is formed from a low misoriented background. Questions such as "How is this region formed?" or "What does it represent?" are discussed in this section.

5.4.1 Are initial GNDs dominating the formation of rotated regions?

Figure 5.11 shows the apparent GND traces (in white) at cycles 0, 11, 50, 80 100 and 120 on top of the misorientation map after 120 cycles, where rotated region **F** is clearly defined. As can be observed, the physical location of the initial GND traces does not match with region **F**. This is different for region **B** where the rotated area after 120 cycles is clearly related to the presence of pre-existing immobile dislocations. The evolution of the GND traces shows a clear redistribution of the pre-existing GNDs and the appearance of new GNDs that are responsible for the evolving rotated regions. The location of these regions can be determined by pre-existing dislocations or simply evolving from the accumulation of new GNDs such as region **F**. Thus, the presence of the initial mobile/immobile dislocations can play a role in the microstructural evolution as they can act as pinning points or dislocation sources and participate in the development of dislocation ensembles.
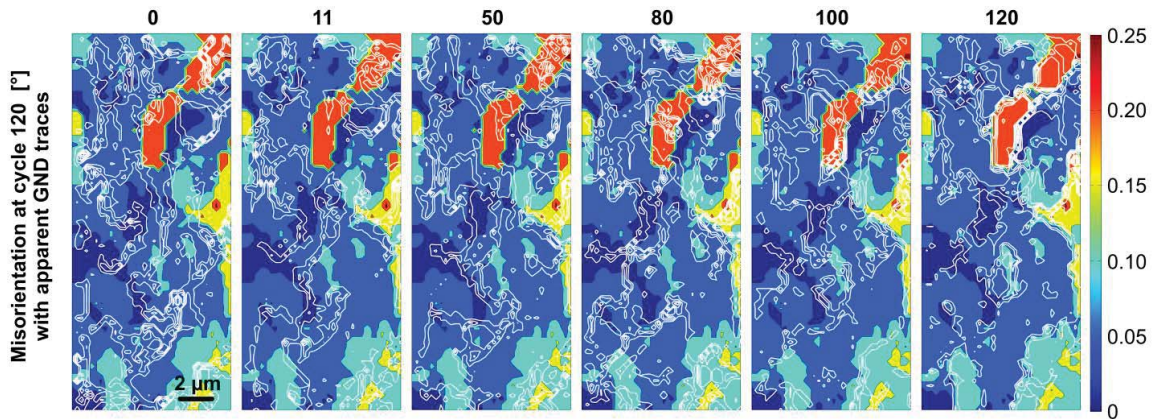
Figure 5.11 Evolution of the GND density traces at cycles 0, 11, 50, 80, 100 and 120 on top of the misorientation map after 120 cycles

5.4.2 Understanding dislocation microstructure in region **F**

A bottom-up process is going to be followed in order to understand the formed dislocation microstructure in region **F**. First the evolution of the Laue reflection shown in Figure 3.11 for position **1F** (inside region **F**) is discussed. Next, the observed misorientation, rotation, lattice curvatures and GND traces are interpreted in terms of dislocation structures. Finally, an overall picture of the evolved dislocation microstructure is suggested.

Implications derived from the evolution of Laue reflections

Laue reflections provide insights into lattice rotations and defect organization inside the illuminated volume. In Figure 3.11, the (400) peak obtained in position **1F** at step 0 is a representation of a single crystal with some imperfections in the illuminated volume. After cycling, the peak gets fragmented into several sub-peaks, and the

position of the new sub-peaks is changing when the misoriented region **F** is forming. That means that the illuminated volume has obtained several misoriented microscopic crystallites/domains and that the crystal has a mosaic structure along the integrated volume. The higher the shift the higher the misorientation value between the crystallite and the initial orientation. After 120 cycles, the reflection shows a main strong peak shifted from the initial position with some residual traces. This means that part of the volume has the same misoriented orientation and some crystallites are less misoriented comparing to initial orientation. The rotation direction of the new crystallite is mainly about *Y*-axis according to Figure 3.13 and Figure 3.14. A schematic illustration of the evolution of the diffracting volumes at cycle 0, 100 and 120 in position **1F** of region **F** is shown in Figure 5.12.
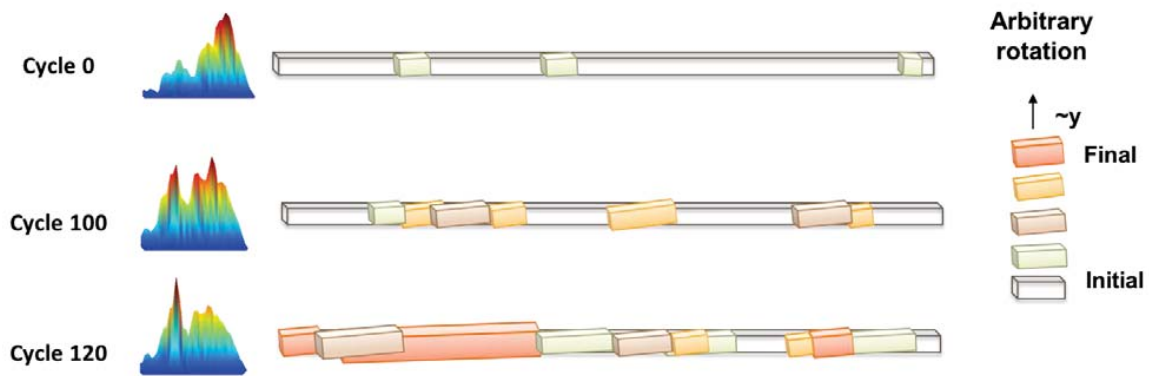
Figure 5.12 Illustration of microstructural evolution of position 1 in region **F**

The interpretation in terms of microstructural evolution can be derived from the observations made by Hancock and Grosskreutz in tension-compression fatigued copper single crystal oriented with 0.5 Schmid factor on the primary slip and 0.47 on the critical slip (Hancock and Grosskreutz, 1969). After 4¼ cycles only primary slip is activated and as it can be observed in Figure 5.13, the microstructure consists of bundles of dislocations separated by almost dislocation free regions. These bundles tend to be oriented along the $[1\bar{2}1]$ direction, which correspond to the X-ray beam direction as drawn in the figure. The alignment at this early stage is not perfect though. It is reported that the majority of the observed bundles are formed by primary edge dislocations, which over a portion of their length form dipoles. They observe the presence of traces belonging to critical and conjugate slip, which interact with the primary dislocations and may be the cause of the truncation of the bundles. After 20 cycles, an increase in dislocation density (both primary and secondary) is observed and the bundles get extended along their length by continued entrapment.

This process is compatible and reasonable with the observations derived from the evolution of the Laue reflection: the dislocations pile up with the cycles and eventually extend to almost the whole length of the thickness while increasing density. The fact that the main rotation is observed around *Y*-axis (Figure 3.13 and Figure 3.14) suggests that the bundle of piled up dislocations is not perfectly aligned to the *Z*-axis. This was also noted by Yang et al. (Yang et al., 2001) who followed the evolution of dislocation configurations by the ECCI technique. It was observed that the arrangement of dislocation distributions gradually transforms with increasing cycle numbers before the saturated vein-channel structure is formed. They reported that the initial distribution of dislocations after 40 cycles can be quite disordered comparing to the saturated stage.
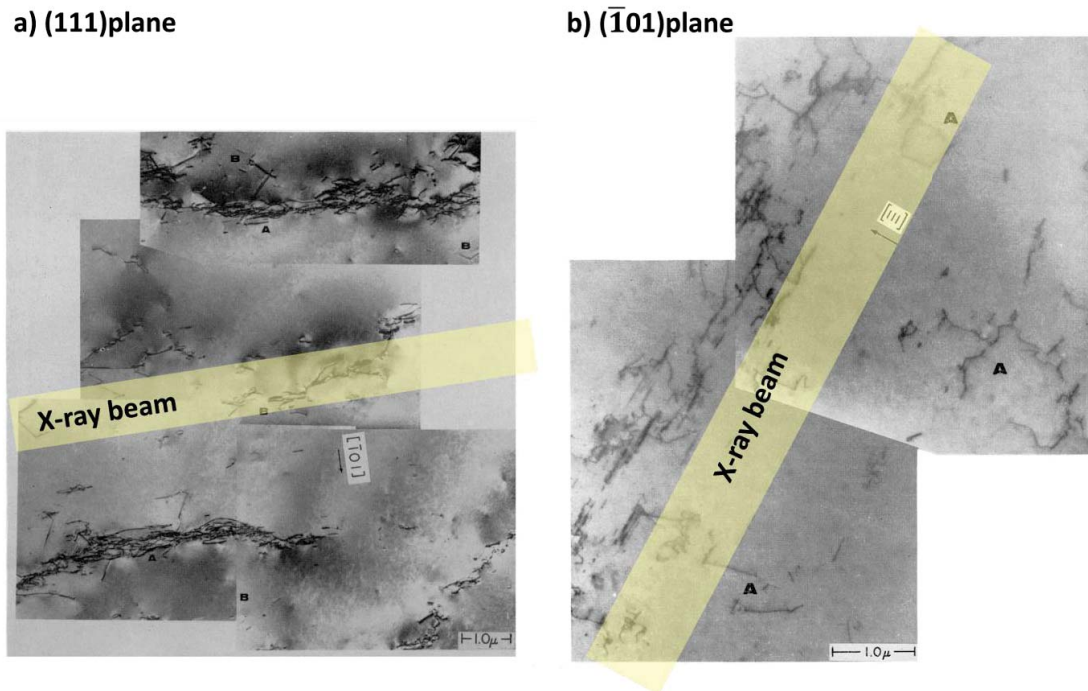
Figure 5.13 TEM images of dislocation structures after 4¼ cycles of copper at γ_{Tot}=0.75% after (Hancock and Grosskreutz, 1969)

The evolution of the dislocation structure corresponding with our Laue analysis is schematically shown in Figure 5.14. At the beginning there are a few dislocations due to the sample preparation: some mobile and other immobile for our shear set-up. After the first 100 cycles, the mobile ones are swept away and primary edge dislocations start piling up in form of dipoles by pinning to the immobile dislocations. After 120 cycles, their density has increased and part of the illuminated volume has the same orientation slightly different form the initial one due to the distortion created by almost perfect horizontal dislocations. The relative narrow orientation spread of the new orientation (Figure 3.14) can be ascribed to the formation of dipoles in the veins.

Figure 5.14 Illustration of the evolution of dislocation pile-up in region **F** (position 1)

Implications derived from the rotation and GNDs

Figure 5.15 shows the distribution of misorientation, ω_x, ω_y and ω_z, apparent GND density and the length of GNDs in region **F**.
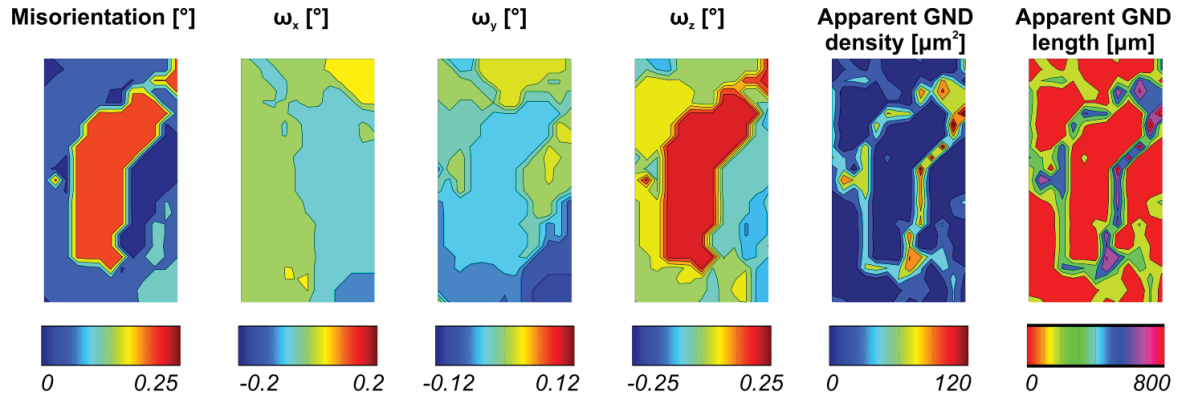
Figure 5.15 Misorientation, ω_x, ω_y and ω_z, rotations, apparent GND and GND length maps of region **F** after 120 cycles

The accumulation of edge dipoles on the primary (111) slip plane with Burgers vectors $[\bar{1}01]$ causes rotation about an axis parallel to the $[1\bar{2}1]$ direction –i.e. the dislocation line direction (Mughrabi, 2006a). In Figure 5.15-b-c-d it can be observed that the major rotation of region **F** is in fact about the Z axis= $[\bar{1}2\bar{1}]$. Still, the alignment of dislocation ensembles in other areas of the sample is expected to evolve during more cycles and to continue till saturation stage (Yang et al., 2001).

The amount of misorientation observed in our Laue analysis is in good agreement with the range of values reported by other authors (Mughrabi, 2006b; Wilkens et al., 1980). A misorientation angle of 0.33° around the primary edge dislocation line was reported for a copper single crystals deformed in the PSB formation plateau regime. The misorientation for a vein is expected to be lower (Mughrabi, 2006a). Assuming that the primary edge dislocations are arranged in a way that they form a wall in the perimeter of region **F**, the misorientation angle θ_m across the boundary is defined by *eq.* 22 (section 2.3.5).

Figure 5.15-a shows that $\theta_m = 0.22°$ which leads to a mean distance of 66 nm between dislocations. In addition, Figure 5.15-f gives an average length of ~500-600 μm in the perimeter of region **F**. In the ideal case where dislocations would be totally extended along the sample's thickness (~30 μm) 16 to 20 edge primary dislocations would be arranged in ~0.5×0.5 μm² area (defined by the scanning step size and X-ray beam size). Assuming a wall distribution, this would correspond to a distance of 25-32 nm between dislocations. In spite of all assumptions these values are in a relatively good agreement with a 30 nm dipole distance observed in saturation (Neumann, 1987; Suresh, 1998). According to the observations of Buchinger et al. these values are independent of the applied strain amplitude (Buchinger et al., 1985). Moreover, the fact that region **F** does not contain internally GNDs but is surrounded by a GND wall (Figure 5.15-e) supports the description of accumulation of edge dipoles, since the latter do not contribute to curvature (Arsenlis and Parks, 1999).

Implications derived from the distribution of lattice curvatures in region F

Veins are reported to have a characteristic width of 1.5 μm in saturation (Laird et al., 1986). The feature observed in region **F** is however larger. In order to derive a geometrical interpretation of region **F** the lattice curvatures plotted in Figure 3.6 are analyzed.

κ_{zx} and κ_{zy} can be directly attributed to the presence of primary edge GND walls in the boundary of region **F** as drawn in Figure 5.16. From the elastic distortion field of an infinite edge dislocation with its line along Z it can be derived that only κ_{zx} and κ_{zy} should have non-zero values (see appendix G).
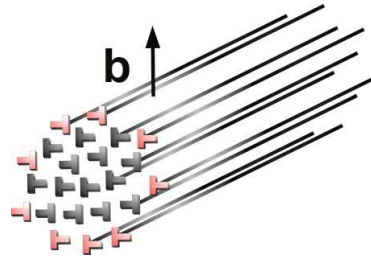
Figure 5.16 Schematic of dislocations forming dipoles in a vein. Excess of dislocations around the vein contribute to GNDs

Therefore if the vein would consist only of long edge dislocations in dipoles, the other lattice curvature components should be zero. It is however not the case in our observations, in fact κ_{zx} and κ_{zy} have lower values comparing to the other components.

In order to understand this, simulations have been done by N. Grilli for four configurations:

1- A straight bundle
2- A bundle inclined towards the *Y*-axis (*Y*-inclined bundle)
3- A bundle inclined towards the *Y*- and the *X*-axis (*Y&X*-inclined bundle)
4- Configuration where two bundles, both inclined towards the *Y*-axis (Two inclined bundle)

The schematic and geometrical details are shown in Figure 5.17.

		Straight vein	Y-inclined vein	Y&X-inclined vein	Two inclined veins
Dimensions					
	Projected height (h)	1 µm	2 µm	2 µm	4 µm
	Height of each cuboid	h_1= 1 µm	h_1= 1 µm h_2= 2 µm h_3= 1 µm	h_1= 1 µm h_2= 2 µm h_3= 1 µm h_4= 1 µm	h_1= 2 µm h_2= 2 µm
	Projected width (w)	1µm	1 µm	2 µm	1µm
	Width of each cuboid	w_1= 1 µm	w_1= 1 µm w_2= 1 µm w_3= 1 µm	w_1= 1 µm w_2= 1 µm w_3= 2 µm w_4= 1 µm	w_1= 1 µm w_2= 1 µm
	Projected length (l)	1 µm	1 µm	1.5 µm	2 µm
	Length of each cuboid	l_1= 1 µm	l_1= 0.375 µm l_2= 0.250 µm l_3= 0.375 µm	l_1= 0.375 µm l_2= 0.250 µm l_3= 0.375 µm l_4= 0.500 µm	l_1= 2 µm l_2= 2 µm
	Y-inclination (α_y)	-	76°	76°	26.5°
	X-inclination (α_y)	-	-	69°	-

Figure 5.17 Schematic and geometrical details of simulated bundles

As shown in Figure 5.18, the bundles are embedded in a 5x5x'l' μm³ block (Block1) where 'l' is different for each configuration (refer to Figure 5.17). The block is embedded in another 10x10x'l' μm³ block (Block2) as illustrated in Figure 5.18. Dislocation-based plasticity model based on (Grilli et al., 2015) is applied to Block1 and von Mises yield criterion (Mises, 1913) is applied to Block2. Periodic dislocation fluxes are imposed to avoid size effects and the displacement is applied in Block2 as shown by the arrows. Each configuration is subjected to one full cycle at applied strain of ~0.50%, after which the primary dislocations are trapped around the immobile bundle, a configuration that resembles the one in Figure 5.16.
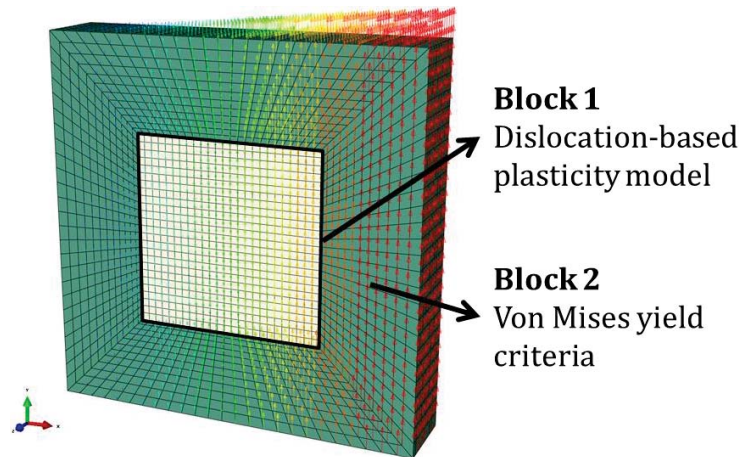
Figure 5.18 Applied simulation geometry and conditions

Figure 5.19 shows the rotation about *Z*-axis and apparent GND density distributions for the different bundle geometries (see Figure 5.17 and text above for description of each configuration). All of them show positive rotation about *Z*-axis but the rotation value is higher for the straight bundle than for the case of two inclined clusters. The configurations of *Y*-inclined and *Y&X*-inclined bundles have intermediate rotation values. Interestingly, the apparent GND density maps show that an inclination across the thickness is necessary in order to have apparent GNDs in the lateral walls. Pure straight configuration only has apparent GND density at the top and bottom of the rotated area. In the special case of two inclined clusters the apparent GND density has no clear structure.
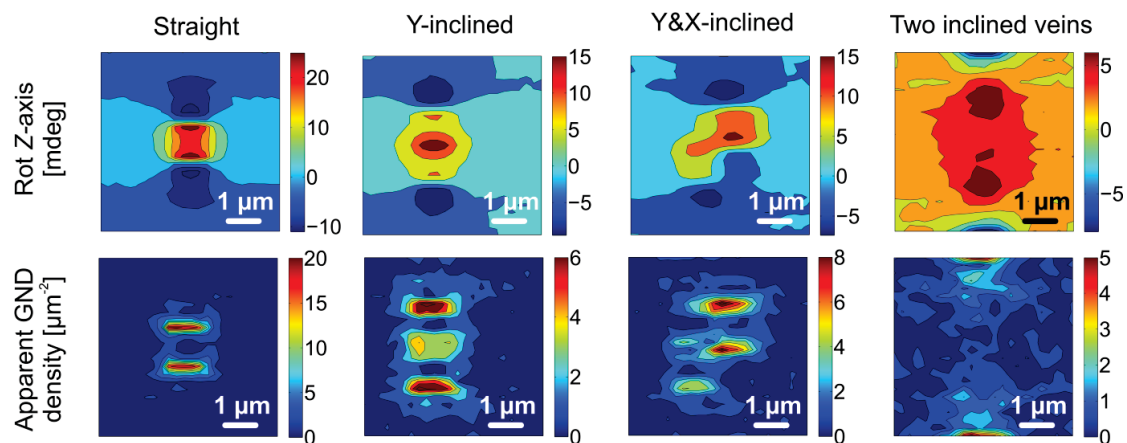
Figure 5.19 Rotation along Z (a) and apparent GND density (b) of different simulated bundle geometries (Courtesy of N. Grilli)

The statistical distributions of each lattice curvature and dislocation density tensor components of each bundle configuration are graphically depicted as boxplots in Figure 5.20 (see Appendix D for detailed information about statistical representation as boxplots). It can be observed that the distributions of most of the components (κ_{xx},

κ_{xy} κ_{yx}, κ_{yy}, α_{zz} and $\alpha_{xx} - \alpha_{yy}$) are very similar in all the geometries: the values are slightly higher in the *Y*-inclined case than in the other configurations. κ_{zx} and κ_{zy}, on the other hand, are extremely sensitive to the bundle configuration. Their outlier values are highly influenced (at least a factor of two) when changing the geometry from straight to any of the other three configurations. These results can explain what is experimentally observed.
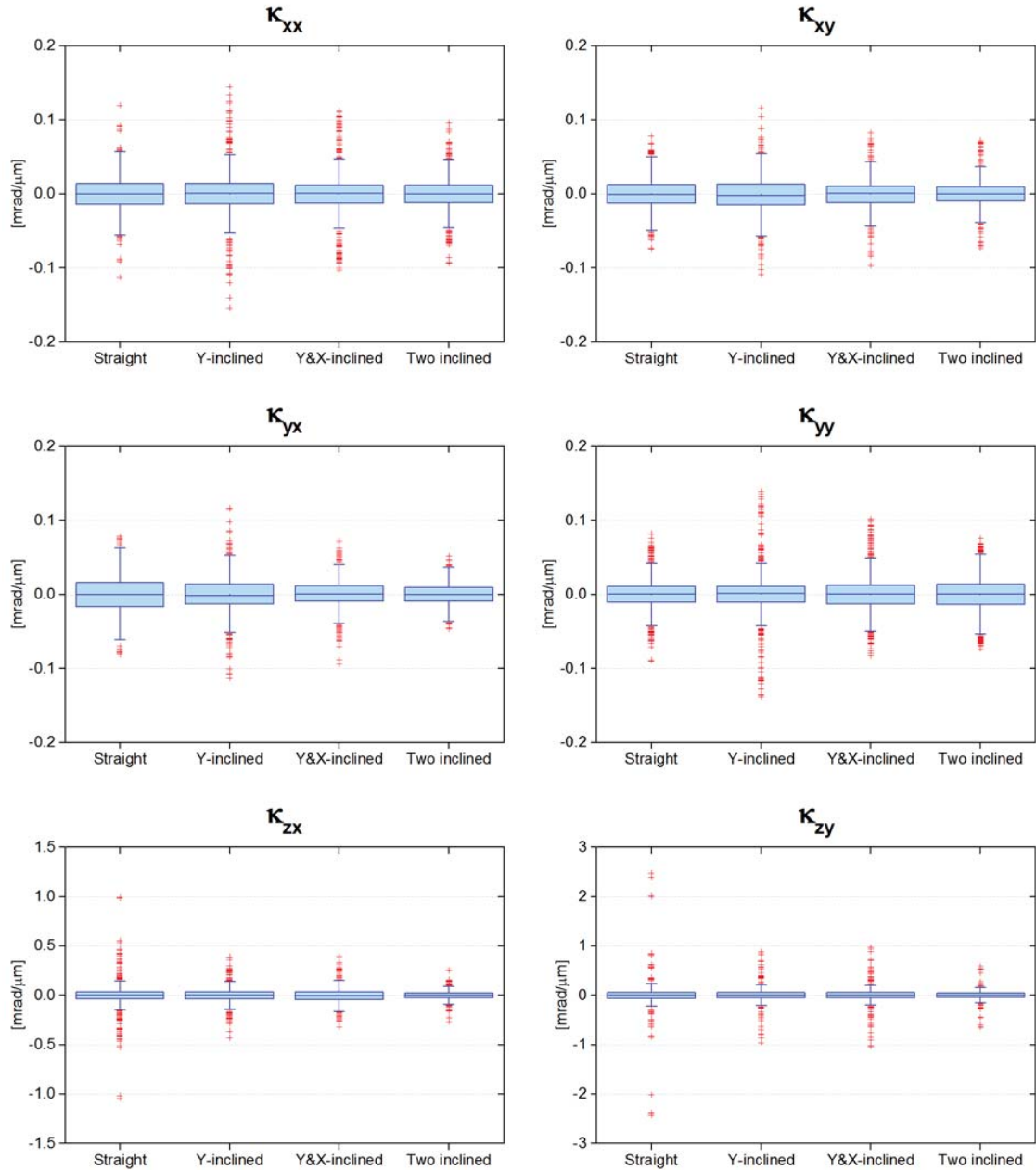
Figure 5.20 Influence of different geometries in the lattice curvature and dislocation density tensor components

The distribution of each lattice curvature components of a *Y&X*-inclined bundle is going to be analyzed further. A new simulation has been done on a longer bundle than that shown in Figure 5.17. The schematic and geometrical details are shown in Figure 5.21 where the bundle can be divided in 4 sections, each one 1 µm long. The first section is straight in *Z*-axis, section 2 is inclined in *Y*-axis, section 3 is inclined in *X*-axis and the last section is straight in *Z*-axis.

Dimensions of long Y&X-inclined vein	
Projected height (h)	2 µm
Height of each cuboid	h_1= 1 µm h_2= 2 µm h_3= 1 µm h_4= 1 µm
Projected width (w)	2 µm
Width of each cuboid	w_1= 1 µm w_2= 1 µm w_3= 2 µm w_4= 1 µm
Projected length (l)	4 µm
Length of each cuboid	l_1= 1 µm l_2= 1 µm l_3= 1 µm l_4= 1 µm
Y-inclination (α_y)	45°
X-inclination (α_y)	45°
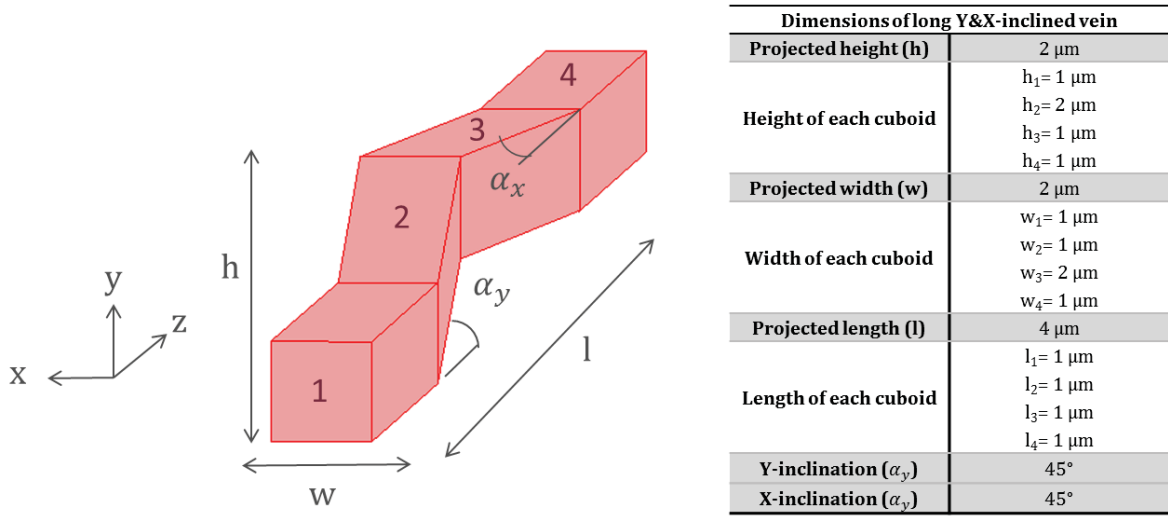
Figure 5.21 Schematic and geometrical details of long *Y&X*-inclined bundle configuration

Figure 5.22 shows the distribution maps of each lattice curvature component for the *Y&X*-inclined long bundle configuration. In the right side of each box a schematic of each lattice is shown. The experimental results are added to the same figure for easier comparison. One can observe several similarities when comparing the simulated and experimental distributions:

- Simulated κ_{xx} and κ_{zx} components have vertical boundaries in the lateral walls of the bundle. Similar to experimental results, the signs are reversed in the left and right walls. The distribution of the κ_{yx} component is not as defined as the one of κ_{xx} and κ_{zx} components, but faint left and right walls can be distinguished. The sign is, however, reversed comparing to experimental values. This is related to the average *Y*- rotation field obtained (see appendix H) and is discussed below.

- Simulated κ_{xy} and κ_{zy} components have horizontal boundaries in the upper and lower walls of the bundle. The signs are reversed in the upper and lower walls, and the signs match when comparing to experimental results. The distribution of κ_{yy} also shows reversed signs in the upper and lower walls but the sign and distribution do not have strong correlation with the experimental observations.
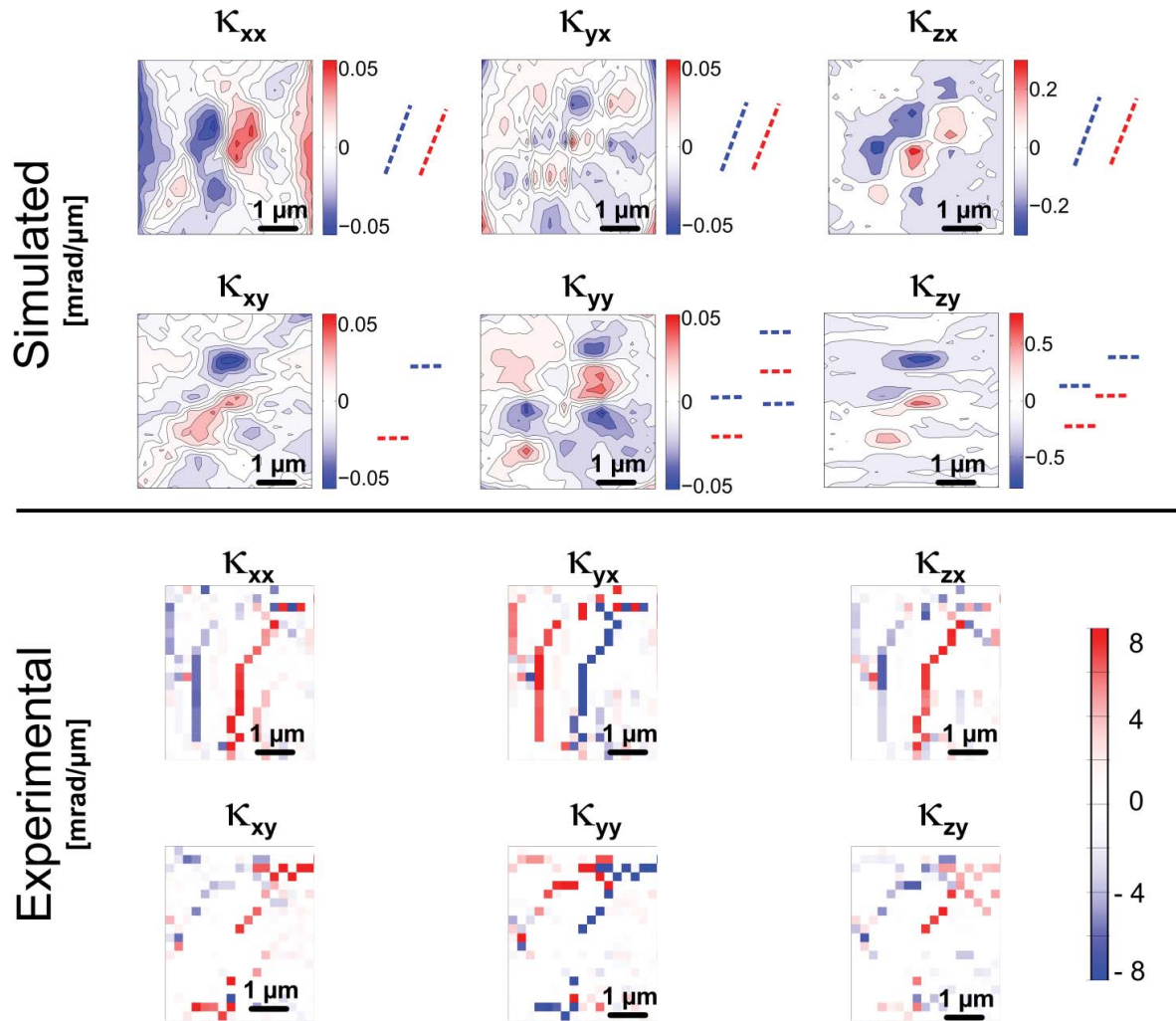
Figure 5.22 Distribution of lattice curvature components of the simulated *Y&X*-inclined long bundle (courtesy of N. Grilli) and summary of experimental results

Figure 5.22 also shows some differences between simulated and experimental data. While all the experimental maps do not show any trace inside region **F**, some of the simulated lattice curvatures do. The discrepancy relies on the fact that simulated maps are consequence of integration along the depth, which can be sectioned. Figure 5.23 shows the sectional maps of all lattice curvature components. The sectional rotation distributions are given in appendix H.

One can observe that in all sections the simulated κ_{zx} and κ_{zy} show localized traces forming the left-right walls or upper-lower walls of the vein with same sign as in experiments. The values are rather similar in all sections and they are higher compared to the other lattice curvatures. The greatest variation is observed in section 3 where the values of κ_{zx} double those of the other sections. This corresponds to the part where the vein is inclined along *X*-axis and the *X*- and *Z*-rotation are the highest (see appendix H).
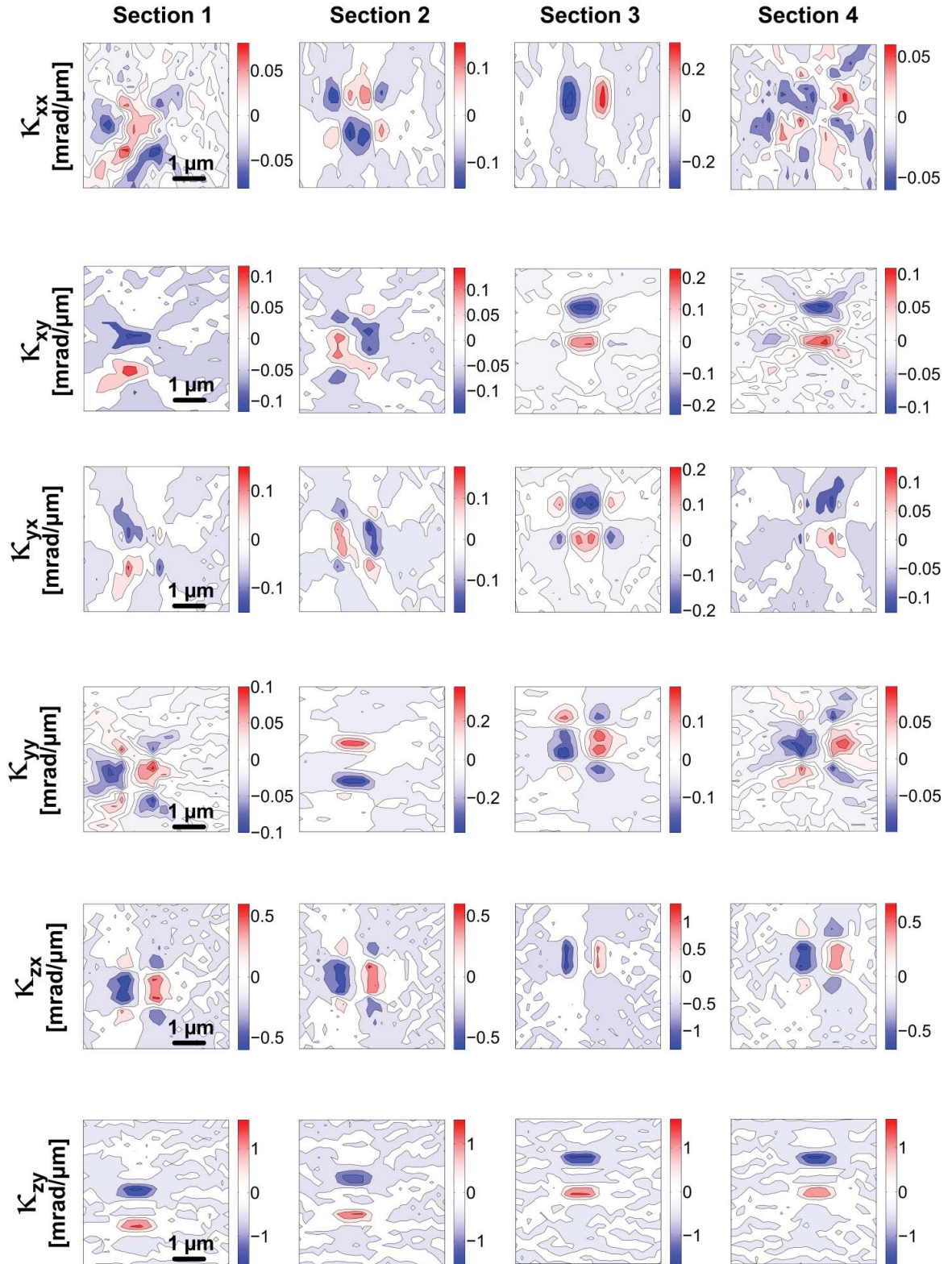
Figure 5.23 Sectional κ_{xx} and κ_{zy} lattice curvature maps of a *Y-X*-inclined long bundle (courtesy of N. Grilli)

When analyzing the maps of the other four components κ_{xx}, κ_{xy}, κ_{yx} and κ_{yy}, it is found that the distribution of the lattice curvatures is different for each cuboid:

- There is no standard structure of κ_{xx} in the straight sections (1 and 4) where the vein is located: in section 1, for instance, the inner part of the vein has positive κ_{xx} values surrounded by negative values outside the vein; in section 4 the left and right walls have negative and positive κ_{xx} values respectively. In the Y-inclined section 2, the κ_{xx} traces are mainly in the upper and lower walls due to the gradient induced by the inclination. In the X-inclined section 3, the lattice curvature is only localized in the left and right walls, and the values are highest. Besides they match in sign with those measured experimentally: left negative, right positive. Therefore section 3 resembles more the experimental data.
- In sections 1, 3 and 4, κ_{xy} mark the upper and lower walls of the vein. The signs are in agreement with experimental observations. The κ_{xy} values are highest in section 3, similar as what was observed for κ_{xx}. In the Y-inclined section 2, the κ_{xy} traces are localized in the left-right walls of the vein due to the gradient induced by the inclination.
- κ_{yx} shows similar values for all four sections. In the straight sections (1 and 4) there is no defined structure where the vein is located. In the Y-inclined section 2, the κ_{yx} traces are located in the left-right walls similar to those observed experimentally and with the same signs. In the X-inclined section 3, on the other hand, the κ_{yx} traces mark the upper-lower walls of the vein. This difference is induced by the particular inclination in each section, a piece of information that is lost when analyzing the averaged lattice curvature distribution. This causes the dissimilarities between the experimental and averaged computed lattice curvature maps (see Figure 5.22).
- The κ_{yy} traces in the straight sections (1 and 4) and in the X-inclined section 3 have non-zero values in the left-right walls. Their values are however lower when comparing to those of Y-inclined section 2. There, the κ_{yy} traces mark the upper-lower walls analogue to the experimental data, and they have same sign. Similar as for κ_{yx}, this information is lost in the averaged plots shown in Figure 5.22.

In summary, the sectional analysis of the bundle reveals that vertical and horizontal inclinations are required to explain the experimentally obtained lattice curvature distributions. Even if with Laue micro-diffraction technique in transmission mode, one cannot resolve the sectional distribution of the lattice curvatures along the depth because the information obtained is averaged, synergy with simulations helps to elucidate the obtained results and give an interpretation.

Final interpretation of region F

The comparison between simulations and experiments lead to a picture wherein region **F** corresponds with the onset of a vein formation. The vein is formed by primary edge dipoles extended partially along the thickness of the sample and is slightly inclined vertically and horizontally in the third direction. A schematic is given in Figure 5.24. The saturation stage has not been reached because a characteristic feature of that phase is the appearance of slip bands in the surface (Grosskreutz, 1971), which have not been detected in out sample.

Figure 5.24 3D illustration of the shape of the vein in region **F**

5.5   Assessment of the transmission Laue micro-diffraction methodology

The method here developed is a quasi 2D approach. The signal is integrated over the thickness of the sample and the microstructural evolution is followed based on the crystal orientation obtained by indexing each diffraction pattern according to the maximum intensity criterion. The center of mass criteria cannot be used to define the position of the peaks since this in insensitive to the evolution of emerging regions (see Figure 2.23). As an illlustration the evolution of misorientation angle of single slip oriented S1-L sample has been calculated using the center of mass criteria and plotted in Figure 5.25. Comparing to Figure 3.3 there is no clear evidence of formation of region **F** and one can neither follow the fragmentation observed in the upper right corner region **B**.
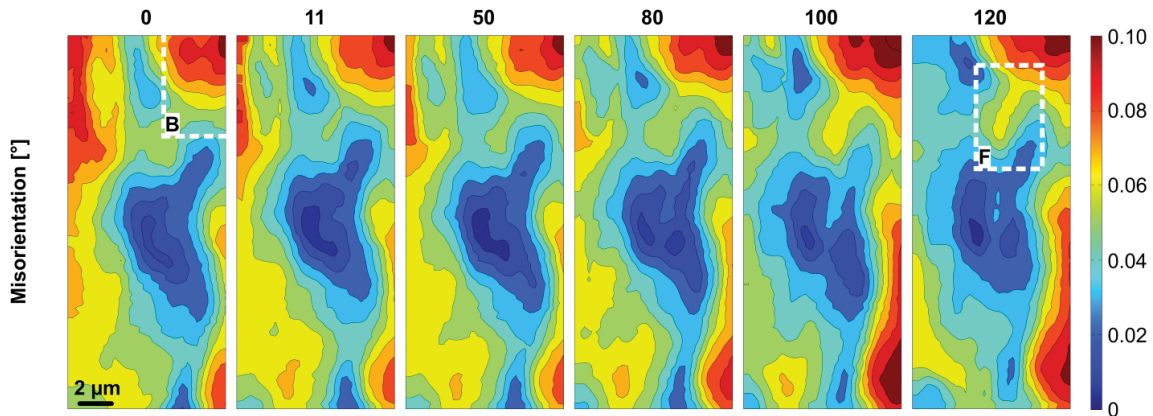
Figure 5.25 Evolution of misorientation angle of sample S1-L using center of mass criteria

The principle of the used methodology is rather similar to EBSD: once the averaged orientation in each point is obtained, it is compared to a fixed reference (misorientation map and ω_x, ω_y and ω_z maps) or to the neighbouring point (distribution of lattice curvatures, dislocation density tensor components and apparent GND traces). The methodology when applied in transmission can be source of several errors and the following points have to bear in mind:

-   X-ray micro-diffraction could underestimate GND densities due to the relatively coarse size and larger beam size comparing to EBSD. Wright et al. (Wright et al., 2015) showed that GND values tend to increase with decreasing orientation precision and that this effect is notorious at <200 nm step sizes. In our experiments, a step size of 300 nm is used.
-   As the X-ray beam size is larger than the step size used (~3:1 ratio) there is an overlap in the patterns. Tong et al. (Tong et al., 2015) however reported that pattern overlap in HR-EBSD measurements does not create significant artefacts in residual elastic strains and GND density near boundaries, even at step sizes as small as 200 nm.
-   By working in transmission mode the GND densities could on the other hand be overestimated. The disorientations between two neighboring points, A and B, are calculated. These points are adjacent in the X-Y plane (300 nm apart) but may not be in the third direction due to the thickness of the sample (in this thesis ~ 30 µm).
-   The elastic strain gradient is ignored when calculating the GND densities. Several authors have reported that its omission affects the measured dislocation density tensor (Acharya and Knops, 2013; Mohamed et al., 2015). It is reported that for a complete understanding of the underlying dislocation structure the elastic strain gradient should be measured.

On the other hand, the advantage of working in Laue transmission is that each diffraction pattern is collected in a particular (x,y) position which makes easier the determination of spatial maps as no DAMX is required (Larson et al., 2002; Yang et al., 2004). This is a huge benefit particularly for thin samples. In addition, the fast acquisition time of the DECTRIS EIGER 4M detector allows acquiring spatially resolved maps in a relatively short time. As a

consequence the evolution of the microstructure can be followed at several stages of fatigue and it is not restricted to limited scans as it is the case with 3D X-ray Laue diffraction (Mohamed et al., 2015). One of the main drawbacks is of course that the diffraction patterns cannot be resolved along the integrated depth.

All the 2D maps shown in Chapter 3 and Chapter 4 provide only part of the information acquired by Laue micro-diffraction technique since each diffraction pattern harbors the information about the integrated volume. Even if the integrated signal cannot be resolved in the beam direction, the orientation spread in the thickness can be calculated using the template matching approach suggested by Gupta et al. (Gupta and Agnew, 2009). The technique has shown for instance that the orientation spread is higher in single slip oriented samples than in double slip due to different sample preparation procedure. It has also provided the orientation spread of new formed regions (e.g. region **F** in S1-L sample - Figure 3.14) or the evolution in orientation spread upon cycling even when the 2D resolved maps do not show variations (region **B** in S1-L - Figure 3.17, region **A** in S2-Cp - Figure 4.10 or region **B** in S2-Cl - Figure 4.22).

The template matching technique performed on the collected diffraction patterns has however some limitations related to the intensity distribution of the MicroXAS beamline (see section 2.2). The template matching technique fails to cover the whole area that is defined as a peak as explained in section 2.3.6. Figure 5.26 shows a representative example of the result obtained in point **A'** in 1S-R (see section 3.4.5). Four peaks are shown: the white crosses define the area of the peak. Note that they are not in the same scale as in Figure 3.16 and direct comparison should be avoided. On top all the orientation matches with different color are plotted and the energy values for fulling the Bragg condition of each reflection are also shown in the figure. The (400) and ($\bar{2}\bar{2}0$) reflections are completely covered and have energy ranges further away from 17 keV. On the other hand, the reflections which have energies closer to 17 keV ((004) and (0$\bar{2}\bar{2}$)) are not fully covered. By analyzing the energy distribution of the MicroXAS beamline Figure 2.21 one can observe that for the used undulator gap of 5 mm there is an intensity drop at 17 keV (12th harmonic). The correlation between the intensity drop and the uncovered areas in the Laue peaks evidence the influence of the beam intensity distribution in the template matching procedure. As a consequence the entire orientation spread along the thickness cannot be determined.
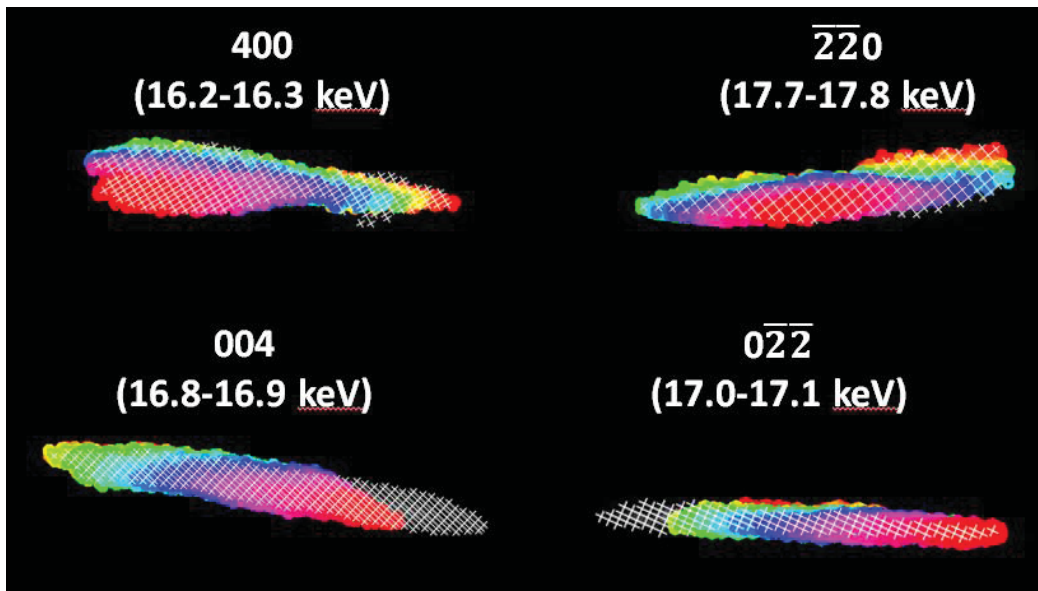
Figure 5.26 Results of template technique in point **A'** in 1S-R

The visual representation of the orientation matches helps to understand the orientation correlation between the physical positions in different peaks. For instance, while the orientation matches are distributed vertically in the (400) and ($\bar{2}\bar{2}0$) peaks, the distribution is horizontal in the (004) and (0$\bar{2}\bar{2}$) peaks. This points to the fact that in samples containing defects the position of maximum intensity in all reflections do not necessarily yield to the

same orientation. That is why the indexation error in single slip samples is higher than in double slip samples. Also, the higher the amount of peaks to index the higher can be the source of indexation error due to energy diversity in each reflection. This is the case when comparing coplanar and collinear samples (see sections 3.3.6, 3.4.6, 4.1.7 and 4.2.7 for values).

The rotation sensitivity of the technique depends on the sample-to-detector distance and position of the reflection in the detector. Figure 5.27 illustrates the influence of both parameters and the analysis yields to the following conclusions:

- The diffraction pattern has been simulated for sample oriented to collinear slip at two different sample-to-detector distances: 65 mm and 80 mm (Figure 5.27-a left and right respectively). The closer the detector the more spots are detected.
- Figure 5.27-b shows the zoom of two reflections located at different positions in the detector. Peak 1 is closer to the ordinate axis and Peak 2 closer to abscissa axis. Rotations about X-, Y- and Z-axis have been simulated from the reference orientation. The arrows point the rotation direction and the length corresponds to 0.5° rotation about each axis. One can observe that depending on the physical position of the reflection on the detector (λ and 2θ dependent), the direction and length of the arrow varies. Generally speaking, in transmission geometry rotations about X- and Y- axis are detected along radial direction and rotation about Z-axis along azimuthal.
- The table given in Figure 5.27-c summarizes the rotation sensitivity defined as pixel/° of both peaks at different sample to detector distance. Because of the physical location of the peak on the detector, peak 1 is more sensitive to rotation about X-axis while peak 2 is to Y-axis. In both cases and due to transmission geometry the Z-axis is the less sensitive among the three rotations.
- When the detector is moved away from the sample the sensitivity of the peaks increases. The drawback is that some peaks are lost. Peak 1 for instance is on the limit of the area detector for sample-to-detector distance of 80 mm. This approach can be used in collinear orientation where many spots are collected at 65 mm distance. In single slip and coplanar oriented samples however only 4-6 reflections are detected and increasing the distance will move the Laue spots out of the detector area.
- The final rotation sensitivity is given by the indexation of all the peaks.

a)
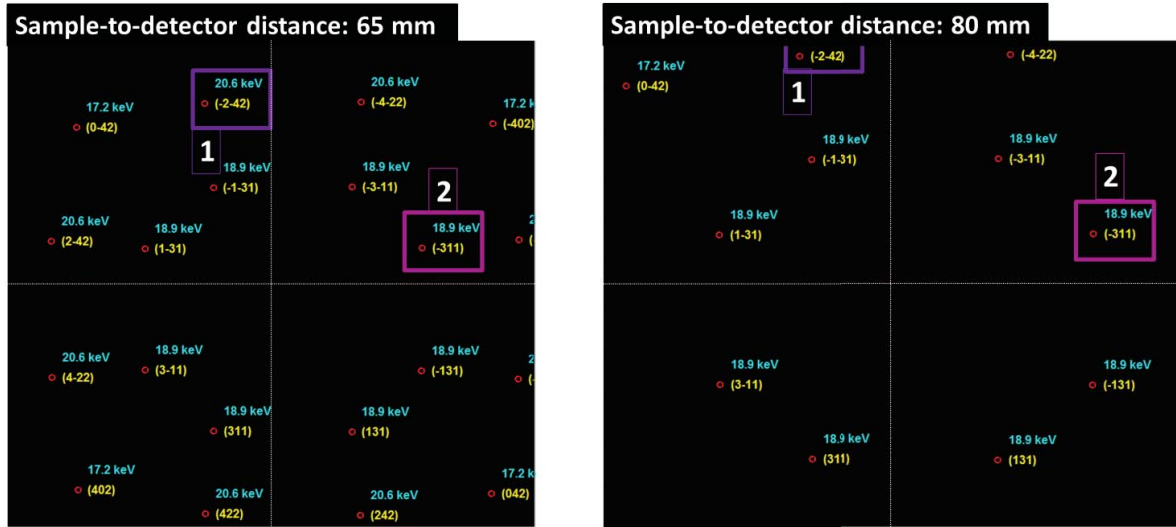
b)
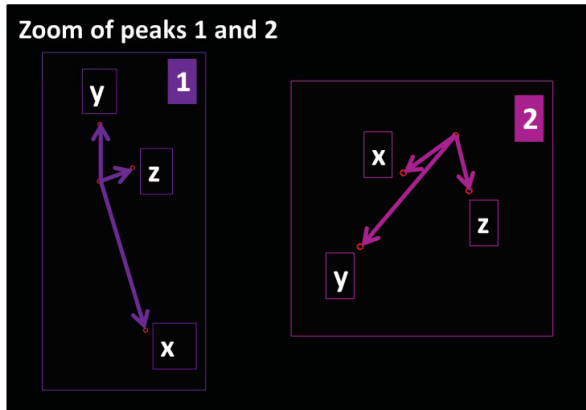
c)

Sample to detector distance	Axis rotation	Rotation sensitivity (pixel/°)	
		Peak 1	Peak 2
65 mm	X	63.6	21.1
	Y	22.8	40.9
	Z	16.9	10.4
80 mm	X	78.1	25.4
	Y	28.1	50.1
	Z	20.9	13.4

Figure 5.27 Rotation sensitivity of the Laue technique depending on the sample to detector distance and peak position

To sum up the assessment, the presented technique is for the moment the only technique that can follow lattice rotation evolution and distinguish the influence of the initial microstructure and its redistribution in the formation of new regions. The technique is particularly suitable for 2D dislocation structures (see S1-L case in section 3.3 and its interpretation in 5.4). Even if the expected rotation during the vein-channel structure formation in single slip oriented samples is about the Z-axis the current method can still follow the lattice rotation evolution. Note that the analyzed peaks are generally streaked in the radial direction but are rather narrow in the azimuthal direction. Therefore any azimuthal variation is a representation of rotation about Z-axis regardless of being the axis with lower rotation sensitivity.

Chapter 6   Conclusion

6.1   Achieved results

This project was undertaken to design a novel in-situ Laue mechanical test to follow the crystal rotation caused by dislocation patterning during early stages of fatigue. To accomplish this purpose the project has been divided in two phases: a development phase and an experimental phase.

During the development phase the following tasks have been completed:

- A new miniaturized device that can deform samples in reversed-shear mode during Laue diffraction has been developed and integrated at the MicroXAS beamline of SLS.
- In parallel the sample geometry has been designed to have simultaneously sufficient robustness during sample manipulation and a local thin area where Laue scans in transmission mode can be obtained.
- The sample preparation route has been devised to minimize the damage. Picosecond laser ablation has been applied to prepare the critical thin area required for the X-ray diffraction experiments.
- An analysis methodology to understand dislocation pattern evolution has been developed.
- A DECTRIS EIGER 4M detector has been integrated for the first time at the MicroXAS beamline of SLS.

The developed approach allows following the evolution of rotations during cyclic shear of Cu single crystals in a volume of $\sim 10 \times 25 \times 30$ μm^3 at relatively fast speed ($\sim$ 30-40 min/map). Information on rotational gradients and GND densities can also be extracted.

During the experimental phase, the initial steps in the formation of the dislocation patterning during cyclic deformation of elementary fcc copper single crystals are explored. Samples with different crystal orientations (single crystal, coplanar and collinear) have been cyclically deformed up to a maximum of 120 cycles during in-situ Laue micro-diffraction. The orientation dependency and spatial distributions of the lattice rotations caused by dislocation arrangements have been determined in terms of accumulated strain.

The investigation of the single slip oriented samples at low initial strain amplitudes has shown that:

- A homogenization process occurs in early cycles. The process is more evident in samples where the initial microstructure is not too damaged.
- Early formation of dislocation patterning can be followed by Laue micro-diffraction. The new misoriented regions are surrounded by a GND wall and do not have apparent GNDs inside.
- The presence of the initial mobile/immobile dislocations plays a role in the microstructural evolution as they can act as pinning points or dislocation sources and determine the physical position of veins.
- The misorientation spread of the emerged regions across the sample thickness can be analyzed with pattern matching approaches (Gupta and Agnew, 2009).

On the other hand, the following conclusions can be drawn from the study of the double slip oriented samples at higher initial strain amplitudes:

- The initial heterogeneities in the sample are strongly dependent on the sample preparation route.
- The homogenization process and pattern formation depends on the imposed strain amplitude and crystal orientation. A proper design of the multistep mechanical test is required to observe microstructural changes in the spatially resolved lattice rotation maps.
- The 3D arrangement of dislocation in double slip oriented samples complicates the follow-up of crystal rotation represented in 2D maps since the dislocation arrangement is not anymore expected to be quasi-

2D and therefore all sub-structure in the third direction are integrated in the diffraction patterns. The evolution of misorientation spread can however, to some extent, be followed with pattern matching approaches but the misorientation between the crystallites observed in Laue peaks cannot be quantified.

In summary, the approach developed permits following dislocation structures during fatigue while providing quantitative information on the transition from uniform to non-uniform dislocation structures. The procedure sacrifices on the fully 3D aspect but it brings the time resolved aspects and the spatially resolved GND density evolution required to validate ongoing simulations. On that note, our technique is one step further towards synergies with computational models. Interestingly, it is applied on a sample volume that is very similar what advanced modelling methods can now simulate. The error made by integration will depend on the design of the deformation experiment i.e. the character of the GND network expected. For instance it can be used to validate 3DDD models or density based dislocation dynamics models (e.g. (Hussein et al., 2015; Po et al., 2014; Sandfeld and Zaiser, 2015)) when applied in deformation geometries where the formation of 2D dislocation patterns is expected such as for instance dislocation accumulation in veins or persistent slip bands (Déprés et al., 2004; Grilli et al., 2015). However, the validation of many multi-slip deformation geometries during which 3D cell structures are formed are limited (Chen et al., 2013; Hussein and El-Awady, 2016a; Sandfeld and Zaiser, 2015; Xia and El-Azab, 2015a). For that purpose, the 3D X-ray Laue diffraction (Larson et al., 2002) is more suitable at the expense of losing time resolution.

To conclude in-situ Laue micro-diffraction in transmission mode has a large potential to facilitate a breakthrough in our understanding of 2D dislocation patterning and our possibilities to predict failure by advancing computational models due to its time resolution. The proposed technique is complementary to 3D X-ray Laue diffraction and 3D-EBSD, both restricted to a snapshot in time of the microstructure. All together they have the power to boost synergies between modelling and experiment and get better insight of the basics of dislocation patterning, which is still an open question.

6.2   Future development

In terms of directions for future research, further work should explore paths to overcome the major limitations detected in the present study:

- The sample preparation procedure should be revised in order to improve the initial quality of the samples. It has been shown that the addition of a second annealing has reduced the initial heterogeneities. Longer annealing times and/or gentler machining can help diminishing the introduced damage. Subjecting the samples to a final electropolishing step would help removing the possible damage induced by picosecond laser ablation. Concurrently the gauge section of the sample would be thinner and less volume would be integrated by the X-ray beam. This would help analyzing the shape of Laue reflections and orientation spread along the thickness. The drawback is the difficulty to control the electropolishing process by avoiding creating trenches or holes that would compromise the suitability of the sample for the mechanical test.
- A more robust system in the beamline that permits not retracting the detector away from the machine every time the sample has to be changed would give better calibration and therefore the source of indexation error would be minimized. This is restricted by the limited space available taking into account the dimensions of the machine and the need of having the detector relatively close to the sample to collect sufficient Laue spots.
- Another type of limitation to consider is the harmonic intensity distribution of the X-ray beam at the MicroXAS beamline. In other beamlines dedicated to white beam applications (for instance BM32 at ESRF), a bending magnet is used to produce a completely smooth energy distribution. This is achieved at the cost of lower fluxes and therefore lower intensities in Laue peaks.
- Due to the integrated volume and the orientation scattering across the thickness of the sample, the shape of Laue peaks is observed to be generally rather complex. In these cases the approach of Barabash and Ice (Barabash and Ice, 2014) is not able to unravel the arrangement of dislocation. Several forward-

models have been developed to help interpreting intricate Laue diffraction data (Korsunsky et al., 2012; Song et al., 2010). Starting from models that represent the microstructure of the material, artificial/synthetic diffraction patterns are simulated based on diffraction experiment conditions. The calculated Laue diffraction spots from virtual samples can be compared and contrasted with the experimental ones. The first stages of a bottom-up Laue diffraction approach has been developed in our group (SNF 132699 project), this should be further elaborated and applied to determine what dislocation ensembles have been developed.

A number of possible future studies using the same experimental set up are apparent. The present technique is proved to be particularly valuable to study the formation of 2D dislocation patterns in fatigue (e.g. dislocation accumulation in veins, walls or formation of PSBs). Additionally, it would be interesting to assess the crystal rotation maps at maximum/minimum loads when one expects to obtain the highest rotation. At the moment the time required for each scan could induce creep and thus influence the evolution of dislocation patterning. On the other hand, the same analysis methodology can also be applied to single crystal, bicrystals or oligocrystals subjected to fatigue shear or other mechanical tests (e.g. biaxial deformation, strain path changes), which would bring more insight into the lattice rotation evolution under complex strain paths.

References

Acharya, A., and Knops, R.J. (2013). An observation on the experimental measurement of dislocation density. ArXiv13010869 Cond-Mat.

Acharya, A., and Roy, A. (2006). Size effects and idealized dislocation microstructure at small scales: Predictions of a Phenomenological model of Mesoscopic Field Dislocation Mechanics: Part I. J. Mech. Phys. Solids *54*, 1687–1710.

Ackermann, F., Kubin, L.P., Lepinoux, J., and Mughrabi, H. (1984). The dependence of dislocation microstructure on plastic strain amplitude in cyclically strained copper single crystals. Acta Metall. *32*, 715–725.

Ahmed, J., Wilkinson, A.J., and Roberts, S.G. (1997). Characterizing dislocation structures in bulk fatigued copper single crystals using electron channelling contrast imaging (ECCI). Philos. Mag. Lett. *76*, 237–246.

Ahmed, J., Wilkinson, A.J., and Roberts, S.G. (1999). Study of dislocation structures near fatigue cracks using electron channelling contrast imaging technique (ECCI). J. Microsc. *195*, 197–203.

Ahmed, J., Roberts, S.G., and Wilkinson, A.J. (2006). Characterizing dislocation structure evolution during cyclic deformation using electron channelling contrast imaging. Philos. Mag. *86*, 4965–4981.

Ames, M., Markmann, J., and Birringer, R. (2010). Mechanical testing via dominant shear deformation of small-sized specimen. Mater. Sci. Eng. A *528*, 526–532.

Amodeo, R.J., and Ghoniem, N.M. (1990). Dislocation dynamics. II. Applications to the formation of persistent slip bands, planar arrays, and dislocation cells. Phys. Rev. B *41*, 6968–6976.

Ananthakrishna, G. (2007). Current theoretical approaches to collective behavior of dislocations. Phys. Rep. *440*, 113–259.

Argon, A. (2007). Strengthening Mechanisms in Crystal Plasticity (Oxford University Press).

Arsenlis, A., and Parks, D.. (1999). Crystallographic aspects of geometrically-necessary and statistically-stored dislocation density. Acta Mater. *47*, 1597–1611.

Ashby, M.F. (1970). The deformation of plastically non-homogeneous materials. Philos. Mag. *21*, 399–424.

Attodyne website (2013). Picosecond Laser Applications: http://www.attodynelasers.com/micromachining/.

Bakó, B., and Hoffelner, W. (2007). Cellular dislocation patterning during plastic deformation. Phys. Rev. B *76*, 214108.

Barabash, R.I., and Ice, G.E. (2005). Microdiffraction Analysis of Hierarchical Dislocation Organization. In Encyclopedia of Materials: Science and Technology, (Elsevier), pp. 1–18.

Barabash, R.I., and Ice, G.E. (2014). Diffraction Analysis of Defects: State of the Art. In Strain and Dislocation Gradients from Diffraction, (Imperial College Press), pp. 1–52.

Barabash, R., Ice, G.E., Larson, B.C., Pharr, G.M., Chung, K.-S., and Yang, W. (2001). White microbeam diffraction from distorted crystals. Appl. Phys. Lett. *79*, 749–751.

Barabash, R.I., Ice, G.E., Larson, B.C., and Yang, W. (2002). Application of white x-ray microbeams for the analysis of dislocation structures. Rev. Sci. Instrum. *73*, 1652.

Barabash, R.I., Ice, G.E., and Walker, F.J. (2003). Quantitative microdiffraction from deformed crystals with unpaired dislocations and dislocation walls. J. Appl. Phys. *93*, 1457.

Barabash, R.I., Ice, G.E., and Pang, J.W.L. (2005). Gradients of geometrically necessary dislocations from white beam microdiffraction. Mater. Sci. Eng. A *400–401*, 125–131.

Barnoush, A. (2012). Correlation between dislocation density and nanomechanical response during nanoindentation. Acta Mater. *60*, 1268–1277.

Blondé, R., Jimenez-Melero, E., Huizenga, R., Zhao, L., Wright, J., Brück, E., van der Zwaag, S., and van Dijk, N. (2014). High-resolution X-ray diffraction investigation on the evolution of the substructure of individual austenite grains in TRIP steels during tensile deformation. J. Appl. Crystallogr. *47*, 965–973.

Bouilly, D., Perez, D., and Lewis, L.J. (2007). Damage in materials following ablation by ultrashort laser pulses: A molecular-dynamics study. Phys. Rev. B *76*.

Brinckmann, S., and Van der Giessen, E. (2004). A discrete dislocation dynamics study aiming at understanding fatigue crack initiation. Mater. Sci. Eng. A *387–389*, 461–464.

Buchinger, L., Stanzl, S., and Laird, C. (1985). Dislocation structures in copper single crystals fatigued at low amplitudes. Philos. Mag. A *50*, 275–298.

Butler, G.C., Stock, S.R., McGinty, R.D., and McDowell, D.L. (2002). X-Ray Microbeam Laue Pattern Studies of the Spreading of Orientation in OFHC Copper at Large Strains. J. Eng. Mater. Technol. *124*, 48.

Calcagnotto, M., Ponge, D., Demir, E., and Raabe, D. (2010). Orientation gradients and geometrically necessary dislocations in ultrafine grained dual-phase steels studied by 2D and 3D EBSD. Mater. Sci. Eng. A *527*, 2738–2746.

Chapman, S.J., Xiang, Y., and Zhu, Y. (2016). Homogenisation of a Row of Dislocation Dipoles from Discrete Dislocation Dynamics. SIAM J. Appl. Math. *76*, 750–775.

Chen, Y.S., Choi, W., Papanikolaou, S., and Sethna, J.P. (2010). Bending Crystals: Emergence of Fractal Dislocation Structures. Phys. Rev. Lett. *105*, 105501.

Chen, Y.S., Choi, W., Papanikolaou, S., Bierbaum, M., and Sethna, J.P. (2013). Scaling theory of continuum dislocation dynamics in three dimensions: Self-organized fractal pattern formation. Int. J. Plast. *46*, 94–129.

Cheng, A.S., and Laird, C. (1981). Mechanisms of fatigue hardening in copper single crystals: The effects of strain amplitude and orientation. Mater. Sci. Eng. *51*, 111–121.

Chichkov, B.N., Momma, C., Nolte, S., Alvensleben, F. von, and Tünnermann, A. (1996). Femtosecond, picosecond and nanosecond laser ablation of solids. Appl. Phys. A *63*, 109–115.

Chung, J.-S., Isa, S., Greene, V., Broadwater, O., Liu, W., and Ice, G.E. (2007). Multiple differential-aperture microscopy. Nucl. Instrum. Methods Phys. Res. Sect. Accel. Spectrometers Detect. Assoc. Equip. *582*, 212–214.

Clouet, E., Caillard, D., Chaari, N., Onimus, F., and Rodney, D. (2015). Dislocation locking versus easy glide in titanium and zirconium. Nat. Mater. *14*, 931–936.

Cui, Y., Liu, Z., Wang, Z., and Zhuang, Z. (2016). Mechanical annealing under low-amplitude cyclic loading in micropillars. J. Mech. Phys. Solids *89*, 1–15.

Dausinger, F., Hugel, H., and Konov, V.I. (2003). Micromachining with ultrashort laser pulses: from basic understanding to technical applications. H.P. Weber, V.I. Konov, and T. Graf, eds. pp. 106–115.

Demir, E., Raabe, D., Zaafarani, N., and Zaefferer, S. (2009). Investigation of the indentation size effect through the measurement of the geometrically necessary dislocations beneath small indents of different depths using EBSD tomography. Acta Mater. *57*, 559–569.

Déprés, C., * C.F.R., and Fivel, M.C. (2004). Low-strain fatigue in AISI 316L steel surface grains: a three-dimensional discrete dislocation dynamics modelling of the early cycles I. Dislocation microstructures and mechanical behaviour. Philos. Mag. *84*, 2257–2275.

Déprés, C., Robertson, C.F., and Fivel, M.C. (2006). Low-strain fatigue in 316L steel surface grains: a three dimension discrete dislocation dynamics modelling of the early cycles. Part 2: Persistent slip markings and micro-crack nucleation. Philos. Mag. *86*, 79–97.

Déprés, C., Fivel, M., and Tabourot, L. (2008). A dislocation-based model for low-amplitude fatigue behaviour of face-centred cubic single crystals. Scr. Mater. *58*, 1086–1089.

Déprés, C., Prasad Reddy, G.V., Robertson, C., and Fivel, M. (2014). An extensive 3D dislocation dynamics investigation of stage-I fatigue crack propagation. Philos. Mag. *94*, 4115–4137.

Devincre, B., Kubin, L., and Hoc, T. (2007). Collinear superjogs and the low-stress response of fcc crystals. Scr. Mater. *57*, 905–908.

deWit, R. (1973). Theory of disclinations: IV. Straight disclinations. J. Res. Natl. Bur. Stand. Sect. Phys. Chem. *77A*, 607.

Dingreville, R., Karnesky, R.A., Puel, G., and Schmitt, J.-H. (2015). Review of the synergies between computational modeling and experimental characterization of materials across length scales. J. Mater. Sci. *51*, 1178–1203.

Dmitrieva, O., Dondl, P.W., Müller, S., and Raabe, D. (2009). Lamination microstructure in shear deformed copper single crystals. Acta Mater. *57*, 3439–3449.

Echlin, M.P., Straw, M., Randolph, S., Filevich, J., and Pollock, T.M. (2015). The TriBeam system: Femtosecond laser ablation in situ SEM. Mater. Charact. *100*, 1–12.

El-Awady, J.A., Ghoniem, N.M., and Mughrabi, H. (2007). Dislocation modelling of localized plasticity in persistent slip bands. TMS Annu. Meet.

El-Azab, A. (2006). Statistical mechanics of dislocation systems. Scr. Mater. *54*, 723–727.

El-Naaman, S.A., Nielsen, K.L., and Niordson, C.F. (2016). On modeling micro-structural evolution using a higher order strain gradient continuum theory. Int. J. Plast. *76*, 285–298.

Erel, C. (2015). Dislocation Dynamics Simulations of Persistent Slip Bands during Fatigue of FCC Metals. University of California.

Fourmeau, M., Børvik, T., Benallal, A., Lademo, O.G., and Hopperstad, O.S. (2011). On the plastic anisotropy of an aluminium alloy and its influence on constrained multiaxial flow. Int. J. Plast. *27*, 2005–2025.

Fournet, R., and Salazar, J.M. (1996). Formation of dislocation patterns: Computer simulations. Phys. Rev. B *53*, 6283–6290.

Franěk, A., Kalus, R., and Kratochvíl, J. (1991). Model of early stage of dislocation structure formation in cyclically deformed metal crystals. Philos. Mag. A *64*, 497–511.

Funk, W., and Blank, E. (1984). Shear testing of monocrystalline alloys incorporating the measurement of local and integral strains. Mater. Sci. Eng. *67*, 1–11.

Gómez-García, D., Devincre, B., and Kubin, L.P. (2006). Dislocation Patterns and the Similitude Principle: 2.5D Mesoscale Simulations. Phys. Rev. Lett. *96*, 125503.

Grilli, N., Janssens, K.G.F., and Van Swygenhoven, H. (2015). Crystal plasticity finite element modelling of low cycle fatigue in fcc metals. J. Mech. Phys. Solids *84*, 424–435.

Groma, I., and Bakó, B. (2000). Dislocation Patterning: From Micro- to Mesoscale Description. Phys. Rev. Lett. *84*, 1487–1490.

Groma, I., and Balogh, P. (1999). Investigation of dislocation pattern formation in a two-dimensional self-consistent field approximation. Acta Mater. *47*, 3647–3654.

Grosskreutz, J.C. (1971). The mechanisms of metal fatigue (I). Phys. Status Solidi B *47*, 11–31.

Guitton, A., Irastorza-Landa, A., Broennimann, R., Grolimund, D., Van Petegem, S., and Van Swygenhoven, H. (2015). Picosecond pulsed laser for microscale sample preparation. Mater. Lett. *160*, 589–591.

Gupta, V.K., and Agnew, S.R. (2009). Indexation and misorientation analysis of low-quality Laue diffraction patterns. J. Appl. Crystallogr. *42*, 116–124.

Gupta, V.K., and Agnew, S.R. (2010). A Simple Algorithm to Eliminate Ambiguities in EBSD Orientation Map Visualization and Analyses: Application to Fatigue Crack-Tips/Wakes in Aluminum Alloys. Microsc. Microanal. *16*, 831–841.

Gutierrez-Urrutia, I., Zaefferer, S., and Raabe, D. (2013). Coupling of Electron Channeling with EBSD: Toward the Quantitative Characterization of Deformation Structures in the SEM. JOM *65*, 1229–1236.

Hähner, P. (1996). Stochastic dislocation patterning during cyclic plastic deformation: A theory of the formation of persistent slip band and matrix structures. Appl. Phys. Mater. Sci. Process. *63*, 45–55.

Hancock, J.R., and Grosskreutz, J.C. (1969). Mechanisms of fatigue hardening in copper single crystals. Acta Metall. *17*, 77–97.

Harzic, R.L., Huot, N., Audouard, E., Jonin, C., Laporte, P., Valette, S., Fraczkiewicz, A., and Fortunier, R. (2002). Comparison of heat-affected zones due to nanosecond and femtosecond laser pulses using transmission electronic microscopy. Appl. Phys. Lett. *80*, 3886–3888.

Hata, S., Miyazaki, H., Miyazaki, S., Mitsuhara, M., Tanaka, M., Kaneko, K., Higashida, K., Ikeda, K., Nakashima, H., Matsumura, S., et al. (2011). High-angle triple-axis specimen holder for three-dimensional diffraction contrast imaging in transmission electron microscopy. Ultramicroscopy *111*, 1168–1175.

Hesselbarth, H.W., and Steck, E. (1992). A Simulation of Dislocation Patterning Derived from Cellular Automata. Solid State Phenom. *23–24*, 445–454.

Heyer, J.-K., Brinckmann, S., Pfetzing-Micklich, J., and Eggeler, G. (2014). Microshear deformation of gold single crystals. Acta Mater. *62*, 225–238.

Hochrainer, T., Sandfeld, S., Zaiser, M., and Gumbsch, P. (2014). Continuum dislocation dynamics: Towards a physical theory of crystal plasticity. J. Mech. Phys. Solids *63*, 167–178.

Hofmann, F., and Korsunsky, A.M. (2013). High-Energy Transmission Laue (HETL) Micro-Beam Diffraction. In Strain and Dislocation Gradients from Diffraction, (IMPERIAL COLLEGE PRESS), pp. 82–124.

Hofmann, F., Song, X., Abbey, B., Jun, T.-S., and Korsunsky, A.M. (2012). High-energy transmission Laue micro-beam X-ray diffraction: a probe for intra-granular lattice orientation and elastic strain in thicker samples. J. Synchrotron Radiat. *19*, 307–318.

Hofmann, F., Abbey, B., Liu, W., Xu, R., Usher, B.F., Balaur, E., and Liu, Y. (2013). X-ray micro-beam characterization of lattice rotations and distortions due to an individual dislocation. Nat. Commun. *4*.

Holt, D.L. (1970). Dislocation Cell Formation in Metals. J. Appl. Phys. *41*, 3197–3201.

Huang, E.-W., Barabash, R.I., Ice, G.E., Liu, W., Liu, Y.-L., Kai, J.-J., and Liaw, P.K. (2009). Cyclic-loading-induced accumulation of geometrically necessary dislocations near grain boundaries in an Ni-based superalloy. JOM *61*, 53–58.

Hussein, A.M., and El-Awady, J.A. (2016a). Quantifying dislocation microstructure evolution and cyclic hardening in fatigued face-centered cubic single crystals. J. Mech. Phys. Solids.

Hussein, A.M., and El-Awady, J.A. (2016b). Surface roughness evolution during early stages of mechanical cyclic loading. Int. J. Fatigue *87*, 339–350.

Hussein, A.M., Rao, S.I., Uchic, M.D., Dimiduk, D.M., and El-Awady, J.A. (2015). Microstructurally based cross-slip mechanisms and their effects on dislocation microstructure evolution in fcc crystals. Acta Mater. *85*, 180–190.

Hußnätter, W., and Merklein, M. (2008). Characterization of material behavior under pure shear condition. Int. J. Mater. Form. *1*, 233–236.

Hutchinson, J.W. (1976). Bounds and Self-Consistent Estimates for Creep of Polycrystalline Materials. Proc. R. Soc. Math. Phys. Eng. Sci. *348*, 101–127.

Hÿtch, M.J., and Minor, A.M. (2014). Observing and measuring strain in nanostructures and devices with transmission electron microscopy. MRS Bull. *39*, 138–146.

Ice, G.E., and Barabash, R.I. (2007). Chapter 79 White Beam Microdiffraction and Dislocations Gradients. In Dislocations in Solids, F.R.N. Nabarro and J.P. Hirth, ed. (Elsevier), pp. 499–601.

Ice, G.E., Barabash, R.I., and Walker, F.J. (2005). Characterization of nano and meso scale deformation structures with intense X-ray synchrotron sources. Compos. Part B Eng. *36*, 271–277.

Ice, G.E., Budai, J.D., and Pang, J.W.L. (2011). The Race to X-ray Microbeam and Nanobeam Science. Science *334*, 1234–1239.

Jakobsen, B., Poulsen, H.F., Lienert, U., Almer, J., Shastri, S.D., Sørensen, H.O., Gundlach, C., and Pantleon, W. (2006). Formation and Subdivision of Deformation Structures During Plastic Deformation. Science *312*, 889–892.

Jakobsen, B., Poulsen, H.F., Lienert, U., and Pantleon, W. (2007). Direct determination of elastic strains and dislocation densities in individual subgrains in deformation structures. Acta Mater. *55*, 3421–3430.

Jakobsen, B., Poulsen, H.F., Lienert, U., Bernier, J., Gundlach, C., and Pantleon, W. (2009). Stability of dislocation structures in copper towards stress relaxation investigated by high angular resolution 3D X-ray diffraction. Phys. Status Solidi A *206*, 21–30.

Jandeleit, J., Urbasch, G., Hoffmann, H.D., Treusch, H.-G., and Kreutz, E.W. (1996). Picosecond laser ablation of thin copper films. Appl. Phys. Mater. Sci. Process. *63*, 117–121.

Jiang, J., Britton, T.B., and Wilkinson, A.J. (2013). Evolution of dislocation density distributions in copper during tensile deformation. Acta Mater. *61*, 7227–7239.

Jiang, J., Britton, T.B., and Wilkinson, A.J. (2015). The orientation and strain dependence of dislocation structure evolution in monotonically deformed polycrystalline copper. Int. J. Plast. *69*, 102–117.

Jiang, J., Zhang, T., Dunne, F.P.E., and Britton, T.B. (2016). Deformation compatibility in a single crystalline Ni superalloy. Proc. Math. Phys. Eng. Sci. R. Soc. *472*.

Jing, S., Zhenxi, G., and Manling, S. (2016). Slip system determination of dislocations in alpha-Ti during in situ TEM tensile deformation. Acta Metall. Sin. *52*, 71–77.

Joo, H.D., Kim, J.S., Kim, K.H., Tamura, N., and Koo, Y.M. (2004). In situ synchrotron X-ray microdiffraction study of deformation behavior in polycrystalline coppers during uniaxial deformations. Scr. Mater. *51*, 1183–1186.

Judelewicz, M., Künzi, H.U., Merk, N., and Ilschner, B. (1994). Microstructural development during fatigue of copper foils 20–100 μm thick. Mater. Sci. Eng. A *186*, 135–142.

Kassner, M.E., Geantil, P., Levine, L.E., and Larson, B.C. (2009). Long-range internal stresses in monotonically and cyclically deformed metallic single crystals. Int. J. Mater. Res. *100*, 333–339.

Kiener, D., Motz, C., Grosinger, W., Weygand, D., and Pippan, R. (2010). Cyclic response of copper single crystal micro-beams. Scr. Mater. *63*, 500–503.

Kirchlechner, C., Imrich, P.J., Grosinger, W., Kapp, M.W., Keckes, J., Micha, J.S., Ulrich, O., Thomas, O., Labat, S., Motz, C., et al. (2012a). Expected and unexpected plastic behavior at the micron scale: An in situ μLaue tensile study. Acta Mater. *60*, 1252–1258.

Kirchlechner, C., Grosinger, W., Kapp, M.W., Imrich, P.J., Micha, J.-S., Ulrich, O., Keckes, J., Dehm, G., and Motz, C. (2012b). Investigation of reversible plasticity in a micron-sized, single crystalline copper bending beam by X-ray μLaue diffraction. Philos. Mag. *92*, 3231–3242.

Kirchlechner, C., Imrich, P.J., Liegl, W., Pörnbacher, J., Micha, J.-S., Ulrich, O., and Motz, C. (2015). On the reversibility of dislocation slip during small scale low cycle fatigue. Acta Mater. *94*, 69–77.

Kolář, M., Beneš, M., Kratochvíl, J., and Pauš, P. (2015). Numerical Simulations of Glide Dislocations in Persistent Slip Band. Acta Phys. Pol. A *128*, 506–510.

Konijnenberg, P.J., Zaefferer, S., and Raabe, D. (2015). Assessment of geometrically necessary dislocation levels derived by 3D EBSD. Acta Mater. *99*, 402–414.

Korsunsky, A.M., Hofmann, F., Abbey, B., Song, X., Belnoue, J.P., Mocuta, C., and Dolbnya, I. (2012). Analysis of the internal structure and lattice (mis)orientation in individual grains of deformed CP nickel polycrystals by synchrotron X-ray micro-diffraction and microscopy. Int. J. Fatigue *42*, 1–13.

Kratochvíl, J. (1988). Dislocation pattern formation in metals. Rev. Phys. Appliquée *23*, 419–429.

Kratochvíl, J., and Sedláček, R. (2003). Pattern formation in the framework of the continuum theory of dislocations. Phys. Rev. B *67*, 94105.

Kratochvíl, J., and Sedláček, R. (2008). Statistical foundation of continuum dislocation plasticity. Phys. Rev. B *77*, 134102.

Kratochvíl, J. (2001). Self-organization model of localization of cyclic strain into PSBs and formation of dislocation wall structure. Mater. Sci. Eng. A *309–310*, 331–335.

Kristan, J., and Kratochvíl, J. (2007). Interactions of glide dislocations in a channel of a persistent slip band. Philos. Mag. *87*, 4593–4613.

Kristan, J., and Kratochvíl, J. (2010). Bowing out of a dislocation from wall of persistent slip bands (PSB). Int. J. Mater. Res. *101*, 680–683.

Krivoglaz, M.A. (1969). Theory of X-ray and thermal-neutron scattering by real crystals (Plenum Press).

Kubin, L. (2013). Dislocations, Mesoscale Simulations and Plastic Flow (Oxford University Press).

Kubin, L.P. (1993). Dislocation Patterning during Multiple Slip of F.C.C. Crystals. A Simulation Approach. Phys. Status Solidi A *135*, 433–443.

Kubin, L., Devincre, B., and Hoc, T. (2008). Modeling dislocation storage rates and mean free paths in face-centered cubic crystals. Acta Mater. *56*, 6040–6049.

Kubin, L.P., Fressengeas, C., and Ananthakrishna, G. (2002). Chapter 57 Collective behaviour of dislocations in plasticity. In Dislocations in Solids, F.R.N.N. and M.S. Duesbery, ed. (Elsevier), pp. 101–192.

Laird, C., Charsley, P., and Mughrabi, H. (1986). Low energy dislocation structures produced by cyclic deformation. Mater. Sci. Eng. *81*, 433–450.

Landau, P., Shneck, R.Z., Makov, G., and Venkert, A. (2010). In-situ TEM study of dislocation patterning during deformation in single crystal aluminum. J. Phys. Conf. Ser. *241*, 12060.

Larson, B.C., Yang, W., Ice, G.E., Budai, J.D., and Tischler, J.Z. (2002). Three-dimensional X-ray structural microscopy with submicrometre resolution. Nature *415*, 887–890.

Larson, B.C., El-Azab, A., Yang, W., Tischler, J.Z., Liu, W., and Ice, G.E. (2007). Experimental characterization of the mesoscale dislocation density tensor. Philos. Mag. *87*, 1327–1347.

Larson, B.C., Tischler, J.Z., El-Azab, A., and Liu, W. (2008). Dislocation Density Tensor Characterization of Deformation Using 3D X-Ray Microscopy. J. Eng. Mater. Technol. *130*, 21024.

Le Harzic, R., Breitling, D., Weikert, M., Sommer, S., Föhl, C., Valette, S., Donnet, C., Audouard, E., and Dausinger, F. (2005). Pulse width and energy influence on laser micromachining of metals in a range of 100 fs to 5 ps. Appl. Surf. Sci. *249*, 322–331.

Leclere, C., Cornelius, T.W., Ren, Z., Davydok, A., Micha, J.-S., Robach, O., Richter, G., Belliard, L., and Thomas, O. (2015). *In situ* bending of an Au nanowire monitored by micro Laue diffraction. J. Appl. Crystallogr. *48*, 291–296.

Legros, M. (2014). In situ mechanical TEM: Seeing and measuring under stress with electrons. Comptes Rendus Phys. *15*, 224–240.

Leitz, K.-H., Redlingshöfer, B., Reg, Y., Otto, A., and Schmidt, M. (2011). Metal Ablation with Short and Ultrashort Laser Pulses. Phys. Procedia *12*, 230–238.

LeSar, R. (2014). Simulations of Dislocation Structure and Response. Annu. Rev. Condens. Matter Phys. *5*, 375–407.

Levine, L.E., Larson, B.C., Yang, W., Kassner, M.E., Tischler, J.Z., Delos-Reyes, M.A., Fields, R.J., and Liu, W. (2006). X-ray microbeam measurements of individual dislocation cell elastic strains in deformed single-crystal copper. Nat. Mater. *5*, 619–622.

Levine, L.E., Geantil, P., Larson, B.C., Tischler, J.Z., Kassner, M.E., Liu, W., Stoudt, M.R., and Tavazza, F. (2011). Disordered long-range internal stresses in deformed copper and the mechanisms underlying plastic deformation. Acta Mater. *59*, 5803–5811.

Levine, L.E., Okoro, C., and Xu, R. (2015). Full elastic strain and stress tensor measurements from individual dislocation cells in copper through-Si vias. IUCrJ *2*, 635–642.

Li, P., and Zhang, Z.F. (2014). Physical origin of surface slip morphologies induced by regular self-organized dislocation patterns in fatigued copper single crystals. J. Appl. Phys. *115*, 33504.

Li, P., Li, S.X., Wang, Z.G., and Zhang, Z.F. (2011). Fundamental factors on formation mechanism of dislocation arrangements in cyclically deformed fcc single crystals. Prog. Mater. Sci. *56*, 328–377.

Li, S.F., Lind, J., Hefferan, C.M., Pokharel, R., Lienert, U., Rollett, A.D., and Suter, R.M. (2012). Three-dimensional plastic response in polycrystalline copper *via* near-field high-energy X-ray diffraction microscopy. J. Appl. Crystallogr. *45*, 1098–1108.

Li, S.X., Li, X.W., Zhang, Z.F., Wang, Z.G., and Lu, K. (2002). On the formation of deformation bands in fatigued copper single crystals. Philos. Mag. A *82*, 3129–3147.

Li, X.W., Hu, Y.M., and Wang, Z.G. (1998). Investigation of dislocation structure in a cyclically deformed copper single crystal using electron channeling contrast technique in SEM. Mater. Sci. Eng. A *248*, 299–303.

Liu, W., and Ice, G.E. (2014). X-ray Laue Diffraction Microscopy in 3D at the Advanced Photon Source. In Strain and Dislocation Gradients from Diffraction, (IMPERIAL COLLEGE PRESS), pp. 53–81.

Liu, D., He, Y., Tang, X., Ding, H., Hu, P., and Cao, P. (2012). Size effects in the torsion of microscale copper wires: Experiment and analysis. Scr. Mater. *66*, 406–409.

Liu, G.S., House, S.D., Kacher, J., Tanaka, M., Higashida, K., and Robertson, I.M. (2014). Electron tomography of dislocation structures. Mater. Charact. *87*, 1–11.

Liu, Y., Wang, H., and Zhang, X. (2016). In Situ TEM Nanoindentation Studies on Stress-Induced Phase Transformations in Metallic Materials. Jom *68*, 226–234.

Lynch, P.A., Kunz, M., Tamura, N., and Barnett, M.R. (2014). Time and spatial resolution of slip and twinning in a grain embedded within a magnesium polycrystal. Acta Mater. *78*, 203–212.

Maass, R. (2009). In-situ Laue diffraction on deforming micropillars.

Maaß, R., Van Petegem, S., Van Swygenhoven, H., Derlet, P.M., Volkert, C.A., and Grolimund, D. (2007). Time-Resolved Laue Diffraction of Deforming Micropillars. Phys. Rev. Lett. *99*.

Maaβ, R., Grolimund, D., Van Petegem, S., Willimann, M., Jensen, M., Van Swygenhoven, H., Lehnert, T., Gijs, M.A.M., Volkert, C.A., Lilleodden, E.T., et al. (2006). Defect structure in micropillars using x-ray microdiffraction. Appl. Phys. Lett. *89*, 151905.

Madec, R., Devincre, B., and Kubin, L.. (2002). Simulation of dislocation patterns in multislip. Scr. Mater. *47*, 689–695.

Madec, R., Devincre, B., Kubin, L., Hoc, T., and Rodney, D. (2003). The Role of Collinear Interaction in Dislocation-Induced Hardening. Science *301*, 1879–1882.

Mader, S., Thieringer, H., and Seeger, A. (1963). Work Hardening and Dislocation Arrangement of Fcc Single Crystals .2. Electron Microscope Transmission Studies of Ni-Co Single Crystals and Relation to Work-Hardening Theory. J. Appl. Phys. *34*, 3376-.

Maeder, X., Mook, W.M., Niederberger, C., and Michler, J. (2011). Quantitative stress/strain mapping during micropillar compression. Philos. Mag. *91*, 1097–1107.

Magid, K.R., Florando, J.N., Lassila, D.H., LeBlanc, M.M., Tamura, N., and Morris, J.W. (2009). Mapping mesoscale heterogeneity in the plastic deformation of a copper single crystal. Philos. Mag. *89*, 77–107.

Margulies, L., Winther, G., and Poulsen, H.F. (2001). In Situ Measurement of Grain Rotation During Deformation of Polycrystals. Science *291*, 2392–2394.

Marichal, C.R.M. (2013). Plasticity in bcc single crystals investigated by Laue diffraction during micro-compression. École polytechnique fédérale de Lausanne EPFL.

Marichal, C., Van Swygenhoven, H., Van Petegem, S., and Borca, C. (2013). {110} Slip with {112} slip traces in bcc Tungsten. Sci. Rep. *3*.

Marichal, C., Srivastava, K., Weygand, D., Van Petegem, S., Grolimund, D., Gumbsch, P., and Van Swygenhoven, H. (2014). Origin of Anomalous Slip in Tungsten. Phys. Rev. Lett. *113*.

Mathworks website Kernel Distribution - MATLAB & Simulink - http://ch.mathworks.com/help/stats/kernel-distribution.html.

Mathworks website Box plot - MATLAB boxplot - http://ch.mathworks.com/help/stats/boxplot.html.

Matsuda, A. (1977). The Plastic Deformation of Iron Single Crystals with Shear Tests in {110}⟨111⟩ and {112}⟨111⟩ Slip Systems. Trans. Jpn. Inst. Met. *18*, 214–220.

Mayer, C., Li, N., Mara, N., and Chawla, N. (2015). Micromechanical and in situ shear testing of Al–SiC nanolaminate composites in a transmission electron microscope (TEM). Mater. Sci. Eng. A *621*, 229–235.

Mayr, C., Eggeler, G., Webster, G.A., and Peter, G. (1995). Double shear creep testing of superalloy single crystals at temperatures above 1000 °C. Mater. Sci. Eng. A *199*, 121–130.

Meijer, J. (2004). Laser beam machining (LBM), state of the art and new opportunities. J. Mater. Process. Technol. *149*, 2–17.

Melisova, D., Weiss, B., and Stickler, R. (1997). Nucleation of persistent slip bands in Cu single crystals under stress controlled cycling. Scr. Mater. *36*, 1061–1066.

Minárik, V., Beneš, M., and Kratochvíl, J. (2010). Simulation of dynamical interaction between dislocations and dipolar loops. J. Appl. Phys. *107*, 61802.

Mises, R. v (1913). Mechanik der festen Körper im plastisch- deformablen Zustand. Nachrichten Von Ges. Wiss. Zu Gött. Math.-Phys. Kl. *1913*, 582–592.

Miyauchi, K. (1984). A proposal of a planar simple shear test in sheet metals. Sci. Pap. Inst. Phys. Chem. Res. *78*, 27–40.

Mohamed, M.S., Larson, B.C., Tischler, J.Z., and El-Azab, A. (2015). A statistical analysis of the elastic distortion and dislocation density fields in deformed crystals. J. Mech. Phys. Solids *82*, 32–47.

Mompiou, F., Caillard, D., Legros, M., and Mughrabi, H. (2012). In situ TEM observations of reverse dislocation motion upon unloading in tensile-deformed UFG aluminium. Acta Mater. *60*, 3402–3414.

Morawiec, A. (2004). Orientations and Rotations (Berlin, Heidelberg: Springer Berlin Heidelberg).

Mughbrabi, H., Ackermann, F., and Herz, K. (1979). Persistent Slipbands in Fatigued Face-Centered and Body-Centered Cubic Metals. In Fatigue Mechanisms, J. Fong, ed. (100 Barr Harbor Drive, PO Box C700, West Conshohocken, PA 19428-2959: ASTM International), pp. 69-69–37.

Mughrabi, H. (1971a). Electron Microscope Investigations of Dislocation Arrangement of Deformed Copper Single Crystals in Stress-Applied State .1. Dislocation Arrangement at End of Stage I. Philos. Mag. *23*, 869-.

Mughrabi, H. (1971b). Electron Microscope Investigations of Dislocation Arrangement of Deformed Copper Single Crystals in Stress-Applied State .2. Dislocation Arrangement in Stage Ii. Philos. Mag. *23*, 897-.

Mughrabi, H. (1971c). Electron Microscope Investigation of Dislocation Arrangement of Deformed Copper Single Crystals in Stress-Applied State .3. Comparison of Some Characteristic Quantities of Dislocation Structure in Stress-Applied and Stress-Removed States. Philos. Mag. *23*, 931-.

Mughrabi, H. (1978). The cyclic hardening and saturation behaviour of copper single crystals. Mater. Sci. Eng. *33*, 207–223.

Mughrabi, H. (2006a). Deformation-induced long-range internal stresses and lattice plane misorientations and the role of geometrically necessary dislocations. Philos. Mag. *86*, 4037–4054.

Mughrabi, H. (2006b). Dual role of deformation-induced geometrically necessary dislocations with respect to lattice plane misorientations and/or long-range internal stresses. Acta Mater. *54*, 3417–3427.

Mughrabi, H., Ungár, T., Kienle, W., and Wilkens, M. (1986). Long-range internal stresses and asymmetric X-ray line-broadening in tensile-deformed [001]-orientated copper single crystals. Philos. Mag. A *53*, 793–813.

Needleman, A., and Gil Sevillano, J. (2003). Preface to the viewpoint set on: geometrically necessary dislocations and size dependent plasticity. Scr. Mater. *48*, 109–111.

Nellessen, J., Sandlöbes, S., and Raabe, D. (2015). Effects of strain amplitude, cycle number and orientation on low cycle fatigue microstructures in austenitic stainless steel studied by electron channelling contrast imaging. Acta Mater. *87*, 86–99.

Neumann, P. (1987). Dislocation Dynamics in Fatigue. Phys. Scr. *1987*, 537.

Niederberger, C., Mook, W.M., Maeder, X., and Michler, J. (2010). In situ electron backscatter diffraction (EBSD) during the compression of micropillars. Mater. Sci. Eng. A *527*, 4306–4311.

Nye, J.F. (1953). Some geometrical relations in dislocated crystals. Acta Metall. *1*, 153–162.

Oddershede, J., Schmidt, S., Poulsen, H.F., Margulies, L., Wright, J., Moscicki, M., Reimers, W., and Winther, G. (2011). Grain-resolved elastic strains in deformed copper measured by three-dimensional X-ray diffraction. Mater. Charact. *62*, 651–660.

Oddershede, J., Wright, J.P., Beaudoin, A., and Winther, G. (2015). Deformation-induced orientation spread in individual bulk grains of an interstitial-free steel. Acta Mater. *85*, 301–313.

Oh, S.H., Legros, M., Kiener, D., and Dehm, G. (2009). In situ observation of dislocation nucleation and escape in a submicrometre aluminium single crystal. Nat. Mater. *8*, 95–100.

Overton, W.C., and Gaffney, J. (1955). Temperature Variation of the Elastic Constants of Cubic Elements. I. Copper. Phys. Rev. *98*, 969–977.

Pang, J.W.L., Liu, W., Budai, J.D., and Ice, G.E. (2014). Inhomogeneous deformation behavior in intercrystalline regions in polycrystalline Ni. Acta Mater. *65*, 393–399.

Pantleon, W. (2008). Resolving the geometrically necessary dislocation content by conventional electron backscattering diffraction. Scr. Mater. *58*, 994–997.

Pantleon, W., Wejdemann, C., Jakobsen, B., Lienert, U., and Poulsen, H.F. (2009). Evolution of deformation structures under varying loading conditions followed in situ by high angular resolution 3DXRD. Mater. Sci. Eng. A *524*, 55–63.

Pantleon, W., Wejdemann, C., Jakobsen, B., Poulsen, H.F., and Lienert, U. (2014). High-Resolution Reciprocal Space Mapping for Characterizing Deformation Structures. In Strain and Dislocation Gradients from Diffraction, (IMPERIAL COLLEGE PRESS), pp. 322–357.

Perreault, B., Viñals, J., and Rickman, J.M. (2016). Impact of lattice rotation on dislocation motion. Phys. Rev. B *93*, 14107.

Pham, M.-S., and Holdsworth, S.R. (2013). Evolution of Relationships Between Dislocation Microstructures and Internal Stresses of AISI 316L During Cyclic Loading at 293 K and 573 K (20 °C and 300 °C). Metall. Mater. Trans. A *45*, 738–751.

Pham, M.S., Solenthaler, C., Janssens, K.G.F., and Holdsworth, S.R. (2011). Dislocation structure evolution and its effects on cyclic deformation response of AISI 316L stainless steel. Mater. Sci. Eng. A *528*, 3261–3269.

Po, G., Mohamed, M.S., Crosby, T., Erel, C., El-Azab, A., and Ghoniem, N. (2014). Recent Progress in Discrete Dislocation Dynamics and Its Applications to Micro Plasticity. JOM *66*, 2108–2120.

Pollock, T.M., and LeSar, R. (2013). The feedback loop between theory, simulation and experiment for plasticity and property modeling. Curr. Opin. Solid State Mater. Sci. *17*, 10–18.

Poulsen, H.F., Schmidt, S., Jensen, D.J., Sørensen, H.O., Lauridsen, E.M., Olsen, U.L., Ludwig, W., King, A., Wright, J.P., and Vaughan, G.B.M. (2014). 3D X-ray diffraction microscopy. In Strain and Dislocation Gradients from Diffraction, (IMPERIAL COLLEGE PRESS), pp. 205–253.

Prinz, F., and Argon, A. (1980). Dislocation Cell-Formation During Plastic-Deformation of Copper Single-Crystals. Phys. Status Solidi -Appl. Res. *57*, 741–753.

Rittel, D., Lee, S., and Ravichandran, G. (2002). A shear-compression specimen for large strain testing. Exp. Mech. *42*, 58–64.

Roters, F., Eisenlohr, P., Hantcherli, L., Tjahjanto, D.D., Bieler, T.R., and Raabe, D. (2010). Overview of constitutive laws, kinematics, homogenization and multiscale methods in crystal plasticity finite-element modeling: Theory, experiments, applications. Acta Mater. *58*, 1152–1211.

Rouault-Rogez, H. (1990). Comportement à haute température du superalliage monocristallin à base nickel CMSX-2. Thèse de doctorat. Impr. Ecole nationale sup. electrochim. electrometall.

Sandfeld, S., and Zaiser, M. (2015). Pattern formation in a minimal model of continuum dislocation plasticity. Model. Simul. Mater. Sci. Eng. *23*, 65005.

Sandfeld, S., Hochrainer, T., Gumbsch, P., and Zaiser, M. (2010). Numerical implementation of a 3D continuum theory of dislocation dynamics and application to micro-bending. Philos. Mag. *90*, 3697–3728.

Saxlová, M., Kratochvíl, J., and Zatloukal, J. (1997). The model of formation and disintegration of vein dislocation structure. Mater. Sci. Eng. A *234–236*, 205–208.

Schäfer, C., Urbassek, H.M., and Zhigilei, L.V. (2002). Metal ablation by picosecond laser pulses: A hybrid simulation. Phys. Rev. B *66*.

Schwarz, K.W., and Mughrabi, H. (2006). Interaction and passing stress of two threading dislocations of opposite sign in a confined channel. Philos. Mag. Lett. *86*, 773–785.

Shehadeh, M.A. (2012). Multiscale dislocation dynamics simulations of shock-induced plasticity in small volumes. Philos. Mag. *92*, 1173–1197.

Song, Hofmann, F., and Korsunsky, A. (2010). Dislocation-based plasticity model and micro-beam Laue diffraction analysis of polycrystalline Ni foil: A forward prediction. Philos. Mag. *90*.

Stafe, M., Marcu, A., and Puscas, N.N. (2014). Pulsed Laser Ablation of Solids (Berlin, Heidelberg: Springer Berlin Heidelberg).

Suresh, S. (1998). Fatigue of Materials (Cambridge University Press).

Swygenhoven, H.V., and Petegem, S.V. (2010). The use of Laue microdiffraction to study small-scale plasticity. JOM *62*, 36–43.

Tong, V., Jiang, J., Wilkinson, A.J., and Ben Britton, T. (2015). The effect of pattern overlap on the accuracy of high resolution electron backscatter diffraction measurements. Ultramicroscopy *155*, 62–73.

Vattré, A., Devincre, B., Feyel, F., Gatti, R., Groh, S., Jamond, O., and Roos, A. (2014). Modelling crystal plasticity by 3D dislocation dynamics and the finite element method: The Discrete-Continuous Model revisited. J. Mech. Phys. Solids *63*, 491–505.

Viladot, D., Véron, M., Gemmi, M., Peiró, F., Portillo, J., Estradé, S., Mendoza, J., Llorca-Isern, N., and Nicolopoulos, S. (2013). Orientation and phase mapping in the transmission electron microscope using precession-assisted diffraction spot recognition: state-of-the-art results. J. Microsc. *252*, 23–34.

Walgraef, D., and Aifantis, E.C. (1985a). On the formation and stability of dislocation patterns—I: One-dimensional considerations. Int. J. Eng. Sci. *23*, 1351–1358.

Walgraef, D., and Aifantis, E.C. (1985b). Dislocation patterning in fatigued metals as a result of dynamical instabilities. J. Appl. Phys. *58*, 688.

Walgraef, D., and Aifantis, E.C. (1986). Dislocation patterning in fatigued metals: Labyrinth structures and rotational effects. Int. J. Eng. Sci. *24*, 1789–1798.

Wejdemann, C., Poulsen, H.F., Lienert, U., and Pantleon, W. (2013). In Situ Observation of the Dislocation Structure Evolution During a Strain Path Change in Copper. JOM *65*, 35–43.

Wilkens, M., Herz, K., and Mughrabi, H. (1980). An X-Ray Diffraction Study of Cyclically and of Unidirectionally Deformed Copper Single Crystals. Z. Für Met. *71*, 376–386.

Wilkinson, A.J. (2011). Assessment of lattice strain, rotation and dislocation content using electron back-scatter diffraction. J. Phys. Conf. Ser. *326*, 12004.

Wilkinson, A.J., and Britton, T.B. (2012). Strains, planes, and EBSD in materials science. Mater. Today *15*, 366–376.

Wilkinson, A.J., Meaden, G., and Dingley, D.J. (2006a). High-resolution elastic strain measurement from electron backscatter diffraction patterns: New levels of sensitivity. Ultramicroscopy *106*, 307–313.

Wilkinson, A.J., Meaden, G., and Dingley, D.J. (2006b). High resolution mapping of strains and rotations using electron backscatter diffraction. Mater. Sci. Technol. *22*, 1271–1278.

Winter, A.T., Pedersen, O.R., and Rasmussen, K.V. (1981). Dislocation microstructures in fatigued copper polycrystals. Acta Metall. *29*, 735–748.

Wright, S.I., and Nowell, M.M. (2009). A Review of In Situ EBSD Studies. In Electron Backscatter Diffraction in Materials Science, A.J. Schwartz, M. Kumar, B.L. Adams, and D.P. Field, eds. (Springer US), pp. 329–337.

Wright, S.I., Field, D.P., and Nowell, M.M. (2015). Post processing effects on GND calculations from EBSD-based orientation measurements. IOP Conf. Ser. Mater. Sci. Eng. *89*, 12049.

Xia, S., and El-Azab, A. (2015a). Computational modelling of mesoscale dislocation patterning and plastic deformation of single crystals. Model. Simul. Mater. Sci. Eng. *23*, 55009.

Xia, S.X., and El-Azab, A. (2015b). A preliminary investigation of dislocation cell structure formation in metals using continuum dislocation dynamics. IOP Conf. Ser. Mater. Sci. Eng. *89*, 12053.

Xiao, S., Schöps, B., and Ostendorf, A. (2012). Selective Ablation of Thin Films by Ultrashort Laser Pulses. Phys. Procedia *39*, 594–602.

Yamasaki, S., Mitsuhara, M., Ikeda, K., Hata, S., and Nakashima, H. (2015). 3D visualization of dislocation arrangement using scanning electron microscope serial sectioning method. Scr. Mater. *101*, 80–83.

Yang, J., Li, Y., Li, S., Ma, C., and Li, G. (2001). Simulation and observation of dislocation pattern evolution in the early stages of fatigue in a copper single crystal. Mater. Sci. Eng. A *299*, 51–58.

Yang, W., Larson, B.., Tischler, J.., Ice, G.., Budai, J.., and Liu, W. (2004). Differential-aperture X-ray structural microscopy: a submicron-resolution three-dimensional probe of local microstructure and strain. Micron *35*, 431–439.

Zaefferer, S. (2011). A critical review of orientation microscopy in SEM and TEM. Cryst. Res. Technol. *46*, 607–628.

Zaefferer, S., and Elhami, N.-N. (2014). Theory and application of electron channelling contrast imaging under controlled diffraction conditions. Acta Mater. *75*, 20–50.

Zhang, J. -l., Zaefferer, S., and Raabe, D. (2015). A study on the geometry of dislocation patterns in the surrounding of nanoindents in a TWIP steel using electron channeling contrast imaging and discrete dislocation dynamics simulations. Mater. Sci. Eng. A *636*, 231–242.

Zhou, C., Reichhardt, C., Olson Reichhardt, C.J., and Beyerlein, I.J. (2015). Dynamic Phases, Pinning, and Pattern Formation for Driven Dislocation Assemblies. Sci. Rep. *5*, 8000.

Zhu, Y., and Chapman, S.J. (2014). A Natural Transition Between Equilibrium Patterns of Dislocation Dipoles. J. Elast. *117*, 51–61.

Zimmermann, J.R.A. (2011). In-situ Laue Diffraction During Compression of Directionally Solidified Mo Micropillars. École polytechnique fédérale de Lausanne EPFL, n° 5196.

Zimmermann, J., Van Swygenhoven, H., Marichal, C., Van Petegem, S., Borca, C., Bartova, B., Oveisi, E., and Hebert, C. (2012a). Slip in directionally solidified Mo-alloy micropillars – Part I: Nominally dislocation-free pillars. Acta Mater. *60*, 4604–4613.

Zimmermann, J., Van Swygenhoven, H., Van Petegem, S., and Borca, C. (2012b). Slip in directionally solidified Mo-alloy micropillars—Part II: Pillars containing defects. Acta Mater. *60*, 4614–4622.

Appendix

A. Drawings of the geometry of the sample

<div style="text-align:center">

Dimensions

Schematic

</div>
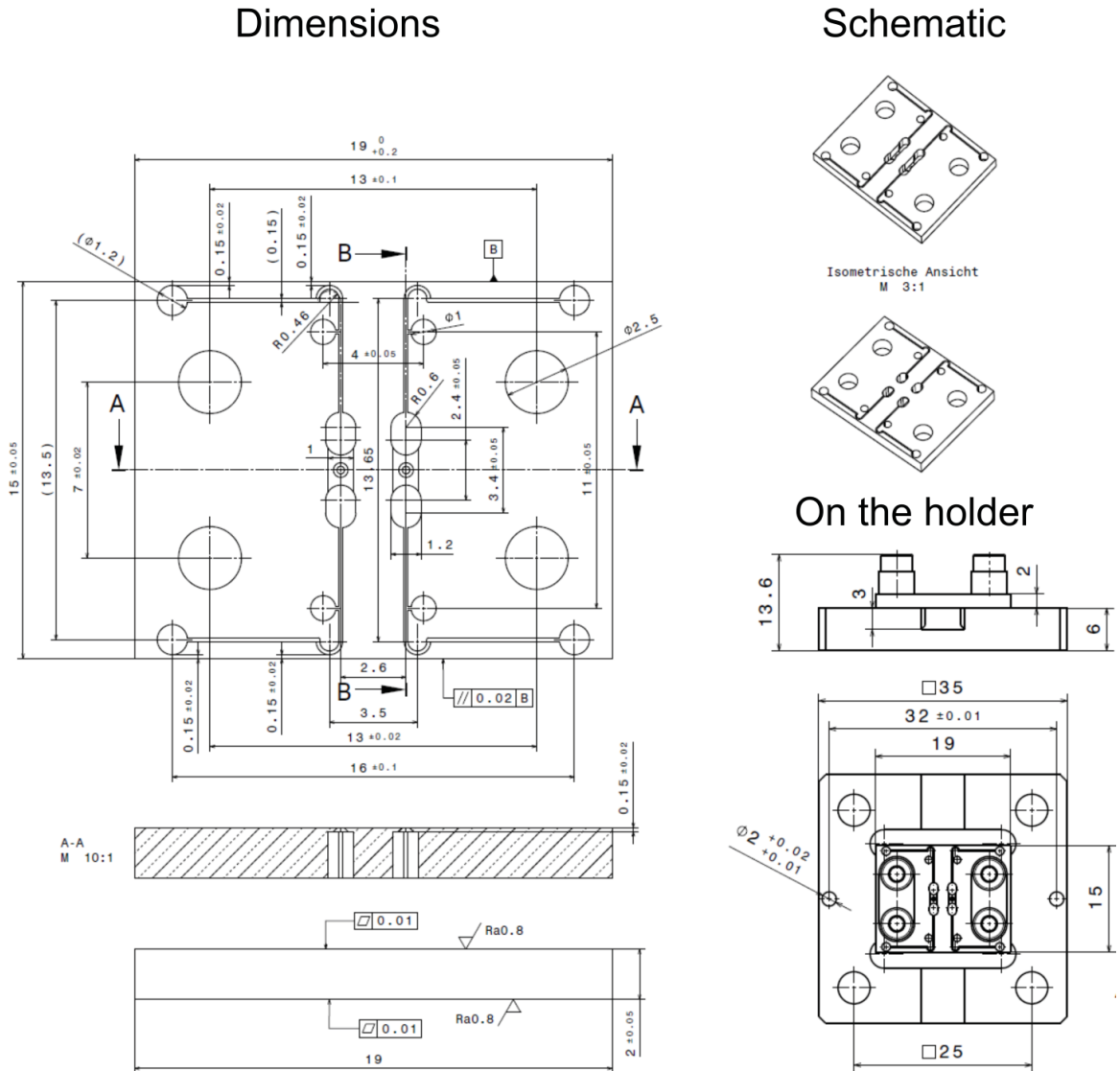
Appendix Figure 1 Drawings of the geometry of the sample

B. Simulation model and materials parameters

The computational method used for the simulations in this thesis is based on the CPFE method and the dislocation based constitutive laws are implemented in the DAMASK, Düsseldorf Advanced Material Simulation Kit, code. For more details see (Grilli et al., 2015; Roters et al., 2010).

The CPFE method is formulated within the framework of finite strains and the deformation gradient $\boldsymbol{F}$ is multiplicatively decomposed into elastic and plastic components:

$$\boldsymbol{F} = \boldsymbol{F}_e\boldsymbol{F}_p$$

The elastic deformation gradient is related to the stress by an anisotropic elastic stiffness:

$$S = C_{ij}(F_e F_e - I)/2$$

On other hand, the plastic deformation evolves as $L_p F_p$ where L_p is the velocity gradient owing to the plastic deformation. In the crystal plasticity formulation L_p is defined as the sum of the shear rates ($\dot{\gamma}^\alpha$) on all slip systems (α):

$$L_p = \sum_{\alpha=1}^{n} \dot{\gamma}^\alpha m^\alpha \otimes n^\alpha$$

where vectors m^α and n^α are, respectively, unit vectors describing the slip direction and the normal to the slip plane of the slip system α.

Constitutive laws based on the phenomenological description (Hutchinson, 1976) are used to relate the plastic shearing rate on the αth slip system to the resolved shear stress, τ^α:

$$\dot{\gamma}^\alpha = \dot{\gamma}_0 \left| \frac{\tau^\alpha}{g^\alpha} \right|^n sgn(\tau^\alpha)$$

with $\dot{\gamma}_0$ as a reference shear strain rate, g^α as slip system resistance parameter and n the stress exponent.

The slip system resistance evolves from g_o to g_{sat} with shear , γ^β as:

$$\dot{g}^\alpha = \sum_{\beta} h_o h_{\alpha\beta} \left| 1 - \frac{g^\beta}{g_{sat}} \right|^a |\dot{\gamma}^\beta|$$

Pure copper single crystal parameters from (Déprés et al., 2008; Dmitrieva et al., 2009; Overton and Gaffney, 1955) have been used.

Appendix Table 1 summarizes the material parameters used for the simulations done in this thesis.

Appendix Table 1 Material parameters used for simulations

Elastic constant [GPa]	c_{11}	165.00
	c_{12}	117.52
	c_{44}	75.68
Stress exponent	n	20
Initial value of slip resistance parameter [MPa]	g_o	10
Saturation value of slip resistance parameter [MPa]	g_{sat}	30
Reference shear strain rate	$\dot{\gamma}_0$	0.01
Hardening paremeter	$h_{\alpha\beta}$	1
	a	0.01
	h_o	100

C. Drawings of the machine
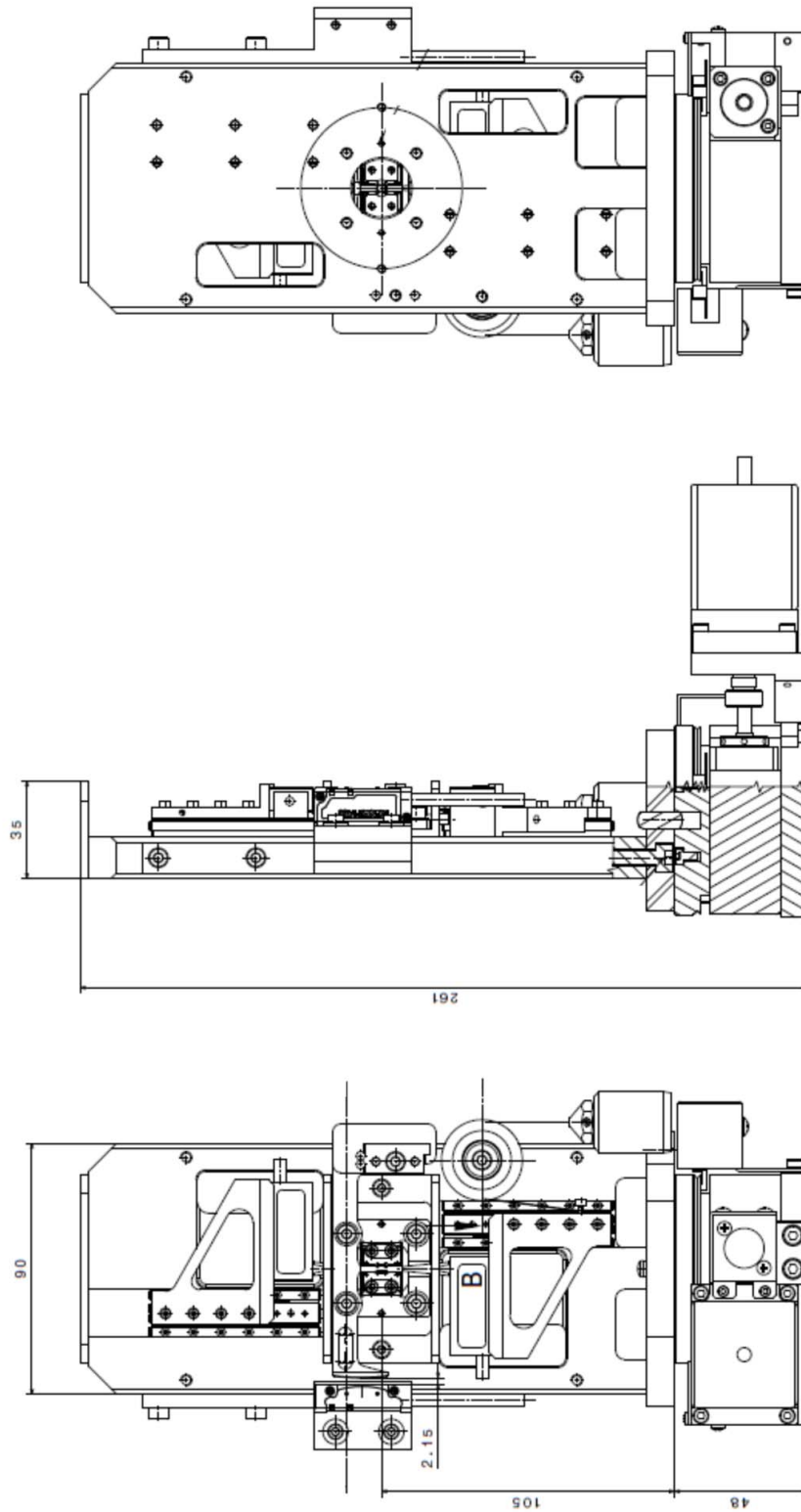
Appendix Figure 2 Drawings of the machine

D. Statistical representation of data

In this thesis two statistical representations are used: the probability density function (PDF) and boxplots. Both of them are briefly discussed in this section.

Probability density function

The *PDF* of misorientation angle and amount of rotation around the *X-, Y-*, and *Z-* axes (ω_x, ω_y and ω_z) are given by the non-parametric normal kernel distribution. The kernel distribution is suitable when one wants to avoid making assumptions about the distribution of the data. The kernel distribution builds the PDF by creating an individual probability density curve for each data value and then summing the smooth curves. This approach creates one smooth, continuous probability density function for the data set. More information can be found in (Mathworks website).

On the other hand, the *mode* is the value that appears most often in a set of data. In the PDF is the value at which its probability mass function takes its maximum value. In this thesis sub-mode is called to the maximum value of a sub-peak.

Appendix Figure 3 shows graphically all the concepts. The smaller dashed curves are the probability distributions for each value in the sample data and the larger solid curve is the overall kernel distribution.
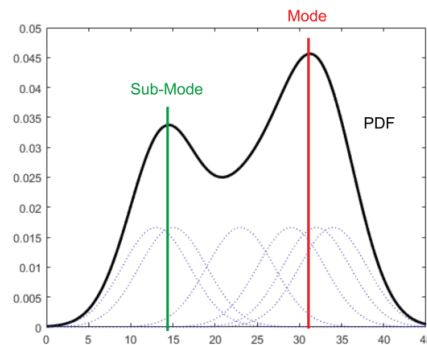
Appendix Figure 3 Non-parametric normal kernel distribution and definition of mode and sub-mode. Adapted from (Mathworks website)

Boxplots

The box plot is a quick way of examining one or more sets of data graphically. Each box represents the middle fifty of the population. The tops and bottoms of each box are the 25th and 75th percentiles of the samples, respectively. The total length of the box is the interquartile range (IQR). The whiskers, in other words the arms, extend till 1.5×IQR. The line inside the box is the sample median. The points plotted as '+' symbol are outliers that are values outside the |1.5*IQR| range. The maximum and minimum outlier defines the total range of the distribution. The visual representation of a boxplot is given in Appendix Figure 4.
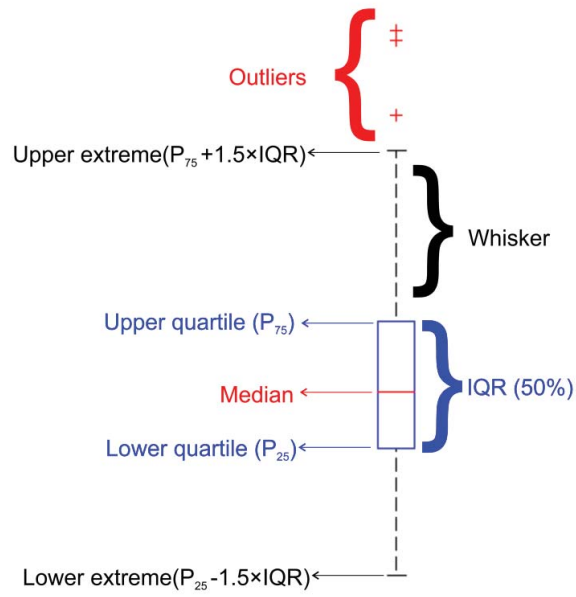
Appendix Figure 4 Visual representation of a boxplot. Adapted from (Mathworks website)

E. Evolution of the slip resistance parameter in single slip sample
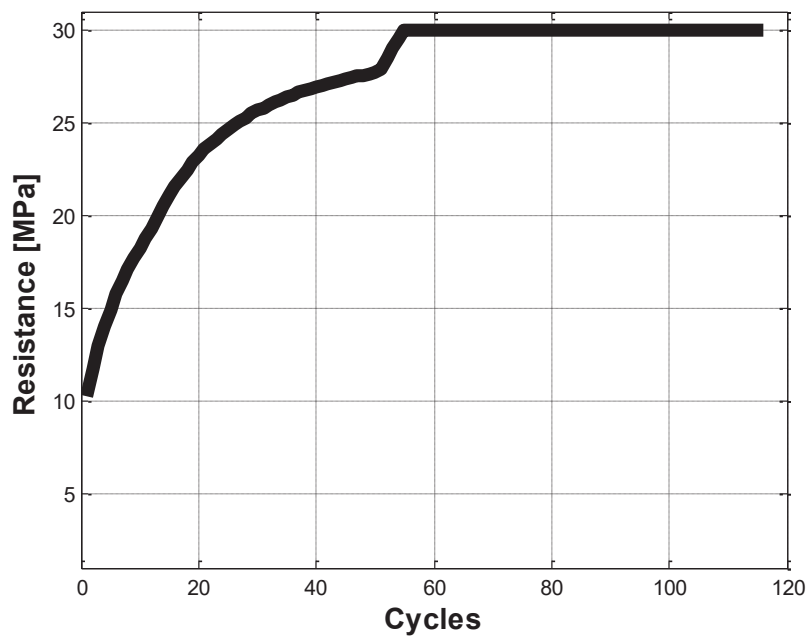
Appendix Figure 5 Evolution of the slip resistance parameter in single slip sample

F. Relationship between computed and experimental strains

Orientation	Fit	Norm of residuals
Single slip		0.046476
Coplanar		0.18426
Collinear		0.055124

Appendix Figure 6 Linear fits between computed and experimental strains

G. Lattice curvatures of infinite edge dislocation with its line along Z-axis

As explained in section 2.3.3, the curvature tensor κ_{ij} describes the relative misorientation and is defined as the gradient of the rotation about the 'i' axis along the 'j' direction:

$$\kappa_{ij} = \frac{\partial \theta_i}{\partial x_j} \quad \text{with} \quad \{i, j\} = \{x, y, z\}$$

where $\boldsymbol{\theta}$ is the lattice rotation vector:

$$\theta_k = -\frac{\epsilon_{kij}\omega_{ij}}{2} \quad \text{with} \quad \{i, j, k\} = \{x, y, z\}$$

and where $\boldsymbol{\omega}$ is the lattice rotation tensor (Pantleon, 2008).

This yields to:

$$\theta_x = \omega_{zy} \qquad \theta_y = \omega_{xz} \qquad \theta_z = \omega_{yx}$$

The lattice rotation field is defined as:

$$\omega_{ij} = \frac{1}{2}\left(\frac{\partial u_i}{\partial x_j} - \frac{\partial u_j}{\partial x_i}\right) \quad \text{with} \ \ \{i,j\} = \{x,y,k\}$$

where u is the elastic distortion field (Acharya and Knops, 2013).

The elastic distortion field of a straight dislocation in an infinitely extended isotropic body with the dislocation line along the Z- axis is as follows (deWit, 1973):

$$u_x = b_x\left[\frac{\varphi}{2\pi} + \frac{x_x x_y}{4\pi(1-\nu)\rho^2}\right] + \frac{b_y}{4\pi(1-\nu)}\left[(1-2\nu)\ln\rho + \frac{x_y^2}{\rho^2}\right]$$

$$u_y = -\frac{b_x}{4\pi(1-\nu)}\left[(1-2\nu)\ln\rho + \frac{x_{yx}^2}{\rho^2}\right] + b_y\left[\frac{\varphi}{2\pi} + \frac{x_x x_y}{4\pi(1-\nu)\rho^2}\right]$$

$$u_z = \frac{b_z \varphi}{2\pi}$$

where

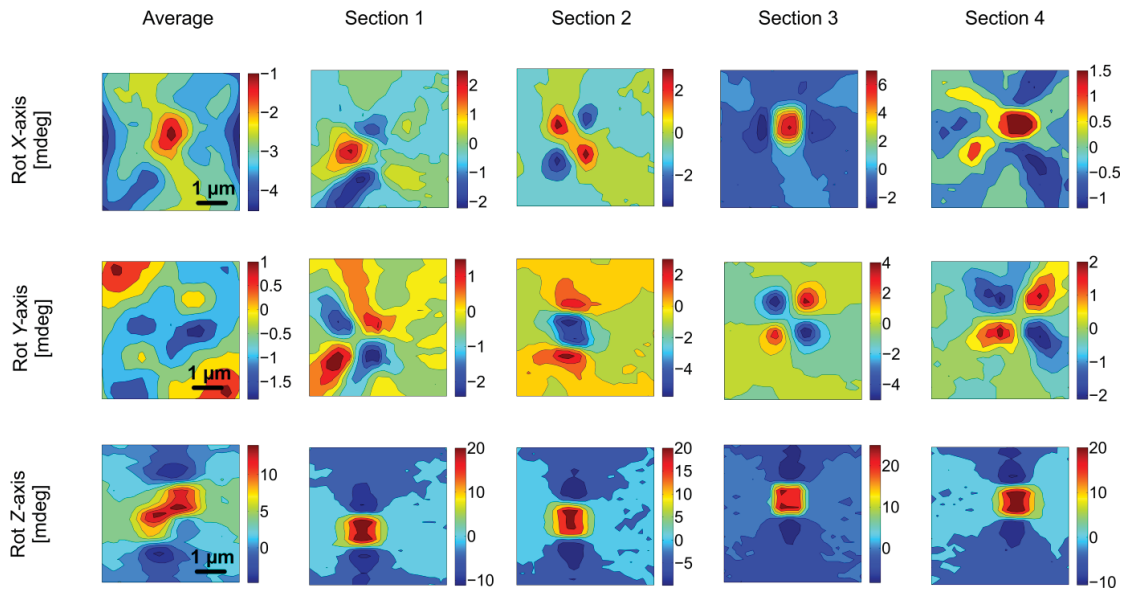$$\rho = \sqrt{x_x^2 + x_y^2}$$

$$\varphi = \tan^{-1}\left(\frac{x_y}{x_x}\right)$$

Now, computing:

$$\omega_{zy} = \frac{1}{2}\left(\frac{\partial u_z}{\partial x_y} - \frac{\partial u_y}{\partial x_z}\right) = 0$$

$$\omega_{xz} = \frac{1}{2}\left(\frac{\partial u_x}{\partial x_z} - \frac{\partial u_z}{\partial x_x}\right) = 0$$

$$\omega_{yx} = \frac{1}{2}\left(\frac{\partial u_y}{\partial x_x} - \frac{\partial u_x}{\partial x_y}\right) \neq 0$$

This yield to the fact that $\theta_z(x,y)$ is the only non-zero component and therefore κ_{zx} and κ_{zy} are the only lattice curvatures induced by an infinite edge dislocation with its line along Z-axis.

H. Average and sectional rotation fields of long *Y&X*-inclined long bundle

Appendix Figure 7 Average and sectional rotation fields of the *Y&X*-inclined long bundle

Curriculum Vitae

PERSONAL INFORMATION

Name, Surname	**Ainara Irastorza Landa**
Date of birth	September 6, 1988
Place of birth	Zarautz, Spain

EDUCATION

06/2012 – Present	**École polytechnique fédérale de Lausanne (EPFL)** PhD Materials Science and Engineering, Prof. H. Van Swygenhoven Located at PSI-Villigen	Switzerland
09/2006 – 04/2012	**Tecnun, University of Navarra** Mechanical Engineering. Minor in Materials Science	Spain
09/2011 – 03/2012	**Carnegie Mellon University (CMU)** Final Master Project, Prof. J. O. Hollinger	USA
09/2010 – 12/2010	**Technical University of Denmark (DTU)** Exchange student under ERASMUS programme	Denmark

PUBLICATIONS

JOURNALS

- Betz, B., Rauscher, P., Harti, R. P., Schäfer, R., **Irastorza-Landa, A.,** Van Swygenhoven, H., Kaestner, A., Hovind, J., Pomjakushina, E., Lehmann, E., Grünzweig C. (2016) Magnetization response of the bulk and supplementary magnetic domain structure in high-permeability steel laminations visualized in situ by neutron dark-field imaging. Accepted in Phys. Rev. Applied
- **Irastorza-Landa, A.,** Van Swygenhoven, H., Van Petegem, S., Grilli, N., Bollhalder, A., Brandstetter, S., and Grolimund, D. (2016). Following dislocation patterning during fatigue. Acta Mater. 112, 184–193.
- Guitton, A., **Irastorza-Landa, A.,** Broennimann, R., Grolimund, D., Van Petegem, S., and Van Swygenhoven, H. (2015). Picosecond pulsed laser for microscale sample preparation. Mater. Lett. 160, 589–591.
- Averick, S.E., Paredes, E., **Irastorza, A.,** Shrivats, A.R., Srinivasan, A., Siegwart, D.J., Magenau, A.J., Cho, H.Y., Hsu, E., Averick, A.A., et al. (2012). Preparation of Cationic Nanogels for Nucleic Acid Delivery. Biomacromolecules 13, 3445–3449.
- **Irastorza, A.,** Luque, A., Aldazabal, J., Martinez-Esnaola, J.M., and Gil Sevillano, J. (2010). On the effect of intergranular nanocracks on the shear-coupled migration of tilt boundaries. Ciênc. Tecnol. Mater. 22, 32–39.

CONFERENCE PAPERS

- **Irastorza, A.,** Luque, A., Aldazabal, J., Martínez-Esnaola, J.M., Gil-Sevillano, J. (2010). Size Effect in the Shear-Coupled Migration of Tilt Boundaries with Intergranular Nanocracks. Anales de Mecánica de la Fractura 27, 491-496
- **Irastorza, A.,** Luque, A., Aldazabal, J., Martínez-Esnaola, J.M., Gil-Sevillano, J. (2009) Estudio atomístico de la propagación de grietas en monocristales de Fe- agrietados. Anales de Mecánica de la Fractura 26, 388-393

SUBMITTED

- **Irastorza-Landa, A.**, Grilli, N., Van Swygenhoven, H., *Laue micro-diffraction and crystal plasticity finite element simulations to reveal a vein structure in fatigued Cu*

IN PREPARATION

- **Irastorza-Landa, A.**, Grilli, N., Van Swygenhoven, H., *Effect of pre-existing immobile dislocations on the evolution of geometrically necessary dislocations during fatigue*

CONFERENCES/WORKSHOPS

- **Materials Research Society MRS Fall Meeting,** Boston, USA, Nov 29 – Dec 4, 2015
  Oral: In-situ Laue Micro-Diffraction During Cyclic Plastic Deformation of Copper Under Shear
- **17th International Conference on the Strength of Materials, ICSMA17,** Brno, Czech Republic, Aug 9 – 14, 2015
  Oral: In-situ Laue Micro-Diffraction During Cyclic Plastic Deformation of Copper Under Shear
- **9th European Solid Mechanics Conference, ESMC15,** Madrid, Spain, July 6 – 10, 2015
  Oral: In-situ Laue Micro-Diffraction During Cyclic Plastic Deformation of Copper Under Shear
- **Materials Research Society MRS Fall Meeting**, Boston, USA, Nov 30 – Dec 4, 2014
  Oral: In-situ Laue Micro-Diffraction During Cyclic Plastic Deformation of Copper Under Shear
- **Materials Science Engineering, MSE**, Darmstadt, Germany, Sept 23 – 25, 2014
  Oral: In-situ Laue Micro-Diffraction During Cyclic Plastic Deformation of Copper Under Shear
- **20th Users' Meeting & Workshops**, Hsinchu, Taiwan, Sept 10 – 12, 2014
  Oral: Miniaturized mechanical testing during Laue diffraction
- **GDRiCNRS Mecano General Meeting**, Thun, Switzerland, Sept 4 – 5, 2014
  Oral: In-situ Laue micro-diffraction during cyclic plastic deformation of copper under shear
- **Materials Science & Technology MS&T'13**, Montreal, Canada, Oct 27 – 31, 2013
  Oral: Plasticity in W and W6%Re: in-situ Laue diffraction
- **Nanomechanical Testing in Materials Research & Development IV**, Olhão, Portugal, Oct 6 – 11, 2013
  Poster: Anomalous slip in W and W6%Re: in-situ Laue micro-diffraction
- **Euromat 2013**, Sevilla, Spain, Sept 8 – 13, 2013
  Poster: Anomalous slip in W and W6%Re: in-situ Laue micro-diffraction
- **GDRiCNRS Mecano General Meeting**, Düsseldorf, Germany, 18 – 19 July 2013
  Oral: Anomalous slip in W and W6%Re: in-situ Laue diffraction